World Renewable Energy Congress – Sweden

8–13 May, 2011
Linköping, Sweden

Editor

Professor Bahram Moshfegh

Linköping Electronic Conference Proceedings, 57
Linköping University Electronic Press
Linköping, Sweden, 2011

http://www.ep.liu.se/ecp_home/index.en.aspx?issue=057
ISBN: 978-91-7393-070-3
ISSN 1650-3740 (online)
ISSN 1650-3686 (print)

Volume 9

Marine and Ocean Technology

Table of Contents

Assessment of a multi-cell fabric structure as an attenuating wave energy converter

M.R.Hann[1,*], J.R.Chaplin[1], F.J.M. Farley[1]

[1] University of Southampton, UK
* Corresponding author. Tel: +44 23 8059 4656, E-mail: mrh1g08@soton.ac.uk

Abstract: Fabriconda is an attenuating wave energy device constructed from inelastic fabric. It is a flooded distensible tube constructed from a series of smaller flooded tubes, called cells, joined longitudinally. This paper presents a theory to predict the shape a Fabriconda forms at different tube and cell pressures and shows it successfully predicts the shape of a model Fabriconda. A 1D linear finite difference simulation based on the conservation of fluid momentum and mass in both the central tube and cells provides a prediction of the free bulge wave speed along the device. Experiments using a piston to artificially generate a bulge wave within the central tube of a model Fabriconda have produced bulge speeds that demonstrate good agreement with these predictions.

Keywords: *Wave energy, Wave power device, Finite difference model*

Nomenclature

θ	half-vertex angle	
n	number of cells	
s	cell arc-length	m
p_t	tube pressure	Pa
p_c	cell pressure	Pa
r	radius of curvature of cell	m
T_1	fabric tension of cell – external interface	N
T_2	fabric tension of cell – tube interface	N
x	cell horizontal chord length	m
R	central tube radius	m
A_t	central tube cross-sectional area	m^2
A_c	cell cross-sectional area	m^2
A_0	initial, static cross-sectional area	m^2
ρ_o	density	$kg{\cdot}m^{-3}$

1. Introduction

The Anaconda wave energy converter [1], [2] consists of a submerged and flooded rubber distensible tube lying perpendicular to incoming wave fronts. As the waves pass over, they induce a series of travelling bulges in the tube, and an internal oscillatory flow. If the speed of free bulge waves is close to that of the external water waves, energy is progressively transferred to the flow inside the tube, terminating in a power take-off system.

The purpose of this paper is to outline initial work on a fabric version of the Anaconda, named the Fabriconda [3], [4]. In the Fabriconda, distensibility is provided not by the elasticity of the walls (as in the Anaconda), but by the form of construction of the tube. A number of tubes (or 'cells') made of inelastic fabric are joined together longitudinally to form a larger central tube (Fig.1). The tube and the cells are separately flooded. Local changes in the cross-sectional area of the tube are facilitated by changes in the shapes of the surrounding cells. When the cells are circular, the tube area is at a minimum; when the cells are flat it is at a maximum. The tube's distensibility and the speed of free bulge waves in it depend on the ratio of the pressure in the tube to that in the cells.

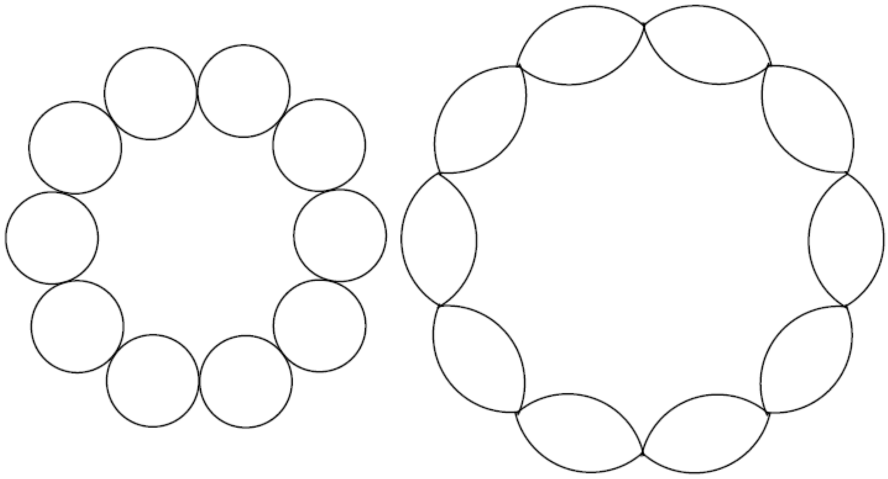

Fig. 1. Example cross-section of a Fabriconda with 10 cells, showing the structure at its minimum cross-section and at its medium point [3].

The potential advantages of this construction are that it removes the danger of aneurysm that can occur in rubber tubes. It also substantially reduces energy losses through hysteresis and construction may be cheaper. This paper presents the static shape theory of the Fabriconda and compares this with experimental results. A 1D finite difference model of the tube is introduced and used to predict the Fabriconda's free bulge speed. A comparison with measurements of free bulge speed is made.

2. Methodology

2.1. Static shape

The cells are lenticular in shape and are formed by the intersection of two circular arcs (fig. 2.). The geometry of a Fabriconda with *n* cells can be defined via the half vertex angle, θ. The half vertex angle depends on the fluid pressures p_t and p_c within the tube and cells and the arc length s, the width of fabric from which half a Fabriconda cell is constructed.

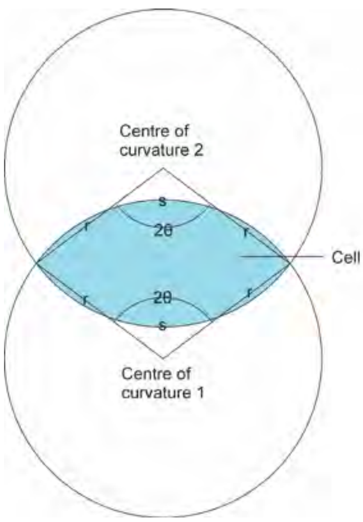

Fig. 2. – The formation of a lenticular shaped cell by two circular arcs.

By comparing the ratio that arc length s represents of the circle circumference to the ratio that 2θ represents of the whole circle equation 1 for circle radius is found:

$$r = \frac{s}{2\theta} \tag{1}$$

Simple geometry now gives *x*, the cell chord length and *R* the central tube radius (fig. 3.).

$$x = \frac{s\sin(\theta)}{\theta} \tag{2}$$

$$R = \frac{s\sin(\theta)}{2\theta\sin\left(\frac{\pi}{n}\right)} \tag{3}$$

Finally cell and tube areas can be defined, again in terms of the variable θ.

$$A_c = 2\left(\frac{s^2}{4\theta} - \frac{s^2 \sin(2\theta)}{8\theta^2}\right) \tag{4}$$

$$A_t = n\left(\frac{s^2 \sin^2(\theta)}{4\theta^2 \tan\left(\frac{\pi}{n}\right)} - \frac{s^2}{4\theta} + \frac{s^2 \sin(2\theta)}{8\theta^2}\right) \tag{5}$$

Each cell has two boundaries, the first between the cell and the external environment and the second between the cell and the tube. The pressure difference across these two boundaries generates separate tensions in the fabric defining the boundary, T_1 and T_2 (fig. 3).

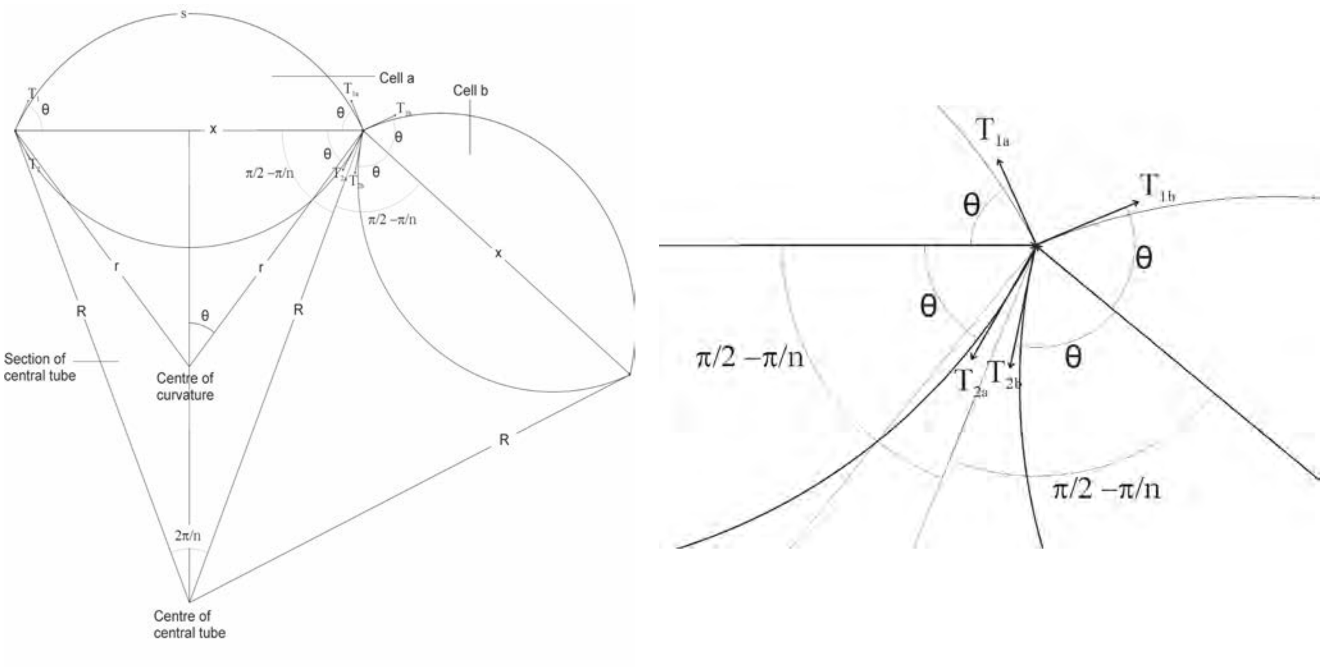

Fig. 3. Geometry of two Fabriconda cells

At the joint between cells the two tensions from each cell must balance. Using this condition a relationship between θ and T_2 and T_1 can be found:

$$\tan(\theta) = \frac{T_2 + T_1}{T_1 - T_2} \tan\left(\frac{\pi}{n}\right) \tag{6}$$

The two tensions are given by the pressure differences across the two boundaries and the cell radius of curvature. Applying this half vertex angle, and hence Fabriconda geometry, is defined in terms of cell and tube pressure:

$$\tan(\theta) = \frac{2p_c - p_t}{p_t}\tan\left(\frac{\pi}{n}\right). \tag{7}$$

2.2. 1D finite difference model

Predictions of how free bulge speed varies with the fluid pressure within the tube and cell have been made using a 1D finite difference model of the Fabriconda. The fabric is assumed to act as an inelastic membrane. Linear conservation of momentum (equation 8) and continuity (equation 9) are applied to the flow in a single cell and the 1/*n*th segment of central tube defined by that cell.

$$\rho_0 \frac{\partial u}{\partial t} = -\frac{\partial p}{\partial x} \tag{8}$$

$$\frac{\partial A}{\partial t} = -A_0 \frac{\partial u}{\partial x} \tag{9}$$

By differentiating equation 8 with respect to position and equation 9 with respect to time, velocity is eliminated from the problem, giving equation 10 to describe flow in the tube segment and equation 11 describing the flow in the cell.

$$\frac{\partial^2 A_t}{\partial t^2} = \frac{A_{to}}{\rho}\frac{\partial^2 p_t}{\partial x^2} \tag{10}$$

$$\frac{\partial^2 A_c}{\partial t^2} = \frac{A_{co}}{\rho}\frac{\partial^2 p_c}{\partial x^2} \tag{11}$$

Equations 4 and 5 are substituted into 10 and 11 to give two equations describing the dynamic properties of the device in terms of both tube and cell pressure. A Du Fort-Frankel finite difference scheme is applied to give two quadratic equations (equations 12 and 13) in terms of tube and cell pressure. The two pressures are solved at each time step using a Newton iteration method:

$$F = zp_{ti,j+1}^2 + yp_{ti,j+1} + mp_{ti,j+1}p_{ci,j+1} + wp_{ci,j+1} + vp_{ci,j+1}^2 + q = 0 \tag{12}$$

$$G = z_1 p_{ti,j+1}^2 + y_1 p_{ti,j+1} + m_1 p_{ti,j+1}p_{ci,j+1} + w_1 p_{ci,j+1} + v_1 p_{ci,j+1}^2 + q_1 = 0 \tag{13}$$

A sinusoidal fluctuation is applied to the bow boundary condition and the speed at which the resulting pressure bulge propagates along the Fabriconda tube is measured.

2.3. Experimental set-up and measurements

A 7.0m long, 10 cell, model Fabriconda with a cell arc length of 0.121 ± 0.003m was constructed to verify the static shape theory as well as to provide measurements of free bulge speed. The experimental set-up is shown in figure 4. The model was constructed from 450 decitex woven Nylon and each cell and the central tube had a 0.16mm latex inner tube inserted to make the device water tight. The central tube was connected to a 250mm diameter piston cylinder at one end and a 250mm diameter pipe with a 90^{o} bend at the other. This pipe was the first part of a power take off system not relevant to these measurements. The cells were closed at the piston cylinder end and connected to a cell reservoir via 1.4m long, 25mm diameter pipes at the other. The top of central tube was 100mm below the water surface.

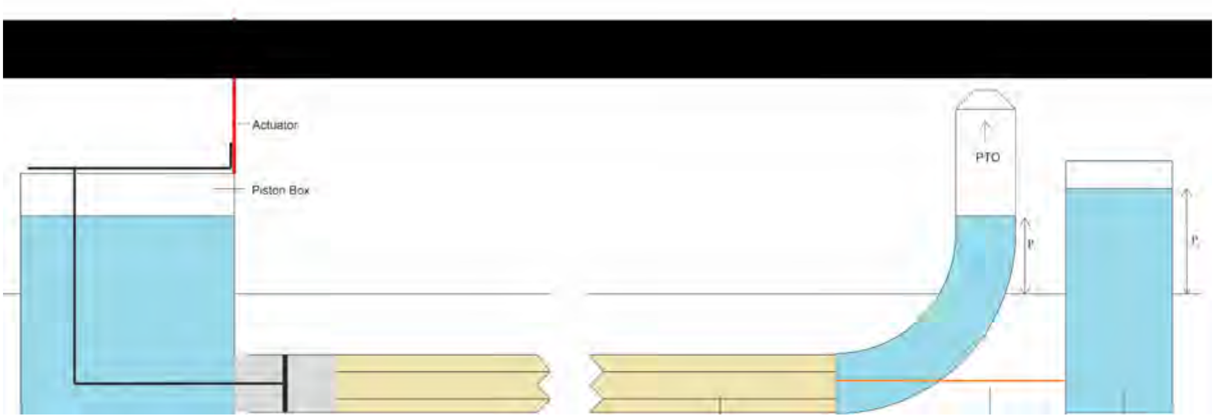

Fig. 4. Experimental set-up with piston in the main tube to artificially generate bulge waves.

Pressures within the model were measured simply using manometers connected to each cell and the central tube. To verify the static shape theory the model was inflated to various cell and tube pressure combinations and cell chord length (x) of the top cell measured using callipers.

Free bulge speed was measured by artificially generating bulge-waves using an actuator driven piston [5] producing a single sinusoidal oscillation. Nine pairs of 50mm long strain gauges were attached to a single cell, spaced evenly along the device with a separation of 75.0cm. These gauges recorded the curvature of the cell and hence the passage of the bulge produced by the piston oscillation. The time difference between the bulge arriving at each gauge allowed the bulge speed to be calculated.

3. Results

3.1. Static inflation shape

For various tube and cell pressures, figure 5 compares measured cell chord lengths with those obtained from the static theory above. Values of θ are calculated using equation 7 from the measured inflation pressures.

Agreement is seen to be satisfactory; the coefficient of determination (R^2) value between experimental values and theory is 0.97.

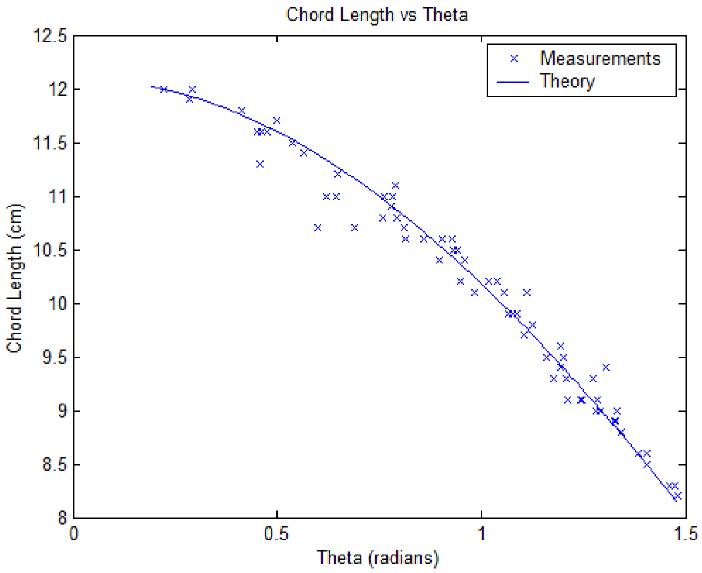

Fig. 5. Chord length measured from modelled during the inflation of a model Fabriconda compared to the value predicted by theory.

3.2. Bulge speed simulations and measurements

Figure 6 shows an example output from the strain gauge pairs attached to a cell of the model Fabriconda as a bulge wave generated by a piston oscillation propagates along the tube. Two speeds were measured by identifying the time difference between the two sets of equivalent points indicated in figure 6, the trough and the peak of the pressure bulge. The outputs used are from the 1st and 7th gauges as these provided the data sets that covered the longest available interval, 4.5m. Specific measurement points for the 9th gauge could often not be obtained owing to strong reflections from the tube end.

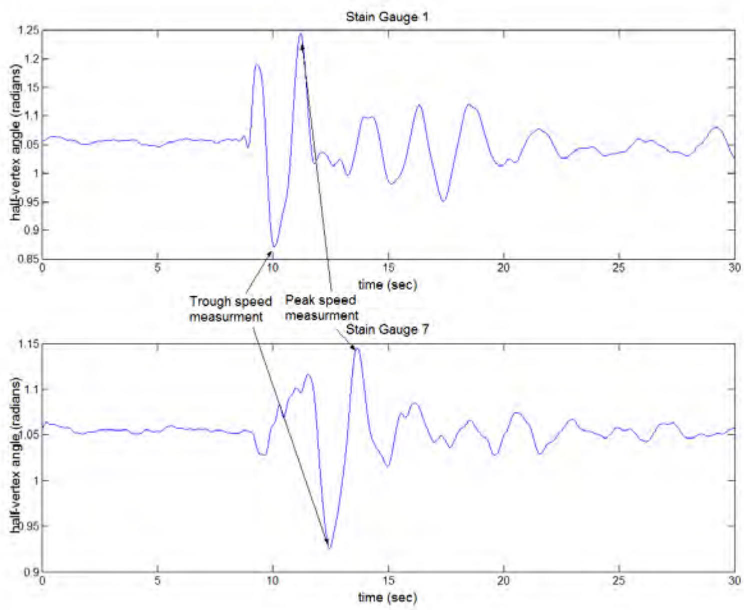

Fig. 6. Example gauge output showing free bulge propagation when p_t = 25.7m and p_c = 82.7m

Measurements of bulge speeds were made for a constant cell pressure at a head of 82.7cm, with tube pressures between a head of 4.2 cm and 39.0cm. The 1D finite difference model was used to provide predictions of how the speed of the free bulge propagation changed in this pressure regime. Figure 7 shows the results of these simulations and the experimental results found from the two pairs of points indicated in figure 6.

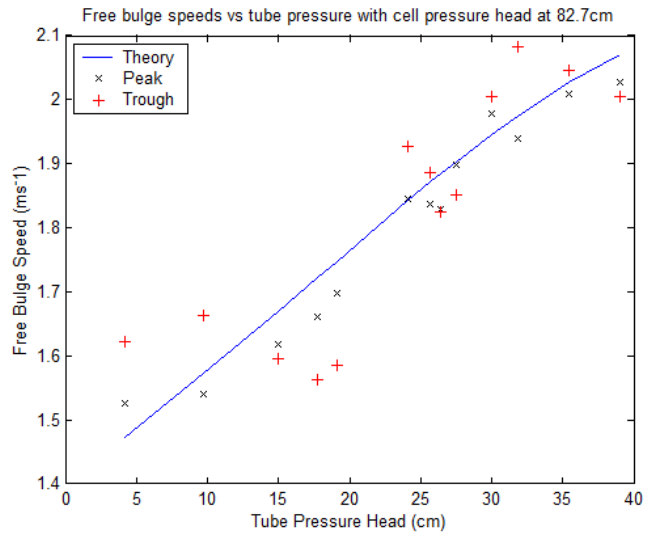

Fig. 7. Simulated and measured free bulge speed vs. tube pressure at a constant cell pressure.

4. Discussion

The results of the stationary inflation experiments (fig. 4) show good agreement between measured values and those predicted by theory. The theory assumes that the Fabriconda is fully submerged, which was the case during experimental measurements. An actual Fabriconda will actually be partially floating on the surface and bending in the vertical plane, potentially leading to distortions away from the symmetrical shape assumed in a similar fashion to that reported for floating cylindrical containers [6]. However the impact of this is likely to be small since changes in elevation along the device would be much less than the internal pressure head.

Measurements of the speed of bulge waves generated by an externally driven piston at one end of the tube show a good correlation with those predicted from numerical simulations, especially with respect to the propagation of the peaks in the strain gauge signals. These correspond to peaks in the half-vertex angle of the cell and correspondingly a trough in the bulge wave as the overall Fabriconda cross-section area reaches a minimum. The bulge speeds predicted by simulation in the tube pressure region investigated ranged from 1.47 ms^{-1} to 2.07 ms^{-1}. It is predicted that greater tube pressures should result in higher bulge speeds. Further experimentation is planned for these higher pressures.

5. Conclusion

This paper has introduced the concept of the Fabriconda, a distensible tube attenuating wave energy converter made from inelastic fabric. A theory for the static shape of the device has been presented along with experimental confirmation of its predictions. One-dimensional linear finite difference modelling suggests that the Fabriconda can be tuned to a wide range of different bulge speeds, and experimental results seem to confirm these predictions over a limited pressure range. Future work will measure experimentally the propagation speed of a free bulge wave versus both tube and cell pressure at higher pressure combinations before numerical and experimental measurements are made of Fabriconda capture width and bandwidth.

References

[1] Chaplin, J.R., Farley, F.J.M., Prentice, M.E., Rainey, R.C.T., Rimmer, S.J., Roach, A.T. Development of the anaconda all-rubber WEC, Proceeding of the 7th European Wave and Tidal Energy Conference, Lisbon 2007

[2] Farley, F.J.M., Rainey, R.C.T. Anaconda - The bulge wave sea energy converter. Technical Note 5 Nov 2006, online www.bulgewave.com, 2006

[3] Farley, F.J.M. All fabric Anaconda . Marine Energy Devices Ltd. Confidential memo paper, 2008.

[4] Farley, F.J.M. Fabriconda design and power take-off. Marine Energy Devices Ltd. Confidential memo paper, 2008.

[5] Heller, V., Chaplin, J. R., Farley, F. J. M, Hann, M. R. and Hearn, G. E. Physical model tests of the anaconda wave energy converter. In, First European Congress of the IAHR, Edinburgh, Scotland 2010

[6] Hawthorne, W. The early development of the dracone flexible barge, Proceedings of the institution of mechanical engineers 175, 1961, pp 52-83

The WaveCat© – Development of a new Wave Energy Converter

Gregorio Iglesias[1,*], Hernán Fernández[1], Rodrigo Carballo[1], Alberte Castro[1], Francisco Taveira-Pinto[2]

[1]*University of Santiago de Compostela, Spain*
[2]*Faculty of Engineering, University of Porto, Portugal*
** Corresponding author. Tel: +34 982823650, Fax: +34 982285926, E-mail: gregorio.iglesias@usc.es*

Abstract: The development of efficient, reliable Wave Energy Converters (WECs) is a fundamental prerequisite for wave energy to become a commercially viable energy source. Intensive research is currently under way on various technologies, among which WaveCat©—a new WEC recently patented by the University of Santiago de Compostela. The purpose of this paper is to present the WaveCat concept and the ongoing work toward its development. WaveCat is a floating offshore WEC whose principle of operation is wave overtopping. It consists of two hulls, like a catamaran (hence its name). Unlike a catamaran, however, the hulls are not parallel but convergent—they are joined at the stern, forming a wedge in plan view. The methodology adopted to develop this patent is based on physical model tests which are described in the paper. A 1:30 model was tested in a wave tank under regular and irregular waves; waves and overtopping rates were measured, as were the model displacements—the latter using an advanced motion capture system. The data thus obtained will be used to validate a 3D numerical model currently under development, which in turn will be used to optimize the design of WaveCat for best performance.

Keywords: *Wave energy converter, Overtopping, Physical modelling, Numerical modelling, CFD.*

Nomenclature

α	*wedge angle*	[–]
H	*wave height (regular waves)*	*m*
H_s	*significant wave height (irreg. waves)*	*m*
T	*wave period (regular waves)*	*s*
T_p	*peak wave period (irreg. waves)*	*s*

1. Introduction

In order to reduce the emissions of greenhouse gases it is crucial to work along two lines. The first is to develop the already operational renewable energy sources, such as wind or photovoltaic energy. The second is to research and develop new energy sources [1]. Among these, marine renewable energy has a great potential for development in Europe. The European Science Foundation estimates that "by 2050 Europe could source up to 50% of its electricity needs from Marine Renewable Energy" [2]. Although Marine Renewable Energy comprises many different energy sources (offshore wind, wave energy, tidal currents, ocean currents, salinity gradient, thermal gradient and marine biomass), those with the highest potential are arguably wave energy, offshore wind and tidal energy. Two main issues must be resolved, however, for wave energy to become a fully established, commercially viable energy source. First, the wave resource along the coastline must be assessed; it presents significant spatial and temporal variations (e.g. [1, 3-4]), as is the case of other renewables. Second, efficient, reliable and low-impact Energy Converters (WECs) must be developed. This paper deals with WaveCat, a recently patented WEC. Its objectives are: (i) to present the WaveCat concept; and (ii) to describe the methodology used for its development, centred around physical model tests conducted in a 3D wave tank.

2. The WaveCat concept

WaveCat is a floating WEC intended for offshore deployment (water depths of 50-100 m), which has the advantage of a higher wave energy potential relative to onshore or nearshore locations (wave energy decreases as waves approach the shoreline). Another advantage of WaveCat is its low visual impact. The name WaveCat alludes to the fact that it is composed of two hulls, like a catamaran. Unlike a catamaran, however, these hulls are not parallel but convergent. The single-point mooring to a catenary-buoy allows the device to swing as the wave direction changes, thereby ensuring that the wedge opening always faces the waves (Figure 1). As waves propagate into the wedge, their height is enhanced by the convergence of the lateral boundaries (the hulls) until, eventually, they overtop the inner hull sides. Overtopping water is temporarily collected in on-deck tanks. The higher water level in these tanks relative to the sea level is taken advantage of to propel ultra-low head turbines as the water is drained back to sea. A fundamental issue in designing a WEC—especially an offshore WEC—is its survivability, i.e. its ability to sustain heavy storm conditions. The design of WaveCat includes a number of elements aimed at survivability, most notably the possibility of varying the angle formed by the hulls (hereafter referred to as wedge angle) between 120º and 0º according to the sea state. When a storm approaches, the angle is reduced to 0º, i.e. the wedge is closed, thereby transforming WaveCat into a monohull—similar to a conventional ship from the standpoint of seakeeping. Freeboard and draft are also variable: in the model they were varied by means of solid ballast; in the prototype, ballast tanks filled with water will be used (as in ships). The prototype hull length is 90 m.

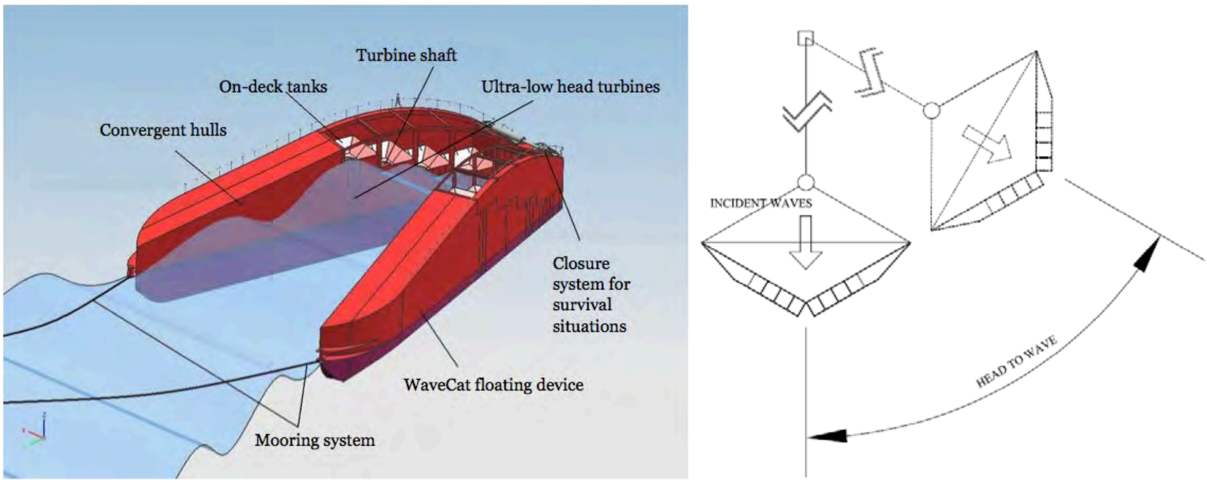

Fig. 1. The WaveCat concept (left) and a plan view of the single-point mooring system (right).

3. Methodology

The research and development of WaveCat combines physical and numerical modeling. So far, physical model tests in a wave tank have been completed. The methodology of these tests is the focus of this section (subsections 3.1 to 3.3). The numerical model, which is currently under development, is briefly presented in subsection 3.4.

3.1. Physical model

The 3D model, constructed of marine board, represented the WaveCat at a 1:30 scale (Figure 2). Tests were conducted at the wave tank of the University of Porto, with dimensions of 28 × 12 × 1.25 m; at its centre was a pit with dimensions of 4.5 × 2 × 1.5 m (Figure 3). The catenary-buoy mooring system was anchored at the front end of the pit (Figure 4). Wave generation was carried out with a directional (multielement) piston-type wavemaker. The experimental setup included six wave gauges aligned with the centreline of the tank, and four other on the model (one for each water tank). The quiescent water depth in the tank was set to 0.90 m (or 2.40 m in the central pit) for all tests.

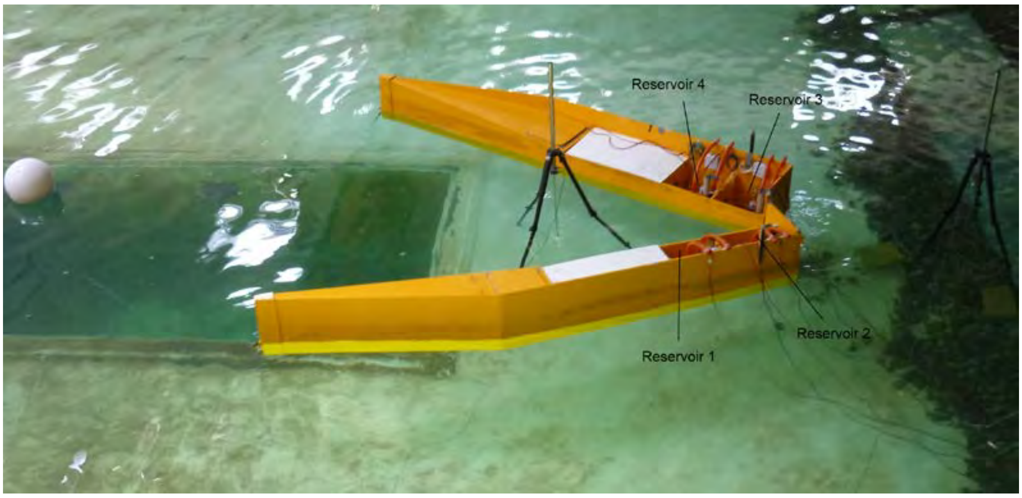

Fig. 2. The physical model in the wave tank with its four reservoirs for collecting overtopping water.

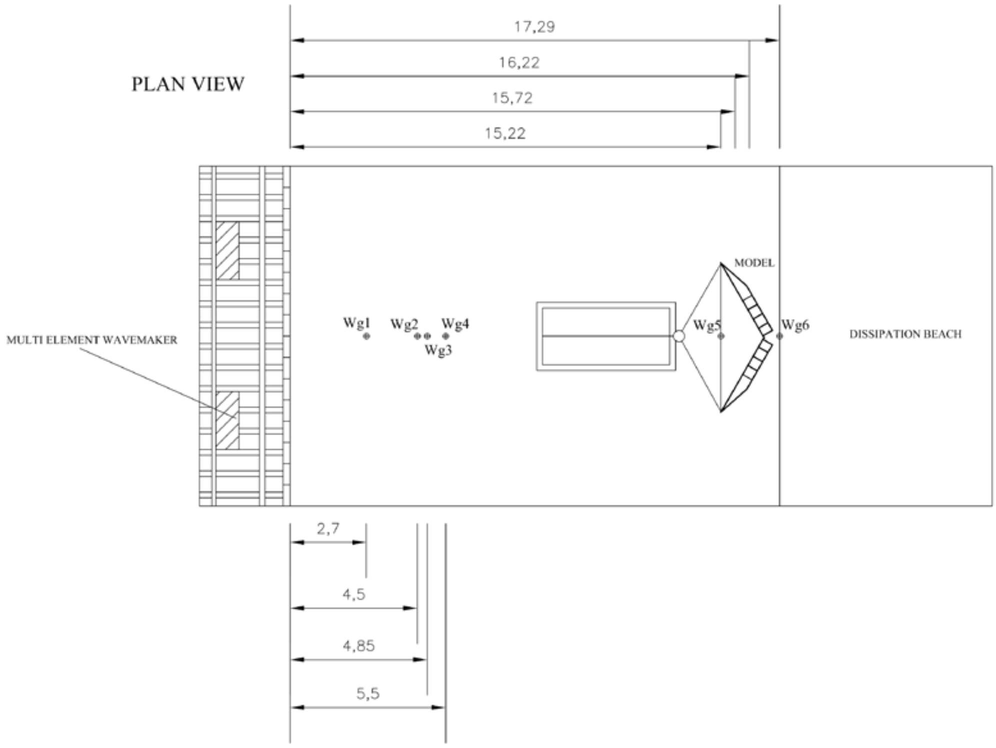

Fig. 3. Wave tank layout and experimental setup, showing the WaveCat model and the location of the wave gauges outside the model (Wg1 to Wg6). [Dimensions in *m*].

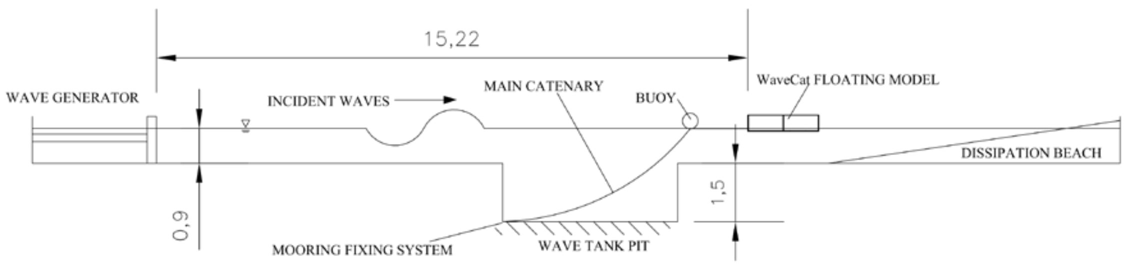

Fig. 4. Longitudinal section of the wave tank showing the model and the catenary-buoy mooring system. [Dimensions in *m*].

3.2. Experimental campaign

In total, the experimental campaign comprised 43 tests, 25 of which with regular waves and 18 with irregular waves. The wedge angle (α) was varied between four values: 30º, 45º, 60º and 90º. Three quiescent freeboard values (F_b) were used: 0.04 m, 0.09 m and 0.10 m. Regular waves were in the ranges H = 0.07 – 0.10 m and T = 1.65 – 2.20 s. Irregular waves varied in the ranges H_s = 0.067 – 0.100 m and T_p = 1.83 – 2.20 s. For illustration the parameters in some of the tests (the irregular wave tests with the lowest freeboard) are shown in Table 1.

Table 1. Parameters in the irregular wave tests with a quiescent freeboard F_b = 0.04 m.

Test case	α (°)	H_s (m)	T_p (s)
AA07_I3	60	0.083	2.013
AA07_I5	60	0.100	2.196
AB07_I3	90	0.083	2.013
AB07_I5	90	0.100	2.196
AD07_I3	45	0.083	2.013
AD07_I5	45	0.100	2.196
AE07_I3	30	0.083	2.013
AE07_I5	30	0.100	2.196

Each of the four water reservoirs (two per hull) in the WaveCat model is equipped with a pump and a control system (Figure 5). The control system operates based on the water level in the reservoir as measured by a capacitance-type gauge. The pump begins to function when the water reaches a certain (maximum) level, and stops when it has gone down to a minimum value. The water level in two reservoirs, #3 and 4, during the test AD07_I5 is shown in Figure 6; the intervals of pump operation correspond to the near vertical lines of the graph. A typical record of the free surface level during the same test is shown in Figure 7.

In the model, for simplicity, the pumps worked with a constant flowrate, and during (generally short) intervals of time. It is important to mention that this pumping system in the model is not intended to replicate the functioning of the turbines in the prototype, but merely to allow a longer test duration. Instead, the control system in the prototype will aim for continuous operation of the turbines, with the tanks acting as buffers to provide continuous outflow toward the turbines in spite of the discontinuous nature of the overtopping events. The outflow rate in the prototype will be set by its own control system so as to maintain the continuous turbine operation, taking into account the overtopping rate (which depends on the sea state) and the turbine-generator characteristics.

3.3. Measurement of model displacements

During the tests, the displacements of the model under wave action were recorded by means of a motion capture system consisting of three infrared video cameras, reflective elements on the model, a dedicated computer and *ad hoc* software. The cameras detected the positions of a number of small reflective spheres installed at different points on the model (Figure 8). Their motions were then converted by the system software into model displacements along the three coordinate axis (heave, surge, sway) and rotations around them (roll, pitch, yaw). For illustration, the pitch and roll of the model during test AD07_I5 are shown in Figure 9.

Fig. 5. Pump and control system in one of the water reservoirs of the model.

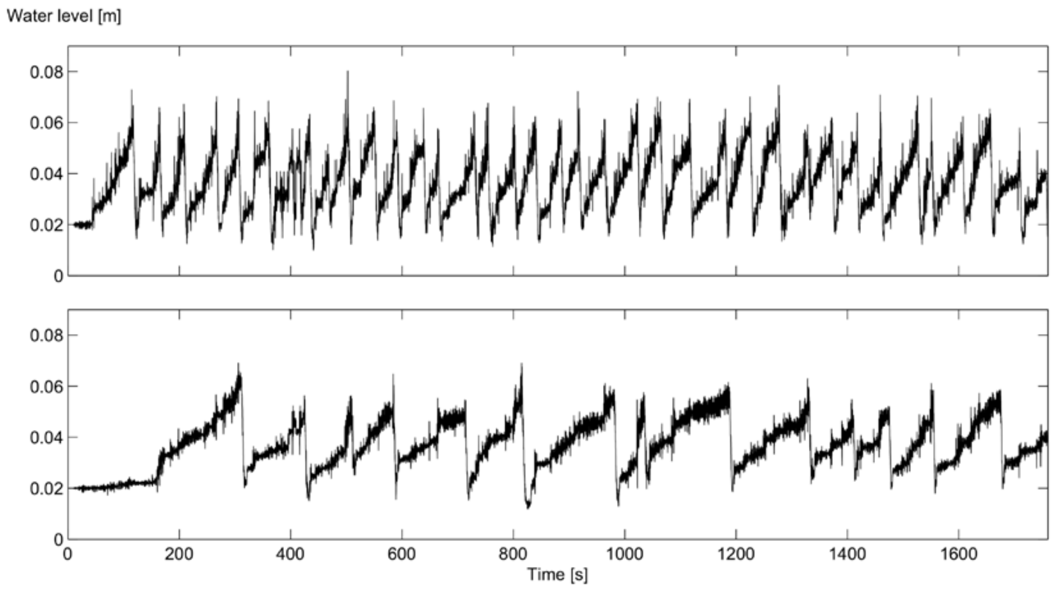

Fig. 6. Water level in reservoirs #3 (aft reservoir, above) and #4 (fore reservoir, below) during test AD07_I5. [Refer to Figure 3 for the location of the reservoirs in the model].

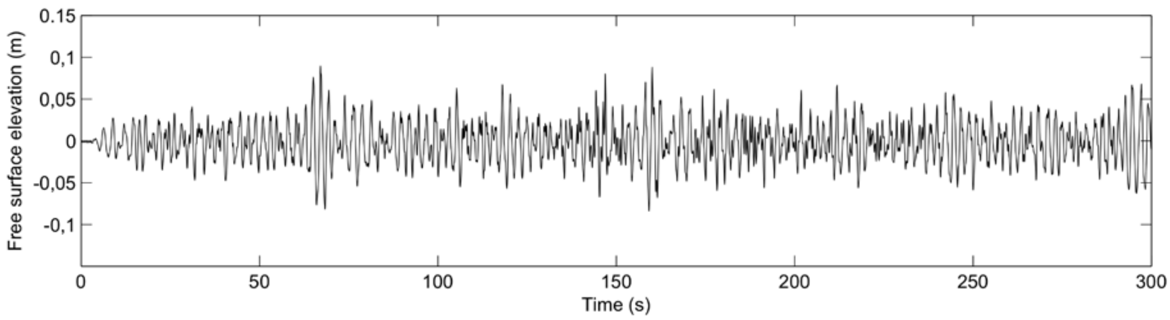

Fig. 7. Free surface elevation signal at the wave gauge in front of the model (Wg4) during test AD07_I5. [For clarity, only the first 5 min of the test are shown].

3.4. Numerical model

The development of a numerical model for WaveCat started with a 2D RANS-VOF model. This model was successfully validated using results from 2D physical model tests carried out in the wave flume of the University of Santiago de Compostela. Currently a 3D numerical model is being implemented; the model solves the RANS (Reynolds-Averaged Navier-Stokes) equations with a volume-of-fluid approach, using a state-of-the-art parallel code (Star-CCM+). The model simulates the WaveCat response as a floating body interacting with waves. It is expected that this model will be validated in the (hopefully near) future based on the results of the physical model tests presented above. A preliminary image from a simulation is shown in Figure 10.

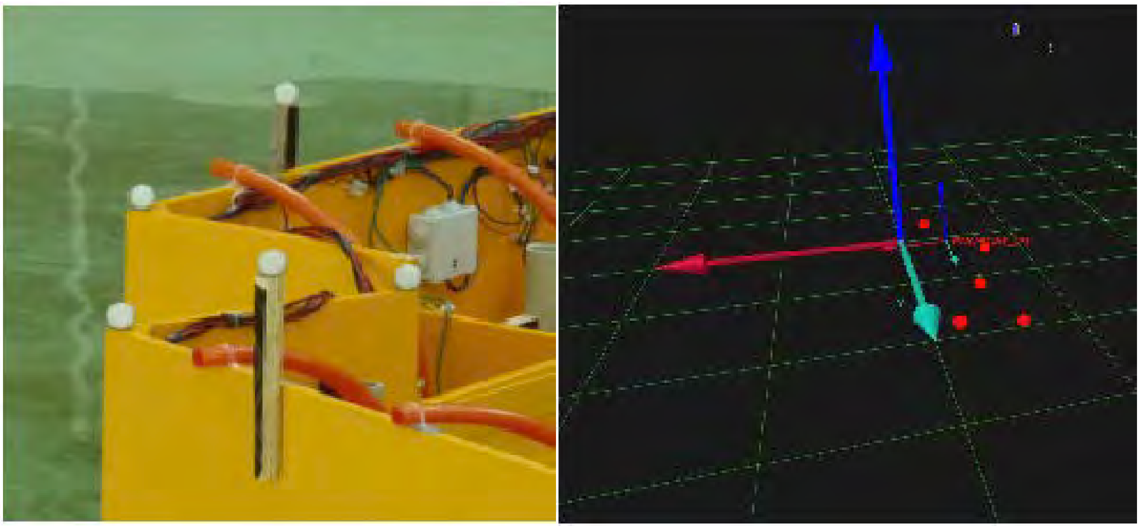

Fig. 8. White reflective spheres on the model (left) and detected by the motion capture system (right).

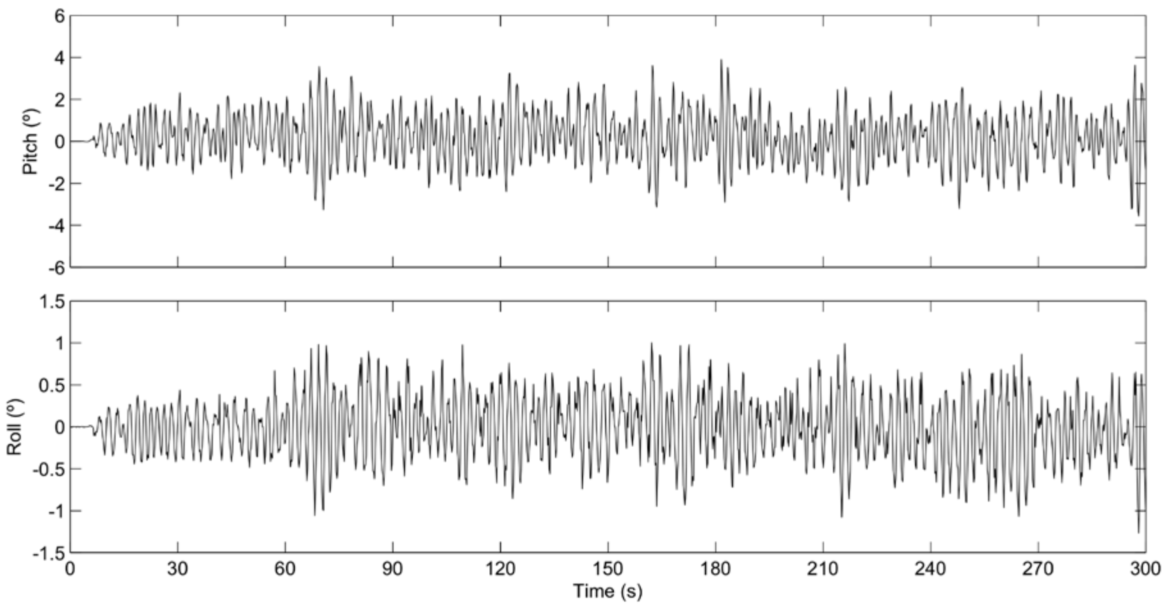

Fig. 9. Pitch and roll during test AD07_I5. [For clarity, only the first 5 min of the test are shown].

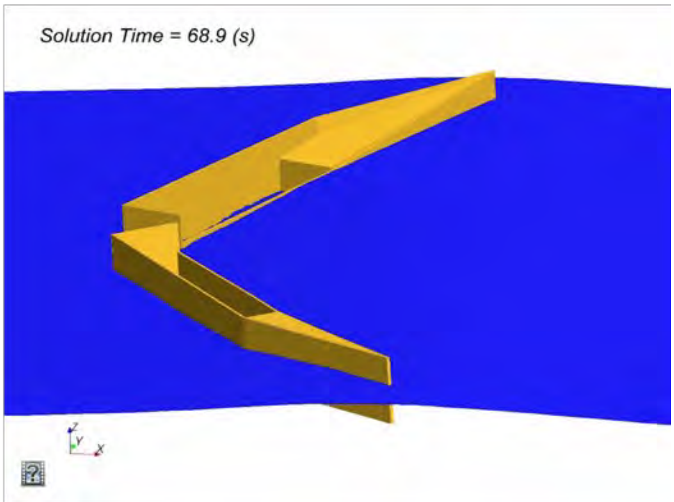

Fig. 10. One of the video frames of a simulation with the 3D numerical model under development.

4. Results and Discussion

The present paper presents the WaveCat, a recently patented WEC, and the ongoing work to develop it as a commercially viable system. A 1:30 model was constructed and tested in a large wave tank. In total 43 tests were carried out, both with regular and irregular waves. In addition to the wave parameters (wave height and period in the case of regular waves, significant wave height and peak period in the case of irregular waves), two fundamental model parameters were varied in the tests: wedge angle and freeboard. The motions of the model during the tests were measured by means of a motion capture system which included three infrared video cameras.

The results of the tests may be classified into three different levels or categories. First, on a conceptual level, the tests enabled to verify the WaveCat as a valid concept for wave energy conversion. The second level concerns the design of WaveCat and, in particular, of the water reservoirs. In the tested model the two reservoirs in each hull have the same volume and occupy the same length along the hull side. In Figure 6 it is apparent that the aft reservoir (#3) experiences significantly heavier overtopping than the fore reservoir (#4) during test AD07_I5. This imbalance was consistently observed throughout the experimental campaign, the aft reservoir collecting larger volumes of water than the fore reservoir. If the turbine-generator configuration in the prototype is the same for both reservoirs, this consistent difference in overtopping rates is clearly suboptimal. One method to overcome this problem is to increase the volume of the fore reservoir by extending its length along the hull side at the expense of the aft reservoir, to the extent necessary to balance the overtopping rates. The other is to maintain the same volume and length along the hull side for both reservoirs, as in the tested model, but to use different turbine-generator configurations in the prototype—the aft reservoir would have a turbine-generator with greater rated power than the fore reservoir, in accordance with its larger overtopping rate. Although the first option would appear to be more attractive, no definitive decision has been taken so far. Finally, the third level of results comprises the time series of overtopping rates and model displacements and rotations gathered during the tests, which will be used to validate the 3D numerical model currently under development. Once validated, the model will be used to optimize the design of WaveCat for best efficiency under a given set of wave conditions, which will be chosen according to the wave climate of the deployment area. Thus, the physical model tests presented in this paper are a crucial step in the development process of this new WEC.

The WaveCat concept (Section 2) presents four main advantages with respect to other WECs. In the first place, its design with two converging hulls and, in particular, the fact that the angle between them can be varied according to the sea state constitute a significant asset for survivability; in effect, under extreme (storm) conditions the wedge can be closed, thereby transforming WaveCat into a monohull vessel. In the full size WaveCat, a "locking system" will be provided to keep both hulls together during a storm without creating excessive stresses on the bow hinge. The freeboard on the outer hull sides is considerably larger than that on the inner hull sides. With no waves overtopping the inner hull sides, the survivability of WaveCat is greatly enhanced. The second advantage of the WaveCat design is that the wedge angle can be varied during normal operation to optimize the efficiency—the smaller the waves, the larger the wedge angle. Third, the moving parts activated by the waves are only the turbine-generators; there are no complex joints moving with the passage of each wave, as is the case of other WECs. This may be expected to result in better reliability—and reliability is a key aspect of economic viability. Finally, the water tanks are placed along the hulls, rather than at the back of the wedge; therefore, the motions of WaveCat in waves may be expected to affect the overtopping rate less, merely causing a displacement along the hull of the point where overtopping begins. If the wave tanks along the hulls were substituted by a single tank at the back of the wedge, the motions of the WEC—in particular, its heave—could significantly reduce the overtopping rates under resonant conditions.

5. Conclusions

The development of a new Wave Energy Converter is a long process. At the current stage of development of WaveCat, wave tank tests of a 1:30 model were successfully completed, with an experimental setup that included an advanced motion capture system. With these physical model tests, involving many different sea states and model configurations (different wedge angles and freeboards), the WaveCat concept as a wave energy conversion system was verified. A second conclusion refers to the design of the water reservoirs. In view of the consistent imbalance in overtopping rates that was found during the experimental campaign there are two main options. Either the design of the tested model is kept in the prototype, in which case the turbine-generator configuration in the aft reservoirs must be different from that in the fore reservoirs (with greater rated power in the aft reservoirs), or the volume of the fore reservoir is increased at the expense of the aft reservoir, in which case the same turbine-generator configuration can then be used for both reservoirs. Finally, the data on model motions (displacements and rotations) and overtopping rates obtained in the experimental campaign presented in this paper will be the basis on which the 3D numerical model currently under development will be validated. This model will enable to optimize the design of WaveCat for best performance under specified wave conditions. Upon optimization, the next step will be the construction of a full-size demonstrator and its sea trial.

References

[1] G. Iglesias, M. López, R. Carballo, A. Castro, J.A. Fraguela, P. Frigaard, Wave energy potential in Galicia (NW Spain), Renewable Energy 34, 2009, pp. 2323-2333.

[2] European Science Foundation, Marine Board Vision Document 2, 2010.

[3] G. Iglesias, R. Carballo, Wave energy potential along the Death Coast (Spain), Energy 34, 2009, pp. 1963-1975.

[4] G. Iglesias, R. Carballo, Wave energy resource in the Estaca de Bares area (Spain), Renewable Energy 35, 2010, pp. 1574-1584.

Extreme Loads on the Mooring Lines and Survivability Mode for the Wave Dragon Wave Energy Converter

S. Parmeggiani[1,*], J. P. Kofoed[2], E. Friis-Madsen[3]

[1] *Wave Dragon Ltd., London, United Kingdom*
[2] *Aalborg University, Aalborg, Denmark*
[3] *Wave Dragon Aps, Copenhagen, Denmark*
* *Corresponding author. E-mail: stefano@wavedragon.net*

Abstract: One of the main challenges Wave Energy Converters have to face on the road towards commercialization is to ensure survivability in extreme condition at a reasonable capital costs. For a floating device like the Wave Dragon, a reliable mooring system is essential. The control strategy of the Wave Dragon aims at optimizing the power production by adapting the floating level to the incoming waves and by activating the hydro-turbines and regulating their working speed. In extreme conditions though, the control strategy could be changed in order to reduce the forces in the mooring system, lowering the design requirements with almost no added cost. The paper presents the result of the tank testing of a 1:51.8 scale model of a North Sea Wave Dragon in extreme wave conditions of up to 100 years of return period. The results show that the extreme loads in the main mooring line can be reduced by approximately 20-30% by lowering the crest level and balancing the device to lean a little towards the front.

Keywords: *Wave Dragon, Wave Energy Converter, Survivability, Mooring system, Control strategy*

1. Introduction

Wave Energy Converters (WECs) have to withstand extreme events that put very high standards on their design requirements, increasing capital costs. From an economical point of view, such expenditure can be justified only by high performance in the often mild operational conditions where these devices operate for the main part of their lifetimes. One of the challenges the industry has to face in this early phase to help commercialization is therefore to jointly reduce the capital expenditures due to the survivability in extreme conditions and increase the performance in operational conditions. An efficient control strategy can help to meet both requirements with very low added cost.

1.1. The Wave Dragon WEC – Mooring system and control strategy

The Wave Dragon (WD) is a floating, slack-moored WEC of the overtopping type. Incoming waves are focused by two wing reflectors towards a ramp where they surge up and overtop into a reservoir placed at a higher level than the Mean Water Level (MWL). Energy is extracted as the stored water is led back to the sea through a set of low head hydro-turbines.

For an off-shore floating device like the WD the mooring system represents one of the main components ensuring the survivability. The mooring system of the WD consists of slack mooring chains of equal length distributed in circular spread, see Fig. 1. These are connected to a Catenary Anchor Leg Mooring (CALM) buoy, which again is connected to the WD platform and wings. An additional single mooring line can be connected to the rear of the platform to limit the excursions of the device.

The control strategy of the WD has three components: in a time scale of hours, the first one is aimed at optimizing the floating level of the device according to the incoming wave height in order to maximize the overtopping flow; in the time scale of minutes, the second one is the on/off regulation of the propeller turbines, which ensures a high storage efficiency of the reservoir; finally, in the time scale of seconds, the third one is the speed control of the turbines to ensure a constant high efficiency of the turbine-generators.

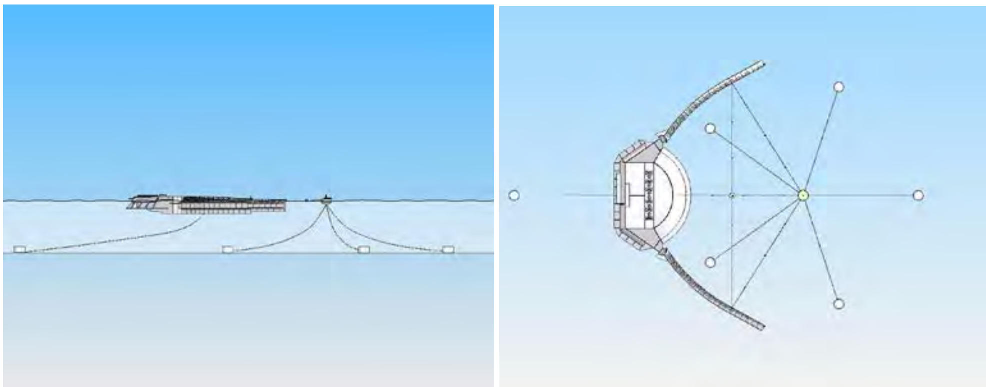

Fig. 1. Conceptual mooring system of the Wave Dragon WEC.

In extreme conditions the goal of the control strategy should no longer be to optimize the performance, but to limit the forces in the mooring system and in the structure in general. In this sense by keeping the floating level low the forces in the mooring line connecting the device to the CALM buoy, also called the main mooring line, can be decreased. This kind of control, which is hereafter referred to as the *survivability mode* of the WD, can help reducing the design requirements on the mooring system.

The paper presents the results of an experimental investigation conducted on the 1:51.8 scale model of a North Sea WD to assess the efficiency of the mentioned control strategy. Different wave and setup conditions have been tested and their influences on the forces in the main mooring line and on the dynamic response of the device have been established.

In the following the tests and data analysis procedure used are presented. From the results the efficiency of the survivability mode is assessed and important considerations regarding the stability of the device are drawn. Finally, the main conclusions and future work required are presented.

2. Method

The study has been conducted through the wave tank testing of a scale model of the WD at the deep water basin of the Hydraulic and Coastal Laboratories of Aalborg University during October 2010.

2.1. Test setup

The model tested is at 1:51.8 length scale of a North Sea WD, which has a rated power of 4 MW in a wave climate of 24 kW/m. The proposed mooring system was schematically reproduced, connecting the model to an anchor at the front through the main mooring line, the stiffness of which was modeled by means of a spring to deliver the horizontal compliance. Two mooring lines at the back have been used with the only purpose of keeping the device in position.

The forces in the main mooring line (F), as well as the movements of the device in surge (S), heave (H) and pitch (P), have been recorded during the tests.

2.2. Tested conditions

The wave states considered are extreme waves with return period of 10, 50 and 100 years typical of the Danish part of the North Sea. The number of wave states tested has been increased by considering for each of them three different values of peak wave steepness $S_p = H_s/L_p$ (-), being H_s (m) the significant wave height and L_p (m) the peak wave length. All waves have been generated as irregular according to a JONSWAP spectrum with peak enhancement factor 3.3. The water depth considered corresponds to 33.7 m in full scale.

The influence of the height of the crest freeboard above the mean water level (R_c) and of the directionality of the waves, expressed through the s parameter of the Cos^{2s} spreading function, have been investigated leading to a total of 42 tests. The values of the parameters considered in the study are resumed in Table 1, where the wave states are described by their H_s and peak period T_p.

Table 1. Summary of the parameters considered in the study (values are given in full scale).

Parameter name	Description	Values
T_{r10}	Wave with return period of 10 years	H_s = 8 m, T_p = 13.1 s
T_{r50}	Wave with return period of 50 years	H_s = 9 m, T_p = 13.8 s
T_{r100}	Wave with return period of 100 years	H_s = 10 m, T_p = 14.5 s
S_p (-)	Peak wave steepness	S_{p0}: standard wave state S_{p+1}: Hs increase of 0.5 m S_{p-1} = Tp increase of 1 s
s (-)	Spreading coefficient	s_1 = 20 (2D waves) s_2 = 2 (3D waves) s_3 = 10 (mildly 3D waves)
R_c (m)	Crest level above MWL	R_{c1} = 4 m R_{c2} = 3 m R_{c3} = 2 m R_{c4} = 1 m

2.3. Floating stability

During the tests it has been observed that the model had a natural tendency to trim backwards. This behavior was found to affect the recorded forces too, as the less stable the device was, the higher were the forces. Its influence was found to be comparable to the one due to the R_c modifications and was therefore also investigated. Following this, some modifications to the model lead to consider one setup with high stability for each R_c, as the floating level was well maintained horizontally in average, and one with low stability.

2.4. Data analysis

For both forces and movements the extreme values are estimated as the average of the 1/250th of the highest values recorded for each time series, denoted $X_{1/250}$, X being the variable considered. Other statistical values such as the mean value X_m and standard deviation X_{stdev} have been used in the data analysis. As these quantities have been evaluated on records of 30 min, corresponding in average to 1000 waves, their reliability is considered good.

In each of the cases tested the R_c has been derived from the mean heave by applying a vertical offset according to the model geometry. The waves have been recorded by a 2D rig of 7 wave gauges. The analysis of the wave records allowed to separate the incident and reflected components according to the Mansard–Funke method. The first one has been the only considered in the data analysis, characterized by the values of H_s, T_p and s.

3. Results

In the following the most significant results of the tests are shown in a non-dimensional form. The extreme forces are presented as

$$F_{nd} = \frac{F_{1/250}}{\rho \cdot g \cdot H_{m0} \cdot A_c} (-) \qquad (1)$$

where H_{m0} (m) is the significant wave height derived from the frequency domain analysis and A_c (m^2) is the cross sectional area of the ramp of the WD, calculated as the product of average ramp width and total height (from crest to draft).

The non-dimensional heave and surge are calculated respectively as $H_{nd} = H_{1/250}/H_{m0}$ (-) and $S_{nd} = S_{1/250}/H_{m0}$ (-), while the pitch is directly considered as $P_{1/250}$ (deg).
In order to consider both the dependency on R_c and on L_p the independent variable chosen is the non-dimensional product of $S_p \cdot R = R_c/L_p$ (-). $R = R_c/H_s$ (-) is the non-dimensional crest level, a parameter usually considered when dealing with overtopping.

The reference system has been chosen so that displacements in surge are positive in the direction of the wave propagation, those in heave upwards and the rotations in pitch as they lower the back of the device.

The R_c tested have been grouped in High (R_{c1}, R_{c2}), Mid (R_{c3}) and Low (R_{c4}). As for both High and Low R_c no significant difference was observed in the results between low and high stability, all the tests have been grouped into a total of 4 dataset for the data analysis: High R_c, Mid R_c-low stability, Mid R_c-high stability and Low R_c.

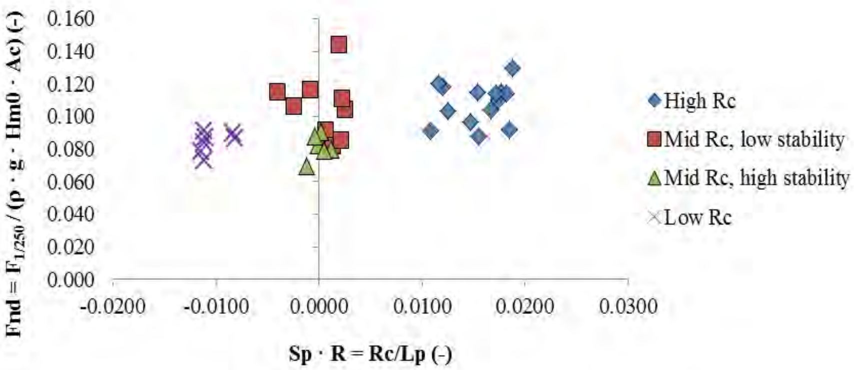

Fig. 2. Non-dimensional extreme forces in the main mooring line for 2D waves (s_1).

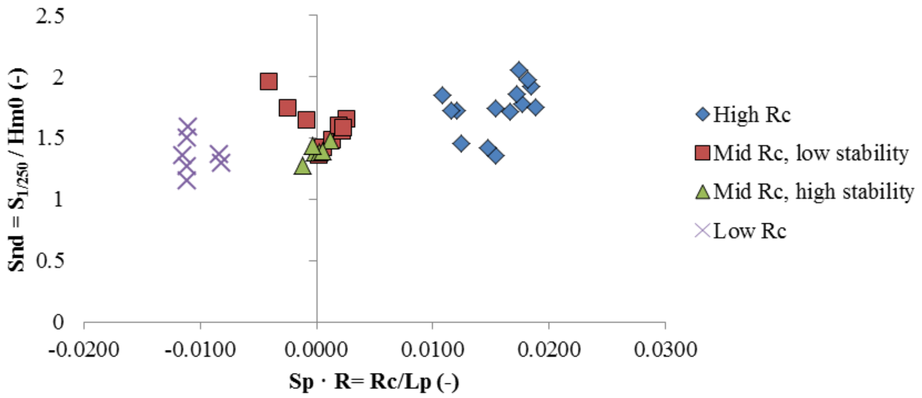

Fig. 3. Non dimensional extreme response in surge for 2D waves (s_1).

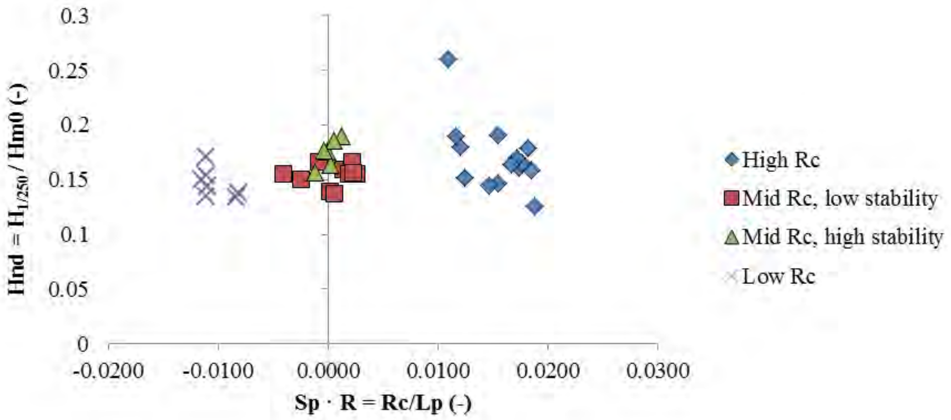

Fig. 4. Non dimensional extreme response in heave for 2D waves (s_1).

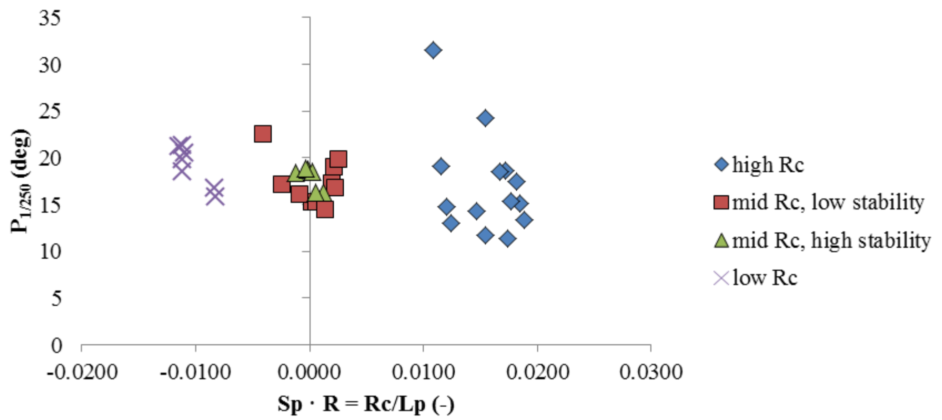

Fig. 5. Extreme response in pitch (deg) for 2D waves (s_1).

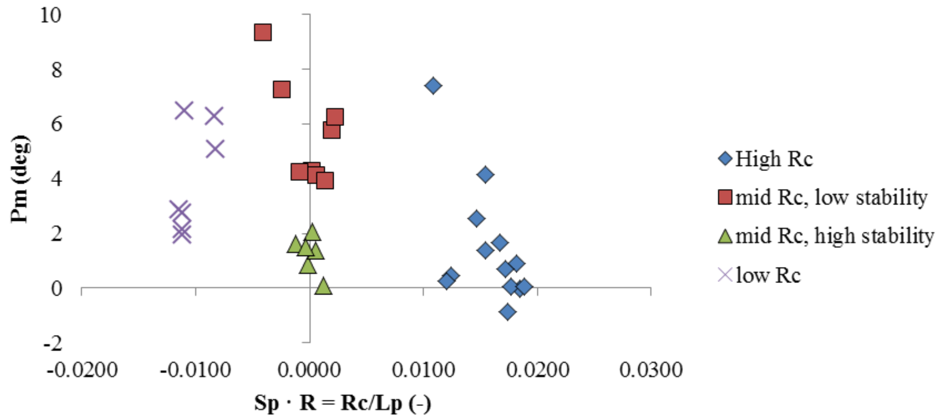

Fig. 6. Mean pitch position, or trim (deg) for 2D waves (s_1).

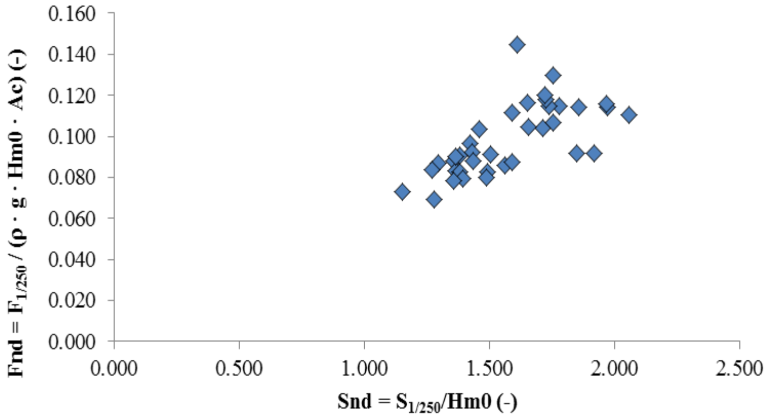

Fig. 7. Direct proportionality between non-dimensional extreme response in surge and non-dimensional extreme forces in the main mooring line, for 2D waves (s_1).

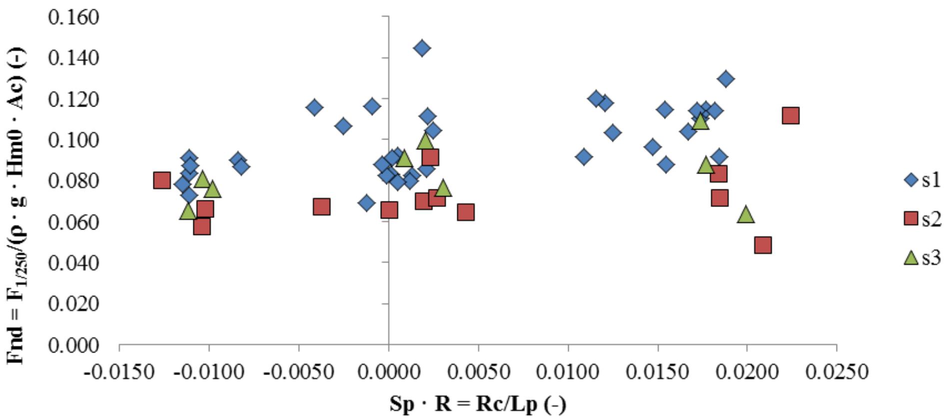

Fig. 8. Difference in the non-dimensional extreme forces in the main mooring line due to variation in the wave directionality.

4. Discussion

Fig. 2 shows two very important facts. First of all the forces in the main mooring line are reduced at lower crest levels, confirming the assumption behind the proposed survivability mode. This gets to the point where it could be considered to lower the crest level even down to negative mean values, which would not make sense in terms of power production, highlighting once more how the control strategy differs switching from operational to extreme conditions.

The floating of the device at negative values of the R_c can be explained by considering the hydrodynamics of the model during the tests: at very low floating levels the waves are completely overpassing the model, which determines a negative mean value R_c over the test duration. Nonetheless the buoyancy of the model is still higher than its weight. Therefore as the waves stop, the R_c is raised up again to the target (positive) floating level.

Fig. 2 also shows how the mooring forces are highly influenced by the floating stability. The forces in the Mid R_c dataset is are fact in the order of the ones recorded at High R_c when the stability of the device is low, while they become comparable to the ones recorded at Low R_c as the stability is increased.

Fig. 6 shows how this behavior can be well described in terms of mean pitch, the mean position around which the device oscillates, also known as trim. Focusing on the Mid R_c dataset, at low stability the values of P_m are much larger than at high stability. When the mean pitch increase, the device is tilted backwards and it also increases the surface against which the waves can exert pressure on the lower part of the device; as P_m approaches zero instead (or even as it becomes negative) proportionally more waves are hitting the ramp and as they surge it up the forces on the structure are reduced.

From a comparison of Fig. 2 and Fig. 3 it can be seen how the extreme forces in the main mooring line follow very much the extreme response in surge. This is confirmed also in Fig. 7, where a direct proportionality between the extreme response in surge and extreme forces can be seen.

The extreme response in heave (Fig. 4) is quite constant and independent on the R_c, while the pitch shows a tendency to increase within each dataset as the R_c lowered (Fig. 5).

Fig. 8 shows how the directionality of the waves has a significant influence on the forces. In all the cases tested the forces are reduced as the waves become 3D, due to the balancing of the components with opposite directions of the forces exerted by the waves on the device, which are not transmitted to the mooring system.

5. Conclusions and further work

The efficiency of the proposed survivability mode is assessed. As the floating level is lowered the extreme forces in the main mooring line can be reduced in the order of 20-30%.
For the Wave Dragon this can be achieved simply by emptying the air chambers as a storm is foreseen. With no further control this condition can maintained even in the case of loss of the grid connection: a “fool-proof” passive system ensuring a high survivability.

The pitch stability of the device also plays an important role in the determination of the mooring forces, especially at intermediate R_c. In this study the stability has been described in average, by considering the mean value of the pitch. A reduction in this reduces the extreme forces recorded. Nevertheless it is here suggested that a more sensible parameter, possibly able to describe also the instant stability of the device, is found and used for further analysis of this behavior.

Acknowledgement

The first author acknowledges the support from the FP7 Marie Curie Actions of the European Commission, via the Initial Training Network wavetrain2 (contract-Nº MCITN-215414).

References

[1] J. P. Kofoed, P. Frigaard, Development of Wave Energy Devices: the Danish case, Journal of Ocean Technology, Vol. 4, No 2, 2009.

[2] NIRAS, Wave Dragon 1:4.5: up-scaling of mooring system, EU contract ENK5-CT-2002-00603, Work package 2.6, deliverable 33, 36& 43, September 2006.

[3] J. Tedd et al., Model Testing of Forces in the Reflector Joint and Mooring Forces on Wave Dragon, DCE Technical Report No. 27, Aalborg University, Department of Civil Engineering, 2005.

[4] T. Hald, J. Lynggaard, Hydraulic Model Tests on Modified Wave Dragon, Technical Report, Project No. ENS-51191/00-0067, Aalborg University, Department of Civil Engineering, 2001.

[5] J. W. Kamphuis, Introduction to coastal engineering and management, World Scientific, Advanced series on Ocean Engineering, Volume 16, 2000

Design of a 100 GWh wave energy plant

Jayashankar.V[1,*], Mala.K[1], Kedarnath.S[1], Jayaraj.J[1], Omezhilan.U[2], Krishna.V[1]

[1] IIT Madras, Chennai, India
[2] Kings College of Engg., Pudukottai, India
* Corresponding author. Tel: +91-44-22574427, Fax: +914422574427, E-mail:jshankar@ee.iitm.ac.in

Abstract: The near shore Oscillating Water Column (OWC) based wave energy plant shows enormous promise for the commercialization of wave energy. The design details of such a plant, with an average incident energy of 24 kW/m and capable of producing 100 GWh over a two year period are described. The caisson, which could be a part of a breakwater, is constructed in a modular fashion in widths of 20 m. The power module is built around a 4.5 m diameter twin unidirectional impulse turbine with a rating of 900 kW. A key feature of the design is to combine the output from several OWCs into a single power module. Simulations show that the efficiency of the turbine can exceed 60 % from 10 to 100 % of the rated power. It is shown that a breakwater length of about 660 m with 11 such turbine generators is sufficient to meet the design requirement, with an overall wave to wire efficiency of about 36 %. The power electronics interface to the grid could be implemented with doubly fed induction generators or variable speed synchronous generators directly obtainable from the wind power industry. Laboratory experiments on a model turbine are used to validate the main claims.

Keywords: *OWC, twin unidirectional turbine topology, doubly fed induction machine*

Nomenclature

C_a	*input coefficient*	DP	*differential pressure* .... Pa
C_t	*torque coefficient*	J	*moment of inertia* .... kgm^2
phi	*flow coefficient*	T	*torque* .... Nm
η	*efficiency*	w	*angular velocity* .... $rad{\cdot}s^{-1}$
		Q	*volumetric flow rate* .... $m^3{\cdot}s^{-1}$

1. Introduction

The Oscillating Water Column (OWC) based wave energy plant is probably the most researched approach in the conversion of wave energy to electrical energy. Several documented demonstration plants around the world, in places such as Japan [1], India [2], UK [3] and Portugal [4], attest to the allure of the concept. In this approach, the energy conversion occurs in three steps. The variations in sea surface elevation (ocean waves) are converted to pressure fluctuations in the OWC. A turbine converts this pneumatic power into mechanical shaft power and an electrical generator coupled to the turbine gives electrical power. The overall efficiency of the conversion from wave to wire is given by

$$\eta = \eta_a * \eta_t * \eta_g \tag{1}$$

where η_a is the efficiency of the OWC
η_t is the efficiency of the turbine, and
η_g is the efficiency of the generator

The hydro dynamic efficiency of the plant can exceed 60% as reported in [1]. Table1 shows a summary of the reported experience with the OWC based wave energy plants mentioned above. The two different configurations of the Indian wave energy plant are shown in Fig. 1. The vertical axis 2 m Wells turbine power module is shown in Fig. 1a, while Fig. 1b shows the horizontal axis twin 1 m Wells turbine power module.

Table 1. Design details and performance of OWC plants

Plant	OWC effective area (dimension)	η_{OWC}	Power module		Comment
			Turbine	Generator	
Sakata port	115 m^2 (6 x 20)	> 60%	Twin 1.337m Wells'	60 kW 1800 - 2000 rpm	Variable speed
Vizhinjam	67.5 m^2 (6.75 x 10)	> 60%	2 m Wells	110 kW 1000 rpm	Fixed speed
Pico	144 m^2 (12 x 12)	> 50%	2.3 m Wells	440 kW 750 - 1500 rpm	Variable speed
LIMPET	126m^2 6x 21	> 60%	2.6 m Wells	2 x 250 kW 1050 rpm	Fixed speed

Fig. 1a. The Indian wave energy plant, 1991

Fig. 2b. The Indian wave energy plant, 1996

A recent study by the Carbon Trust [5] also describes the features of possible designs of near shore OWC plants. A generic OWC is assumed to perform with hydrodynamic efficiency of 42 %, utilizing a turbine operating with 65 % efficiency and a generator having 91 % efficiency, yielding an overall efficiency (wave to wire) of 24.8 %. In this work we consider the design of a plant which could yield a wave to wire efficiency of 36 % based on a new power module design. The proposed design satisfies the requirement for a plant producing 100 GWh over a two year period [6].

2. The twin unidirectional impulse turbine topology

An impulse turbine for use with unidirectional flow was proposed in [7]. The characteristics of the turbine under steady flow are shown in Fig. 2. The efficiency of the turbine is also illustrated in Fig. 2. It is seen that the turbine is capable of operating with efficiency better than 60%, for flow coefficients ranging from 0.317 to 0.948. A new power module incorporating two such turbines was proposed in [8] and the experimental results were shown in [9]. Conceptually, the topology uses two unidirectional turbines in conjunction with fluidic diodes as shown in Fig. 3. The fluidic diode assists in ensuring unidirectional airflow across the turbines, allowing only negligible flow in the reverse direction. The guide vane/ rotor blade profile also provides a significant contribution towards the higher impedance in the reverse direction. A consequence of this fact is the high efficiency in each cycle.

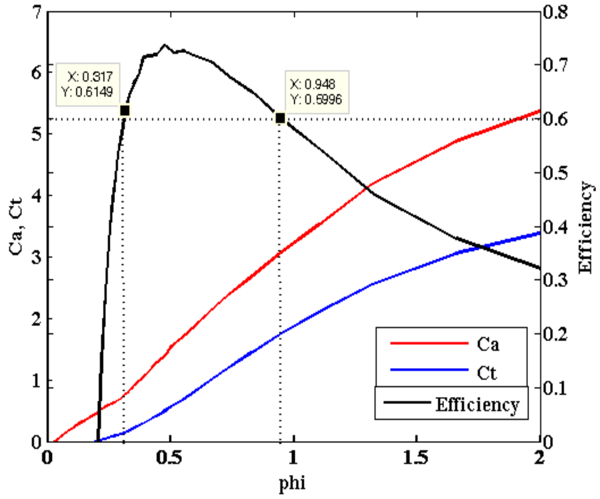

Fig. 2. Characteristics of unidirectional impulse turbine

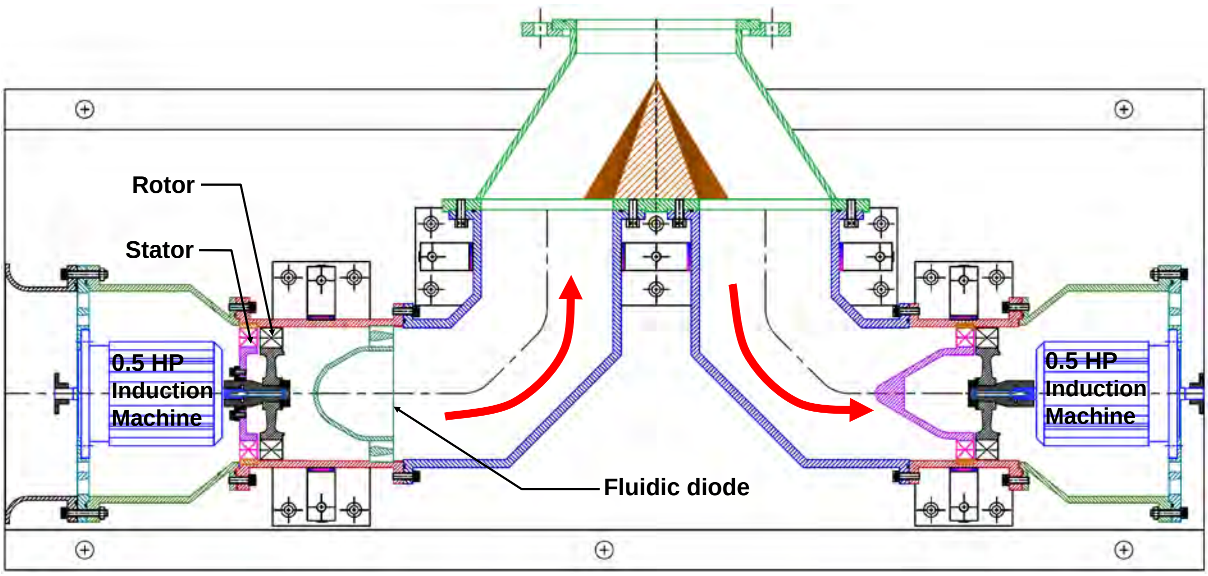

Fig. 3. Sectional view of the laboratory model of twin unidirectional turbine topology

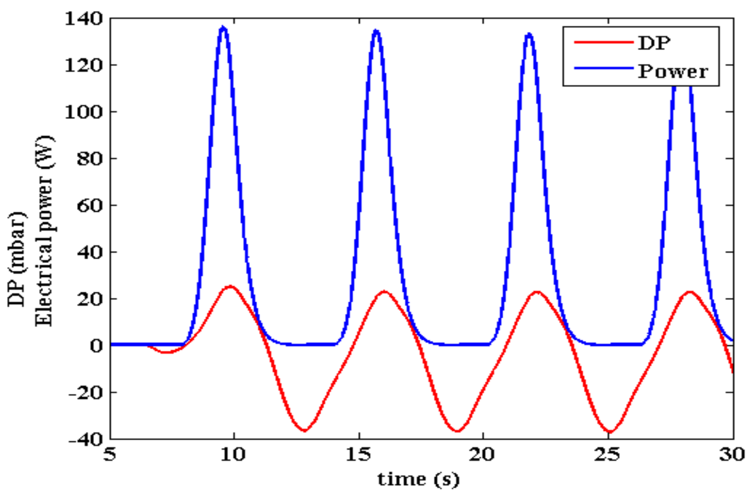

Fig. 4 . Measured parameters of single 165 mm turbine, coupled to a 375 W dc generator

The laboratory results on a 165 mm turbine with induction generator [9] showed that the concept was valid. In order to characterize the forward and reverse flow characteristic of the unidirectional turbine, an experiment was performed with a single turbine subjected to oscillating flow in a facility described in [9]. The turbine was coupled to a 180 V, 375 W, 3000 rpm dc generator with a fixed resistive load. As seen in Fig. 4, the positive stroke produces a power of 135 W with a differential pressure of 2.2 kPa. In the reverse flow the differential pressure is 3.7 kPa, thus clearly highlighting the differing impedances. In this experiment the generator was. A further realisation was the notion that the unidirectional turbine topology permits the summing of pneumatic outputs from different OWCs with a single turbine of a large diameter.

3. Design of a power module for a 20 m OWC

The incident yearly wave power input is assumed to be 24 kW/m. Thus the average wave power for an OWC with 20 m opening is 480 kW. With an OWC efficiency of 0.6, the average pneumatic power is 288 kW. This would give an average mechanical output of 184.3 kW with 64% turbine efficiency with turbine diameter of 2.6 m. Assuming that the plant should have the capability to withstand incident wave energy as high as 40 kW /m occasionally, the mechanical output will be 307 kW. With three OWCs feeding a single turbine the rating is 922 kW. The turbine diameter is now 4.5 m. It may be remembered that the average mechanical output of this combination would be 553 kW, corresponding to 24 kW/m of incident wave power.

We now consider the simulation of a turbine of diameter 4.5m when connected to an induction generator. Fig. 5 shows the basic block diagram of the simulation and has been extensively described and validated in [10]. The input to the program is the differential pressure time series obtained from a typical recording in the Indian wave energy plant. The record is scaled in order to cater to the overall range that will be encountered in the proposed design.

The program evaluates the expression

$$J\frac{dw}{dt} = T_t - T_g - T_l \qquad (2)$$

where J is the moment of inertia of the system

T_t and T_g are the turbine and generator torques

T_l is the term accounting for losses

The operation of the power module is highlighted in Fig.6, which illustrates the time variation of the relevant parameters of the power module. The differential pressure (DP) across the turbine, the pneumatic power (P_a), the mechanical power (P_m) and the flow coefficient (Phi), are all illustrated in Fig.6. In this run of 8 minutes, the average mechanical power from the turbine was approximately 500 kW which is close to the yearly average power. It may also be noted that the peak mechanical power obtained was around 3.4 MW, which is very similar to the power ratings in wind energy industry as well. By allowing summation of the pneumatic outputs of multiple OWCs with a larger diameter turbine, the twin turbine topology reaches power ratings similar to those seen in the wind power industry. This would enable the direct utilization of wind power modules in OWC based wave energy plants as well.

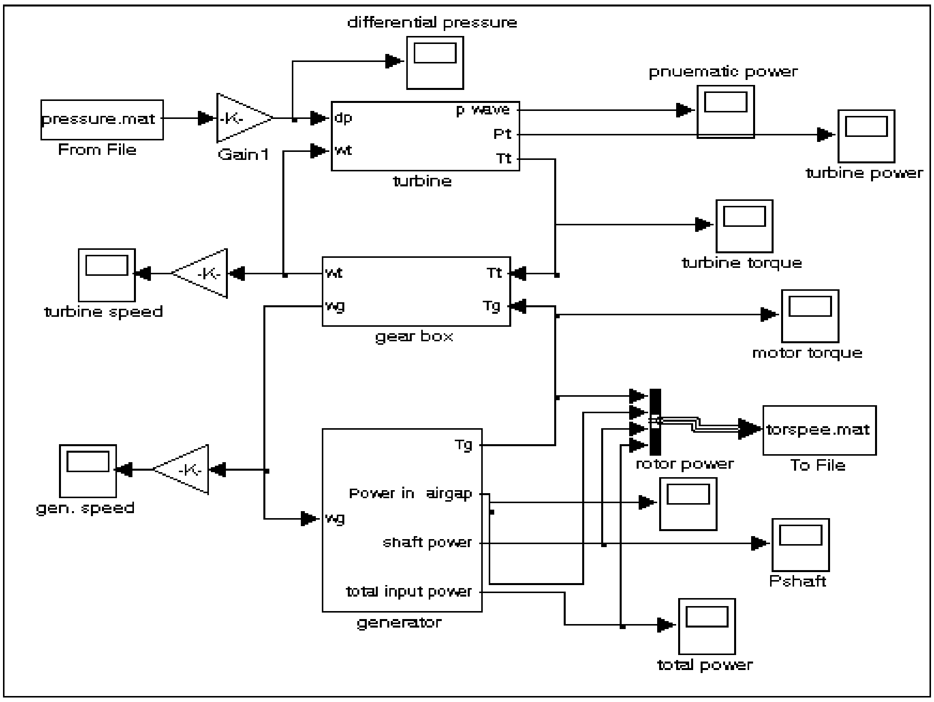

Fig. 5. Block diagram of simulation of 4.5 m diameter turbine coupled to an induction generator

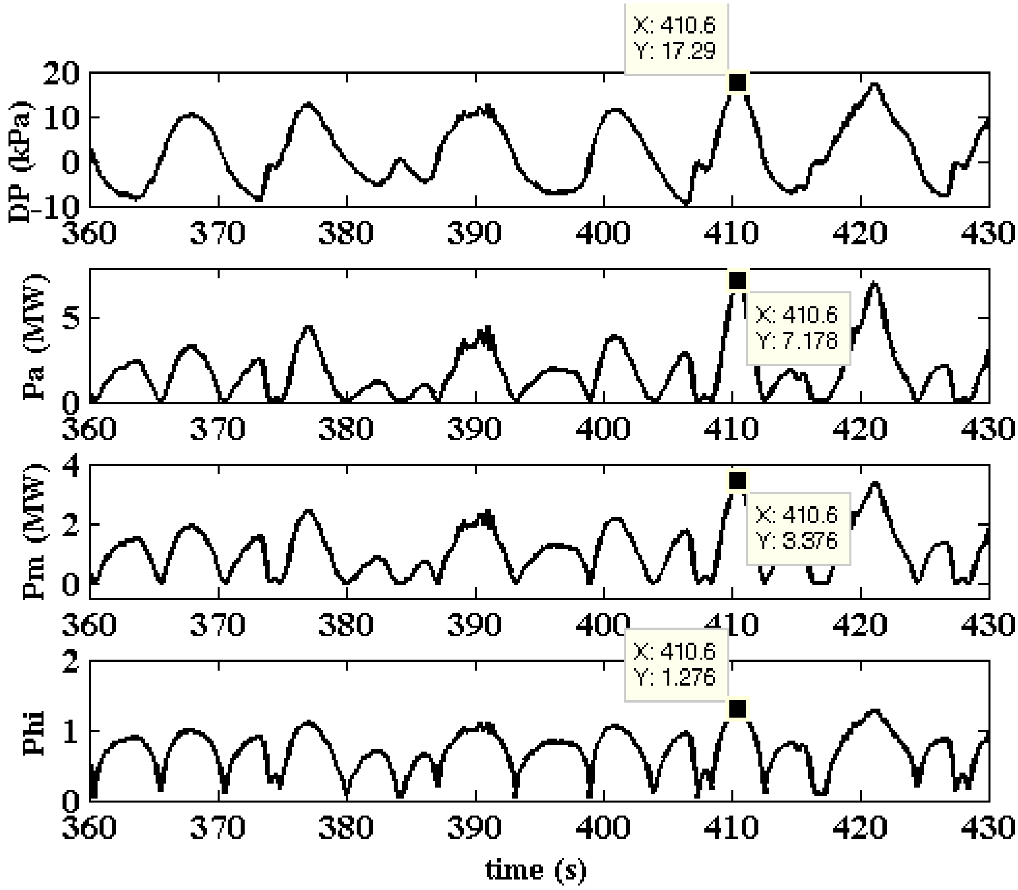

Fig. 6. Simulated plots highlighting the operation of 4.5 m, 200 rpm turbine

The simulation is repeated for several values of pneumatic incident energy. Fig. 7 shows the mechanical power over the range of incident pneumatic power for speeds of 150 rpm, 200 rpm and 375 rpm. The upper axis corresponds to the incident wave power with an assumed hydrodynamic efficiency of 0.6 for the OWC. It can be seen from Fig. 7 that higher speeds of operation tend to give better efficiency at increased power levels, while lower speeds tend to give better efficiency at reduced wave power levels. This point is clearly delineated in Fig. 8, which shows the average efficiency. It is evident from the graph that efficiency can be significantly improved over a wide range of input wave power, if the turbine speed is made to vary, as opposed to a fixed speed operation It is very important to note that high efficiency can be obtained by operating over a range of speeds varying by nearly a factor of 2. Variable speed power modules from the wind power industry may be easily adapted for this purpose.

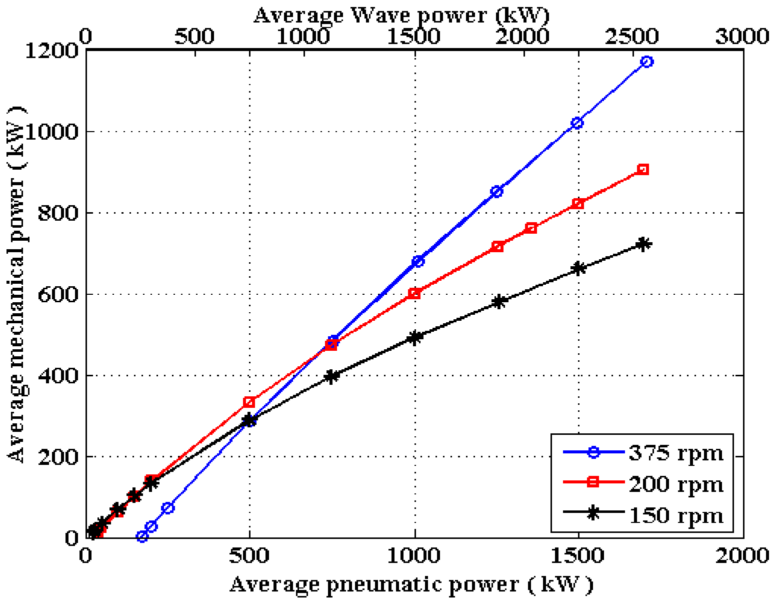

Fig. 7. Average mechanical powers for the variable speed operation of the 4.5 m turbine

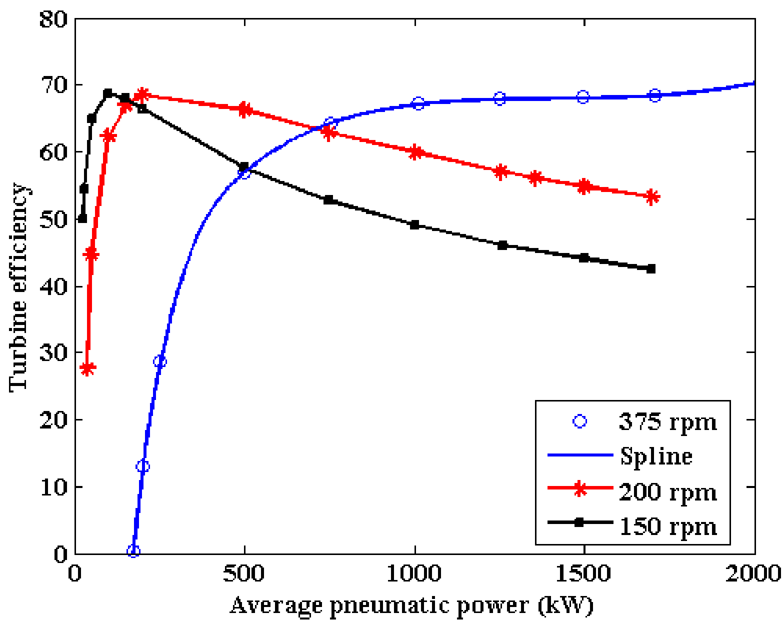

Fig. 8. Average turbine efficiency for the variable speed operation of the 4.5 m turbine

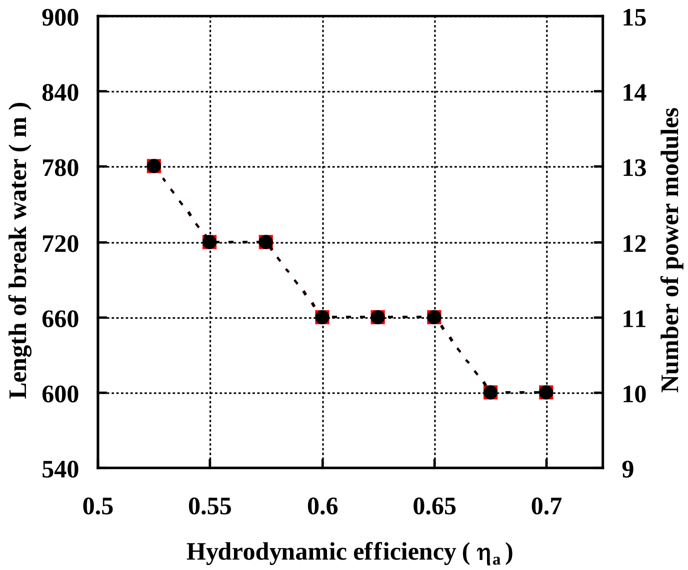

Fig. 9. Influence of the hydrodynamic efficiency on the modular design of the 100 GWh wave energy plant

4. Implications for a 100 GWh plant

It was shown in the previous section that a single 4.5 m diameter turbine could be designed for an average power of 553 kW. Taking a generator efficiency of 94%, each turbine generator set (i.e. the power module) would now be capable of generating 519 kW of electrical power on average. A requirement of 100 GWh over two years implies a 5707 kW plant with 100 % availability. Thus 11 turbine generators will be sufficient to produce the requirement of 100 GWh. A breakwater integrated design of such a plant would cover a length of 660 m, operating at 60 % hydrodynamic efficiency. The modular design is not significantly altered even if the efficiency of wave capture is different. Fig. 9 indicates the number of power modules required to cater to the requirement of 100 GWh, over the expected range of hydrodynamic efficiencies. The size of the corresponding break water is also indicated in Fig.9.

The important features are that the power electronics interface is directly obtainable from the wind industry. This implies that a doubly fed machine which can cater to such a speed variation of 200 to 375 rpm will be adequate for this purpose. With a peak rating of 922 kW doubly fed machines as well as permanent magnet synchronous machines with converters are available. These correspond to the Type C and Type D types of power modules in the wind industry [11].

5. Conclusions

A twin unidirectional turbine power module in an OWC plant can produce an average efficiency of above 60% over a wide range of input excitation. The twin unidirectional turbine topology allows a single turbine generator set, to capture the pneumatic outputs of multiple OWCs. Eleven turbine generator sets of 4.5 m diameter, spread over a 660 m breakwater integrated OWC plant, are sufficient to produce 100 GWh over a period of two years. Variable speed operation is suggested to maintain high efficiency over a wide range of expected incident wave power. Doubly fed induction machines as well as the synchronous machines, commonly used in wind power industry, can be used for the power module in the wave energy plant.

Annexure

The equivalent circuit parameters of the $6\,\mathrm{kV}$, $12.5\,\mathrm{kW}$ induction generator used in the simulation of the 4.5 m unidirectional turbine were taken from [12]. They are as follows.

$R_1 = R_2 = 0.018\ \Omega$
$X_1 = X_2 = 0.18\ \Omega$
$X_m = 14.4\ \Omega$

Acknowledgement

The authors wish to express their heart felt gratitude to Dr. T.Setoguchi, Saga University, Japan for all his help over the years. The authors would also like to thank the NIOT, India for their support in developing the necessary experimental facility required for this research.

References

[1] Ohno H., Funakoshi T., Saito K., Oikawa K., and Takahashi S., Interim report on the Second Stage of Field Experiments on a Wave Power Extracting Caisson In Sakata Port, *ODEC*, 1993, pp. 173-182.

[2] Ravindran M., Jayashankar V., Jalihal P. and Pathak A.G., The Indian Wave Energy Program – an overview, Teri Information Digest on Energy 7(3), 1997, pp.173-188.

[3] Heath, T., Whittaker, T.J.T and Boake, C.B., The design, construction and operation of the LIMPET wave energy converter, Proceedings of the 4th European Wave Energy Conference, 2000, pp. 49-55.

[4] Le Crom, Brito-Melo A.,Neumann F., Sarmento A.J.N.A., Portuguese grid connected OWC power plant: Monitoring Report, Proceedings of the 20th International Offshore and Polar Engineering Conference, 2010.

[5] Marine Energy Challenge: Oscillating Water Column wave energy converter evaluation report, © The Carbon Trust, 2005.

[6] The Saltire prize challenge. Available online: http://www.scotland.gov.uk/Topics/Business-Industry/Energy/Action/leading/saltire-prize; April 1, 2003 [accessed13.09.09].

[7] Takao M., Setoguchi T., Kaneko K., Kim TH, Maeda H. and Inoue M., Impulse turbine for Wave power conversion with Air flow rectification system, International Journal of Offshore and Polar Engineering 12(2), 2002, pp.142 – 146.

[8] Jayashankar V., Anand S., Geetha T et al., A twin unidirectional topology for OWC based wave energy plants, Renewable Energy 34, 2009, pp. 692-698.

[9] Mala K., Jayaraj J., Jayashankar V. et al., A twin unidirectional impulse turbine topology for OWC based wave energy plants - Experimental validation and scaling, Renewable Energy 36, 2011, pp. 307-314.

[10] Anand S, Jayashankar V, Nagata S, Toyota K, Takao M, Setoguchi T., Performance estimation of bi-directional turbines for wave energy plants, International Journal of Thermal Science 15(4), 2007, pp.346 -52.

[11] Michalke G., "Benefits for the development of wave and tidal energy conversion from the lessons learned in wind energy", 3rd International Conference on Ocean Energy, 2010.

[12] Ion Boldea, Variable speed generators, CRC press, 2006, pp.1-16.

The Wave Excitation Forces on a Floating Vertical Cylinder in Water of Infinite Depth

William Finnegan[1], Martin Meere[2], Jamie Goggins[3,*]

[1] College of Engineering and Informatics, National University of Ireland, Galway, Ireland
[2] School of Mathematics, Statistics and Applied Mathematics, National University of Ireland, Galway, Ireland
[3] Ryan Institute for Environmental, Marine and Energy Research, National University of Ireland, Galway, Ireland
* Tel: +35391492609, E-mail: jamie.goggins@nuigalway.ie

Abstract: When carrying out any numerical modeling it is vital to have an analytical approximation to insure that realistic results are obtained. The numerical modeling of wave energy converters is an efficient and inexpensive method of undertaking initial optimisation and experimentation. Therefore, the main objective of this paper is to determine an analytical solution for the heave, surge and pitch wave excitation forces on a floating cylinder in water of infinite depth. The boundary value problem technique, using the method of separation of variables, is employed to derive the velocity potentials throughout the fluid domain. A Fourier transform is used to represent infinite depth. Additionally, Havelock's expansion theorem is used to invert the complicated combined Fourier sine/cosine transform. An asymptotic approximation is taken for low frequency incident waves in order to create an analytical solution to the problem. Graphical representations of the wave excitation forces with respect to incident wave frequencies for various draft to radius ratios are presented, which can easily be used in the design of wave energy converters.

Keywords: *Infinite depth, Wave energy, Wave structure interaction, Wave water problem*

Nomenclature

a	*radius of cylinder*	m
A	*amplitude of incident wave*	m
b	*draft of cylinder*	m
F	*force*	N
F_c	*Fourier cosine transform*	
$F_{1,ext}$	*surge excitation force*	N
$F_{3,ext}$	*heave excitation force*	N
G	*gravity*	$m \cdot s^{-2}$
k_0	*wavenumber*	m^{-1}
m	*integer*	
n_j	*j-component of the normal*	
$p_m(\xi)$	*coefficient*	
q_{m0}	*coefficient*	
$q_m(\xi)$	*coefficient*	
r	*radius*	m
S_B	*wetted surface*	
t	*time*	
v	*flow velocity*	$m \cdot s^{-1}$
x	*horizontal coordinate*	m
z	*vertical coordinate*	m
ε_m	*Neumann symbol*	
θ	*polar coordinate*	*rads*
ξ	*separation constant*	
ρ	*density*	$kg \cdot m^3$
φ	*frequency domain velocity potential*	$m \cdot s^{-1}$
φ_I	*incident wave velocity potential*	$m \cdot s^{-1}$
$\varphi_s^{\,i}$	*interior scattering velocity potential*	$m \cdot s^{-1}$
$\varphi_d^{\,e}$	*exterior diffraction velocity potential*	$m \cdot s^{-1}$
$\varphi_s^{\,e}$	*exterior scattering velocity potential*	$m \cdot s^{-1}$
Φ	*time domain velocity potential*	$m \cdot s^{-1}$
ω	*wave angular frequency*	s^{-1}

1. Introduction

One of the main stages in the design of wave energy converters (WECs) is the numerical modelling of a given converter. In this paper, an analytical solution for the wave excitation forces on a floating cylinder in water of infinite depth is provided. The solution will act as a method of validating the results from numerical models of WECs, as it provides an estimation of forces on a cylinder representation of an arbitrary shaped axisymmetric WEC.

The solution of the scattering and radiation problem for floating bodies, in finite or infinite depth water, has being explored for decades for a various shapes of bodies. In 1948, Fritz Ursell[1] explored the forces on an infinitely long horizontal floating cylinder in infinitely deep water and, in 1955, Sir Thomas Havelock[2] solved the radiation problem for a floating half-immersed sphere in infinitely deep water. In 1971, Garrett[3] solved the scattering problem by determining the vertical force, horizontal force and torque for a circular dock in water of finite depth. In 1975, Black[4] looked at the wave forces on bodies which are vertically axisymmetric using an integral equation formulation in water of finite depth. In 1981, Yeung[5] presented a set of theoretical added mass and damping coefficient for a floating cylinder in finite depth, which he also truncated for the infinite depth problem. In 2003, Bhatta and Rahman[6] used a similar technique as Havelock to solve, although using a semi-analytic solution, the scattering and radiation problem for a floating vertical cylinder in water of finite depth. Previously, an analytical solution for wave excitation forces on a floating cylinder in water of infinite depth has not been derived. Therefore, the solution derived in this paper is for a semi-submerged vertical cylinder in infinite depth water. A boundary value problem is used to derive an analytic solution, from the scattering problem, for the heave, surge and pitch excitation forces.

2. Methodology

The problem considers a vertical cylinder, of radius, *a*, and with a draft, *b*, which can move in surge, heave or pitch motion, and an incident wave of amplitude, *A*, and angular frequency, *ω*, as depicted in Fig. 1. The wave progresses in the positive x-direction with the origin at the still water level (SWL) and the positive z-direction is vertically downwards. In the formulation of the solution, a number of assumptions are used:

- The water is both incompressible, as frequencies are low, and effectively viscid.
- As the air has such a small density, pressure change is negligible and, thus, is at constant pressure.
- The surface tension at air-water interface is negligible.
- The water is at constant density and temperature.
- The Reynolds' number for the flow is sufficiently small for the flow to remain laminar.
- The waves are progressive and only travel in one direction and the wave motion is irrotational.

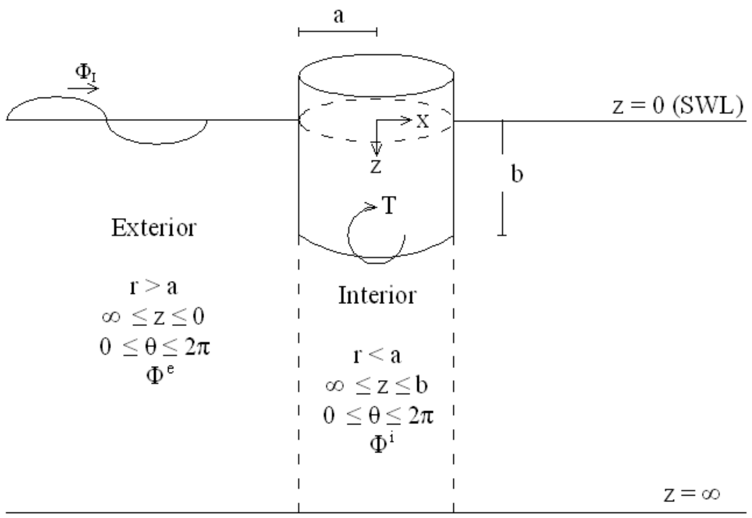

Fig. 1 Graphical set-up of the Boundary Value Problem for a Vertical Cylinder

Yeung[5] and Bhatta and Rahman[6] employed the technique of dividing the domain into two regions, which is used in this paper. The two regions are the interior region, which is the area underneath the cylinder, and the exterior region, which is the remaining area of the fluid (Fig. 1). The problem is solved in the frequency domain. Therefore, the velocity potential, φ, to be solved is transformed to the frequency domain, as follows:

$$\Phi(r,\theta,z,t) = \mathrm{Re}\{\varphi(r,z,\theta)e^{-i\omega t}\} \tag{1}$$

where Φ is the time domain velocity potential, r is radius, θ is the angle, i is the standard imaginary unit, ω is the wave angular frequency of the wave, and φ is the frequency domain velocity potential. The force is then calculated by integrating the velocity potential over the wetted surface area of the cylinder, S_B, using the following equation:

$$\hat{F} = i\rho\omega\int_{SB} \oint \varphi n_j \, dS \tag{2}$$

where ρ is water density, n_j is the j-component of the normal, S is surface and F is the force, where $F = \mathrm{Re}\{\hat{F}e^{-i\omega t}\}$. The equations and boundary conditions that need to be satisfied throughout the problem are: the Laplace's equation, the deep water condition, the free surface equation and the radiation condition, respectively[7]:

$$\nabla^2\varphi = \frac{1}{r}\frac{\partial\varphi}{\partial r} + \frac{\partial^2\varphi}{\partial r^2} + \frac{1}{r^2}\frac{\partial^2\varphi}{\partial\theta^2} + \frac{\partial^2\varphi}{\partial z^2} = 0 \tag{3}$$

$$|\nabla\varphi| \to 0 \text{ as } z \to \infty \tag{4}$$

$$\omega^2\varphi - g\frac{\partial\varphi}{\partial z} = 0 \text{ on } z = 0,\ r \geq a \tag{5}$$

$$\lim_{r\to\infty} \sqrt{r}\left(\frac{\partial\varphi}{\partial r} - ik_0\varphi\right) = 0 \tag{6}$$

where k_0 is the wavenumber ($k_0 = \omega^2/g$). Since the motion is irrotational and incompressible, the Laplace's equation was arrived at by substituting $v = \nabla\varphi$ into $\nabla . v = 0$, where v is the flow velocity. The solution being developed is for infinitely deep water. Thus, the deep water condition defines the flow velocity near the sea bed. The free surface equation defines the velocity potential at the free surface away from the floating body. The radiation condition defines the velocity potential of the wave at the distance from the body when the effect of the body on the wave has dissipated. The scattering problem deals with the excitation force on a fixed body and, therefore, the following structural boundary conditions must be imposed:

$$\frac{\partial\varphi_S^i}{\partial\bar{z}} = 0 \text{ on } \bar{z} = 0, \quad \text{where } \bar{z} = z - b \tag{7}$$

$$\frac{\partial\varphi_S^e}{\partial r} = 0 \text{ at } r = a \tag{8}$$

where φ_S^i and φ_S^e are the interior and exterior scattering velocity potentials, respectively. Since we are dealing with infinite depth, a Fourier sine/cosine transform is employed when dealing with the vertical or z-component. For the interior region, in order to satisfy the structural equation (Eq. (7)) a Fourier cosine transform is required. Therefore, introducing a constant, ξ, yields:

$$F_C\left(\varphi_S^i(r,\theta,\bar{z})\right) = \sqrt{\frac{2}{\pi}}\int_0^\infty \varphi_S^i(r,\theta,\bar{z})\cos\xi\bar{z}\,d\bar{z} \tag{9}$$

$$\Box\ \varphi_S^i(r,\theta,\bar{z}) = \sqrt{\frac{2}{\pi}}\int_0^\infty F_c\left(\varphi_S^i(r,\theta,\bar{z})\right)\cos\xi\bar{z}\,d\xi \tag{10}$$

where F_c is the Fourier cosine transform. The method of separation of variables is used to solve the Laplace's equation (Eq. (3)) in order to formulate an expression for the interior scattering velocity potential φ_S^i, as follows:

$$\varphi_S^i(r,\theta,\bar{z}) = \sum_{m=0}^{\infty}\sqrt{\frac{2}{\pi}}\int_0^\infty p_m(\xi)\frac{I_m(\xi r)}{I_m(\xi a)}\cos\xi\bar{z}\,d\xi\cos m\theta \tag{11}$$

where I_m is the modified first Bessel function of order m and $p_m(\xi)$ is an unknown coefficient.

Kim[8] gives the incident wave velocity potential, φ_I, in the frequency domain for deep water in oblique sea as:

$$\varphi_I(r,\theta,z) = -\frac{gA}{\omega}e^{-k_0 z}\sum_{m=0}^{\infty}\varepsilon_m i^{m+1}J_m(k_0 r)\cos m\theta \tag{12}$$

where J_m is the first Bessel function of order m, ε_m is the Neumann symbol, defined by $\varepsilon_0 = 1$ and $\varepsilon_m = 2$ for $m \geq 1$. Similarly, for the exterior region, when dealing with infinite depth in the method of separation of variables, a Fourier sine/cosine transform is used. In order to satisfy the free surface equation (Eq. (5)), a combination of the Fourier sine and Fourier cosine transform is required. Again, introducing a constant ξ, the following is obtained:

$$F\left(\varphi_d^e(r,\theta,z)\right) = \sqrt{\frac{2}{\pi}}\int_0^\infty \varphi_d^e(r,\theta,z)\left[\xi\cos\xi z - k_0\sin\xi z\right]\cos\xi z\,dz \tag{13}$$

where φ_d^e is the exterior diffraction velocity potential. The Havelock's expansion theorem [9] is used to obtain the inverse Fourier transform. Similarly, the method of separation of variables is used to solve the Laplace's equation (Eq. (3)) in order to formulate an expression for the exterior diffraction velocity potential, which is given as:

$$\begin{aligned}\varphi_d^e(r,\theta,z) = \sum_{m=0}^{\infty}[q_{m,0}&\frac{H_m^{(1)}(k_0 r)}{H_m^{(1)}(k_0 a)}e^{-k_0 z} \\ &+\sqrt{\frac{2}{\pi}}\int_0^\infty \frac{q_m(\xi)}{\xi^2+k_0^2}\frac{K_m(\xi r)}{K_m(\xi a)}\left[\xi\cos\xi z - k_0\sin\xi z\right]d\xi]\cos m\theta\end{aligned} \tag{14}$$

Therefore, since the scattering velocity potential is the sum of the incident and diffraction velocity potentials (i.e. $\varphi_S = \varphi_I + \varphi_d$) and incorporating $-gA\omega^{-1}\varepsilon_m i^{m+1}$ into the $\varphi_d^e(r,\theta,z)$ term in Eq. (14), the scattering velocity potential for the exterior problem is given as:

$$\begin{aligned}\varphi_S^e(r,\theta,z) = \sum_{m=0}^{\infty} -\frac{gA}{\omega}\varepsilon_m i^{m+1}[\{J_m(k_0 r) + q_{m,0}\frac{H_m^{(1)}(k_0 r)}{H_m^{(1)}(k_0 a)}\}e^{-k_0 z} \\ + \sqrt{\frac{2}{\pi}}\int_0^\infty \frac{q_m(\xi)}{\xi^2 + k_0^2}\frac{K_m(\xi r)}{K_m(\xi a)}[\xi\cos\xi z - k_0\sin\xi z]d\xi]\cos m\theta\end{aligned} \tag{15}$$

where $H_m^{(1)}$ is the first Hankel function of order m and K_m is the modified second Bessel function of order m. The unknown coefficients of $p_m(\xi)$ in Eq. (11), and $q_{m,0}$ and $q_m(\xi)$ in Eq. (15), are found by matching the velocity potentials across the boundary at $r = a$. The conditions which are to be satisfied at the boundary are:

$$\varphi_S^e(r,\theta,z) = \varphi_S^i(r,\theta,\bar{z}), \text{ if } b \le z \le \infty \tag{16}$$

$$\frac{\partial\varphi_S^e(r,\theta,z)}{\partial r} = \frac{\partial\varphi_S^i(r,\theta,\bar{z})}{\partial r}, \text{ if } b \le z \le \infty \tag{17}$$

$$\frac{\partial\varphi_S^e(r,\theta,z)}{\partial r} = 0, \text{ if } 0 \le z \le b \tag{18}$$

3. Results

In order to create an analytical solution, asymptotic approximations for the excitation forces are derived for low frequency waves or, in other terms, when the wavenumber, k_0, tends towards zero. Therefore, in addition to Eq. (16)-(18), the approximation that k_0 tends towards zero is imposed when matching the interior scattering velocity potential, given in Eq. (11), and the exterior scattering velocity potential, given in Eq. (15), across the boundary $r = a$ in order to solve for the unknown coefficients $p_m(\xi)$, $q_{m,0}$ and $q_m(\xi)$,. Using this additional approximation, it was found that $q_m(\xi)$ tends to zero and the coefficient, $q_{m,0}$, is approximated as:

$$q_{m,0} = -J_m{}'(k_0 a)\frac{H_m^{(1)}(k_0 a)}{H_m^{(1)}{}'(k_0 a)} \tag{19}$$

and the coefficient, $p_m(\xi)$, is given as:

$$p_m(\xi) = -\frac{gA}{\omega}\varepsilon_m i^{m+1}\sqrt{\frac{2}{\pi}}\{J_m(k_0 a) + J_m{}'(k_0 a)\frac{H_m^{(1)}(k_0 a)}{H_m^{(1)}{}'(k_0 a)}\}\frac{e^{-k_0 b}k_0}{\xi^2 + k_0^2} \tag{20}$$

where prime is the derivative. Therefore, an analytical approximation is created and shown graphically for various draft, b, to radius, a, ratios in Fig. 2-4.

When calculating the surge, or horizontal, excitation force the only non-zero solution is when $m = 1$, as this is the only non-zero solution to the integral $\int \cos m\theta \cos\theta \, d\theta$, which arises in the force calculation. Furthermore, when integrating the velocity potential over the surface area, the integration is performed only over the curved surface of the cylinder and, hence, the exterior velocity potential at $r = a$ is used. Therefore, the surge excitation force, $\hat{F}_{1,ext}$, is given as:

$$\begin{aligned}\hat{F}_{1,ext} &= i\rho\omega\int_{SB}\phi_S^e(r,\theta,z)n_1\,dS = i\rho\omega\int_0^{2\pi}\int_0^b \varphi_S^e(a,\theta,z)n_1\,a\,dz\,d\theta \\ &= -\frac{\rho g A a}{k_0}\sum_{m=0}^{\infty}\varepsilon_m i^m\{J_m(k_0a)-J_m'(k_0a)\frac{H_m^{(1)}(k_0a)}{H_m^{(1)\prime}(k_0a)}\}(1-e^{-k_0b})\int_0^{2\pi}\cos m\theta\cos\theta\,d\theta \qquad (21)\\ &= -\frac{2\pi i\rho g A a}{k_0}\{J_1(k_0a)-J_1'(k_0a)\frac{H_1^{(1)}(k_0a)}{H_1^{(1)\prime}(k_0a)}\}(1-e^{-k_0b})\end{aligned}$$

where $n_1 = -\cos\theta$. Graphical representations of surge excitation forces with respect to incident wave frequencies for various draft to radius ratios of devices are shown in Fig. 2.

When calculating the heave, or vertical, excitation force from the velocity potential, the only non-zero solution is when m is equal to zero due to the integral $\int \cos m\theta\, d\theta$. Furthermore, when integrating the velocity potential over the surface area, the integration is performed only over the base of the cylinder and, hence, the interior velocity potential, at $\bar{z} = 0$, is used. Therefore, the heave excitation force, $\hat{F}_{3,ext}$, is given as:

$$\begin{aligned}\hat{F}_{3,ext} &= i\rho\omega\int_{SB}\phi_S^i(r,\theta,\bar{z})n_3\,dS = i\rho\omega\int_0^{2\pi}\int_0^a \varphi_S^i(r,\theta,0)n_3\,r\,dr\,d\theta \\ &= -i\rho\omega\sqrt{\frac{2}{\pi}}\int_0^{2\pi}\int_0^a\int_0^{\infty}p_m(\xi)\frac{I_m(\xi r)}{I_m(\xi a)}d\xi\,r\,dr\cos m\theta\,d\theta \qquad (22)\\ &= -2\pi i\rho\omega a\sqrt{\frac{2}{\pi}}\int_0^{\infty}p_0(\xi)\frac{I_1(\xi r)}{\xi I_0(\xi a)}d\xi\end{aligned}$$

where $n_3 = -1$. Graphical representations of heave excitation forces with respect to incident wave frequencies for various draft to radius ratios of devices are shown in Fig. 3.

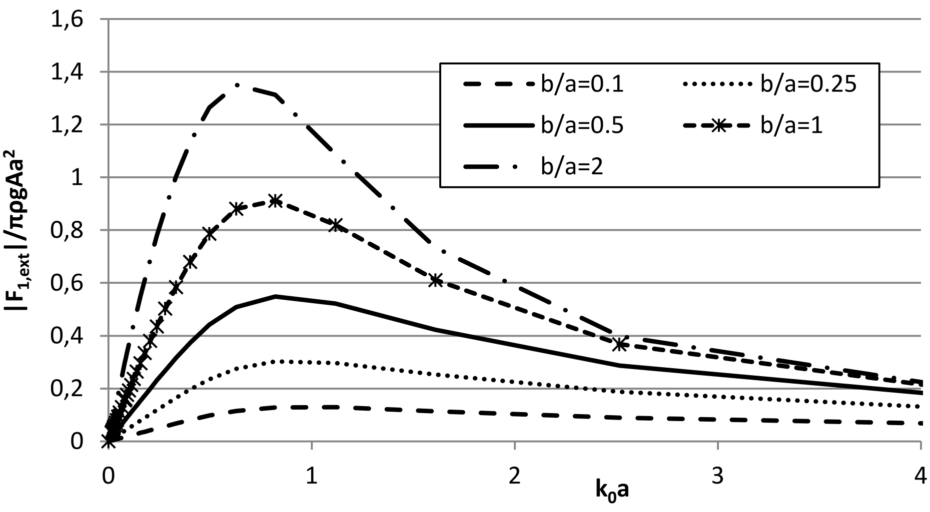

Fig. 2 The normalised surge (or horizontal) excitation force, in the frequency domain, as a function of k_0a for various radius to draft ratios.

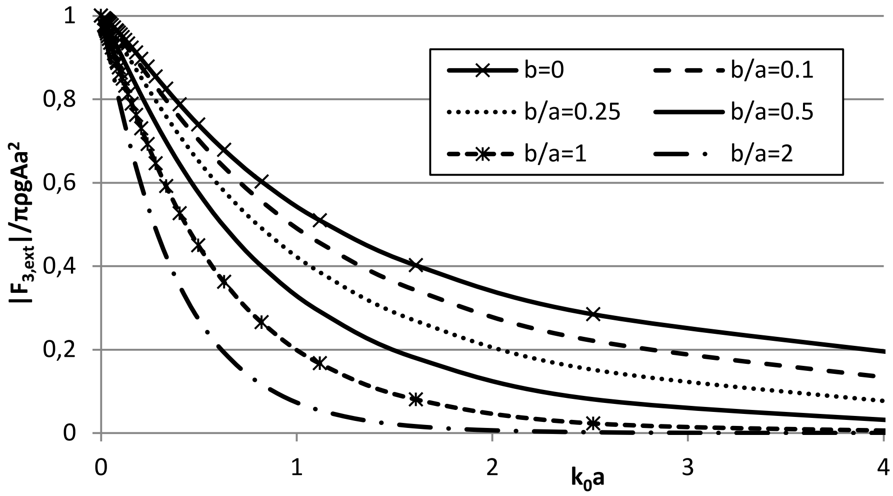

Fig. 3 The normalised heave (or vertical) excitation force, in the frequency domain, as a function of k_0a for various draft to radius ratios.

The pitch, or torque, excitation force arises from the surge and heave forces on the wetted surface of the cylinder. The pitch is taken about the axis which is transverse to the incident wave at the centre of the base, as shown by *T* in Fig. 1. When calculating the pitch the only non-zero solution, similar to surge, is when *m = 1*. Therefore, the pitch excitation force, $\hat{F}_{5,ext}$, is given as:

$$
\begin{aligned}
\hat{F}_{5,ext} &= i\rho\omega\int_{SB} \phi_S(r,\theta,z)n_5 \; dS \\
&= -i\rho\omega\int_0^{2\pi}\int_0^b \varphi_S^e(a,\theta,z)(z-b)\cos\theta \, a \, dz \, d\theta + i\rho\omega\int_0^{2\pi}\int_0^a \varphi_S^i(r,\theta,0)r^2\cos\theta \, dr \, d\theta \\
&= -2\pi i\rho gAa\{J_m(k_0a) - J_m'(k_0a)\frac{H_m^{(1)}(k_0a)}{H_m^{(1)\prime}(k_0a)}\}\int_0^b (z-b)e^{-k_0z} \, dz \\
&\quad + \pi i\rho\omega a^2\sqrt{\frac{2}{\pi}}\int_0^\infty p_1(\xi)\frac{I_2(\xi r)}{\xi I_1(\xi a)}d\xi
\end{aligned}
\tag{28}
$$

Graphical representations of pitch excitation forces with respect to incident wave frequencies for various draft to radius ratios of devices are shown in Fig. 4.

4. Discussion and Conclusions

An analytical solution to determine the heave, surge and pitch wave excitation forces on a floating cylinder in water of infinite depth has been presented in this paper. For ease of use in the design of wave energy converters, a graphical representation of the wave excitation forces with respect to the incident wave frequencies for various draft to radius ratios of devices are given. In particular, the heave, surge and pitch excitation forces, which are the only three forces on an axisymmetric device, were derived. The analytical solutions were obtained using an asymptotic approximation for low frequency incident waves.

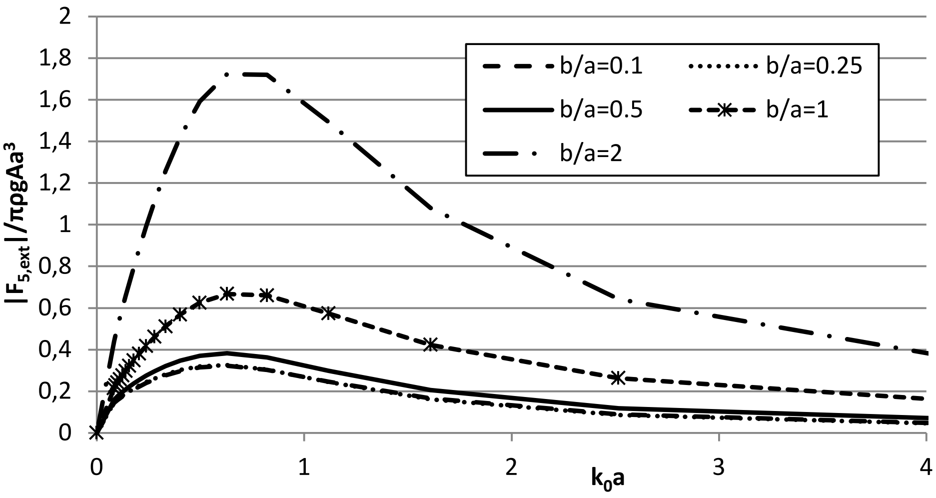

Fig. 4 The normalised pitch (or torque) excitation force, in the frequency domain, as a function of k_0a for various draft to radius ratios.

Acknowledgements

The first author would like to acknowledge the financial support from the National University of Ireland under the College of Engineering & Informatics Postgraduate Fellowship.

References

[1] F. Ursell, On The Heaving Motion of a Circular Cylinder on the Surface of a Fluid, The Quarterly Journal of Mechanics and Applied Mathematics, 2(2), 1949, pp. 218-231.

[2] T. Havelock, Waves due to a F loating Sphere Making Periodic Heaving Oscillations. Proceedings of the Royal Society of London, Series A, Mathematical and Physical Sciences, 231(1184), 1955, pp. 1-7.

[3] C.J.R. Garrett, Wave forces on a circular dock, Journal of Fluid Mechanics, 46(01), 1971, pp. 129-139.

[4] J.L. Black, Wave forces on vertical axisymmetric bodies, Journal of Fluid Mechanics, 67(02), 1975, pp. 369-376.

[5] R.W. Yeung, Added mass and damping of a vertical cylinder in finite-depth waters, Applied Ocean Research, 3(3), 1981, pp. 119-133.

[6] D.D. Bhatta and M. Rahman, On scattering and radiation problem for a cylinder in water of finite depth, International Journal of Engineering Science, 41(9), 2003, pp. 931-967.

[7] C.M. Linton and P.McIver, Handbook of Mathematical Techniques for Wave/Structure Interactions, Chapman & Hall/CRC, 2001.

[8] C.H. Kim, Nonlinear Waves and Offshore Structures, Advanced Series on Ocean Engineering, World Scientific Publishing Co. Pte. Ltd, 2008.

[9] A. Chakrabarti, On the Solution of the Problem of Scattering of Surface-Water Waves by the Edge of an Ice Cover, Proceedings: Mathematical, Physical and Engineering Sciences, 456(1997), 2000 pp. 1087-1099.

2D numerical simulation of ocean waves

Qingjie. Du[*], Y.C. Dennis. Leung

Department of Mechanical Engineering, The University of Hong Kong, Hong Kong, China
** Corresponding author. Tel: +852 51743593, E-mail: qingjie.du@gmail.com*

Abstract: As fossil energy is depleting and global warming effect is worsening rapidly, developing renewable energies become the top priority on most developed and some developing countries. Among different kinds of renewable energies, wave energy attracts more and more attention in recent years due to its high energy density and enormous global amount. However, some technical difficulties still need to be overcome for extracting wave power. In designing a wave energy converter, it is important to develop an efficient method to determine the wave load and predict its response. In this paper, a n umerical investigation of ocean waves is presented. Commercial software code FLUENT is used as a computational platform in this study. Based on the Navier-Stokes equations for viscous, incompressible fluid and Volume of fluid (VOF) method, a two dimensional numerical wave tank is established. Dynamic meshing method is used to simulate the wave maker, and Geo-Reconstruct scheme is used to capture the free surface. A wave-absorbing method employing porous media model is proposed, which can absorb the wave energy efficiently. Moving boundary, wall boundary and pressure-inlet boundary are used to construct the computational domain. Linear regular waves are simulated accurately using the proposed numerical model. The numerical results matched with the theoretical calculation.

Keywords: *Numerical wave flume, FLUENT, VOF method, Dynamic meshing*

Nomenclature

u	*velocity component (x-direction)*	$m{\cdot}s^{-1}$
v	*velocity component (y-direction)*	$m{\cdot}s^{-1}$
ρ	*density*	$kg{\cdot}m^{-3}$
μ	*dynamic viscosity*	$kg{\cdot}m{\cdot}s^{-1}$
p	*static pressure*	Pa
g_x	*body force (x-direction)*	$N{\cdot}Kg^{-1}$
g_x	*body force (x-direction)*	$N{\cdot}Kg^{-1}$
S	*paddle stroke*	m
T	*wave period*	s
k	*wave number*	m^{-1}
h	*wave free surface*	m
ω	*angular frequency*	s^{-1}
f	*body forces*	N

1. Introduction

The World Energy Council (1999) reported that the total globally extractable wave energy is about 2 Terawatts [1], which is the same order of magnitude as the world's total electricity consumption. How to harness this huge energy has attracted more and more scientists' attention. In the design of wave energy converter, predicting wave loads and the structure responses have become increasingly important. In the past, the study of wave-structure interaction is mainly based on physical model experiment, which is both time consuming and money costly. Nowadays, following the rapid development in computational method and computer hardware, numerical simulation of the wave-structure interaction has attracted more and more attention.

The computation of unsteady free-surface flow is a key point in two-phase flow. Hirt and Nichols [2] developed the Volume of fluid (VOF) method to solve the two-phase problem, which uses a geometrical reconstruction scheme to capture the free surface. Wang et al [3] employed a numerical method to simulate the wave group development in long tanks. Zou [4] and Liu [5] used a moving boundary to simulate the piston-type wave maker, and successfully generated regular waves. Wei et al [6] and Chawla [7] implemented a source function method to generate ocean waves, based on Boussinesq model. Based on the 2D form of Navier-Stokes equations, Dong and Huang [8] established a 2 D numerical wave tank to simulate small-amplitude waves and solitary waves. Lu et al [9] numerically simulated wave overtopping against seawalls in regular wave case.

During the last two decades, numerous scientists have developed their numerical methods to simulate ocean waves that are nonlinear and unsteady free-surface flows. In this paper, the research is focused on the simulation of a two-dimensional numerical wave flume. FLUENT is used as the main computational platform. Some User-Define-Function (UDF) has been implemented to simulate the wave maker and wave absorbing bench. Dynamic meshing technique is used to simulate a piston-type wave maker, which can generate both regular and irregular waves. VOF model is used to capture the free surface between water and air. Porous media model acts as the wave absorbing bench to absorb the wave energy. Both linear and nonlinear waves are simulated and compared with theoretical result.

2. Governing equation

In fluid dynamic research, there are several important assumptions. F irst, the fluid being studied is assumed to be a continuum; second, all field involved are differentiable, such as velocity field, pressure field. Moreover, for the water fluid dynamic field, some other sound assumptions are also established. Water is assumed to be Newtonian fluids, and it is incompressible and its density will not change with time. Based on the above assumptions, the Navier–Stokes equation and continuity equation are used to describe the fluid motion, which are also the governing equations in this study.

2.1. Navier–Stokes equation

Equation 1 shows the Navier-Ssokes equation in vector form:

$$\rho\left(\frac{\partial V}{\partial t} + V \cdot \nabla V\right) = -\nabla p + \mu \nabla^2 V + f \tag{1}$$

Rewriting the vector equation explicitly in 2D Cartesian coordinates:

$$\rho\left(\frac{\partial u}{\partial t} + u\frac{\partial u}{\partial x} + v\frac{\partial u}{\partial y}\right) = -\frac{\partial p}{\partial x} + \mu\left(\frac{\partial^2 u}{\partial x^2} + \frac{\partial^2 u}{\partial y^2}\right) + \rho g_x \tag{2.a}$$

$$\rho\left(\frac{\partial v}{\partial t} + u\frac{\partial v}{\partial x} + v\frac{\partial v}{\partial y}\right) = -\frac{\partial p}{\partial y} + \mu\left(\frac{\partial^2 v}{\partial x^2} + \frac{\partial^2 v}{\partial y^2}\right) + \rho g_y \tag{2.b}$$

2.2. Continuity Equation

Equation 3 shows the continuity equation in 2D Cartesian coordinates

$$\frac{\partial u}{\partial x} + \frac{\partial v}{\partial y} = 0 \tag{3}$$

3. Numerical method

3.1. Boundary condition

Given proper boundary condition and initial condition, the above equations can be solved computationally. For a 2D case, given the velocity potential Φ, the boundary conditions are as follows:

(a) dynamic free-surface condition:

$$\frac{\partial \phi}{\partial t} = -g\eta - \frac{1}{2}|\nabla\phi|^2 - \frac{P_0}{\rho} \quad (4)$$

where P_0 is the pressure on the free surface.

(b) kinematic free-surface condition:

$$\frac{\partial \eta}{\partial t} = -\nabla\phi \cdot \nabla\eta + \frac{\partial \phi}{\partial y} \quad (5)$$

(c) No normal-flux condition:

$$\frac{\partial \phi}{\partial n} = 0 \quad (6)$$

applied on the rigid bottom, and at the vertical end-wall of the numerical flume.

In FLUENT, boundary condition (a) and (b) is satisfied by using the VOF scheme, and boundary condition (c) is satisfied by using wall condition.

3.2. Free surface--VOF model

The main goal of the present research is to study the characteristics of ocean waves under different scenarios. In this research, the key problem is how to accurately describe the free surface between the two different phases. In this paper, since all the calculation is based on FLUENT, VOF model is used to simulate the free surface between water and air. The method is based on the idea of so called fraction function α_q. It is defined as the integral of fluid's characteristic function in the control volume (namely volume of a computational grid cell). Basically, when the cell is empty, $\alpha_q = 0$; if the cell is full, $\alpha_q = 1$; if $0 < \alpha_q < 1$, then the volume is the interface between the two phases. For this study, it is a two-phase problem, so q=1,2, representing air and water respectively. q is tracked by solving the continuity equation below for q^{th} fluid.

$$\frac{\partial \alpha_q}{\partial t} + \frac{\partial (u\alpha_q)}{\partial t} + \frac{\partial (v\alpha_q)}{\partial t} = 0 \quad (7)$$

$$\sum_{q=1}^{2} \alpha_q = 1 \quad (8)$$

3.3. Wave maker--dynamic mesh

A piston-type wave maker is simulated using the dynamic mesh technology in this study. Moving boundary is used to model the oscillating paddle in the physical wave maker. A user-defined function (UDF) is used to describe the motion of the oscillating paddle. In order to make the simulation more smoothly, the velocity of the paddle is described as follows:

$$U = \frac{t}{2T}\frac{S}{2}\omega\cos(\omega t) \qquad t \leqq 2T \quad (9.a)$$

$$U = \frac{S}{2}\omega\cos(\omega t) \qquad t > 2T \quad (9.b)$$

where S is the stroke of the paddle, t is the run time, T is the wave period, ω ($\omega = 2\pi/T$)is the angular frequency.

3.4. Wave absorbing bench--Porous media

The mathematic model of the porous medium is defined as:

$$S_i = -\left(\frac{\mu}{\alpha} v_i + C_2 \frac{1}{2} \rho |v| v_i\right) \tag{10}$$

where i represents x, y, z; $\frac{1}{\alpha}$ & C_2 are the coefficients of viscous resistance & inertial resistance respectively.

In this 2D model, only $\frac{1}{\alpha}$ is considered. How to decide the value of $\frac{1}{\alpha}$ is very important. If $\frac{1}{\alpha}$ is too small, the wave energy cannot be absorbed completely and when waves reach the right boundary, it will reflect. If $\frac{1}{\alpha}$ is too large, the fluid property will change dramatically in the interface between the water and porous medium, so the wave will reflect too. In this simulation, the coefficient is defined as a function of the position, which is described by a UDF, in order to make the resistance of the porous medium change smoothly.

3.5. Computational model

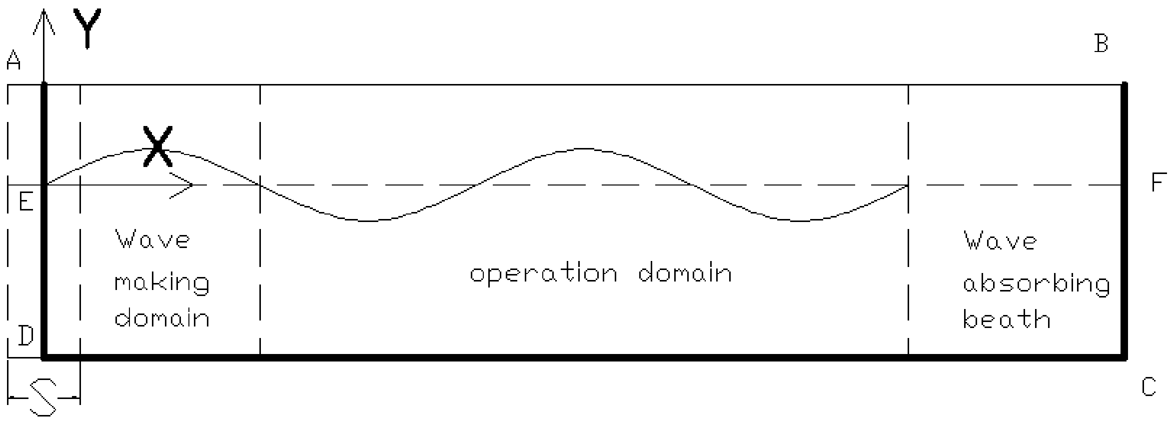

Fig.1 computational model scheme

Fig.1 shows a computation scheme of this study. Boundary AD represents the oscillating paddle; Boundary DC represents the wave flume bottom; Boundary BC represents the end of the wave flume; Boundary AB represents the top of the flume. The Volume of Fluid model is used to describe the free surface between the air and water.

4. Results and discussion

In this study, the numerical model is based on the dimension of a physical wave flume in the laboratory, with a dimension of 9m long and 0.45m high. In this simulation, the initial water depth is 0.3m. A linear regular wave with a wave height at 0.05m and wave period at 1.8s will be simulated by the numerical model. The theoretical analysis will be performed too. The wave form in the whole tank is monitored at certain times. Also the surface elevation history at point x=4.5m, which is the center point of the physical wave tank, is monitored too. These data will be compared with the theoretical result.

Under the assumption of both small amplitude paddle motion and small wave height, linear wavemaker theory has been developed by Dean and Dalrymple [10]. Assuming the original place of the paddle is at x=0, and the wavemaker stroke is S, the angular frequency of the paddle is ω, the wave elevation on the free surface η in the wave tank with water height d is shown as follows:

$$\eta = \frac{S}{2}\left[\frac{4\sinh^2(kd)}{2kd+\sinh(2kd)}\cos(kx-\omega t)\right] \tag{11}$$

$$\omega^2 = gk\tanh(kd) \tag{12}$$

Fig.2 shows the water elevation history at x=4.5m from the time of 40s to 50s. 40s, which is about 20 wave periods, is thought to be long enough for the wave to be fully developed. The black line with stars represents for the numerical result, and the green dotted line represents for the theoretical result.

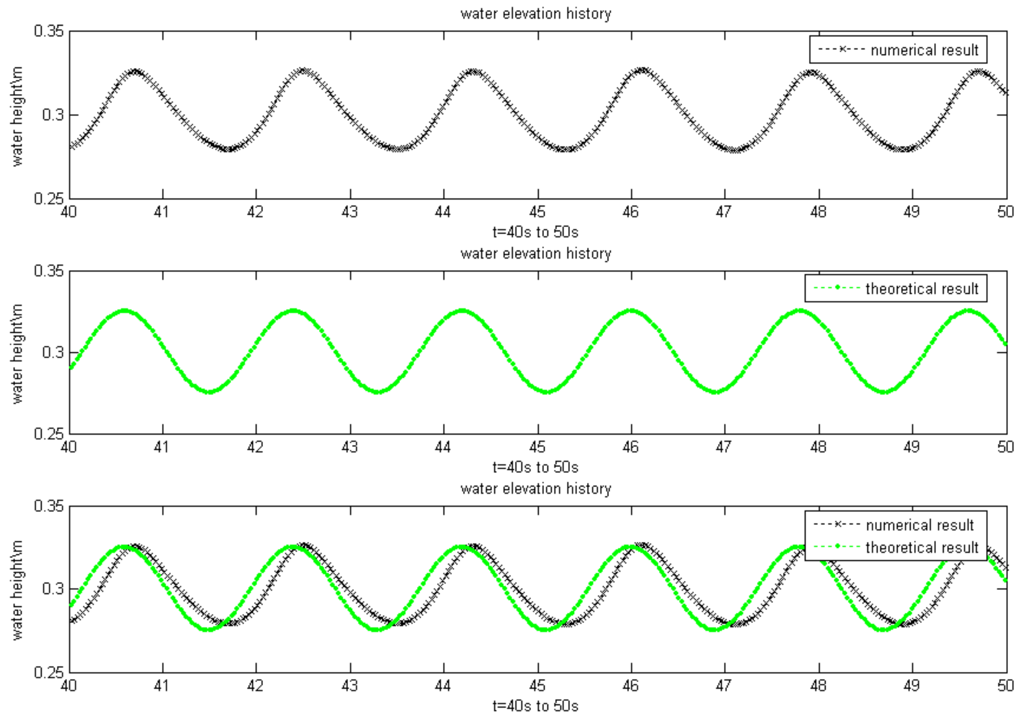

Fig.2 surface elevation history at point x=4.5

Though there is a slight shift in the phase, the numerical result matches the theoretical result well. The phase shift is due to the first 2 periods. In the simulation, during first 2 periods, all the parameters were dividing by 2T for smoothing issue.

Fig.3 shows the water free surface at t=40s, 45s and 50s. The water surface is sinusoidal, which matches the theoretical analysis.

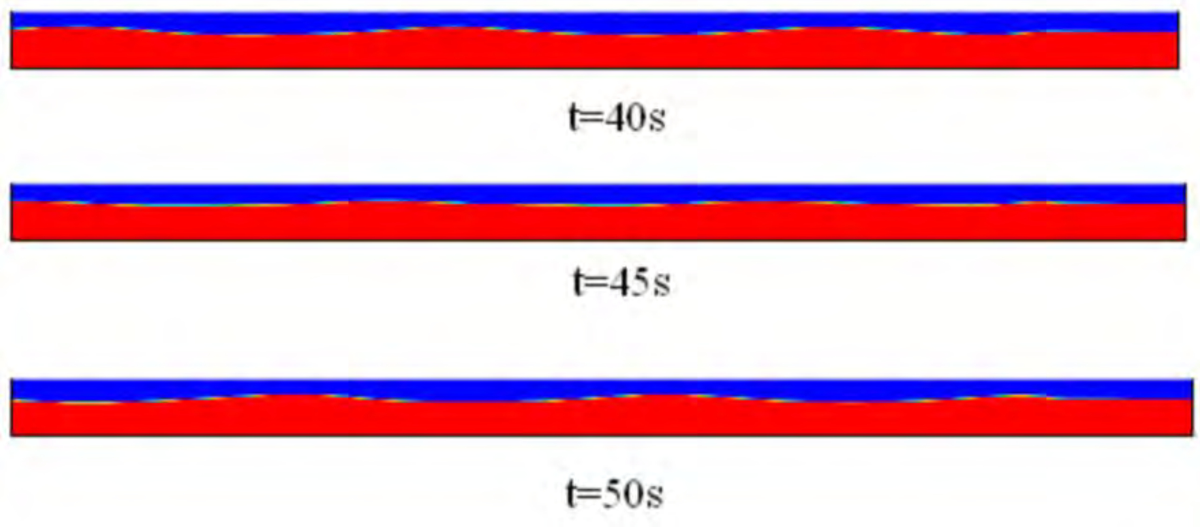

Fig.3 wave surface at t=40s, 45s, 50s

Noted that for the wave absorbing model, the waves are absorbed completely by the porous media in the right part. Otherwise, the waves will reflect since the right boundary condition is wall.

5. Conclusion

In this study, the wave simulation model is developed based on a commercial software FLUENT for modeling fluid flow. Linear regular waves and wave absorbing bench are simulated well with a self-developed numerical model. The simulation of a wave with a wave height of 0.05m and period of 1.8s is conducted successfully. Comparison between the numerical and theoretical results shows that the numerical method works well.

Compared with the physical model experiments, this numerical model is more adaptable. The wave tank dimension can be changed according to the specific situation. The use of this numerical model is costless and is very convenient.

Based on this model, the wave-structure interaction can be studied. What's more important is that it can serve as a platform to predict the hydrodynamic response of wave energy convertors (WECs) in waves, and the result can be used to optimize the WECs.

Acknowledgement

The authors wish to acknowledge the IEEE of the University of Hong Kong for supporting the project.

References

[1] Thorpe, T.W., A brief review of wave energy. ETSU Report Number R-120 for the DTI, 1999.

[2] Hirt, C.W. and B.D. Nichols, Volume of fluid (VOF) method for the dynamics of free boundaries. Journal of Computational Physics, 1981. 39(1): pp. 201-225.

[3] Wang, P., Y. Yao, and M.P. Tulin, Wave group evolution, wave deformation, and breaking: simulations using LONGTANK, a numerical wave tank. International Journal of Offshore and Polar Engineering, 1994. 4(3): pp. 200-205.

[4] Zou, Z., Numerical simulation of nonlinear wave generated in wave flume by VOF technique. Journal of Hydrodynamics, 1996. 11(1): pp. 93-103.

[5] LIU, J.H., Making waves in 2-d numerical flume and feature analysis of the numerical waves. Journal of Sichuan University, 2004. 36(6): pp. 28-31.

[6] Wei, G., J.T. Kirby, and A. Sinha, Generation of waves in Boussinesq models using a source function method. Coastal Engineering, 1999. 36(4): pp. 271-299.

[7] Chawla, A. and J.T. Kirby, A source function method for generation of waves on currents in Boussinesq models. Applied Ocean Research, 2000. 22(2): pp. 75-83.

[8] Dong, C.M. and C.J. Huang, Generation and propagation of water waves in a t wo-dimensional numerical viscous wave flume. Journal of Waterway, Port, Coastal and Ocean Engineering, 2004. 130(3): pp. 143-153.

[9] Lu, Y.j., et al., Numerical simulation of two-dimensional overtopping against seawalls armored with artificial units in regular waves. Journal of Hydrodynamics, 2007. 19(3): pp. 322-329.

[10] Dean, R.G. and R.A. Dalrymple, Water wave mechanics for engineers and scientists. 1984.

The potential of chemical-osmotic energy for renewable power generation

Adel O. Sharif*, Ali. A. Merdaw, Mohammed. I. Sanduk, Sami. M. Al-Aibi, Zena Rahal

Centre for Osmosis Research & Applications, Chemical & Process Engineering Department, University of Surrey, UK
** Corresponding author. T:+44(0)1483686584; F: +44(0)1483686584 email: a.sharif@surrey.ac.uk*

Abstract: This paper presents a study on the potential of osmotic energy for power production. The study includes both pilot plant testing and theoretical modelling including cost estimation. A projected cost of 30 $/MWh of clean electricity could be achieved by using a Hydro-Osmotic Power (HOP) plant if a suitable membrane is used and the osmotic potential difference between the two solutions is greater than 25 bar; a condition that can be achieved in a number of ways.
Results have shown that the membrane system account for 50% - 80% of the HOP plant cost depending on the osmotic pressure difference level. Thus, further development in membrane technology and identifying suitable membranes would have significant impact on the feasibility of the process and the route to market. The results have shown the strong dependency of the produceed power cost on the membrane permeability. The results have also shown that a substantial reduction in the membrane area requirment for a given power output can be acheived as the osmotic pressure differnece between the two solutions increases beyoned 50 bar.

Keywords: *Osmotic Power, Salinity Gradient, Osmotic Energy, Renewable Energy*

1. Introduction

The world's searching for cost-effective renewable energy (RE) sources is continuous and has taken many dimensions and directions. This has become more so, given the current urgency of climate change, dwindling world supplies of conventional fossil fuels, and increased oil prices. Alternative energy sources, including solar, wind, tidal wave, and biomass, have been used to provide secure, sustainable and adequate energy sources. However, expensive equipment and high installation costs of these technologies, coupled with the uneven availability distribution, have prevented them, so far, from being used widely. Affordable, clean, secure, and adequate energy sources remain one of the world's biggest challenges. Similarly, we have the great challenge of sufficient world freshwater availability.

Recent R&D activities at the Centre for Osmosis Research and Applications (CORA) at the University Surrey, and in collaboration with Modern Water plc, have investigated the potential of a relatively unexplored, renewable clean energy source with little or no environmental impacts, namely the Osmotic Energy (OE), or the power of osmosis [1,2]. Osmotic Energy is produced by the osmotic pressure difference between two miscible solutions of different potential energy due to, e.g., the concentration gradient. It is released in the process of mixing a low concentration solution and a high concentration solution, such as in the mixing of freshwater, which is relatively of low osmotic pressure, and seawater, which normally has higher osmotic pressure, through a semi-permeable membrane. The membrane retains the solute movement between the two solutions and only allows pure water. In an osmotic power plant, a large percentage of the osmotic potential difference, or the chemical energy of fresh water is converted into hydraulic pressure.

Theoretically, most of the consumed mechanical energy in the Reverse Osmosis (RO) process is stored in the concentrated solution in the forms of kinetic energy (hydraulic pressure) and osmotic or chemical energy (chemical potential). However, some of the energy dissipates in a form of heat at the high pressure pumps or in the frictional losses through and along the membrane. Up to 50% of this osmotic energy or chemical energy stored in the concentrated solution (brine), which is otherwise wasted, can be converted into mechanical energy through a Pressure Retarded Osmosis (PRO) process and recovered into hydropower [3-5]. This recovered pressure can be used to generate electricity using a hydro-turbine and generator in a similar way to conventional hydropower plants.

For example, each cubic meter of freshwater that runs into the sea with a salinity of about 35 g/*l* has, in theory, a chemical potential difference of about 0.7 kWh of energy [6]. This is because the osmotic pressure difference between seawater and freshwater is around 27 bars, which is theoretically equivalent to a 270 m waterfall. Therefore, each cubic meter of freshwater that runs into the sea could produce 0.7 kW of electricity (based on water flow through the membrane of 1 m^3/h). However, for higher salinity solutions, such as the Dead Sea or other salty lakes (e.g. salinity is higher than 20%), the chemical potential difference is higher and the produced power would be higher. The power production potential, is a function of the solutes concentration difference between two solutions, and does not require one to be freshwater, and the other to be salty water.

The generated hydraulic pressure can be utilised for the production of electricity by utilising the concept of the PRO by using a hydro-turbine and a generator in a form of land based Hydro-Osmotic Power (HOP) plant [7-9], or sub-sea or seabed-anchored plant, termed a Submarine Hydro Electric Osmotic Power Plant (SHEOPP) [10]. The generated hydraulic pressure can also be directly used through PES for pumping or other purposes [11].

The potential of osmotic energy is huge. According to Statkraft, the Norwegian power company, an osmosis-power plant could produce eco-electricity for $50-100 per MWh [12]. Its potential can be increased by combination with other renewable energy sources, such as solar, wind, tidal wave, biomass, and low-grade excess heat to further concentrate salty solutions. The global resource has been estimated at 2.6 TW [13]. The technical potential has been estimated at 2000 TWh/a [14]. Bearing in mind that these figures were derived, based purely on operation between the osmotic potentials of fresh and seawater. Additional opportunities are offered, as briefly mentioned in the introduction, by discharges from the desalination industry.

An economic assessment of a 48 MWe power plant, using the brine from an RO-concentrated seawater plant, estimated the cost of produced electricity at about 28 $/MWh [15,16]. This figure compares to about 29, 22, 12, and 5 $/MWh to produce electricity from nuclear, coal, natural gas and hydropower plants, respectively.

1.1. Open and Closed Cycle HOP Processes

There are a number of ways to recover the osmotic or the chemical energy of concentrated and salty solutions.. For the case of seawater and freshwater, e.g. up to 50% of the OE can be recovered across a semi-permeable membrane in an open cycle system. The low salinity water, Feed Water (FW), is fed at low osmotic and hydraulic pressures to one side of an Osmotic Membrane Unit (OMU), while a Draw Solution (DS), e.g. seawater or brine, is fed to the other side at higher osmotic and hydraulic pressures, where the hydraulic pressure of the DS is normally lower than the osmotic pressure. The discharged concentrated FW is circulated to the freshwater source, while the diluted DS is used to operate a turbine in order to generate power. A more efficient process can be achieved by recycling some of the pressurised solution, leaving the OMU and through a PES to assist in pumping the brine to the OMU. This process is applied when there is a continuous supply of freshwater and seawater, e.g., at a river run-off point to a sea or to a salty lake [12].

Alternatively, a closed cycle HOP plant has also been proposed [1, 10], where a DS can replace the seawater. The draw agent is retained in the system by using a Regeneration Unit (RU), which may be another separation technique, such as evaporation, crystallization, or membrane separation. In the closed cycle HOP plant, the generated hydraulic pressure can be used to produce electricity in a similar way to the open cycle system or could be transferred to other liquids through a PES for pumping processes. The efficiency of the closed HOP system depends on the availability of a low-grade energy source and/or renewable energy sources for the regeneration of the osmotic agents. Examples of renewable energy sources include, solar, geothermal, and wind for evaporation in hot and dry climates or cold temperature for crystallisation in cold climates, and/or waste heat from power and chemical plants anywhere. Recent development has been carried out to the closed-cycle process by usimg ammonia-carbon dioxide solution as DS, which is regenerated by thermal separation [17].

2. Commercial Potential and Cost Estimation

Research and development activities at CORA, and in collaboration with Modern Water plc, have shown that the potential of the hydro-osmotic power (HOP) is far greater than what had been previously assessed by other workers in this field [3,12,18]. CORA activities have involved both pilot plant testing and theoretical studies to investigate the potential of osmotic energy. For a closed-cycle HOP plant, several design and economic parameters have been assumed to carry out the calculations.

For two different, but constant, system permeabilities (A_w), 0.1 and 1 l/m^2.h.bar , Fig. 5 shows the total capital cost, the cost of the produced electricity, and the total required membrane area by using a closed cycle plant for 25 MW net electricity production. The resutls are obtianed for a rnage of osmotic pressure differences, $\Delta\Pi_f$, between the inlet concentrated, DS, and the inlet dilute, FW, to the osmotic membreane unit, OMU. The regenration unit has been assumed to be as another osmotic (FO) unit with similar membrane permeability.

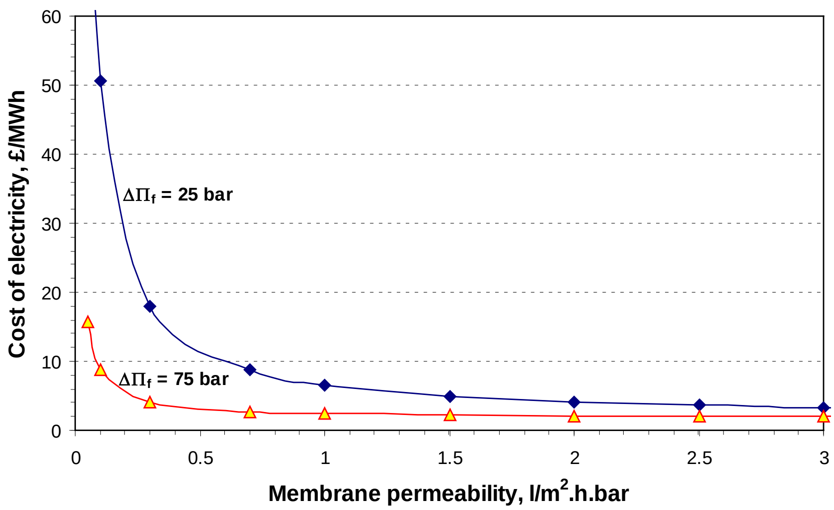

Fig. 5. The estimated cost of electricity of the proposed closed cycle HOP plant for 25 MW net power production at two osmotic pressure differnces $\Delta\Pi_f$) at the FO unit, 25 and 75 bars, by utilising 15 bars hydraulic pressure at the DS side, as a function of the membrane permeability.

It can be clearly noted the high effect of the membrane permeability on the total capital cost due to membrane contribution. The results also show that a substantial reduction in the membrane area requirment for a given power output can be acheived as the osmotic pressure differnece increases beyoned 50 bar. The cost breakdown for such a plant is calculated. More clearly, Fig. 5 shows the cost of electricity as a function of the membrane permeability for two cases of $\Delta\Pi_f$, e.g. 25 and 75 bar, respectively.

The results suggest that for osmotic pressure difference higher than 50 bar, increasing the membrane permeability beyoned 0.3 l/m^2.h.bar has little or no effect on the overall cost of the produced electricity.

3. Experimental Setup

Several pilot plant runs have been carried out with variable DS inlet hydraulic pressure at constant temperature (25^{o}C) and feed flow rates using an OMU module having high surface area (more than 100 m^2). The pilot plant setup is schematically shown in Fig. 2. A controllable needle valve was used to replace the turbine generator assembly. The DS and FW used were aqueous solutions of NaCl salt at different concentrations to simulate fresh water (280 ppm), brackish water (6,900 ppm), seawater (~35,000 ppm), and high salinity water (145,000 ppm).

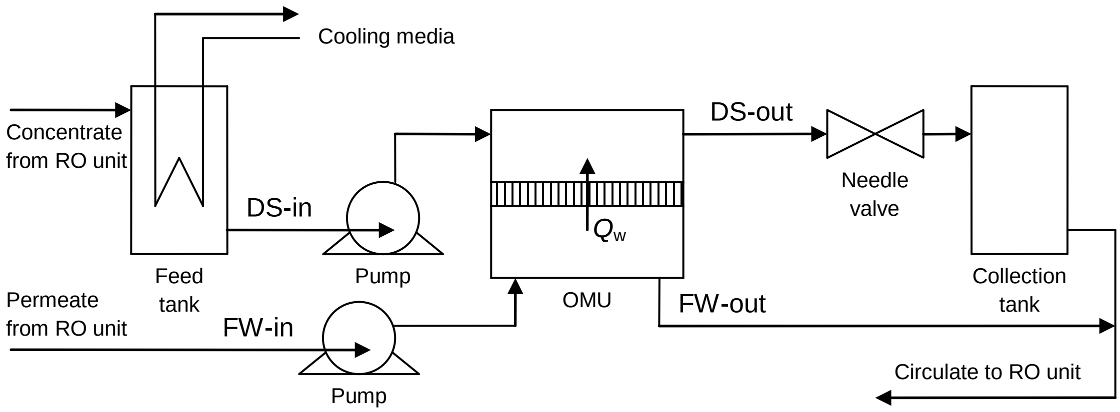

Fig. 2. Schematic diagram for the pilot plant setup.

Table 1 shows the main operational conditions of these three experiments. The discharges from the OMU were circulated to an RO unit to regenerate the concentrated DS as well as the diluted FW. A cooling for the feed tank has been used to control the increase of temperature during operation.

Table 1. The operational conditions for the pilot plant runs

Experiment no.	FW-in		DS-in		$\Delta\Pi_f$, bar
	Concentration, ppm	Flow rate*, l/min	Concentration, ppm	Flow rate, l/min	
1	240	11.1	34560	9.8	27.4
2	6900	10.9	145000	5.5	125.3
3	6900	9.5	34690	5.5	22.1

* Average value

The inlet FW is fed to the module at constant hydraulic pressure, though its flowrate was variable depending on the rate of membrane flux. The concentration measurements at the different locations of the process were obtained by using a portable conductivity meter, while flowrate and pressure measurements were taken from online digital flow meters and pressure gauges, respectively.

4. Results and Discussion

Firstly, the pure water permeability has been measured for the membrane (A_{wm}) by using pure water as feed (into the DS side) at 25^{o}C. The test has been carried out by modifying the OMU to an RO setup. The A_{wm} found to be decreasing with ΔP within the experimental range of 5 to 30 bars, according to the following relationship:

$$A_{wm} = 0.3265 - 0.0045 \ln(\Delta P) \qquad (1)$$

The system permeability (A_w) has then been experimentally determined in a PRO setup as the product from dividing the measured water flux by the net driving pressure ($\Delta\Pi$-ΔP). Each experiment has been referred to by its number as indicated in Table 1. The A_{wm} is also shown in this figure for comparison. The A_{wm} is the upper limit for the A_w; it departs from A_{wm} as the entered solutions become more concentrated or as the ΔP increases. This indicates the effect of the A_{ws}, which is estimated by using Equations (1) and plotted in Fig. 3 as a function of the DS inlet hydraulic pressure.

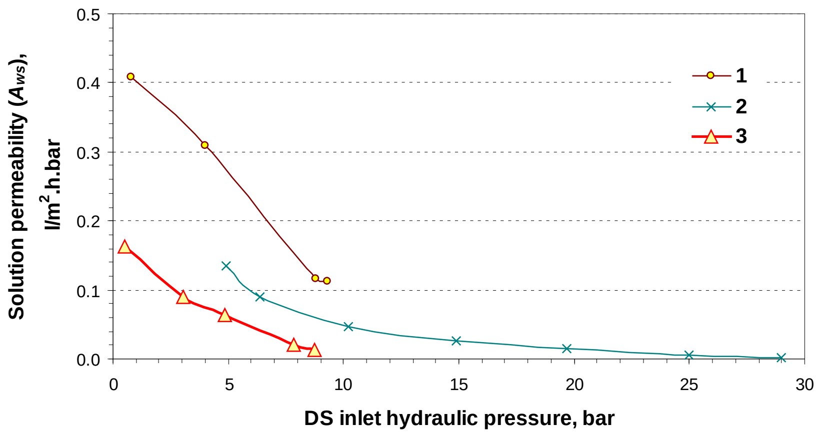

Fig. 3. The solution permeability coefficient (A_{ws}) as a function of the DS inlet hydraulic pressure.

From a comparison between the obtained values for A_{wm} and A_{ws}, the controlling phase for water transfer can be predicted. It can be noted from the case of experiment 1, where freshwater was used as FW and seawater as DS, that the membrane phase controls water transfer at low hydraulic pressures, as A_{wm} value is lower than that of A_{ws}, while at higher hydraulic pressures, the solution phase appear to be the controlling one. In the other two cases of experiments 2 and 3, where higher concentration solutions were used on both sides of the membrane, the A_{ws} was always lower than A_{wm}, which refer to the higher effect of the solution.

The following figures illustrate the calculated P_G, ρ_E, E_S, and W, (The gross power production, energy density, specific energy production and the power obtained from the PRO process respectively) as a function of the hydraulic pressure of the inlet DS. Results shown in Fig. 5 that the produced gross power, P_G, increases as the osmotic pressure (or the solute concentration) difference between the inlet FW and the inlet DS increases. Values of up to 90 watts were obtained when using freshwater as FW and seawater as DS.

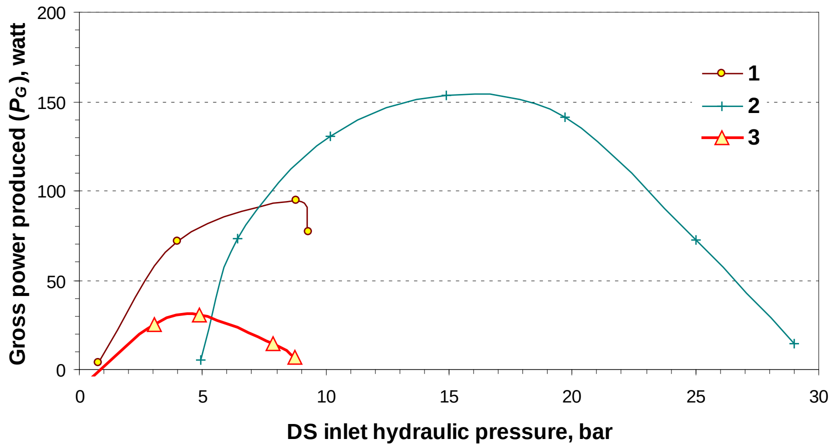

Fig. 4. Gross power produced (P_G) as a function of the DS inlet hydraulic pressure.

By using brackish water as FW with the same DS, less P_G was produced with maximum obtained values of up to 30 watts, while by utilising brackish water as FW and high salinity water as DS, the maximum P_G produced was more than 150 watts.

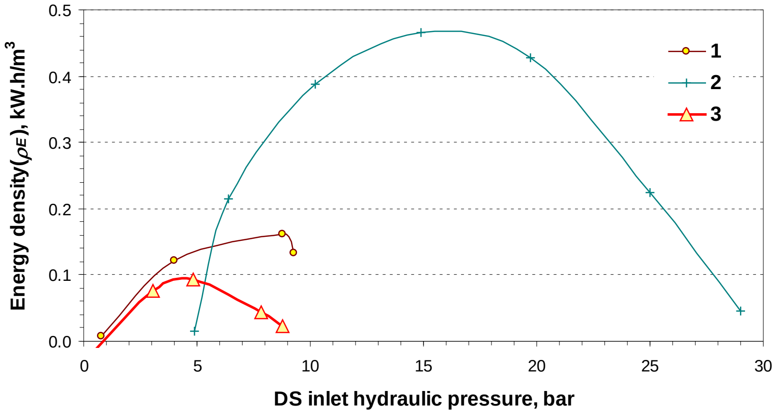

Fig.5. Energy Density (ρ_E) of the Ds as a function of its inlet hydraulic pressure for different osmotic-systems.

The effect of the hydraulic pressure at the DS side on P_G has been found to be dependant on the DS and the FW inlet concentrations, i.e. $\Delta\Pi_f$. However, different results are expected to be obtained with different membrane modules even if similar solutions and operational conditions are utilised. Practically, it has been found that the maximum value of the P_G is achieved when the hydraulic pressure drop at the DS side ($P_{DS\text{-}in}$-$P_{DS\text{-}out}$) becomes at minimum.

Fig. 5 shows the energy density (ρ_E) (in kWh/m^3 or J/m^3) of the input DS as a function of its inlet hydraulic pressure. Results show that the ρ_E, similarly to P_G, increases as the osmotic pressure difference between the FW and the DS increases. Fig. 6 shows the specific power production (E_S) of the system, based on the permeate rate, as a function of the DS feed hydraulic pressure. Results show that the E_S increases as the feed hydraulic pressure of the DS increases; however, it decreases when P_G becomes low and by increasing $\Delta\Pi_f$.

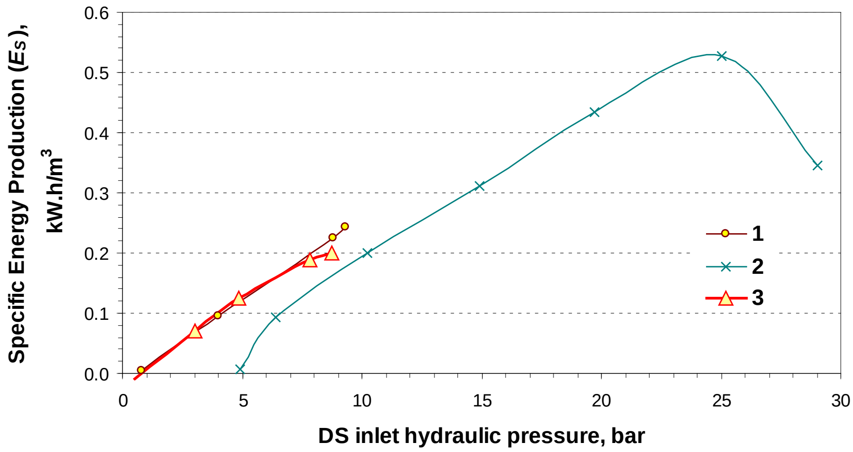

Fig. 6. Specific Energy Production (E_S) as a function of the DS inlet hydraulic pressure for different osmotic systems.

5. Conclusions

In this study both theoretical and experimental investigations of the potential of the osmotic energy (salinity gradient) for power generation have been carried out. The results indicate a high potential of the osmotic energy for power generation using the Hydro Osmotic Process. Several theoretical calculations have been presented, which show e.g. that a clean electricity could be produced using the HOP process at a projected cost of 30 \$/MWh' if a suitable membrane is used, and the osmotic potential difference between the two solutions is greater than 25 bar; a condition that can be readily achieved in many sites around the world. The results also illustrate the effect of the membrane permeability and the osmotic pressure difference across the membrane in the osmotic membrane unit (OMU) on the HOP plant cost and productivity.

This study further presents the pilot plant results under different operational conditions. The experiments show the effect of the physical properties of the FW and the DS solutions on the water permeability across the semi-permeable membrane in PRO processes. The permeability of the membrane is a critical issue when the HOP process feasibility is being evaluated. Increasing of the membrane permeability decreases the capital cost and increases the productivity. The interaction between the fluid properties and the membrane properties need to be considered when these processes are to be developed in future.

It has been experimentally found that the gross power produced is obtained when the hydraulic pressure drop at the draw solution side of the OMU becomes minimal.

Acknowledgements

The financial supports of Modern Water plc and the UK Royal Society Brain Mercer Award for Innovation to undertake this work are gratefully acknowledged. The authors would like to sincerely thank Mr Cliff Crossley of Modern Water for his useful feedback and comments.

References

[1] A. Al-Mayahi, and A.O. Sharif, Energy Generation Method (Osmotic Energy), European Patent number, EP1660772

[2] A.O. Sharif, Separation Method, UK Patent Appl. No. GB0621247.

[3] S. Loeb, Large-scale power production by pressure-retarded osmosis, using river water and seawater passing through spiral modules, Desalination 143 (2002) 115-l 22.

[4] S. Loeb, Method and apparatus for generating power utilizing pressure-retarded-osmosis, US patent, US3906250, Sep 1975.

[5] S. Loeb, Method and apparatus for generating power utilizing pressure-retarded-osmosis, US patent, US4193267, Mar 1980.

[6] K.S. Spliegler, and Y.M. E1-Sayed, The energetics of desalination processes, Desalination 134 (2001) 109-128.

[7] A. Achilli, T.Y. Cath, and A.E. Childress, Power generation with pressure retarded osmosis: An experimental and theoretical investigation, Journal of Membrane Science 343 (2009) 42–52.

[8] A.O. Sharif, Z. Rahal, and A.A. Merdaw, Power from salt water- is water going to be the World's new oil?, Arab Water World XXXIV (2) (2010) 6-9.

[9] S. Loeb, T. Honda, and M. Reali, Comparative mechanical efficiency of several plant configurations using a pressure-retarded osmosis energy converter, Journal of Membrane Science 51 (1990) 323-335.

[10] T. Harrysson, D. Lönn, and J. Svensson, http://exergy.se/goran/cng/alten/proj/97/o/

[11] A.A. Merdaw, A.O. Sharif, and G.A.W. Derwish, Water permeability in polymeric membranes, Desalination 257 (2010) 184-194.

[12] S.E. Skilhagen, J.E. Dugstad, and R.J. Aaberg, Osmotic power - power production based on the osmotic pressure difference between waters with varying salt gradients, Desalination 220 (2008) 476-482.

[13] United Nations Atlas of the Oceans (2004) http://www.oceansatlas.com/unatlas/uses/EnergyResources/Background/Salinity/sp1.html

[14] A.T. Jones, and W. Finley, Recent Developments in Salinity Gradient Power, OCEANS 2003 Proceedings 4 (2003) 2284-2287.

[15] R. J. Aaberg, Ocean energy proposal Salinity Power 2, Statkraft Energi AS, Norway, 2004.

[16] S. Loeb, Energy production at the Dead Sea by pressure-retarded osmosis: challenge or chimera?, Desalination 120 (1998) 247-262.

[17] R.L. McGinnis, J.R. McCutcheon, and M. Elimelech, A Novel Ammonia-Carbon Dioxide Osmotic Heat Engine for Power Generation, Journal of Membrane Science 305 (2007) 13-19.

[18] L. Panyor, Renewable energy from dilution of salt water with freshwater: pressure retarded osmosis, Desalination 199 (2006) 408-410.

Ocean power conversion for electricity generation and desalinated water production

Rafael Ferreira[1,*], Segen Estefen[1]

[1] *COPPE/ Federal University of Rio de Janeiro, Rio de Janeiro, Brazil*
* *Corresponding author. Tel: +55 2125627789, Fax: +55 2125627790, E-mail: rafael@lts.coppe.ufrj.br*

Abstract: Ocean power is a promising source of renewable and alternative energy used to fuel human activities. Generated energy from ocean power devices can be converted into electrical or mechanical energy, which can in turn be used as a driving force together with the desalination and water treatment by reverse osmosis processes. In this article, applications of high pressure wave energy converters (WEC) and hydrokinetic turbine for current energy conversion (TEC), described in Estefen et al [1], are presented. Due to its conceptual design, these ocean energy converters (OEC) are able to transform the hydraulic energy available from the sea into mechanical energy and then in turn into electricity generation, reverse osmosis desalination or as the driving force for hydraulic machines. A theoretical production estimation of wave and currents devices was conducted, which considered their performance from laboratorial tests associated to ocean parameters. Results are promising and indicate that it is indeed possible to supply domestic, industrial and agricultural demands of electricity and/or water, respecting the corresponding standards required.

Keywords: *Ocean power, Wave power, Current power, Desalination, Isolated communities.*

1. Introduction

In recent years, several kinds of ocean power converter prototypes have been developed, according to the expertise of each inventing team and/or specific issues from the local sea where it was planned for. This amount of prototypes indicate that the most suitable technology is not defined yet, i.e., which amongst will be applied to commercial purposes. The conversion technology from ocean power has been developed or adjusted from experience and knowledge in hydraulic and wind projects, besides from the activities performed in the offshore oil industry. According to the classification of Brooke [2] and Pontes & Falcão [3], Wave Energy Converters (WEC) can be sorted by the location in shoreline, near shore and offshore devices or by technology in Oscillating water column systems, Overtopping Systems, Point absorbers systems, Surging devices and other devices.

Tidal energy converters (TEC) can be classified into three main groups: horizontal axis turbines (axial flow), vertical axis turbines (cross flow) and oscillating hydrofoil. The former is based on hydrofoils impulsion from lift force caused by tidal current flow. In the sequence, hydraulic cylinders are driven, which in turn causes the electricity generation. Furthermore, the classification proposed by Bryden and Couch [4] includes Venturi systems, based on turbines endowed with a diffuser to increase the pressure difference.

The concept of high pressure wave power converter, described in Estefen et al [1], is based on the use of an hyperbaric chamber, which stores wave power converted from highly pressurized water. The first version, denominated onshore, works as a bi-supported beam with one beam fixed deep down into the soil and the other on a buoy, which follows the waves´ movement. Once a wave passes by the buoy, it causes beam displacement, which is joined with a hydraulic pump and then pressurizes the water. This pressurized water is stored in a high pressure system, consisting of a hydro-pneumatic accumulator and hyperbaric chamber.

The chamber works as a hydraulic accumulator. When the pressure inside the accumulator reaches its operational level, the water is delivered, through a valve to a hydraulic turbine, which is linked to an electrical generator in order to produce electricity.

Figure 1: Wave power plant using high pressure system as described in Estefen et al [1]
In detail the high pressure system including hyperbaric chamber and accumulator

Power harnessed by ocean devices can be converted into electrical or mechanic energy, and applied as a driving force for engines or even, in the desalination and water treatment from the reverse osmosis process. The produced drinking water can supply households, industries and agricultural irrigation. For domestic use, salt concentration around 300 mg/L is required, including other quality parameters which can be achieved through the reverse osmosis conventional process, pre and post-treatment. Power consumed to pressurize water could be totally supplied by the ocean energy converter system. In industrial processes, e.g. thermo electrical plants, salinity standards similar to humans, around 300 mg/L is required in order to avoid the corrosion of equipment. Finally, in agricultural use, it is possible that large amounts of desalinated water can be produced, allowing irrigation of between 1 to 3 hectares per unit, at severe conditions of hydric demand typical in semi-arid regions.

Power supply is considered to be one of the main issues for economic and social development, since it is applied during the whole process of production and services, providing the basics necessities of modern life. For example, according to Pereira et al [5], Brazilian households without access to electricity stands at 2.8%, the majority of which are from isolated communities and rural areas, limiting electrical supply under conventional means. Such restrictions lead to a large expense of these families incoming in fossil fuels or to employment of old and inefficient techniques to generate power [5]. On the other hand, the same regions which lack electricity beholds a significant amount of alternative and renewable energy sources, for example, solar, wind, hydraulic, tidal and biomass energy. In regard to tidal current power, there are feasible possibilities of supply for isolated communities spread throughout Brazilian and South American territories.

2. Methodology

In order to estimate the amount of power extracted by an Ocean Power Converter (OEC), uneven wave or tide conditions must be considered, but also the device characteristics, the power take-off system, and the control strategy to name a few [6]. The power comprised in the wave incident to a device, according to EPRI [7], is based on two parameters: the significant wave height and its peak period, see Eq. (1).

$$E_u = 0.42 \times (H_S)^2 \times T_P \qquad (1)$$

where E_u is the power of each meter of wavefront in kW/m
H_S is the significant wave height in meters
T_P is the peak period in seconds, being the inverse of frequency where spectra reached its maximum value
The coefficient 0.42 varies according to the wave spectra considered for a specific sea state.

The Eq. (1) can be employed to estimate the amount of power incident from a wave with H_S and T_P known. On the other hand, each device will be able to convert a fraction of wave incident power. In order to estimate the production of each device, a table must be created in which the cell represents the amount of power converted by the device for specific conditions of wave height and peak period. Generally, these results have been obtained through laboratorial or field tests, therefore it reflects only their performance on a small scale.

The wave parameters used as a reference for the calculations below have a significant wave height of 1.6 m and peak period of 6 seconds. The performance of the wave energy converter was obtained in tests with a reduced model, and these conditions reached a level of 18 kW of converted hydropower. The average energy absorbed in each conversion cycle, equivalent to the work done by the piston pump with each passing wave period, is calculated in Eq. (2).

$$\Delta W = \int_0^T P(t)dt = \int_0^T F_P(t)y(t)dt \qquad (2)$$

where F_P is the periodic force exerted on the piston;
y is the piston displacement, consisting of a term of steady state and another transient.

Similarly, the generation of electricity through the power of tidal currents, the potential energy is calculated from Eq. (3).

$$\Delta W = \int_0^T \frac{1}{2} C_P \rho A_{turb} v^3(t)dt \qquad (3)$$

Where C_P is the power coefficient;
A_{turb} is the transversal area of the turbine;
v is the speed sinusoidal of the current.

An energy converter of currents around 7 meters in diameter working in a tidal current speed with a sine wave amplitude of 1.8 m / s and power co-efficiency of 35%, will absorb an amount close to the energy converted by the WEC in the wave conditions presented, equivalent to an average of 18 kW. This amount of energy is absorbed primarily by the drive which is available in the oceans. From this point on, this energy is stored in the form of pressure and can be directed to the generation of electricity in a Pelton turbine or a module of reverse osmosis to produce desalinated water.

The desalination and water treatment for drinking can be accomplished through the process of reverse osmosis coupled with the energy converters of the sea. Reverse osmosis is a water treatment process that uses synthetic semi-permeable membranes to intercept components of water, especially salt particles. Unlike the phenomenological natural osmosis, in reverse osmosis the goal is to produce water with low salt concentration obtained from the introduction of energy in the system. This energy is transformed into a driving force for pumping the water of higher salt concentration through a semi-permeable membrane, thus producing potable water.

In this sense, the pressure reached by the system must be sufficiently greater than the osmotic pressure between the two different salt concentrations before and after the membrane, not only to reach the balance in osmotic pressure, but also to produce a reasonable flow of water permeated, reversing the flow. In the case of converting energy from the high sea pressure [1] these pressure levels are easily achieved through the sizing of pumps attached to the primary conversion module, which provides power to the system.

The salty sea water with salinity levels of 33‰ and temperature of 24ºC has an osmotic pressure equivalent to 27.5 bar. According to marketing literature, working pressure levels of about 55 bar are required to obtain significant flow of desalinated water in the reverse osmosis process. The flow of desalinated sea water, depending on the energy converted from the sea and made to the system can be estimated by integrating the van't Hoff formula for the osmotic pressure, described in Eq. (4). This energy converted by the converter device serves as a driving force, allowing the seawater admission and pumping it to a reverse osmosis module.

$$\Delta W = -\int_{V_1}^{V_2} \pi dV = N \cdot R \cdot T \cdot \ln(V_1 / V_2) \qquad (4)$$

where ΔW is the required energy per pump cycle
N is the number of moles of salt in seawater
R is the universal gas constant
T is the temperature in Kelvin
V_1 e V_2 are the initial and final volumes of the pump piston, their difference represents the volume of water actually pumped.

The energy required to pump a volume through a semi-permeable membrane can be calculated by Eq. (5). The liquid pressure achieved by the system must be greater than the osmotic pressure between the concentrations before and after the membrane, coupled with a pressure associated with the flow of permeated water.

$$W = \int_{V_1}^{V_2} (P_S + \Delta P) dV = \left[\frac{P_{sea} \cdot (1-\alpha/2)}{(1-\alpha)} + \Delta P \right] \cdot \Delta V \qquad (5)$$

where α is the recovery rate of the desalination system.

For the recovery rate of 45%, the energy required to desalinate a liter of water would be 6.5 kJ/L. Taking the energy available in the system to the conditions of wave and current previously calculated as 18 kJ per second and the complete cycle of pumping of 6 seconds, can be obtained from the flow pumped by each cycle in Eq (6).

$$\Delta Q = \Delta V \cdot (1/cycle) = 235 m^3 / day \qquad (6)$$

The reverse osmosis modules available on the market specifically for the desalination of sea water have recovery rates of 40 to 50%. The number of modules to be used for each energy converter device of the sea was estimated from information of a type widely sold for this purpose. Table 1 shows the main parameters of this model.

Table 1. Parameters of the module of reverse osmosis desalination for seawater

Membrane area	35 m²
Unit permeated flow	14 L/hour/m²
Number of elements per pressure vessel	Up to 7
Recovery rate	45%

The production of each element will be 490 L/h and the number of elements required will be obtained by the ratio between the flow obtained by Eq. (4) and this unit flow, resulting in 20 elements. Pressure vessels can include up to seven elements of desalination in the series, which represents the need to install at least three pressure vessels coupled with each module of ocean power converter device. Whereas the recovery rate to feed flow rate will be 521 m³/day of seawater from the sea.

On the other hand, in the reverse osmosis process, as well as in other processes of desalination, wastewater is produced with higher concentrations of salt than the average salinity of the sea. The final disposal of these effluents should be studied carefully to avoid causing damage to the immediate environment, especially marine biota. Studies using models of hydrodynamic circulation and transport of water constituents are desirable for evaluation of local impact. In any case, the use of sea energy for desalination by reverse osmosis is configured as a viable cost effective alternative, especially for locations where there is a scarcity of drinking water, such as on islands and coastal areas which are far from large sources of freshwater.

3. Results

3.1. General applications for the OEC devices

Possible applications for tidal and waves energy are similar to any other energy source, which can be to provide for the electrical system, the seasonality of supply and daily peak time consumption. It can also serve as a complement to thermal energy to replace pollutants in places where few options for energy supply exist. Remote markets and isolated spots, such as villages on islands, coastal and riverside population, units of offshore oil, scientific research and the military, marine farms and fisheries.

3.2. Applications for electricity

In the case of electricity production, each high-pressure ocean power convertor, e.g. described at [1], is able to supply the demand of an average 36 households, considering the wave or current conditions described above with an average residential consumption of 12 kWh/day. Electricity produced from the sea energy converters can be used in a variety of projects, either as a principal supply, or as a supplement to other sources. The first application is domestic supply, especially in residences near marine resources located on the coast where waves or tidal estuaries are present. In South America, there is sparse population along the coast and inland waters, poor supply of electricity can benefit from these types of project. Other applications include the use of electricity in scientific and military bases located on islands and remote locations, hotels and resorts in exploiting the tourist appeal of the device itself and also drive the production of clean and renewable energy.

3.3. Applications for desalinated water

The applications of water treated by reverse osmosis from sea power converters include residential, industrial and agricultural processes through irrigation. The production capacity of treated water per converter module of wave energy or currents has a power equivalent to 18 kW and an average of 235 cubic meters per day, as shown in Eq. (6), which allows for the supply of approximately 940 people.

As an example of industrial use, the water process in power plants must meet very stringent standards for salinity in order to prevent corrosion of equipment. The salinities suitable for this purpose is 300 mg/L, similar to that required for human consumption. The unit consumption of treated water per megawatt hour produced in power plants varies from 180 to 720 U.S. gallons or 0.68 to 2.72 m³, depending on the fuel coal, gas or nuclear power and technology of the cooling tower [7] as shown in Fig. 2.

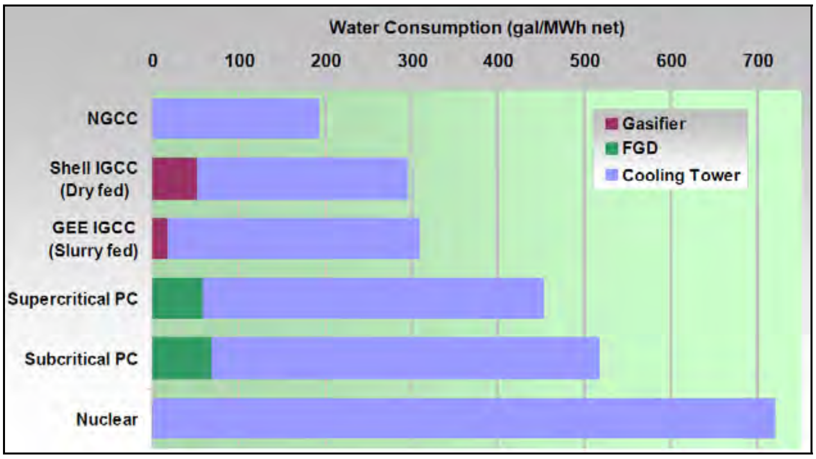

Fig. 2. Water consumption in the processes of coal-fired, gas and nuclear applications. Source: Gerdes and Nichols [7]

Considering the average production of treated water for ocean energy converters of 235 cubic meters per day, you can meet the thermoelectric consumption for the values shown in Table 2.

Table 2. Production of OEC to supply the thermoelectric water consumption

	Combined cycle (dry Tower)	Simple steam cycle (dry tower)
Water consumption	0,11 L/s	0,27 L/s
Power attained for No. of OEC modules	24 MW/Module	10 MW/module

Another application of desalinated water from OEC's is for the service of irrigated crops. Agricultural irrigation is water consumptive, due to the fact high water demand from the crops throughout the growth phase and the planting and irrigation techniques have low levels of efficiency in water management. The quality of irrigation water is usually based on the total content of dissolved salts, measured by the electrical conductivity and sodium adsorption ratio (SAR), assessing the risk of sodicity in soil [8]. The required concentration of dissolved salts in irrigation water is limited to the potential impact on soil structure, corresponding in terms of electrical conductivity to between 250-750 micromhos/cm and, in some cases, 2,250 micromhos/cm. In terms of salt concentration, the values are between 160 and 480 mg/L.

To illustrate this application, the water requirements for cultivation of cane sugar in a Brazilian region characterized by lack of rainfall during summer in the Southern Hemisphere will be described below, along with the possibilities that this demand can be met by OEC modules. The observed rainfall in the Alagoas region during 2008 is presented in Table 3.

Table 3: Average monthly rainfall (mm) in the region of Alagoas (Brazil)

JAN	*FEB*	*MAR*	*APR*	*MAY*	*JUN*	*JUL*	*AUG*	*SEP*	*OCT*	*NOV*	*DEC*
41	206	214	257	256	261	276	238	76	48	12	41

The months of November, December and January show a significant drop of rainfall, resulting in severe consequences for water users in this region. In Fig. 3 (a), the curve shows the agrometeorological cane ratoon, the evolution of the crop water demand throughout its growth in the months of the planting period, August through to July, the harvest season.

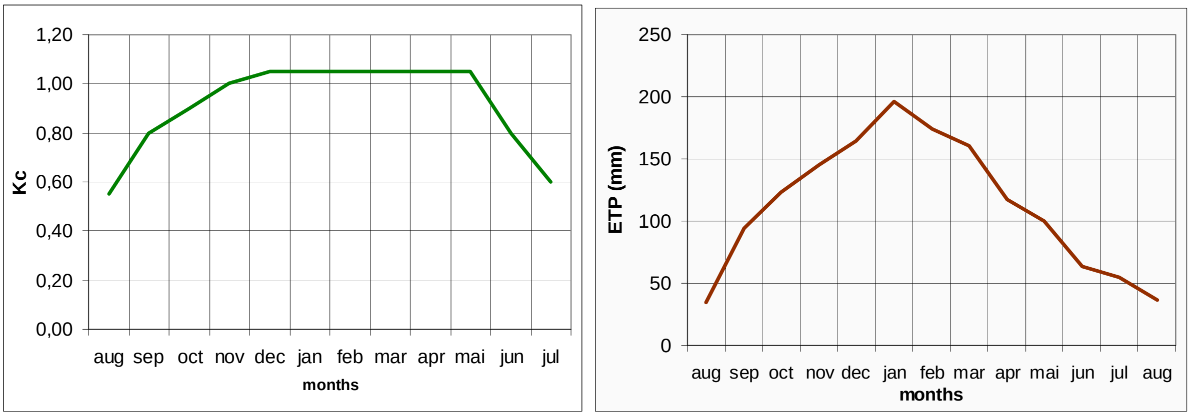

Fig. 3. (a) Agrometeorological curve (Kc) and (b) Evapotranspiration of the sugarcane ratoon (mm)

Thus, the water demand in each month of sugarcane ratoon crop irrigation can be calculated by the difference between the amount of water precipitated and crop evapotranspiration. The amount of irrigation water demand is presented in Table 4.

Table 4: Monthly water demand for irrigation of sugarcane ratoon (in mm)

Month	*AUG*	*SEP*	*OCT*	*NOV*	*DES*	*JAN*	*FEB*	*MAR*	*APR*	*MAY*	*JUN*	*JUL*
Lamina (mm)	85,1	-18,25	-74,8	-133,2	-123	-155,1	32,1	53,6	139,8	156,2	197,2	221,9
Daily irrigation flow (m^3/day/ha)	0	6,1	24,9	44,4	41,0	51,7	0	0	0	0	0	0

As shown in Table 4, negative values mean that there was a demand for irrigation in the corresponding months. The daily flow irrigation during the critical months was calculated taking into account the water depth required. Based on a water salinity content of 300 mg/L and the flow of irrigation in the most critical month of January, it shows that the production of water from ocean energy converter of 18 kW is capable of supplying irrigation in 4.5 hectares of cultivation.

4. Conclusions

An estimation of wave and tidal current power converter production was conducted, which focused on a high pressure system concept [1] developed by Submarine Technology Laboratory at UFRJ (Brazil). The WEC is an oscillating body type, which pumps water to the hyperbaric chamber and uses conventional Pelton turbine coupled with an electrical generator. Also, the hydrokinetic turbine is connected to a hydraulic pump and from this stage it is similar to the architecture described above. Due to its conceptual design, these ocean energy converters (OEC) are able to transform the hydraulic energy available at sea into mechanical energy and then into electricity generation, reverse osmosis desalination or as a driving force for hydraulic machines. As a reference, the energy amount converted by this WEC in a typical wave condition was used for the following calculations, and it was compared to the similar amount generated by the TEC. The estimate indicated that for a significant wave height of 1.6 meters, the WEC can generate 18 kW or 235 m^3/day of desalinated water and the same production can be obtained by the hydrokinetic turbine at a current speed of 1.8 m/s.

Electricity, fresh water and driving force resulting from OEC can be employed in domestic, industrial and irrigation uses, especially in regions which lack these natural resources, *e.g*. islands, coastal and riverside isolated communities. Additionally, industries and agricultural irrigation settled near to the coast can be potential users of treated water and electricity generated by the mentioned OEC. The water supply for each case is simulated herein. For domestic use, each module of WEC or hydrokinetic turbine can supply 940 people. The industrial application was illustrated by the water demand of a thermoelectric plant, providing values of each 10 MW in the Combined Cycle can be supplied by one OEC module, and in the Simple, each 5 MW. The irrigation use was demonstrated through the water consumption of sugarcane cultivation during a critical month associated with low precipitation. In this case, up to 5 hectares of cultivation can be irrigated by the production of one module. Harnessing ocean power is a way to provide decentralized electricity generation which could supply remote sites, promoting the diversification of energy matrix and becoming an economical development vector, especially in coastal communities of developing countries.

Acknowledgements
The authors would like to thank CNPq (*Conselho Nacional de Desenvolvimento Científico e Tecnológico*), Brazilian research agency, for supporting the conference attendance.

References

[1] S. F. Estefen, P. R. Costa, E. Ricarte, and M. M. Pinheiro, Wave energy hyperbaric device for electricity production, in OMAE-2007, San Diego (CA), United States, June 2007.

[2] J. Brooke, Wave Energy Conversion. Elsevier Ocean Engineering, New York, US, 2003.

[3] M. T. Pontes, A. Falcão, Ocean Energies: Resources and Utilization, 18th Congress World Energy Congress, Buenos Aires, Argentina, 2001.

[4] I. G. Bryden, S. J. Couch, ME1—marine energy extraction: tidal resource analysis, Renewable Energy, Volume 31, 2006, pp. 133-139.

[5] A. O. Pereira Jr., J. Soares, R. G. Oliveira, R. P. Queiroz, Energy in Brazil: Toward sustainable development?, Energy Policy, Volume 36, Issue 1, January 2008, pp. 73-83.

[6] G. Hagerman, R. Bedard, Guidelines for preliminary estimation of power production by offshore wave energy conversion devices, Rep. E21 EPRI-WP-US-001, Dec. 2003, pp. 3-10.

[7] K. Gerdes, C. Nichols, Water requirements for existing and emerging thermoelectric plants technologies, Report from DOE/NETL, United States, August 2008, pp. 5-9.

[8] L. A. Richards, (Editor), Agriculture Handbook 60, US Department of Agriculture, United States, 1954, pp.69-82.

Physical Investigation into an array of onshore OWCPs designed for water delivery

Davide Magagna[1,*], Dimitris Stagonas[1], Gerald Muller[1]

[1] Sustainable Energy Research Group, University of Southampton, Southampton, United Kingdom
* Corresponding author. Tel: +44(0) 238059465, Fax: +44 (0)23 8067 7519, E-mail:d.magagna@soton.ac.uk

Abstract: An OWC Wave Pump (OWCP) for seawater desalination is under development at University of Southampton. The paper presents experimental results for work carried out on an array of OCWPs at a scale of 1:40. The interaction between singles components of the array is determined in order to assess the layout which gives the maximum power output from an array of 3 OWCPs. The results provide a benchmark for comparison against the data available in literature obtained from BEM simulation. Results show that amplification of the wave signal up to 4.8 times can be achieved within the array. Increasing the distance between devices by two times the width of the chamber resulted in a reduction of the magnification factor up to 30%.

Keywords: *Arrays, Oscillating Water Column, Separation Distance, Capture width*

Nomenclature

MWL .... *Mean Water Level*
N .... *Number of devices in array*
OWC.………………..*Oscillating Water Column*
OWCP. *Oscillating Water Column Wave Pump*
WEC…………………. *Wave Energy Converter*
q …………………………………*Array Factor*
A *Section of duct* .... m^2
d_s *Separating distance* ... ……………………...m
g *Gravitational constat*..........................$m{\cdot}s^{-2}$
H *Wave height* .... m
h *Water depth*.. m
l *Output duct length* .... m
l_1 *Input duct length*..................................... m
P_a *Power output of Array*…………………..kW
P_s *Power output of a Single device*.............kW
P_{out} *Power output*..kW
Q *Flow rate*... $m^3{\cdot}s$
s_d *Submersion depth*....................................m
T_N *Natural period of Oscillation*.................... s
T_W *Incoming wave period*............................s T
z_r *Removal height*...m
α *Angle of inclination of output duct*........ rad
ρ *density* .... $kg{\cdot}m^{-3}$
ω_D *Wave Frequency*..............................$rad{\cdot}s^{-1}$
ω_N *Natural Frequency Oscillation*.........$rad{\cdot}s^{-1}$

1. Introduction

Recent progresses made on the development of Wave Energy Converters (WECs) have encouraged researchers to evaluate the deployment of arrays of WECs in order to maximize the power-output. Whereas it would seem straightforward that the output obtained from an array of WECs is higher than the power generated by multiple items working separately, the interferences between devices and waves could have a negative effect reducing the overall power output. The effects generated by the geometrical disposition of the device are measured by the q factor, as presented by Babarit in [1]. q represents the ratio between the power output P_a generated by N devices deployed in array configuration, against the power of N devices working autonomously P_s, e.g without interaction.

$$q = \frac{P_a}{N \times P_s} \tag{1}$$

When q≥1 positive effects are obtained by the array disposition of multiple WECs. One of the determining factors in the evaluation of q is the separation distance, d_s, which indicates the space between two devices in the array. The practical role of d_s is to influence the interaction between the radiated waves generated by the oscillation of each single device.

The determination of q, thus far, has been predominantly conducted using numerical phase resolving Models. Mathematical models are used to simulate the wave-device dynamics and to assess the performances of the array. They allow for a faster evaluation of the problem, but present limitations due to the formulation of the problem. Linearization of the equations involved, and assessment of infinitely long arrays being the main case. Alexandre et al [2] investigated the changes in the performances of point absorbers WEC disposed in array by assessing changes in the wave field due to the radiation of each components. Falcao presented the case of power extraction by a periodic linear array OWC (Oscillating Water Column) [3]. Other examples of mathematical model for the evaluation of WECs working in array can be found in [4-6] . The use of physical tests to evaluate the performances of arrays is, however, limited mostly due scaling problems and to the availability of appropriate facilities.

Current research at University of Southampton is focusing on the development of an Oscillating Water Column Wave Pump (OWCP) for water delivery. The device is designed to operate in arrays in order to maximize water delivery and increase the frequency response spectrum. This paper presents the results obtained from physical model tests carried on array of 3 OWCPs.

2. The OWCP and Array Configuration

The OWCP is a resonant type WEC, based on the more common Oscillating Water Column (OWC). The OWCP is designed to exploits the resonant conditions obtained during the oscillatory motion of the water contained in the chamber to deliver water to a fixed height. The OWCP can be considered as an overtopping type of WEC; however it differs from the standard overtopping devices such as the Wave Dragon [7] or the Composite Sea Wall [8], since they exploit the run-up of the water over an inclined ramp to deliver water to a reservoir.

The device is composed of two-part duct; with a horizontal underwater section (input duct), and an inclined pumping section extending above Mean Water Level (MWL) (Figure 1). The OWCP acts as a resonator with natural period of oscillation equal to T_N. To maximize performances the device has to be tuned with the incoming wave period T_W. It is possible to implement resonance control by varying the angle α of inclination of the output duct, e.g. changing the mass of water contained within the OWCP.

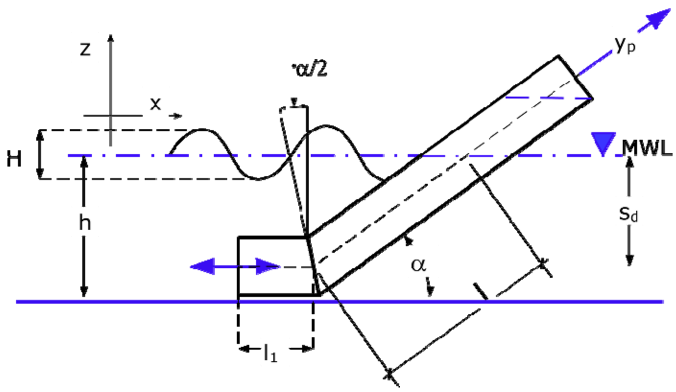

Figure 1. Schematic definition of the OWCP WEC. Where l is the length of the output duct, l_1 is the input duct, y_p the delivery height of water, h water depth, H is the wave height, s_d the submersion depth and α is the angle of inclination.

In order to maximize the delivery of water, the deployment of arrays of multiple OWCPs has been considered. Arrays of 3 OWCPs are considered in this paper. In particular, a close investigation focuses on the deployment of 3 differently tuned OWCPs devices in order to maximize performances and broaden the array response under different wave conditions. The concept of using differently tuned devices is justified by the need to provide a simple resonance control system for the array, and to phase out the destructive radiation waves generated by the downward motion of the column of water exiting the device. Initial results on the response of an array of multiple OWCPs have shown that the deployment of multiple devices broadens the frequency response of the array [9]. The role of the separation distance over the performance is therefore assessed.

3. Methodology

Experimental tests were carried in order to assess the performance of the different configuration of the arrays. The tests were carried in a 4m long, 1.7 m wide and 0.4m deep wave basin. Froude scale was employed with a scale factor Λ=40. Linear waves were generated by a piston type wave maker, with the wave heights ranging between H = 1 - 4.5 cm and period T_W between 0.8 and 2 s. The water depth in the basin was kept at 14 cm, with submersion depth s_d of 7 cm. 7 models of the OWCP were built out of transparent acrylic (3 mm thick). Their characteristics are presented in Table 1.

Table 1. Specifications of the models of the OWCP built for 1:40 scale tests.

Model	Inlet shape	Dimension (mm)	α	l_I (mm)	T_N (s_d=7cm)
OWCPS1	Square	24×20	30º	40	0.851 s
OWCPS2	Square	24×20	30º	40	0.851 s
OWCPS3	Square	24×20	30º	40	0.851 s
OWCP20	Circle	24 ∅	20º	55	1.022 s
OWCP25	Circle	24 ∅	25º	50	0.935 s
OWCP30	Circle	24 ∅	30º	40	0.851 s
OWCP35	Circle	24 ∅	35º	35	0.795 s

The configurations of the array tested are presented in Table 2, along with the separation distances between the devices.

*Table 2. Configurations of the type of arrays tested. The * indicates the device located in the centre of the array. The Square array employs 3 similarly tuned devices.*

Array name	Models used	Separation distances (mm)
Square	OWCPS1- OWCPS2*- OWCPS3	0 – 15– 30 mm
20-25-30	OWCP20- OWCP25*- OWCP30	0 – 30 – 60 mm
20-25-30W	OWCP20- OWCP25*- OWCP30	0 – 30 – 60 mm with reflective wall
25-30-35	OWCP25- OWCP30*- OWCP35	0 – 15 – 30 mm

The arrays are located in the centre of the wave basin, with an absorbing beach installed on the back to reduce the reflection of waves from the walls (Figure 2). Resistance type wave gauges are employed to monitor the wave conditions. Wave Gauges are also installed within each device in the array to determine the lift of water (Figure 3).
The performances of the array and of each device are assessed with the magnification factor, M, given by equation (2).

$$M = \frac{y_p}{H} \tag{2}$$

Where y_p represents the lift of water within each OWCP. By using M to assess the performances of the arrays, the case of no Power Take Off (PTO) installed is evaluated. The power output, P_{out}, of each device can be estimated in relation with to M or y_p, once the delivery height z_r is defined, as shown in equation(3). This relates to the crest Power determined by Margheritini et al. [10] for the assessment of the efficiency of the SSG wave energy device.

$$P_{out} = Q z_r \rho g \tag{3}$$

Where Q represents the flow rate of the delivered water, ρ the water density and g the gravitational constant. For each incoming wave Q can be determined by

$$Q = \left(y_p \sin \alpha - z_r\right) \times \frac{A}{T_W} \tag{4}$$

Where A represents the cross-sectional area of the OWCP duct. For the study presented in this paper the value of Q can be estimated over a wave cycle. For irregular waves, the average Q has to be determined. It has to be noted that both Q and A are both frequency dependent, therefore maximum values of P_{out} can only be achieved close to resonance conditions.

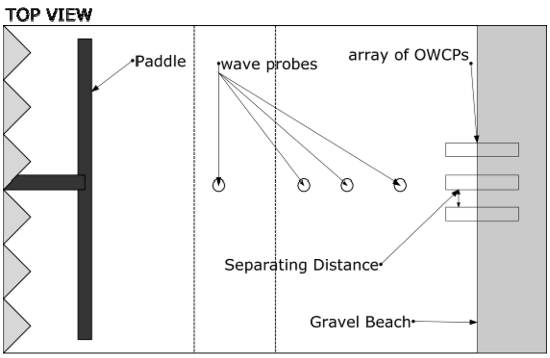

Figure 2. Experimental Setup

Figure 3. Array of 3 OWCP devices

4. Results

The response of each component of the arrays is assessed, and the values of M for different wave conditions is then determined. These are compared in order to determine the effects of the separation distance on the single and overall performance. Figure 4 presents the changes in M with d_s, for the 25-30-35, Square and 20-25-30 arrays configuration. It can be noticed that positive effects towards the delivery in the central pipe are achieved in each array configuration. It can be seen that for the cases when the devices are differently tuned higher values of M are achieved. With increasing separating distances, the values of M drop. On average a reduction in M of 14% is seen by increasing the d_s from 0 to 15 mm, with a further reduction of 12% moving from 15 to 30 mm d_s. Only the OWCP25 (Figure 4.a.) and OWCP20 (Figure 4.b) devices are subject to an increase in M with d_s. In Figure 5 the changes of M for different d_s are assessed along with the changes in the non-dimensional frequency

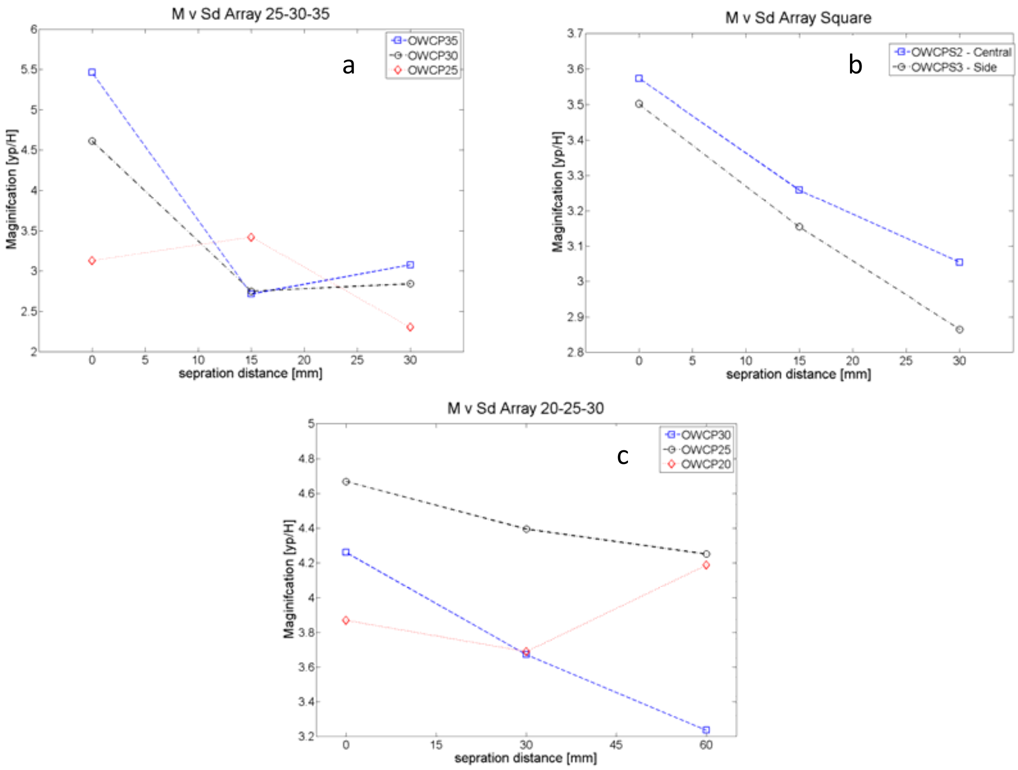

Figure 4.a) Changes in M with d_s for the 25-30-35 Array configuration. b) Changes in M with d_s for the Square Array configuration. c). Changes in M with d_s for the 20-25-30 Array configuration.

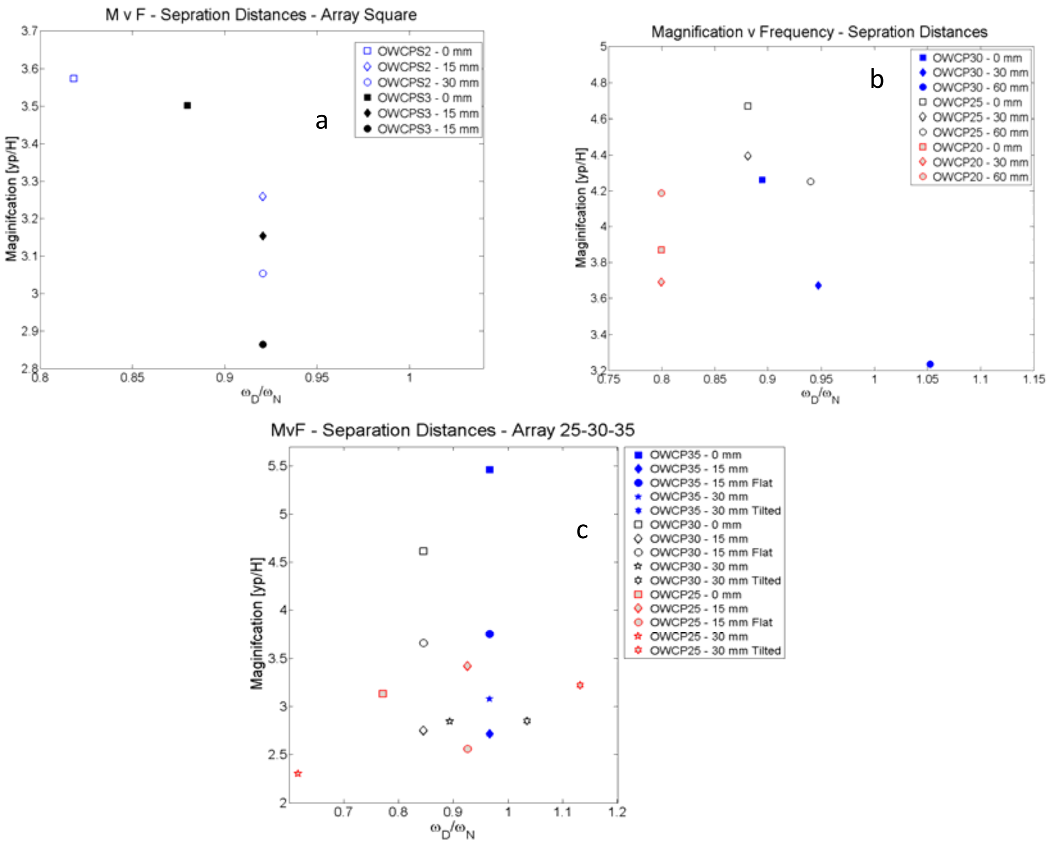

Figure 5. Maximum M against the non dimensional frequency ω_D/ω_N, for different d_s. a) Square Array. b) 20-25-30 Array. c) 25-30-35 Array. The Flat configuration considers the mouth of the device being leveled, whilst Tilted indicates the central pipe being pushed forward compared to side devices.

ω_D/ω_N . The non-dimensional frequency represents the ratio between the angular wave frequency ω_D and the natural frequency of oscillation of the device ω_N. When the ratio is close to 1, each device is operating as a stand-alone and no interferences are affecting the performances of the device. It can be seen that, with the increase in d_s, all devices tend to operate as stand alone, with maximum *M* achieved when ω_D/ω_N=1.

Maximum delivery however are achieved for d_s = 0 mm with $\omega_D/\omega_N \cong 0.8$. It is believed that strong arrays interference affects the damping of the devices, causing as a result a stronger response, hence higher *M* are obtained. Even for the cases presented in Figure 5.b and Figure 5.c different behaviors are observed in the OWCP20 and OWCP25 device. In the first case changes in *M* and d_s do not reflect changes in ω_D/ω_N, whilst for the OWCP25 a wider spectrum of frequencies is obtained.

Figure 6 and Figure 7 present the responses, expressed in terms of *M*, of the central and side device for the Square Array and for the 20-25-30 Array respectively. In both cases it can be seen how higher *M,* 3.57 and 4.67 respectively, are achieved in the central OWCP. Figure 6 and Figure 7 show the effect of ω_D/ω_N and of the wave steepness on *M*, it can be noticed that the area of response of the devices broadens with minimum separating distance. In Figure 6, where results for a Square Array are presented, one can notice that both devices present a similar response, however the central device presents a broader amplification area compared to the OWCPS3 located on the side. In Figure 7, it is possible to notice how the bandwidth response reduces for both the OWCP30 and OCWP25 with increasing d_s. Furthermore, a steady decrease of *M* can be noticed in both devices, indicating negative interaction between devices.

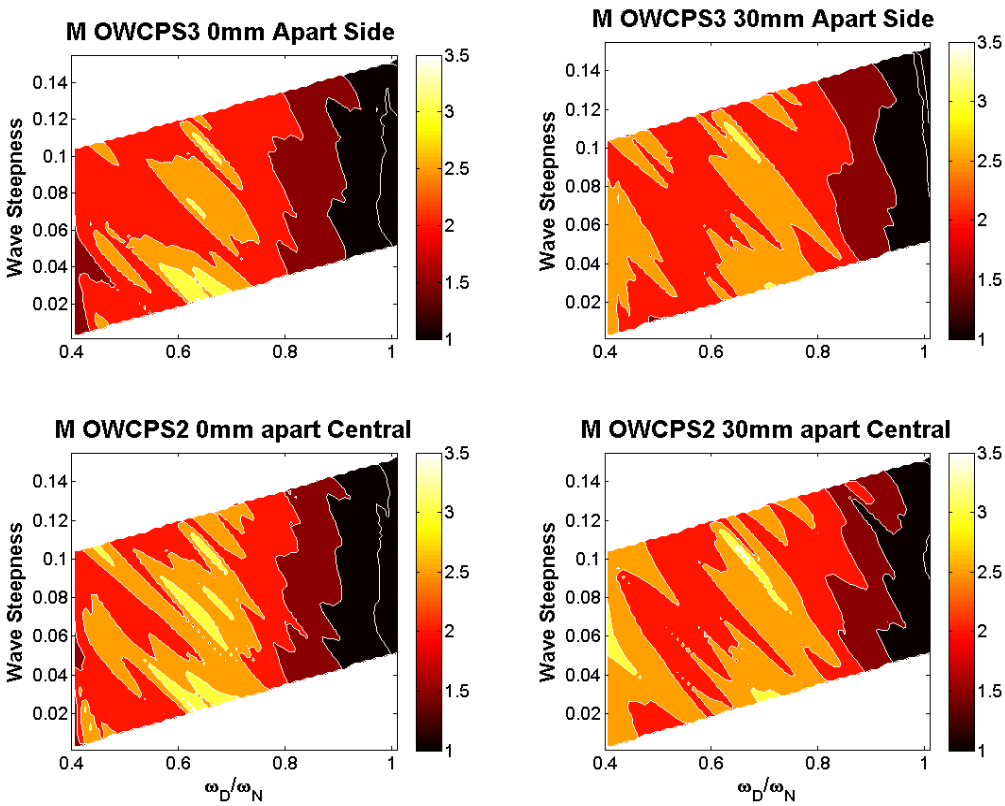

Figure 6. Magnification Factor for the components of the Square Array. Focus in given at the behavior of the side pipe (OWCPS3, top) and at the central pipe (OWCPS2, bottom) for values of s_d=0 and 30 mm (left and right).

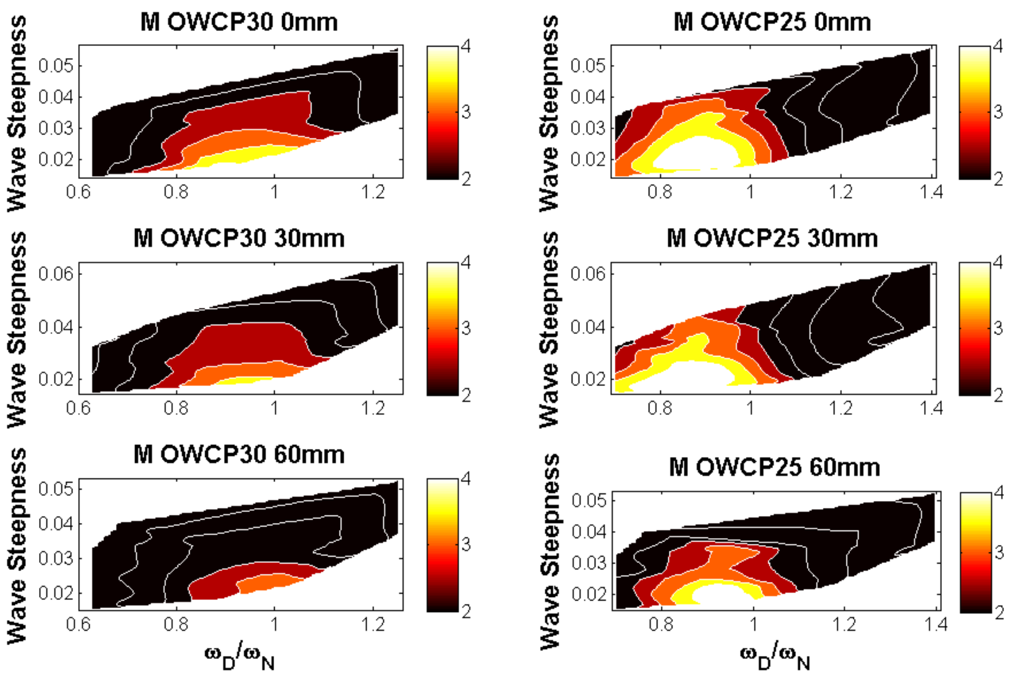

Figure 7 Magnification Factor for the components of the 20-25-30 Array. Focus in given at the behavior of the side pipe (OWCP30, left) and at the central pipe (OWCP25,right) for values of s_d= 0, 30 and 60 mm (top to bottom.).

5. Conclusions

In this paper physical experiments on arrays of onshore OWCP devices have been presented. The main aim was to investigate the role of the separating distances between devices, and how it affected the overall performance of the device and the one of the array. Array installations for WECs have been considered in order to amplify the power output of a single device.

In this paper arrays of similarly tuned devices, as well as differently tuned devices have been investigated. From experimental testing it has been highlighted that when the devices are operating with a minimum separating distance, better performances. In particular, the device located in the centre is positively affected in all the cases investigated.

The results presented show better performances by the arrays with differently tuned devices. Maximum values of M were obtained for the cases when d_s = 0. The values of M varied according to the array configuration with M =5.46 for the 25-30-35 array, M = 4.669 for the 20-25-30 array and M = 3.573 for the square array. Reduction in M of 14% can be expected by increasing s_d of 15 mm, however the reduction is dependent on the configuration. Decrease in M varied between 30% for the 25-30-25 array to 6% for the 20-25-30 for a 30mm increase in the separating distance. The results obtained show that s_d and configuration of the device play a strong role on affecting the performances of the arrays.

This is believed to be due to the different phase responses by the water column exiting the device in the downward motion. In the downward motion the mass of water generates a radiated wave that contrasts the incoming wave train interfering with the energy conversion process in the OWCP. When the devices in the array are phased out, the radiation is minimized and higher M can be achieved. The same can be assumed for 15-30 mm d_s, when the devices are separated the radiated waves affects the operation of the nearer devices.

The work here presented shows that it is possible to increase the bandwidth response of multiple devices by arranging them in array configurations. The overall performances, however, are dependent on the separation distance between the devices and their natural period of oscillation. It has been shown that by reducing to a minimum the distance between the devices, maximum performances can be achieved.

Acknowledgements

The research leading to these results has received funding from the European Community's Seventh Framework Programme (FP7/2007-2013) under grant agreement n°212423.

References

[1] A. Babarit, *Impact of long separating distances on the energy production of two interacting wave energy converters.* Ocean Engineering, 2010. **37**(8-9): p. 718-729.

[2] A. Alexandre, T. Stallard, and P.K. Stansby. *Wave field modification due to a WEC array*. in *Coastlab - Third International Conference on the Application of Physical Modelling to Port and Coastal Protection*. 2010. Barcelona, Spain: Grupo Pacifico.

[3] A.F. Falcão, *Wave-power absorption by a periodic linear array of oscillating water columns.* Ocean Engineering, 2002. **29**(10): p. 1163-1186.

[4] M. Folley and T.J.T. Whittaker, *The effect of sub-optimal control and the spectral wave climate on the performance of wave energy converter arrays.* Applied Ocean Research, 2009. **31**(4): p. 260-266.

[5] P. McIver, *Wave interaction with arrays of structures.* Applied Ocean Research, 2002. **24**(3): p. 121-126.

[6] P.C. Vicente, et al., *Dynamics of arrays of floating point-absorber wave energy converters with inter-body and bottom slack-mooring connections.* Applied Ocean Research, 2009. **31**(4): p. 267-281.

[7] J.P. Kofoed, et al., *Prototype testing of the wave energy converter wave dragon.* Renewable Energy, 2006. **31**(2): p. 181-189.

[8] G. Muller, et al. *Composite Seawalls for Wave Energy Conversion*. in *Coasts, Marine Structures and Breakwaters 2009* 2009. Edinburgh, Scotland, United Kingdom: ICE.

[9] D. Magagna, et al. *Physical investigations into the capture width of an array of OWC Wave Pumps for maximum efficiency*. in *3rd International Conference on Ocean Energy*. 2010. Bilbao, Spain: ICOE

[10] L. Margheritini, D. Vicinanza, and P. Frigaard, *SSG wave energy converter: Design, reliability and hydraulic performance of an innovative overtopping device.* Renewable Energy, 2009. **34**(5): p. 1371-1380.

Preliminary design of the OWEL wave energy converter commercial demonstrator

M. Leybourne[1,2*], W. Batten[1], A.S. Bahaj[1], N. Minns[2] and J. O'Nians[2]

[1] *Sustainable Energy Research Group, University of Southampton, UK*
[2] *IT Power Ltd, Bristol, UK*
* *Tel: +44 1172140517, Fax: +441172140511, E-mail: mark.leybourne@soton.ac.uk*

Abstract: The consortium responsible for the next stage of development of the OWEL wave energy converter will construct and test a large scale, pre-commercial demonstrator. It is expected that this will be installed at Wave Hub during 2013 and grid connected for a testing period lasting around 12 months. This paper reports on the preliminary design work being undertaken in the development of the marine demonstration device. This concentrates primarily on producing a fully costed design by detailing the hydraulic design and aspects of stability as well as providing insight into various design features such as the power take-off, naval architecture, moorings and control. The design is being largely informed by the results of a 12 month research project funded by the South West Regional Development Agency (SWRDA) in which a detailed techno-economic model for a large scale OWEL device was generated.

Keywords: *Wave Energy, Pre-commercial Demonstrator Design, Wave Hub*

1. Introduction

The OWEL (Offshore Wave Energy Limited) wave energy converter is a floating, moored device that uses incident, deep water waves to compress air and drive an air turbine. It is designed to be deployed offshore in energetic deep water locations.

The device concept has been in development for a number of years and has successfully undergone a number of phases of research. The first proved the concept at small scale for a number of different arrangements. A much larger scale device was tested in the second phase in order to demonstrate the ability of the concept to be scaled up. The latest phase of development was funded by the South West Regional Development Agency (SWRDA) and has recently been completed. This incorporated a number of experimental and computational studies to optimise the design and inform the design of the large scale, marine demonstrator. The results from these three phases of testing are reported in detail in [1-4]. A level of confidence has been achieved through the wide variety of results and studies conducted. This has led to the progression of the device and its potential to be developed for commercial deployment.

A pre-commercial, marine demonstration unit is being currently designed for ocean deployment at the Wave Hub facility in the south west of England. This phase of development is intended to demonstrate the performance of a large scale OWEL unit and its ability to be deployed at sea and grid connected, with the overall goal of generating a costed, DNV accredited, full scale, commercial design. This work will represent a critical stage in the commercial route to market. The 3 year £5M project is being funded through a £2.5m award by the UK's Technology Strategy Board (TSB). Private investment will fulfil the remaining half of the required project funds.

This paper presents the initial design of the demonstrator based on the findings from the SWRDA research programme. The design process that will be used to generate the final design is discussed with the associated challenges for such a project and the plans for the future development of OWEL.

2. Principle of Operation

The OWEL converter is a floating duct which is open at one end to capture incident waves. The sides and floor are angled inward to induce a rise in wave height within the duct. As a wave enters the device, it creates a seal with the roof creating a trapped pocket of air ahead of the wave front. As the wave progresses, the air is compressed and passes through an exit pipe to the power take-off system. A schematic of this process is shown in Fig. 1. This proposed method will generate uni-directional air flow meaning standard air turbines can be used instead of the less efficient bi-directional turbines used in oscillating water columns.

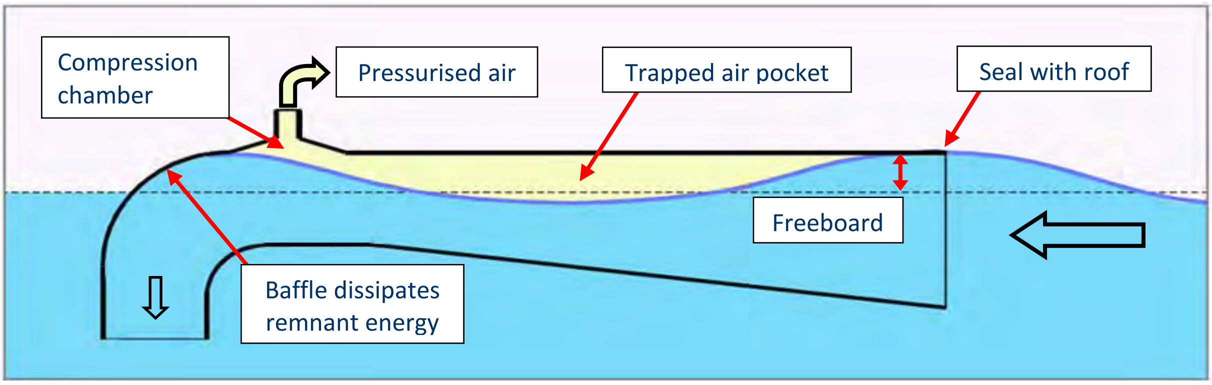

Fig. 1, Schematic of the device operation.

3. Project Overview

The design presented in this paper is considered the initial, baseline design that has been based purely on the results from the previous phases of testing. It is expected that the design will evolve and transform through the course of the project as the various demands from each subsystem are met and compromises made. A significant portion of this project will be spent generating a detailed, engineering design for the demonstration and commercial devices. £2.5m is available to the project through the TSB funding grant with a further £2.5m of co-financing being sought in order to complete the 3 year project from design to decommissioning.

A further aim of the project is to demonstrate the ability of the device to meet the criteria of the successor to the Marine Renewables Development Fund (MRDF). It is therefore intended to keep the device on station for about a year as part of this project in order to verify the consistency of power output, sea-keeping properties and demonstrate reliability and survivability. In addition to the at-sea testing activity, techno-economic modelling will be used to optimise the design so as to minimise the cost of delivered energy.

Effort has been made to progress the OWEL development programme in systematic and methodical order, in line with EMEC standards [5]. By following a logical progression through ever increasing scales, more knowledge has been assimilated and the risk of failure or mistakes, reduced. The results from the previous development phases have provided enough confidence in the device design to progress to a much larger scale. It is anticipated that many lessons will be learnt from testing in an oceanic environment as there are limitations to what can be realised in a laboratory. That being said, the testing to date has identified many key design variables, device characteristics and results that have been fundamental in creating an initial design for the demonstrator.

4. Design Implications from Experimental Results

4.1. 2D Wave Flume Experiments

The 2D testing of a ~1:80 scale model of an OWEL duct, at the University of Southampton showed two regions of peak performance, as shown in Fig 2a. All of the tests were run for a fixed model with mono-chromatic waves. Although these were idealised conditions, a large amount of knowledge was gained from the results of these tests. By running over 200 wave cases for each design configuration it became straight forward to build a detailed picture of the performance and how design changes altered this.

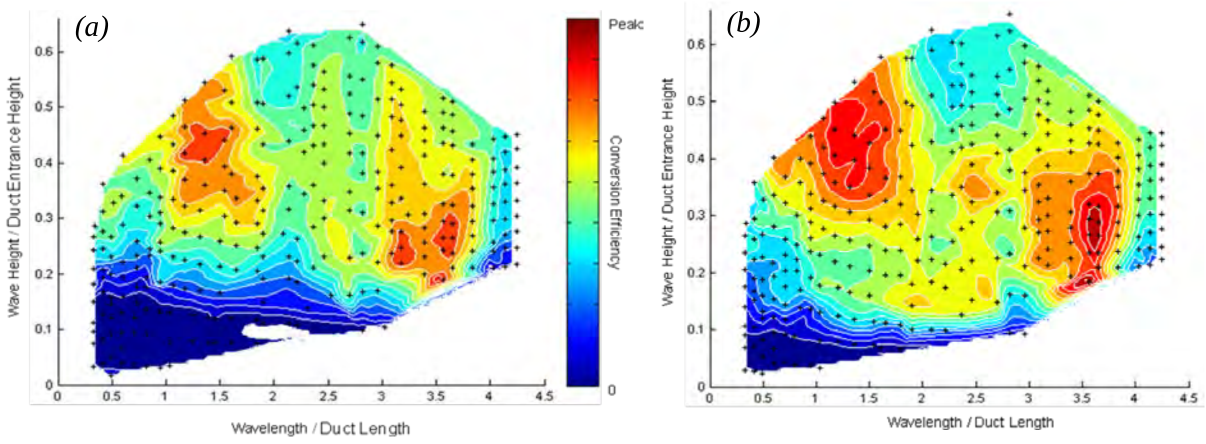

Fig. 2, Non-dimensional performance contour plots for a 2D scale model, in baseline configuration (a) and improved configuration (b).

The experiments resulted in an improved design that featured a re-designed rear duct and also demonstrated that the orientation of the duct is critical to increase performance over a wider range of wave heights. Fig. 2 compares the performance, contour plots as functions of non-dimensionalised wavelength and height, for the original design (a) and the improved design configuration (b). The improved configuration had better performance and wider bandwidths of peak efficiency and was used as the design for the model in the subsequent testing phase.

4.2. 3D Wave Basin Experiments

A series of testing at the wave basin in HMRC, Cork during 2009 generated many results and insights into previously un-investigated aspects of the device. A multi-duct, small scale model (fig. 7) was tested over a range of idealised and realistic conditions with both floating and fixed configurations. A fundamental and detailed understanding of OWEL was gained, including performance, motion and loading characteristics. The non-dimensional, performance contour plot for a floating model, tested in short crested, Bretschneider sea states is shown in Fig. 3. This compares well to the performance shown in Fig. 2, and peak performance was similar. It was found that the bandwidth performance peak widened for a floating model in comparison to a fixed model with mono-chromatic waves.

These results gave confidence in the ability of OWEL to be designed for a particular wave climate, as the peak performance can be shifted to different wavelengths by altering the duct length. Fig. 4 shows the average wave power available at Wave Hub [6], where the peak energy is at T_z=7.5s, H_s=4m, which corresponds to a wavelength/Duct length (λ/DL) ratio of just less than 2. The length of the demonstrator has been dictated by the results of the small scale testing in order to position the peak performance in Fig. 3 at the conditions of maximum energy in Fig. 4.

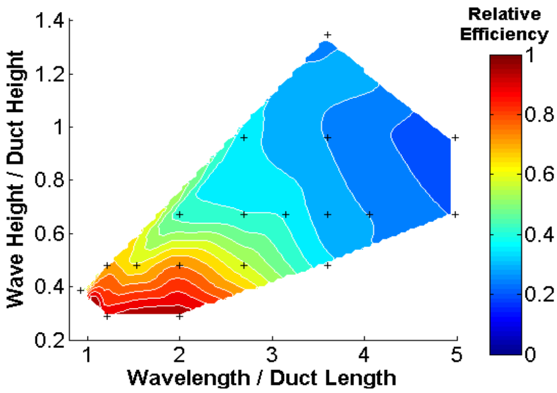

Fig. 3, Performance contour plot, with efficiencies relative to maximum, for a floating 3D model in directional sea states.

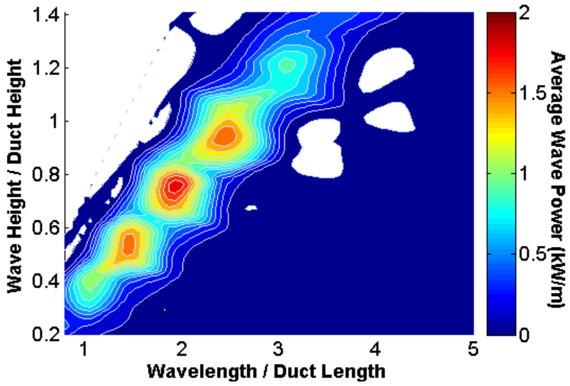

Fig. 4, Average wave power available at Wave Hub

The motions of the small scale, multi-duct OWEL model were measured in realistic, scaled sea states and their effect on performance was investigated. The tests showed that the motions of the duct helped to improve performance for certain sea states. This broadened bandwidth and led to better performance for most sea states and in particular at λ/DL ratios of 2-3. This was because the phase relationship between the incident wave and pitch and surge was such that the model pitched bow down and surged forward into the incident wave. The pulse of power occurred at around a 90° phase lag to the pitch which is thought to be optimum. At the design wave, the motions resulted in a 20% increase in performance over the fixed configuration. This ideal response improves the capture performance of each duct through better wave sealing and air compression within it. This relationship can be seen in the time series motions and power plot in Fig. 5. The RAO (Response Amplitude Operator) plot in Fig. 6 clearly shows the increased pitch and surge motions occurring between 2-3 λ/DL and these are the motions that are beneficial to the power capture. It is therefore important to consider these motions when specifying the naval architecture of the demonstrator. Motions of the design will be assessed using a w ave diffraction code such as ANSYS AQWA to ensure that similar behaviour is exhibited in order to benefit performance.

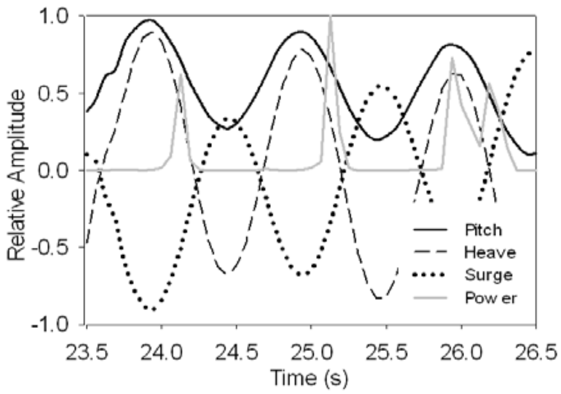

Fig. 5, Time series of motions and power output for a small scale, multi duct model.

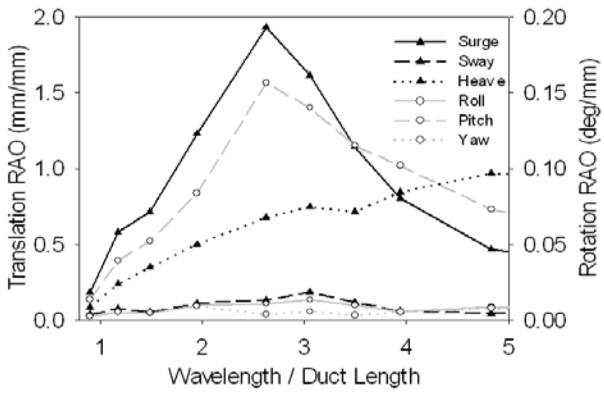

Fig. 6, RAOs for a small scale, multi duct, model of OWEL.

An orifice was used to provide damping to the exiting airflow and the pressure differential across it was measured to determine flowrate and power in order to calculate the conversion efficiency. Fig. 8 shows a typical, time-series pressure trace measuring the pressure drop across the orifice. The dashed line shows the average pressure of the time span which demonstrates that the peak pressures are significantly greater than the average. This type of flow regime is similar to that of an OWC however, unlike an OWC the airflow exhibits very little return flow. Therefore, air flow rectification or self rectifying turbines are not required and so a more conventional air turbine is well suited. A number of orifice sizes were tested in the previous experimental studies to find the optimum applied damping. It is expected that the damping of the air turbine will be variable and so can be controlled to best suit the incident wave climate. This along with the flow rates and pressure data will help to specify the requirements of the turbine characteristics.

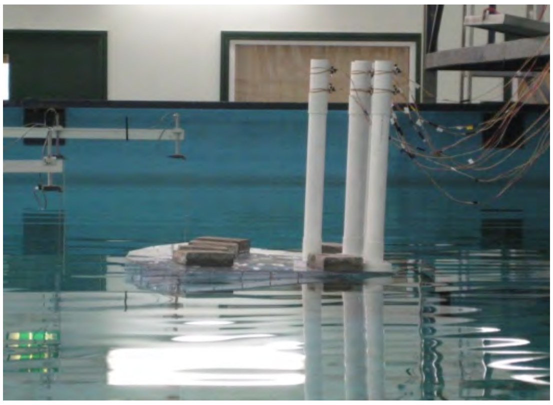

Fig. 7, Experimental testing of a multi- duct, 3D model at HMRC, Cork.

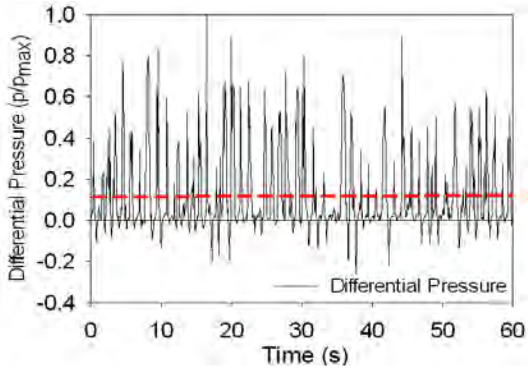

Fig. 8, Plot of normalised, orifice pressure drop for a typical sea state.

Various mooring configurations were also trialled during the wave basin testing and it was seen that different designs have clear effect on the motions of the device as well as the peak and average loads. These small scale moorings, were intended as simple models of a full scale mooring system to provide initial data on the order of the loads that can be expected. As the waves at Wave Hub have low directionality [6], the full scale mooring system will be designed to keep the device on station and orientated towards the predominant wave direction. Computational analysis of the motions and moorings, using a commercial diffraction code, will be undertaken to assess loading and support the final design.

5. Initial Design

5.1. Overview

The Wave Hub, marine demonstrator has been designated the D500 as it is expected to be rated at 500kW. The unit will be a scaled down version of the full scale, commercial design and comprise a single floating duct rather than a large, multi-duct, floating platform as has been previously suggested. This means that a smaller duct can be tested and used as a development platform before a full scale commercial device is designed. An artist's impression and a selection of key figures are given in Fig. 9, whilst the drawings of the initial design are shown in Fig. 10 with the key dimensions and components labelled.

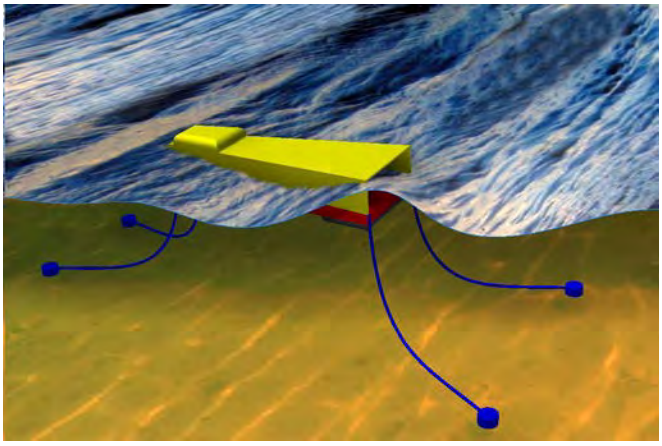

D500 Key Figures	
LOA ca.	42m
Beam ca.	18m
Draft ca.	8m
Lightship ca.	650t
Ballast ca.	300t
Total ca.	900t

Fig. 9, An artist's impression and key figures of the D500 demonstrator.

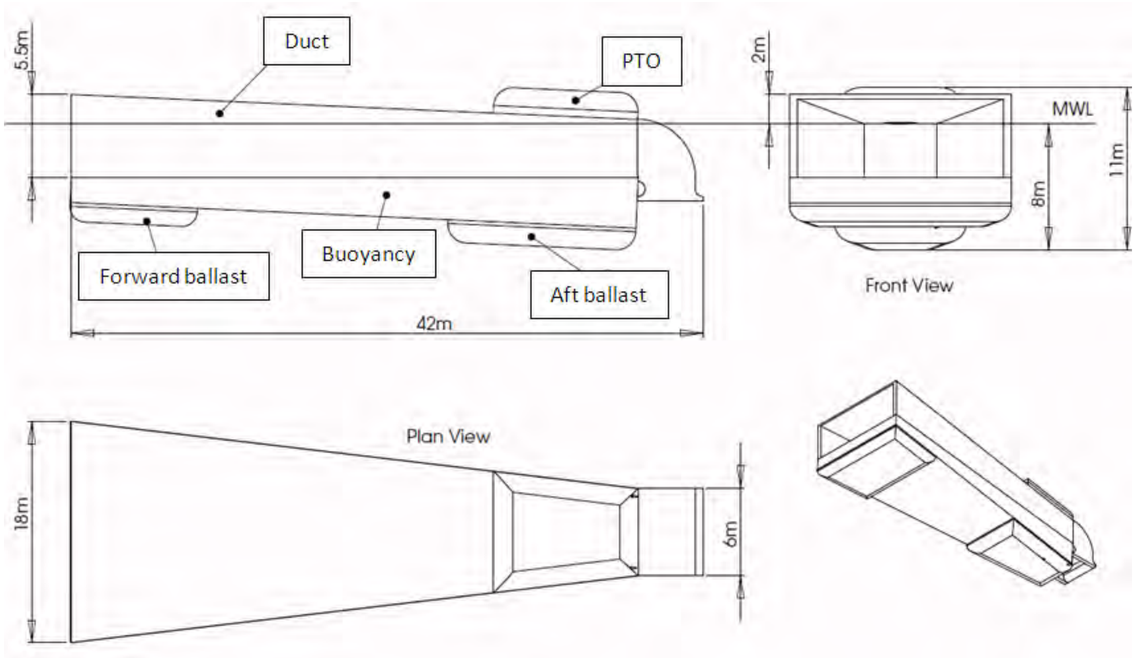

Fig. 10, The general assembly drawings of the initial design of the OWEL demonstrator.

The main duct is likely to be made of steel however concrete is being considered as an alternative material depending on structural loading requirements and costs. The power take-off unit, a turbine and generator set, will be located in a watertight housing at the rear of the duct, above the waterline. Below the main duct will be the main volumes of ballast and buoyancy required to correctly trim the device and determine the motion responses.

A control system to alter the freeboard and natural pitch frequency is being considered. This will involve controlling the volume of air or water in tanks below the duct. By altering the buoyancy, the freeboard can be varied to match the incident wave climate. This also forms a part of the survival strategy in that during storm conditions the freeboard can be reduced to lessen the impact of incident waves on the device. Controlling the position of the ballast about the centre of buoyancy will allow the natural pitch period to be tuned to the optimum value. This will ensure that the phase difference between pitch and wave front is beneficial to the performance as described by the results discussed in the previous section.

5.2. Project Organisation

The demonstrator will be developed by a consortium of organisations that, between them, bring together the wealth of experience needed to successfully deliver a project of this nature. IT Power and OWEL will lead the project whilst the DNV will monitor the design process in order to provide confidence and certify it to DNV standards [7]. In order to best demonstrate the responsibilities of each consortium member, the device can be broken down into its main constituent parts and subsystems, as shown in Fig. 11.

Involving a number of organisations is beneficial to a large and complex project such as the development of a wave energy converter. It brings a wide variety of knowledge into the design process and also clearly demonstrates that third-parties have confidence in the project. Ensuring that the design progresses as planned will be challenging, given the level of communication required between the various consortium partners. A robust design method will be used to facilitate the process, meaning that the design requirements and expectations will be clear.

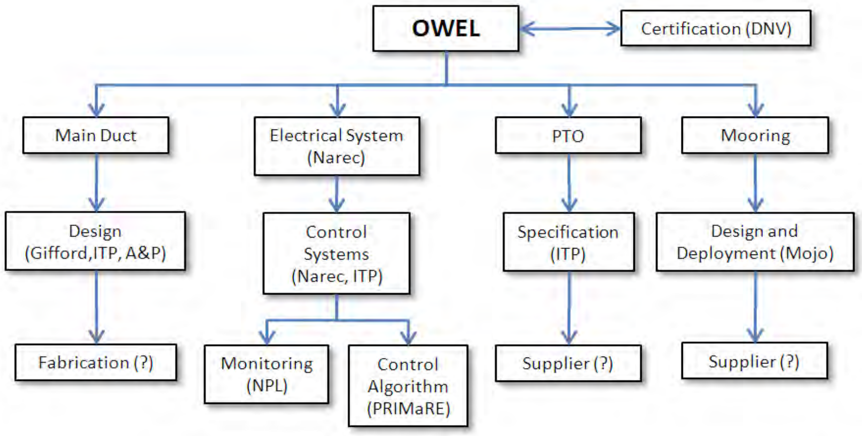

Fig. 11, A chart showing the breakdown of the main subsystems of the OWEL demonstrator and the consortium members responsible.

5.3. *Design Framework*

The design framework that will be used in the process, works by formulating a "Problem Definition" and "Design Solution" for each major subsection or component in the system. The problem definition is a document created to identify the requirements and constraints on the design, which includes stakeholder expectations, design constraints and assumptions, problem boundaries and interfaces. This also includes functional analysis to determine what the design needs to achieve and a validation to check that the problem that has been defined is actually that which requires a solution. A design solution is then generated to meet the requirements of the problem definition. This begins by assessing and recording all possible ideas and alternative designs. A final design is chosen through modelling, life-cycle cost analysis and risk analysis. The solution is then validated against the problem definition to ensure that the design solution fulfils the problem definition, stakeholder expectations and functional requirements.

Consortium members will likely resort to their own design methods to devise design solutions, however, the problem definitions will be created for all necessary design points. This will unify the group as it will be clear what the problem is and the requirements of the solution. It is then the responsibility of the organisation involved with each design point to generate a suitable design solution. This process mitigates any potential confusion over the design requirements and also clearly sets out responsibilities.

6. Future Development

The forthcoming decade is likely to bring about large advances in wave energy device development. In order for a device to have commercial promise, it has to be successfully demonstrated in a marine environment. The industry is therefore gearing itself towards providing proving and development sites for device teams. Once a machine has been proven at an ocean site at large scale, it will most likely be deployed in small arrays of 3-5MW. In order to attract interest from utilities, device deployment of this magnitude will be required, along with demonstrated reliability. OWEL is therefore aiming to develop its converter to meet these capability requirements.

6.1. *Single Duct Commercial unit*

Following on from the Wave Hub demonstrator, a first generation commercial OWEL D1000 will be developed as a refinement of the single duct design. It will incorporate advances made following the lessons learned through the D500, meaning that the output for a single duct should rise. It is envisaged that the first commercial scale deployment of OWEL will feature a number of these single ducts in small array. Deployed in a higher energy wave climate, such as that at the Portuguese Pilot Zone, the improved design will likely be rated at about 1MW per device.

6.2. Multi Duct Commercial unit

A second generation commercial OWEL device could comprise a number of ducts combined to form a large floating platform with a multi-megawatt output. This concept is shown in the artist's impression in Fig. 12. By combining a number of ducts the device could benefit from shared costs of subsystems such as mooring, grid connection, control systems and power take-off. Multiple ducts could also help to smooth power output if the compressed air pulses from each duct were designed to arrive at the turbine of out of phase at staggered times.

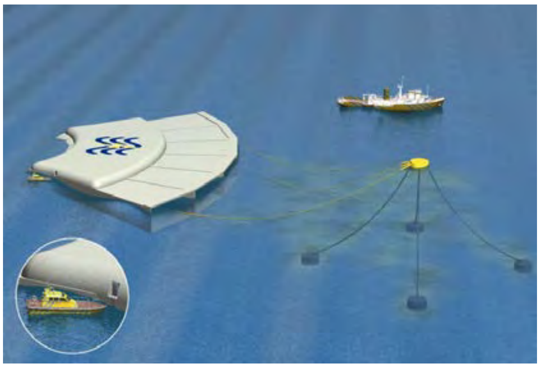

Fig. 12, An artist's impression of a second generation OWEL MD3000 3MW unit

Acknowledgements

The authors gratefully acknowledge IT Power Ltd. Offshore Wave Energy Ltd and the Engineering and Physical Sciences Research Council (EPSRC) for funding this research as part of an Engineering Doctorate study. The Technology Strategy Board (TSB) and the South West Regional Development Agency (SWRDA) are also thanked for funding these phases of the development of OWEL.

References

[1] J. Kemp, A. Derrick, J. O'Nians, and D. Upadhyay. 'The OWEL Wave Energy Converter as a Platform for Combined Wave and Wind Power Generation'. 6th European Wave and Tidal Energy Conference, Glasgow, UK, 2005.

[2] M. Leybourne, W.M.J. Batten, A.S. Bahaj, J. O'Nians and H. Traylor, Preliminary findings from a laboratory scale model of a ducted wave energy converter, 10th World Renewable Energy Congress, Glasgow, UK. 2008.

[3] M. Leybourne, W.M.J. Batten, A.S. Bahaj, J. O'Nians and N. Minns, A Parametric Experimental Study of the 2D Performance of a Ducted Wave Energy Converter. 8th European Wave and Tidal Energy Conference, Uppsala, Sweden. 2009.

[4] M. Leybourne, W.M.J. Batten, A.S. Bahaj, J. O'Nians and N. Minns, Experimental and Computational Modelling of the OWEL Wave Energy Converter. 3rd International Conference on Ocean Energy, Bilbao, Spain. 2010.

[5] B. Holmes, Tank Testing of Wave Energy Conversion Systems. EMEC Standards. European Marine Energy Centre. Orkney, UK. 2009.

[6] Halcrow, Wave Hub Technical Feasibility Study, 2005, Appendix A – Coastal Processes

[7] Det Norske Veritas (DNV), Certification of Tidal and Wave Energy Converters, Offshore ServiceSpecification DNV-OSS-312, 2008.

Investigation of Wave Farm Electrical Network Configurations

Mr. Fergus Sharkey[1,*], Dr. Michael Conlon[2], Mr. Kevin Gaughan[2]

[1] *Dublin Institute of Technology, Dublin, Ireland; ESB International, Dublin, Ireland*
[2] *Dublin Institute of Technology, Dublin, Ireland*
* *Corresponding author: Tel: +353 1 7038000, E-mail: fergus.sharkey@esbi.ie*

Abstract: Wave Energy Converters (WECs) have been in development for a number of decades and some devices are now close to becoming a commercial reality. As such, pilot projects are being developed, particularly in the UK and Ireland, to deploy WECs on a pre-commercial array scale. There is little experience in the wave energy or utility industry of designing and installing electrical networks for WEC arrays with the closest comparison being offshore wind farms. There are some key features of WECs which will ultimately dictate that the electrical configuration differs from that of offshore wind farms.

This paper investigates the potential representative electrical network configurations for small (10MW), medium (40MW) and large scale (150MW) 'wave farms' in order to establish a development path for such projects. The configurations are evaluated for efficiency (power loss), redundancy and short circuit levels. Key interfaces in the electrical infrastructure are identified and discussed. This paper also identifies the key differences between offshore wind farm electrical networks.

Keywords: *Wave Energy, Electrical Network, Array*

1. Introduction

Many countries have ambitious targets by 2020-2030 for ocean energy [1], [2] and there are several ocean energy test facilities with grid connection such as EMEC and Wavehub. Collaborative projects have also explored the area of WEC electrical arrays such as the Equimar Project [3] and these have also been investigated in [4]-[10]. The ultimate ambition is to have large wave farms installed in a similar fashion to offshore wind.

Offshore wind energy projects have been developed up to 300MW installed capacity and it is acknowledged that the industry can serve as a useful source of knowledge for the wave energy sector. Investigating the state of the art in offshore wind farms and also looking at all the information available within the wave energy sector will enable a feasible assessment of wave farms to be studied.

2. Offshore Wind Electrical Systems

A survey of the 25 largest offshore wind farms (as of December 2010) shows that the majority are installed less than 15km from shore and in less than 30m depth. As the installed capacity and distance from shore increased offshore, platform based, substations were required in order to step up the voltage to HVAC (>100kV) for transmission to shore. The requirement for an offshore substation is typically above 100MW capacity or 10km distance from shore.

HVDC transmission will be used in larger offshore wind farms located far from shore such as the BARD Offshore Wind Farm (400MW, 100km from shore) which is expected to be commissioned by 2011. There are also development projects on deepwater wind farms and floating wind turbines [11].

All offshore wind farms have a MVAC infield network, typically 20-36kV, with the majority >30kV. The infield network configuration of offshore wind farms is typically a series of radial circuits containing 7-8 turbines connected back to a central location (either onshore or offshore), as illustrated in Fig. 1. The radial circuit is protected using switchgear in the wind turbines and the substation. The cables in each radial are tapered in size towards the radial extents and this is viewed as the best way to minimise cable costs [12]

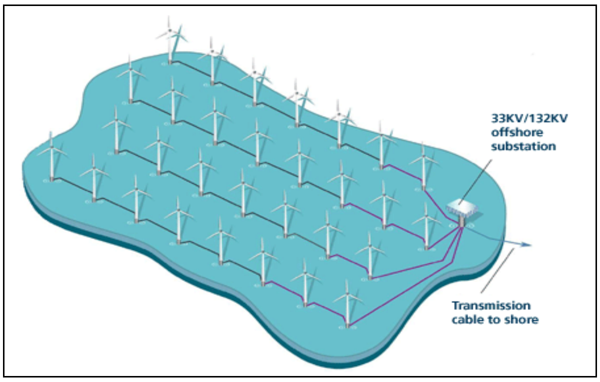

Fig. 1 Typical electrical layout of offshore wind farm [Source: Barrow Wind Farm]

Redundancy and Sectionalising have been proposed in [13] & [14] and have been shown to offer advantages in increasing availability. To date, however, these are rarely utilised due to the inherent additional up front costs.

The average capital expenditure (Capex) for offshore wind in 2009 was €2.3m/MW [15]. From [15] we can also see that for Horns Rev and Nysted offshore wind farms the infield and transmission systems represent ~21% of the total Capex. The electrical system is a significant proportion of the overall investment in a wind farm and, assuming that capacity factors and costs per MW for WECs approach those achieved by offshore wind, then it is expected that the same will hold true for wave energy.

3. Wave Energy Device and Site

The Wave Energy Converter (WEC) used in this study is the Wavebob device [16], which is a point absorber type WEC. The site used for this study is Belmullet, located off the west coast of Ireland, where a test site is currently under development. Using the Wavebob frequency domain model with an electrical rating of 1MW, and a scatter diagram from the test site, the energy yield distribution histogram can be established for a Wavebob device on the site. Fig. 2 shows the energy yield distribution on the site over the course of a year. This demonstrates that almost 20% of energy yield is from >90% output of the device. This information is used in establishing the energy yield efficiency of the electrical network in later sections.

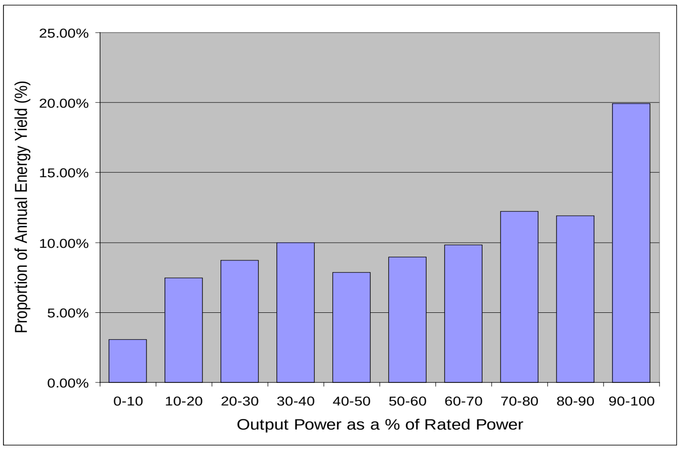

Fig. 2 Energy yield distribution histogram of the Wavebob device at Belmullet

The Wavebob device is designed for 100m+ water depth and is typical of floating WECs. Fitzgerald indicates in [17] that such compliantly moored wave energy converters are likely to be moored close to 100m in general for survivability reasons. The 100m depth contour off the west coast of Ireland lies between 10 and 25km from the shoreline therefore the transmission distance will be selected within this range.

Ultimately the device spacing will be selected based on a variety of factors, namely resource capture and interference [18], [19] mooring footprint [17], marine operation requirements, and minimising cable costs and losses. Therefore 200, 300 and 400 metres device spacings have been selected for this paper. No hydrodynamic interference or directional effects are considered in this paper, however it must be noted that this will limit the maximum rows permissible in an array.

As with offshore wind there will be three types of connection concepts, namely single MV transmission, multiple MV transmission and HV transmission from an offshore substation. As such three candidate wave farms are outlined in Table 1 which will be analysed in this paper.

Table 1 Wave Farms under analysis in this paper.

Wave Farm	Capacity	Distance to Shore	Transmission Voltage	# Transmission Lines
1	10MW	12km	MVAC	1
2	40MW	15km	MVAC	2+
3	150MW	20km	HVAC	1

4. Methodology

The wave farm electrical network will be arranged in radial circuits as this has proven the most cost effective option for offshore wind. For larger arrays a 'forked' radial is utilised as this further reduces cable cross sectional area (CSA) in the radials. The effect of additional redundancy is discussed later. All cables will be three-core XLPE with copper conductors. The methodology is as follows;

- Cables (infield and transmission) are sized for maximum continuous current at 10kV, 20kV & 33kV and, for Wave Farm 3, 132kV. Practical limitations are observed.
- Active Power losses (using lumped parameters) are assessed for the range of 0-100% wave farm output for each case.
- Using the site/device information given in Section 3 the energy yield efficiency for the wave farm is obtained, i.e. the percentage electrical energy delivered in a year.
- If an energy yield efficiency of 96% is not achieved initially then an iterative approach is taken to increase the cable CSA to achieve this target.

For practical limitations a minimum cable CSA of 35mm^2 for 10kV & 20kV and 50mm^2 for 33kV are assumed. A maximum cable CSA of 500mm^2 is assumed as this is one of the largest dynamic cables installed to date in the Maari Oil Field. 10-15 WECs will be connected in each radial depending on the voltage and the total installed capacity. ABB present the practical limitations for transmission at various voltages in [20] which are replicated below in Table 2. These do not account for maximum distances which are of importance when considering very long lines (i.e. >50km) which we are not considering here.

Table 2 - Recommended maximum transmission capacities given in [20]

Voltage	10kV	20kV	30kV	66kV	132kV
Maximum Power	15MW	30MW	50MW	100MW	200MW

For initial wave farms the voltage rating may initially be limited by certain components, notably cable connectors and submarine power equipment. Given sufficient demand it is likely that these components would become available at higher voltages.

Cable parameters for the study are obtained from [21], Nexans and ABB. No sheath or armour losses are considered, however dielectric losses are calculated in all cases. Infield voltage regulation and switching transients are also not considered, but are naturally important considerations for future work.

For larger arrays the short circuit contribution of the grid and generators must be calculated as the short circuit requirements for the cables may result in a larger CSA cable than dictated by the current carrying requirements. Generator selection is critical here as certain generator types will contribute less fault current than others. In [22] fault currents for synchronous and asynchronous generators are given as 15 p.u. and 8 p.u. respectively, whereas double-fed induction generators and power converter interfaced generators contribute approx 1-2 p.u.

5. Results

The layouts of the proposed wave farms illustrated in Fig. 3 are based on a radial approach and within the limitations outlined in Section 4. These are electrical circuit layouts and the physical layout could differ without affecting the cable lengths. These will be analysed according to optimum voltage levels, efficiency and redundancy. The methodology shown in Section 4 will be used to size the cables to achieve 96% energy yield efficiency, i.e. the annual efficiency of exporting MWhrs.

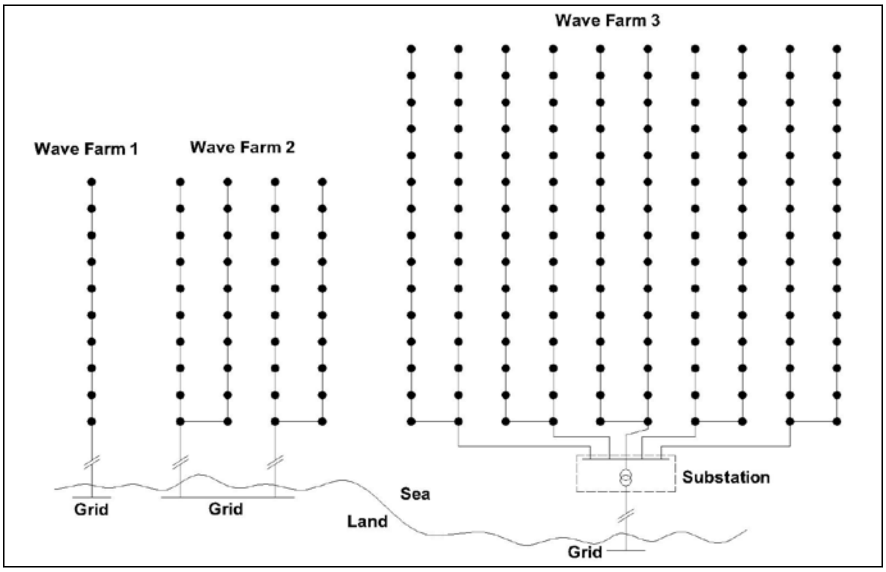

Fig. 3 Selected Wave Farms for Investigation

As mentioned previously this is an iterative process; initially sizing based on maximum continuous current, and then refining based on efficiency. The resultant achievable energy yield efficiencies are illustrated in Fig. 4. >96% energy yield efficiency is achievable in almost all cases, however up to almost 99% is possible for larger wave farms with HVAC connection to shore. Table 3 outlines the cable CSAs required to achieve these figures.

The device spacing has a negligible effect on energy yield efficiency; particularly for larger arrays. Increased spacing will, however, also increase infield cable lengths. The effect of this becomes more pronounced for larger arrays as shown in Fig. 5. Up to 38% increase in cable length is required for larger wave farms when the spacing is doubled.

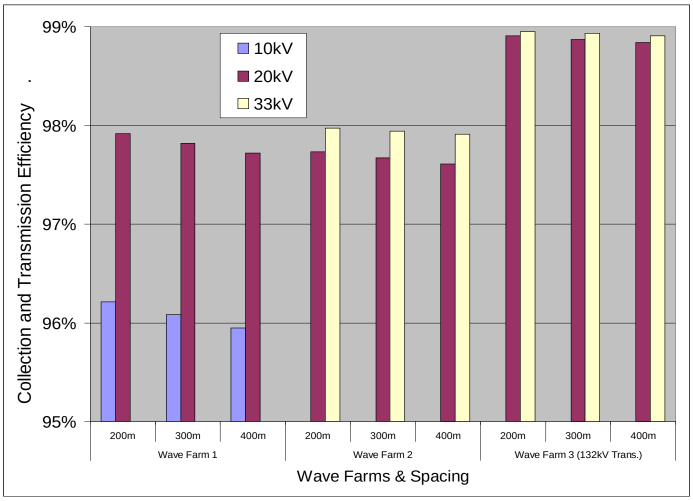

Fig. 4 Achievable Energy Yield Efficiency for Case Study Wave Farms

Table 3 Cable CSA (mm^2) required to achieve efficiencies shown in Fig. 4.

	Wavefarm 1 (10MW)		Wavefarm 2 (40MW)		Wavefarm 3 (150MW)	
	Infield	Transmission	Infield	Transmission	Infield	Transmission
10kV	35-300	400	N/A	N/A	N/A	N/A
20kV	35-95	185	35-95	400	35-500	500*
33kV	N/A	N/A	50*	150	50-300	500*

** Minimum or Maximum limits apply*

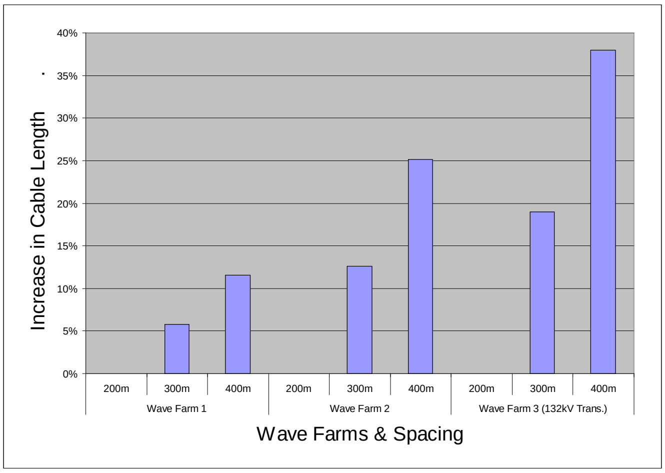

Fig. 5 Percentage Increase in overall farm cable length for spacing increase from 200m.

Redundancy can be added to the network in a variety of ways and has been proven to increase availability while naturally increase cost. Nevertheless, redundancy could have a dual purpose for wave farms as the WEC devices will have to be routinely removed and brought to port facilities for maintenance. Redundant circuits could provide an alternative route for the power during this maintenance period. Fig. 6 shows some possible redundant circuits for Wave Farm 2, which would involve either increasing CSA of cables within the radial or addition of secondary cables running the length of the radial.

Alternatives to redundancy that could be utilised for wave farm maintenance regimes are;

- The availability of ‘standby’ or ‘dummy’ WECs to ‘slot’ into place.
- A system for temporarily ‘bridging’ the gap left by the WEC in the electrical circuit.
- Submarine switchgear allowing continued operation of the infield circuit.

These could prove a more cost effective alternative than additional redundancy.

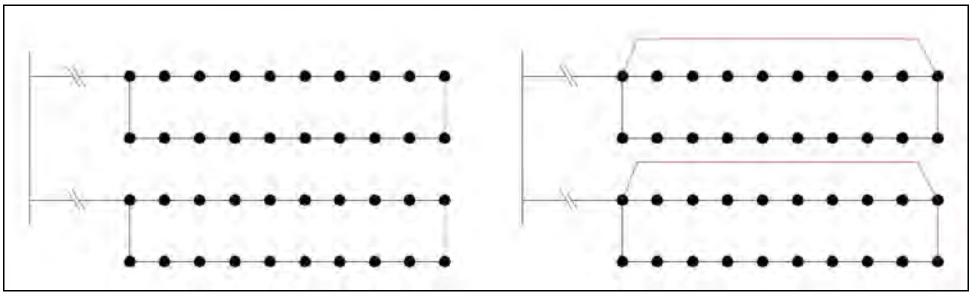

Fig. 6 Wave Farm 2 redundant circuit options

6. Key Interfaces

The studied wavefarms are presented in single line diagrams only. There are a number of key interfaces identified which are a functional part of the wave farm. The key interfaces are;

1. Dynamic Cable to WEC interface
2. Dynamic Cable to Static Cable interface
3. MV Switchgear interface (onboard WEC or seabed installation)
4. Offshore Substation (when applicable)

Interfaces 1, 2 & 3 are of particular interest as they can provide critical functionality in the wave farm system. Some of this functionality overlaps as outlined in Table 4 below. As each of these three key interfaces overlap, each WEC developer must establish the exact functionality and components required for each of these interfaces

.

Table 4 Possible functionality of key interfaces

Functionality of Key Interfaces						
	Connection/Disconnection of WEC	Isolation	Protection	Cable Installation	Deck/Hull Penetration	Maintain Radial Circuit
1	Y	Y**	N	Y	Y	N
2	Y	Y**	N	Y	Y	N
3	Y*	Y	Y	N	N	Y

(with integrated connectors for submarine switchgear; ** with strict control procedures)*

Interface 3 (WEC MV switchgear) is significant to the electrical network as it is a necessary protection function but can also be used for redundancy. Most importantly is its function as part of a safety and isolation system. Submarine switchgear systems have been developed mostly for use in the oil and gas industry.

From [23]; for systems above LV in wind farms (on and offshore), the UK HV safety rules apply [24]. [24] states that in order to work on or near HV power systems the equipment should be isolated and earthed with isolation points and earth points locked where practicable. It would be impractical to expect that submarine switchgear, where required for isolation and earthing, could be locked in this position. The safe control of work would be extremely difficult to undertake given submarine switchgear units.

For interface 4, as is the case in offshore wind, an offshore substation would typically be required for wave farms larger than 100MW. As the wave farm in question will be located in 100m water depth, although the onboard equipment will be identical, the type of foundations typically used in offshore wind farm substations, i.e. monopile, tripod and gravity base, will be impractical. Jacket structures have been used for 'deepwater' sites such as in [11]; however this is only 45m depth. The choices for an offshore substation in 100m water depth would be;

- Strategically locating the wave farm in proximity to a <50m water depth location and locating the offshore substation at an midpoint between the wave farm and the shore

- Building a jacket or compliant tower type structure such as those in use for oil platforms
- Building the substation on a floating platform such as the semi-submersible, tension leg or spar type structures in use for oil platforms
- Locating the offshore substation on the seabed

This key interface requires further study to establish the most cost effective option available.

7. Conclusions

This paper explored the technical issues surrounding a development path for electrical networks for future offshore wave farms. The paper concludes that key issues for offshore wind farm electrical networks are cost and efficiency. Following the same configurations as wind farms electrical networks are developed for small, medium and large wave farms which should provide a high level of efficiency. The characteristics of the Wave Energy converter and the site must be taken into account for establishing the 'true' energy yield efficiency.

It will be possible to establish small wave farms (<15MW) using 10kV infrastructure, however this will lead to large cable sizes within the array and particularly to shore. More suitable voltages are 20kV and 33kV within the array and for transmission up to 100MW with offshore substation and 132kV transmission required for transmission for large scale wave farms (>100MW)

Increasing the device spacing within the wave farm has a negligible effect on energy yield efficiency, particularly for larger arrays and does not require increasing cable CSA. There will, however, be a cost impact from having longer infield cables. Doubling the device spacing could add an additional 38% to the overall cable length of the infield and transmission system.

Redundancy can be introduced to the electrical networks, however at a financial cost. Redundancy may prove more important due to larger numbers of devices per radial in wave farms. Redundancy in the electrical network could form an integral part of the maintenance strategy also, however other solutions could be developed to overcome this.

There are a number of key interfaces which a WEC developer must consider at the early stages of device design. If these key interfaces are managed correctly the WEC can lend itself to a flexible, cost effective, and much standardised electrical network, which will make it attractive for deployment on an array scale.

The key differences between offshore wind and wave farms have been identified;

- WECs have lower MW ratings than wind turbines allowing more devices per radial
- Devices will require removal for maintenance having impact on circuit integrity
- Depth at the site is significantly deeper than any offshore wind farm and distance from shore could be further.
- Devices are not fixed structures making cable installation potentially complicated

References

[1] Offshore Renewable Energy Development Plan 2010 - http://www.dcenr.gov.ie/

[2] UK Renewable Energy Strategy 2009 – www.decc.gov.uk

[3] Equimar Deliverable 5.1 2009 – http://www.equimar.org/

[4] M. Kenny. Electrical Connection Issues for Wave Energy Arrays. Masters Thesis, University College Cork, 2010.

[5] A. Kiprakis, A Nambiar, D. Forehand, A Wallace. Modelling Arrays of Wave Energy Converters Connected to Weak Rural Electrical Networks. International Conference on Sustainable Power Generation and Supply, 2009

[6] Czech, B.; Bauer, P.; Polinder, H.; Korondi, P. Modeling and simulating an Archimedes Wave Swing park in steady state conditions. 13th European Conference on Power Electronics and Applications, 2009.

[7] M. Molinas, O. Skjervheim, B. Sorby, P. Andreasen, S. Lundberg, T. Undeland. Power Smoothing by Aggregation of Wave Energy Converters for Minimizing Electrical Energy Storage Requirements. 7th European Wave and Tidal Energy Conference, 2007.

[8] T. Ahmed, A. Zobaa. Offshore power conditioning system connecting arrays of wave energy converters to the electric power grid. 8th International Conference on Advances in Power System Control, Operation and Management, 2009.

[9] M. Santos, D. Ben Haim, F. Salcedo, J. Villate, Y. Torre-Enciso. Grid Integration of Wave Energy Farms: Basque Country Study. 3rd International Conference on Ocean Energy, 2010

[10] D. O'Sullivan, G. Dalton. Challenges in the Grid Connection of Wave Energy Devices. 8th European Wave and Tidal Energy Conference, Uppsala, Sweden, 2009

[11] S. Breton, G. Moe. Status, Plans and Technologies for Offshore Wind Turbines in Europe and North America. Renewable Energy, 2009. Pg. 646-654

[12] J. Twidell and G. Gaudiosi – Offshore Wind Power. Multi Science Publishing, 2007

[13] H. Landsverk, O. Granhuag, P. Skryten, S. Rafoss. 36kV Vacuum Circuit Breaker Panel - The Perfect Switchgear for Wind. 20th International Conference on Electricity Distribution, Prague, Cezch Republic 2009

[14] J. Yang, J. O'Reilly, J. Fletcher. Redundancy Analysis of Offshore Wind Farm Collection and Transmission Systems. International Conference on Sustainable Power Generation and Supply 2009

[15] R. Green, N. Vasilakos. Economics of Offshore Wind. Energy Policy, 2010. Pg. 1-7

[16] W. Dick. 'Wave Energy Converter'. U.S. Patent Number 6857266

[17] J. Fitzgerald. Position Mooring of Wave Energy Converters. PhD Thesis, Chalmers University, Sweden. 2009 – pp 36

[18] C Fitzgerald, G. Thomas. A Preliminary Study on the Optimal Performance of an Array of Wave Power Devices. 7th European Wave and Tidal Energy Conference, 2007.

[19] P. Ricci, J-B Saulnier, A. Falcao. Point Absorber Arrays: A Configuration Study off the Portuguese West Coast. 7th European Wave and Tidal Energy Conference, 2007.

[20] ABB – Cables for Offshore Wind Farms. www.abb.com

[21] C. Moore. BICC Electrical Cables Handbook 3rd Edition. Blackwell 1997.

[22] P. Karaliolios, A. Ishchenko, E. Coster, J. Myrzik, W. Kling. Overview of Short-Circuit Contribution of Various Distributed Generators on the Distribution Network.

[23] Renewable UK – Wind Turbine Safety Rules. http://www.bwea.com/safety/safety_rules.html

[24] UK National Grid – The Electricity Transmission Safety Rules 3rd Edition. http://www.nationalgrid.com/

Performance analysis of a floating power plant with a unidirectional turbine based power module

Prasad Dudhgaonkar[1], Kedarnath S.[2], Biren Pattanaik[1], Purnima Jalihal[1], Jayashankar V.[2,*]

[1] National Institute of Ocean Technology, Chennai, India
[2] Indian Institute of Technology Madras, Chennai, India

* Corresponding author. Tel: + Tel: +91 4422574427, Fax: +91 4422570509, E-mail: jshankar@ee.iitm.ac.in

Abstract: A major attraction of a floating wave power plant as opposed to a fixed Oscillating water column (OWC) plant is in the cost of construction. The price paid is in the lower efficiency of conversion in the hydrodynamic stage. This puts onus on the subsequent power module stage in achieving an efficiency that is necessary for a commercial plant. A new backward bent ducted buoy (BBDB) was designed in which the power module is a twin unidirectional turbine. Basic experimentation on the power module is done on a turbine with 165 mm diameter and characterized with bidirectional flow with widely varying flow rates. The efficiency is shown to be better than 68% over the expected working range. The details of a plant producing 50 kW for Indian conditions is described. The range of powers over which a BBDB structure compares with a fixed OWC is highlighted.

Keywords: *Wave energy, floating power plant, backward bent ducted buoy.*

1. Introduction

The oscillating water column (OWC) principle is an attractive approach to convert wave energy into electrical energy as exemplified by operational plants in several countries [1]. As of today it is reasonable to expect a wave to wire efficiency of about 24 % with a fixed OWC device [2]. Of this, the OWC efficiency would be about 60 %, and the power module (comprising bidirectional turbine and generator) would be about 40 %. One aspect of the fixed OWC is that the structural cost could lie between 70 to 85 % of the overall cost [3]. This has motivated the development of floating OWCs which promise reduced cost with an accompanying reduction in efficiency in the hydrodynamic stage. The largest of such structures was the Japanese Mighty Whale [4]. While laboratory results predicted a best efficiency of 50 % in the hydrodynamic stage, practical measurements showed that the best efficiency was about 30 %. Hence the overall wave to wire efficiency was closer to 15 %. There have been continuous attempts to improve the efficiency of floating OWCs and the backward bent ducted buoy (BBDB) is one such attempt [5]. In this work we show that an improved power module for the BBDB with variable speed twin unidirectional turbines can achieve 65 % efficiency and thus make the floating structure attractive in spite of the lower hydrodynamic efficiency.

2. The Backward Bent Ducted Buoy (BBDB)

The Backward Bent Ducted Buoy (BBDB) has been conceived as a relatively low cost wave energy device to convert wave energy into electricity. The BBDB has a backwardly inclined oscillation water column, which has been proved to be more effective than a forwardly inclined one. It uses an oscillating column of water in reverse L shaped chamber or duct, such that the open mouth of the duct is away from the incident waves. The horizontal limb has an opening to the sea and is submerged under water. The vertical limb traps a column of air at the upper region of the duct and a regulated vent allows air to pass in and out under cyclic pressure and partial evacuation of air due to oscillating water surface. The enclosed water column is, not influenced by the wave movements around the buoy, whereby it oscillates relative to the wave motion moving the buoy itself. The air current, which arises, drives an air turbine installed above the water column. This airflow becomes a means to produce power. Fig. 1 shows a BBDB which was initially deployed for testing without a power module. It had an equivalent orifice in order to simulate a turbine. The dimensions of the model were determined after model studies as reported in [6]. The Indian conditions require a zero crossing period of about 8 seconds and a significant wave height of 1.2 m yielding average incident energy of 6.3 kW/m. The overall design is based on an improvement in the power module in the work reported in [7].

Fig.1. The BBDB being deployed with an orifice for charactering hydrodynamic performance

3. Basic simulations on fixed guide vane and unidirectional impulse turbines

The design of the BBDB described in [7] was based on a fixed guide vane impulse turbine. It was concluded that an optimum turbine diameter of 1.5m would yield a power output of 30 kW with H_s = 2.25 m and T_z = 8.5 s where H_s and T_z are the significant wave height and zero crossing period respectively. We show that an equivalent power module with a twin unidirectional turbine topology [8] would substantially improve the efficiency of the power module and thus the overall power conversion. In order to validate the concept, studies are done in a turbine of diameter 165 mm coupled to a 375W, 3000 rpm dc generator. An oscillatory flow rig is used to characterize the performance. The diameter was based on two criteria: The oscillatory flow rig is sufficient for characterizing its performance over the entire flow regime and more importantly the damping offered by the turbine matches that of the orifice used in the BBDB hydrodynamic test. This is shown in Fig. 2 which portrays the pressure- flow behavior of the 165mm unidirectional turbine (UDI), a 165 mm fixed guide vane impulse turbine (FGV) and orifices ranging from 52.5 mm to 77.9 mm in diameter. As is known the best hydrodynamic efficiency occurs when the area ratio between the orifice and the OWC water plane lies in the 1/100 to 1/150 range. The 165 mm turbine meets this requirement. Fig. 3 shows a comparison of the performances of FGV turbines and UDI turbines estimated from steady state tests. The comparison is in terms of the efficiency, output shaft powers and the operating flow coefficient ϕ. Both machines operate at 3000 rpm. A fixed speed of operation is initially considered with an induction generator as an option. It is seen that the UDI turbine has a higher efficiency than the FGV turbine. A more important result is established based on a careful study of Fig. 3. It can be seen that the efficiency of the UDI turbine drops when the pneumatic power increases. One solution to remedy this aspect is to consider a variable speed generator as opposed to a fixed speed one. Accordingly Fig. 4

shows the performance of the UDI for various speeds from 1500 rpm to 3500 rpm. The remarkable result that emerges is that with a variable speed machine, the efficiency can be made to remain at about 0.7 over the entire range of operation from 4 W to 160 W. Further the variation in speed is within the range feasible with doubly fed induction machines or permanent magnet synchronous machines.

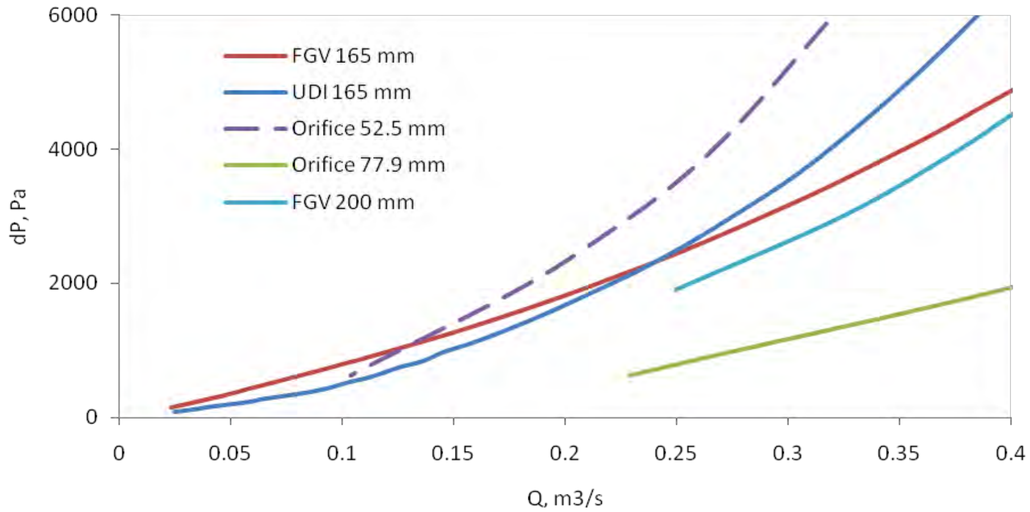

Fig.2: Differential pressure across fixed guide vane impulse turbine and unidirectional impulse turbine for diameter 165 mm for different flow rates (3000 rpm)

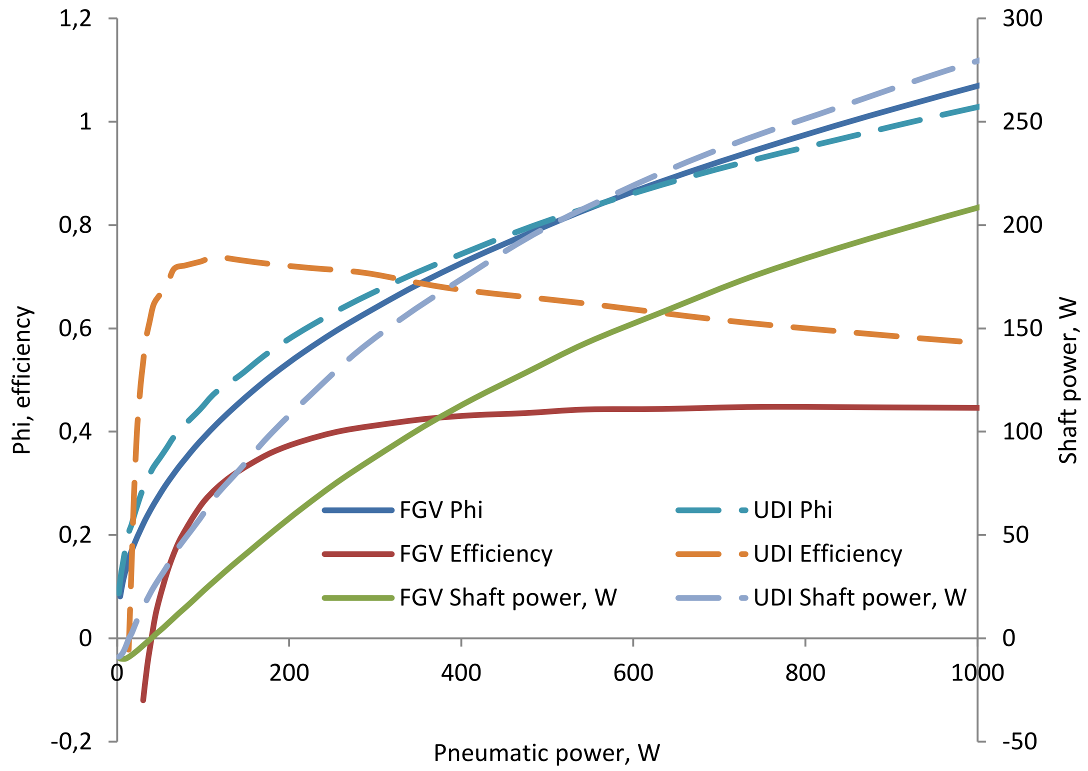

Fig. 3: Comparison of performance of fixed guide vane impulse turbine and unidirectional impulse turbine for diameter 165 mm (3000 rpm)

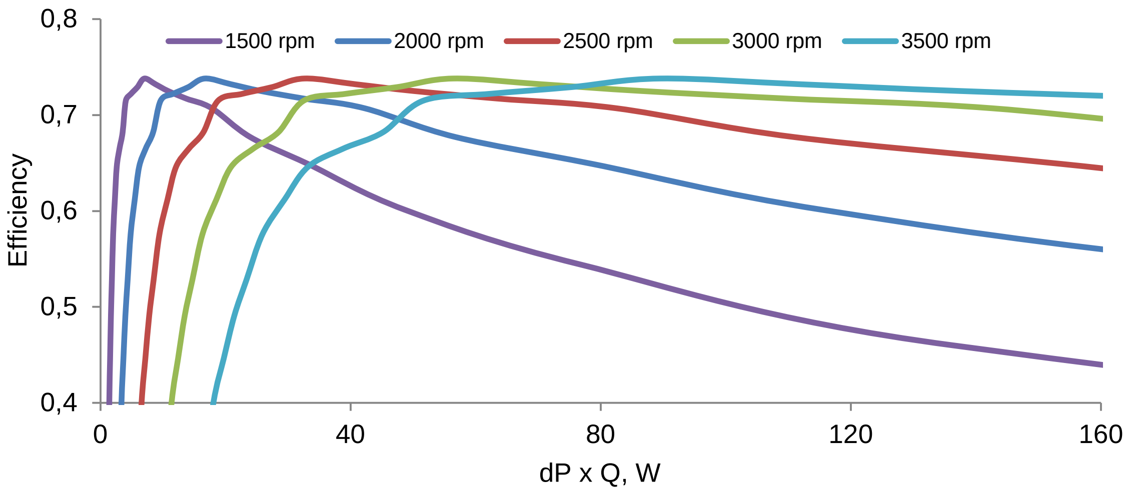

Fig. 4. Estimated performance characteristics for unidirectional impulse turbine of 165 mm diameter over a range of speeds

4. The power module for the BBDB

The prototype BBDB recently made for experiments in Japan had a length of 25 m, breadth of 5.25 m and a draft of 10 m [7]. It could produce a peak output of 30 kW at Hs = 2.25m with a 1.5 m FGV turbine. We now consider the use of a 1.5 m UDI turbine for the same purpose. Fig. 5 shows the comparison. Fig. 5 a compares the shaft output from the two classes of turbines with speeds of 300 rpm and 600 rpm with input powers up to 400 kW. The corresponding efficiencies are shown in Fig 5 b. Fig. 5 b again highlights the importance of variable speed operation for the UDI turbine.

The next section concerns the experimental validation of the UDI concept.

5. Experimental setup for validation of the UDI turbine

The basic experimental setup for oscillatory flow studies was described in [8] wherein it was also shown that induction generators could be used for the power module. In this work a slightly different approach was used. Two pipe sections were independently coupled to the common oscillatory flow rig. One of them housed a 165 mm UDI turbine with a 3000 rpm, 180 V, 375 W dc generator. The other housed an orifice in conjunction with a fluidic diode (bluff body) as shown in Fig. 6. This was to ensure the matching of the turbine damping to that of an appropriate orifice and also to ensure that the intake stroke provides flow to the orifice and the exhaust stroke vents air through the turbine. It can be appreciated that several basic experiments on the performance of various shapes of fluidic diodes could also be tested with this arrangement. In effect it tests the ability of passive fluidic diodes in controlling flow.

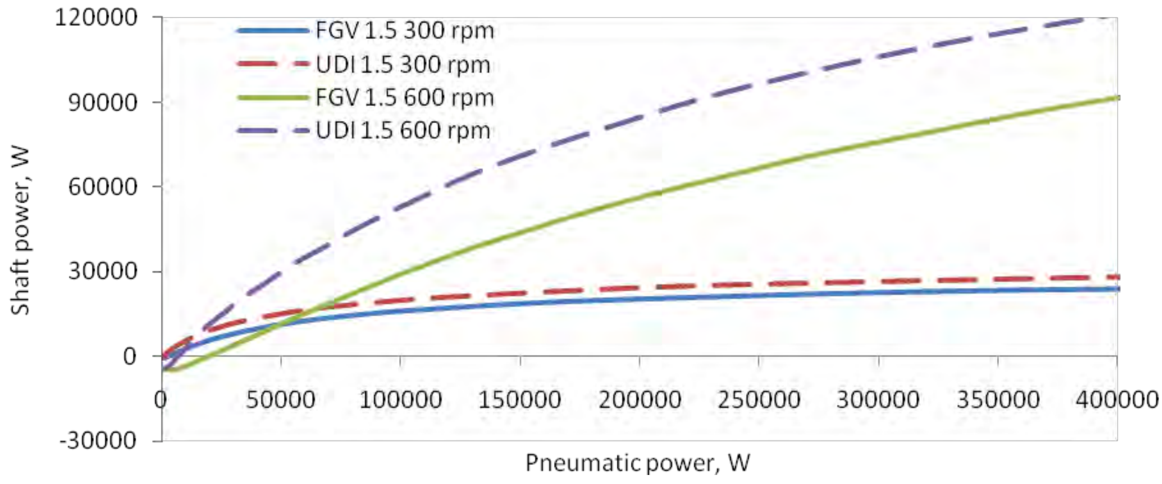

(a)

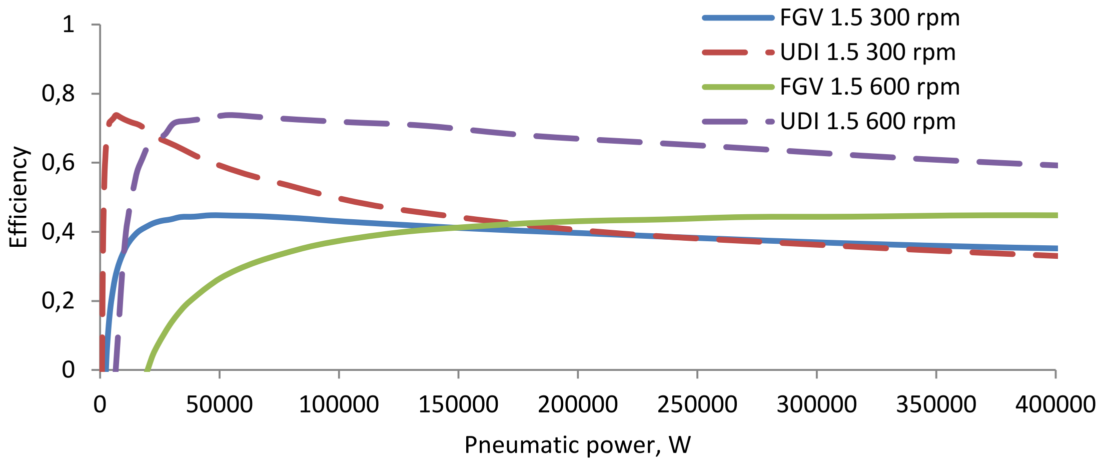

(b)

Fig.5: Comparison of performance of fixed guide vane turbine and unidirectional flow turbine for diameter = 1.5 m for different speeds

Figure 6 presents the comparison of the performance of a FGV turbine of diameter 1.5 m presented in [7] with the estimated performance of a UDI turbine of the same diameter. It can be noted that the variable speed UDI turbine can deliver up to 20 to 30 % more power over FGV turbine. Also the overall wave to wire efficiency of the BBDB with UDI turbine is higher for the entire range of operation.

The quantities measured were pressure across the impulse turbine and the orifice, the turbine inlet duct pressure, the turbine speed, the generator voltage, load current.

Pressure measurements

The differential pressure across the turbine and orifice were measured using calibrated differential pressure transmitters (STD 120) made by M/s. Honeywell.

Voltage and Current measurements

The generator terminal voltage was measured using voltage transducers made by M/s. LEM. The load current was measured using current sensors by M/s. LEM, USA. All of these devices were calibrated before use, with accuracies better than 1%.

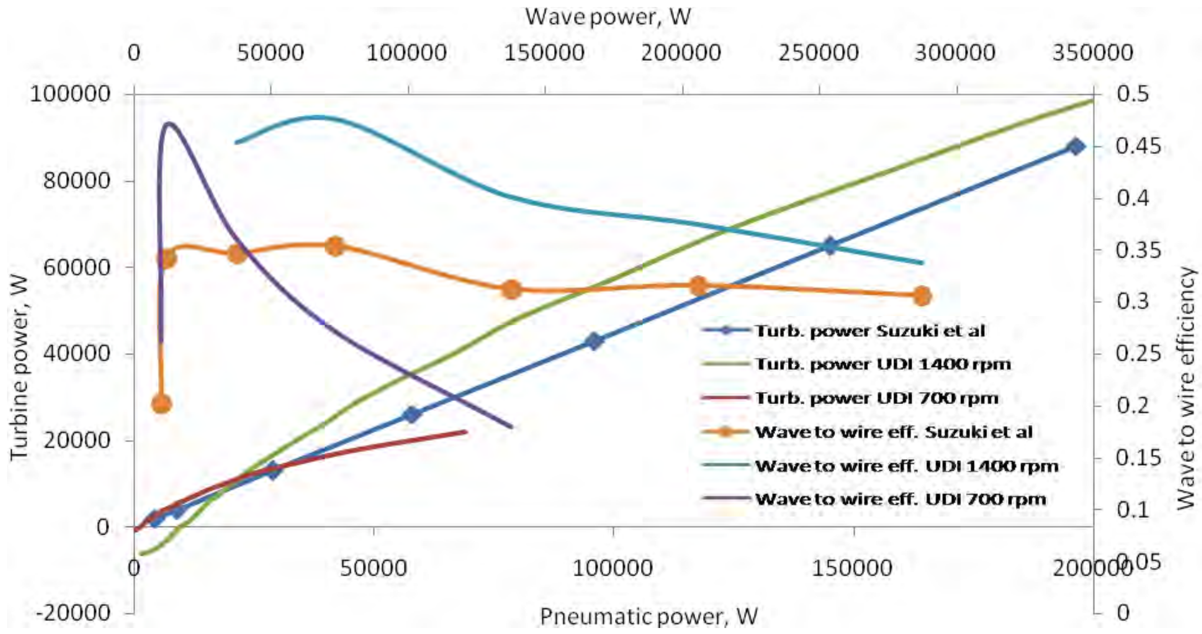

Fig. 6: Estimated power output of a 1.5 m diameter unidirectional impulse turbine

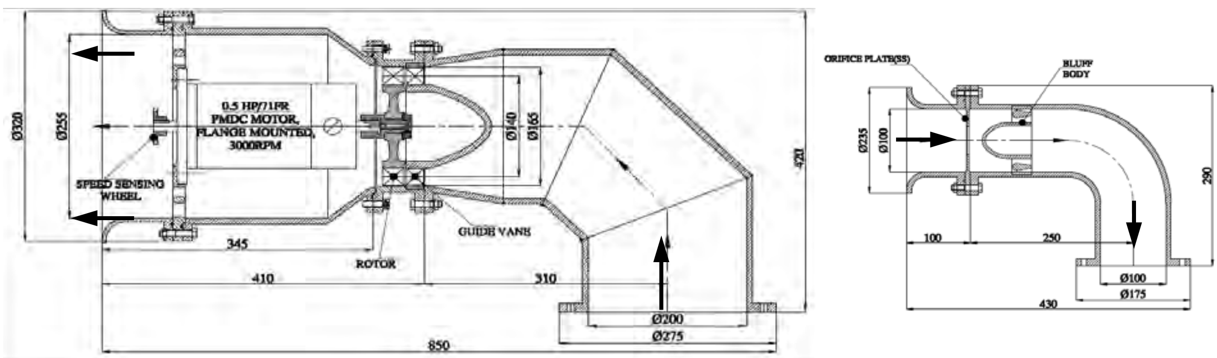

(a) (b)

Fig.7 : 165 diameter unidirectional flow turbine for exhaust and air vent with bluff body for intake

Power and speed

The electrical power was estimated from the generator terminal voltage and load current. The turbine speed was estimated from the generator terminal voltage to within 2% error.

Data acquisition

All the data pertinent to the evaluation were logged by a data acquisition system (DAQ, USB 6215, National Instruments) at 1 kS/s. Low pass filters were employed to remove noise in the signals.

Fig. 8 shows one typical result. It primarily validates the notion of using twin UDI turbines by ensuring appropriate intake and exhaust flow though the turbine and orifice respectively and also quantitatively establishes the efficiency of the turbine. Fig. 8 shows the output from the generator for various stroke lengths of the piston that drives the oscillatory flow. The peak pressure drop observed on the test rig across a 30 mm diameter orifice matched with the peak pressure drop across the turbine.

In effect the experiments and simulation confirm the likely improvements in BBDB performance by replacing the FGV turbine with a UDI turbine.

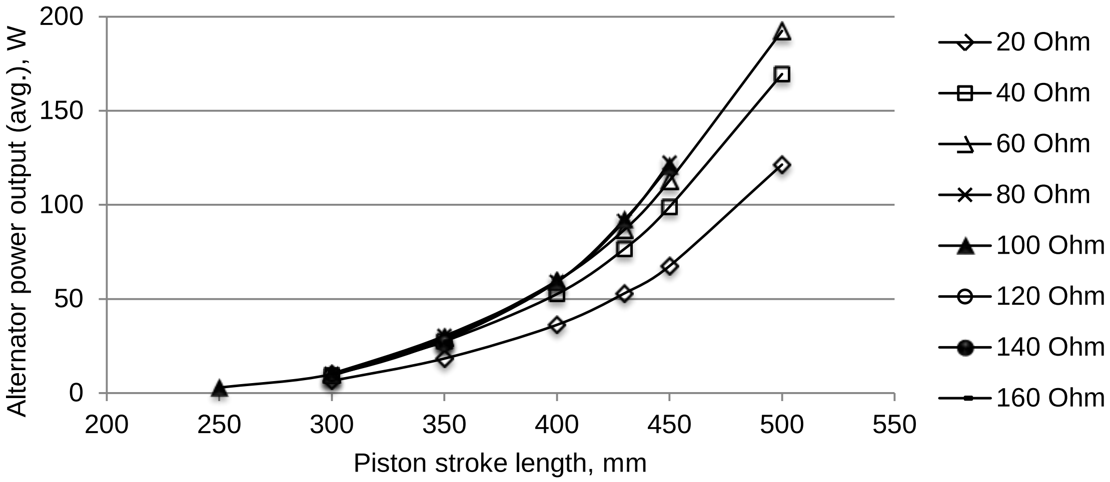

Fig. 8. Average power output of alternator vs. piston stroke length vis-à-vis electrical resistance

6. Conclusions

A power module based on the twin unidirectional impulse turbine topology can substantially improve the efficiency of a BBDB. Experiments on a 165 mm turbine validate the claims of improved efficiency. A 1.5 m turbine can produce about 50 kW in comparison with 30 kW from a fixed guide impulse turbine for the same wave excitation. Variable speed operation is a must in order to retain the high efficiency over the range of operation. There exists a strong case for floating OWCs in several applications involving powers in the tens of kW range.

References

[1] Heath, T., Whittaker, T.J.T & Boake, C.B.; The design, construction and operation of the LIMPET wave energy converter, Wave Energy 2000, 2000

[2] Ohno H., Funakoshi T., Saito K., Oikawa K., and Takahashi S., “Interim report on the Second Stage of Field Experiments on a Wave Power Extracting Caisson In Sakata Port,” *ODEC*, 1993, pp. 173-182.

[3] Marine Energy Challenge: Oscillating Water Column wave energy converter evaluation report, © The Carbon Trust 2005.

[4] Research and development of technology on wave energy utilisation, Jamstec 2004

[5] Masuda Y *et al* “The BBDB an improved floating type wave power device”, Proceedings Ocean 88, pp 1067-1072.

[6] A.G. Pathak, A. Subramaniam, " Performance studies on a scaled model BBDB under regular and random waves ", Proceedings ISOPE, 1999 pp 139-141.

[7] Suzuki *et al* "Performance of OWC type floating wave power plant employing impulse turbine" 3rd International conference on ocean energy, Bilbao, 2010.

[8] Mala K., Jayaraj J., Jayashankar V. et al., "A twin unidirectional impulse turbine topology for OWC based wave energy plants – Experimental validation and scaling," Renewable energy 36, 2011, pp. 307-314.

Impact of tidal stream turbines on sand bank dynamics

Simon P. Neill[1,*], James R. Jordan[1], Scott J. Couch[2]

[1] School of Ocean Sciences, Bangor University, Menai Bridge, UK
[2] Institute for Energy Systems, The University of Edinburgh, Edinburgh, UK
* Corresponding author. Tel: +44 1248 713808, E-mail: s.p.neill@bangor.ac.uk

Abstract: Previous results from one-dimensional model studies have demonstrated that large-scale exploitation of the tidal stream resource could have a significant impact on large-scale sediment dynamics. In this research, we model the impact which such exploitation would have on the dynamics of offshore sand banks. Such banks have an important role in natural coastal protection, since they cause waves to refract and induce wave breaking. As a case study, we examine the Alderney Race, a strait of water between the island of Alderney (Channel Islands) and Cap de la Hague (France). A morphological model is developed, incorporating tidal energy converter (TEC) device operation as a momentum sink in the three-dimensional hydrodynamic module. Through a series of model experiments, we demonstrate the impact which a full-scale (300 MW) TEC array would have on sediment dynamics when sited in the vicinity of headlands and islands. It is important to understand this aspect of the environmental impact of full-scale TEC operation, since headland and island sand banks comprise of readily mobile sediment grain sizes. Therefore, small changes to the tidal regime can have a large effect on the residual sediment transport pathways, and hence sand bank evolution, over the life cycle of a TEC device.

Keywords: *Tidal stream turbines, Tidal energy converter devices, Sediment dynamics, Sand banks, Alderney Race*

1. Introduction

Tidal energy converter (TEC) devices operate by intercepting the kinetic energy in strong tidal currents (typically through a turbine unit). This intercepted energy is then converted to electrical energy through a power take-off system (e.g. an induction generator) and conditioned for dispatch to the electricity network. Theoretically, this is similar to the operation of a typical wind energy device. However, what is significantly different from the wind energy analogy is the environment that TEC devices operate in [1], and the potential for TEC devices to interact with their environment [2]. Given the proliferation of at-sea demonstration devices, the environmental impacts of TEC device operation is a timely issue to consider. The major research questions in the tidal energy context have already been identified [3]. However, progress to-date has been limited in addressing these research issues. The impact of TEC operation on sediment dynamics has yet to be explored in the scientific literature beyond an idealised one-dimensional (1D) model pilot study [4], stimulating the present study.

Extracting energy from a tidal system will lead to an overall reduction in current speed over the larger area domain [2]. This reduction in current speed, even for relatively large TEC array extraction scenarios, is generally quite small. For example, in a tidal channel the impact of energy extraction on current speed U becomes noticeable only when the energy extracted reaches around 10% of the available kinetic energy flux [5], a considerably large amount of energy to extract from a channel. More realistic extraction scenarios (typically 1% of the available kinetic energy) could therefore be perceived to have very little environmental impact. However, bed shear stress is a function of U^2. Therefore, small changes in the tidal currents could potentially lead to large changes in the resulting bed shear stress. Further, the transport of sediments is proportional to an even higher power of velocity than bed shear stress, e.g. total load transport by currents (bedload and suspended load) is a function of $U^{2.4}$

[6]. Therefore, relatively small changes to the residual flow field due to exploitation of the tidal stream resource could have a significant effect on the transport of sediments. This has been reported in a 1 D idealised study of the Bristol Channel (UK), where the morphodynamics were significantly impacted 50 km from the site of energy extraction [4]. In the case of a simple tidal channel or an estuary, much insight can be gained from such 1D model studies, since much of the flow is similarly 1D. However, for more complex situations such as flow past islands and headlands, two- or three-dimensional (2D or 3D) models are required to predict and understand the complexity of the flow field and estimate the impacts of energy extraction.

Strong tidal flow past headlands and islands leads to the generation of large eddy systems, with an opposite sense of vorticity between the flood and ebb phases of the tide [7]. Sand banks form either side of such headlands due to a b alance between the outward-directed centrifugal force and the inward-directed pressure gradient within the eddies [8], leading to a convergence of relatively coarse sand as a function of the instantaneous tidal currents (Fig. 1). The sand banks which form as a result of this convergence can be up to 10 km in length, and have an important role in coastal defence (since offshore banks affect both wave refraction and breaking), and can be a strategic source of marine aggregates. Regions of strong tidal flow past headlands and islands have been listed as potential sites for the exploitation of the tidal stream resource, such as Portland Bill in the English Channel [9], and flow past the island of Alderney in the Channel Islands [10]. The aim of this study is to determine how such exploitation in the vicinity of headlands and islands would affect the maintenance of the associated sand banks. This is addressed through the investigation of a modelling case study: the Alderney Race.

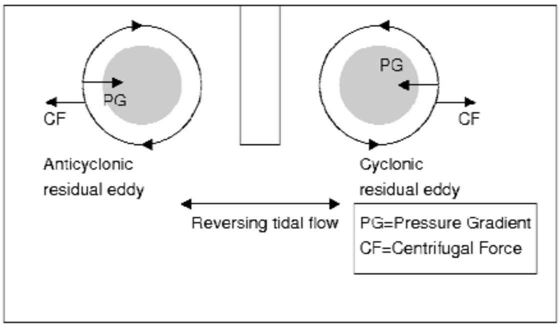

Fig. 1. Headland or island sand bank formation. Reversing tidal flow past the headland or island leads to the generation of eddy systems with an opposite sense of vorticity between the flood and ebb phases of the tide. The outward-directed centrifugal force within each eddy is balanced by an inward-directed pressure gradient. This leads to the inward movement of relatively coarse sediment near the bed (where the centrifugal force is weaker due to bed friction), and the formation of headland or island sand banks. Grey shading indicates the location of sand banks.

2. The Alderney Race

The Alderney Race is a 15 km strait of water separating the island of Alderney (Channel Islands) and Cap de la Hague in France (Fig. 2). With a mean spring tidal range of around 6 m and mean spring tidal currents exceeding 2.5 m/s [11], the Alderney Race presents one of the most hostile environments within the northwest European shelf seas. However, over 20 km^2 of the Race has a w ater depth in the range of 25-45 m, the typical depth range suitable for practical TEC device operation [1] which, in conjunction with consistently high current speeds, represents one of the best opportunities in the world for large-scale exploitation of the tidal stream resource. This opportunity has been recognized by the formation of the Alderney

Commission for Renewable Energy (ACRE), with powers to regulate the operation of marine energy in the territorial waters of Alderney (www.acre.gov.gg). Using current technology, the practical exploitable annual energy output for the Alderney Race has been estimated as 1340 GW h at a rated turbine array capacity of 1.5 GW [10], and a large portion of this energy is contained within the three nautical mile territorial limit of Alderney.

To the south of Alderney there are a series of sand banks known as the South Banks (Fig. 2). The scale of these banks is substantial, 4 km in length and covering an area of seabed around 3 km^2. Hence, the sand banks are important to the economy of Alderney in terms of offering natural coastal protection, as a potential strategic source of marine aggregates, and as a hazard to navigation. The South Banks are maintained by recirculating tidal flows in the lee of Alderney during the ebb phase of the tide (as described in Section 1) and, despite some degree of interannual variability (primarily due to the stochastic nature of waves and wind-driven currents), have persisted in more-or-less their current configuration for several thousand years.

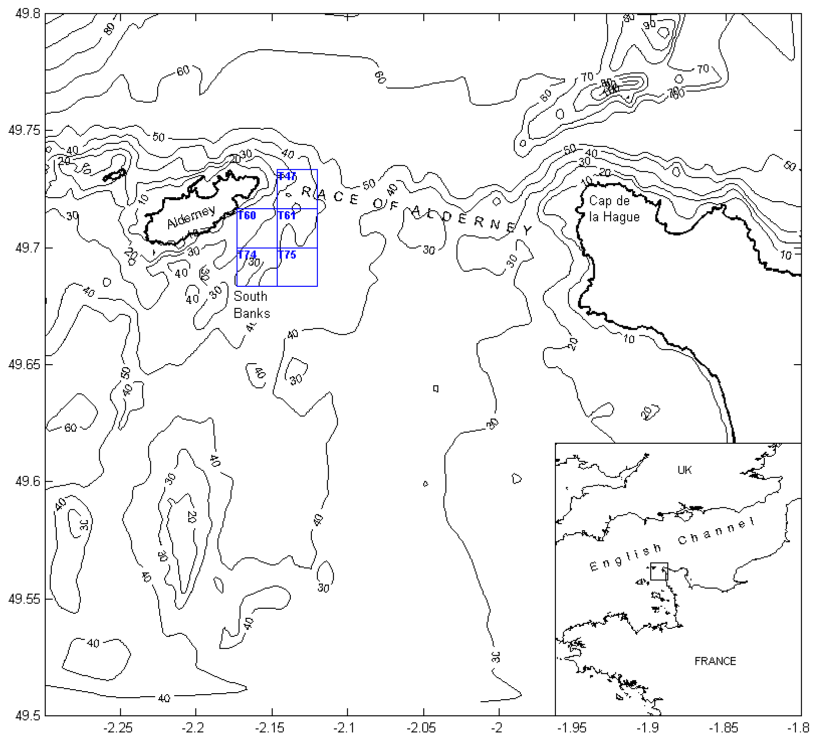

Fig. 2. Bathymetry of the Alderney Race and surrounding waters. Contours are water depths (in metres) relative to mean sea level and squares (labeled T47, T60, T61, T74 and T75) are regions (or blocks) identified by the Alderney Commission for Renewable Energy for exploitation of the tidal stream resource. For scale, the side length of each block is 1 nautical mile (1.85 km). The inset shows the location of the Alderney Race relative to the UK and France.

The ACRE has sub-divided the territorial waters of Alderney into 96 regions, or blocks. Detailed hydrographic and geophysical surveys have been carried out for blocks T60, T61, T74 and T75 (Fig. 2), and it is therefore assumed that these blocks would be developed first if the proposed tidal energy project were to proceed. However, block T47 is of particular interest to the present study since (a) it contains the highest velocities in the western part of the Alderney Race (Section 3), and (b) this location is close to the point of maximum vorticity due to tidal flow past the island. Hence, tidal currents in block T47 have a major controlling influence on the maintenance of the South Banks.

3. The Numerical Model and Baseline Results

Bathymetry for the study region was digitised from Admiralty Charts and interpolated onto a model grid with a horizontal resolution of approximately 150 m, and with 6 terrain-following (sigma) layers in the vertical. The boundary conditions were extracted from a larger area model of the northwest European shelf seas which had a resolution of 1/6° longitude × 1/9° latitude. The 3D POLCOMS model [12] was applied to the Alderney model configuration over a spring-neap cycle, using the dominant semi-diurnal tidal constituents, M_2 and S_2, as boundary conditions. The model of the Alderney region was successfully validated in terms of the magnitude and phase of the M_2 (lunar) and S_2 (solar) elevations at three stations taken from the Admiralty tide tables, and for the magnitude and phase of tidal currents at the location of four tidal diamonds taken from the Admiralty Chart of the region.

3.1. Baseline Results

The model was applied initially to a natural baseline case, in order to understand the residual currents and sediment transport pathways in the absence of artificial energy extraction. The residual currents for a spring-neap cycle are plotted in Fig. 3. Clearly, there are two large residual eddies in the vicinity of Alderney: one due to the ebb currents and one due to the flood currents. The former eddy (to the south of Alderney) is approximately centered over the South Banks, confirming the convergent process which maintains this sand bank (Section 1). Taking a median sediment grain size of 300 μm (medium sand) as representative of the region, the residual sediment transport over a spring-neap cycle is shown in Fig. 4, based on calculations of the total load transport [6]. Although the residual sediment transport vectors are similar to the residual flow field (Fig. 3), there are distinct differences. In particular, the residual sediment transport to the east of Alderney is predominantly directed southwards, partially explaining why the dominant sand bank of the region forms to the south of Alderney, with no corresponding sand bank associated with the residual eddy to the north[1].

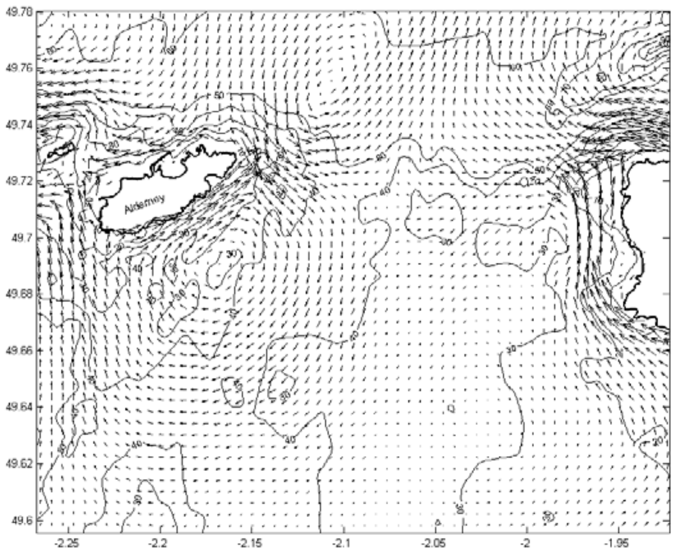

Fig. 3. Modelled residual tidal currents in the Alderney Race for baseline case (no artificial energy extraction). Contours are water depths (in metres) relative to mean sea level. For clarity, every third modelled vector has been plotted in both the x- and y-directions.

[1] In addition, there is a distinct asymmetry in the ambient water depths to the north and south of Alderney.

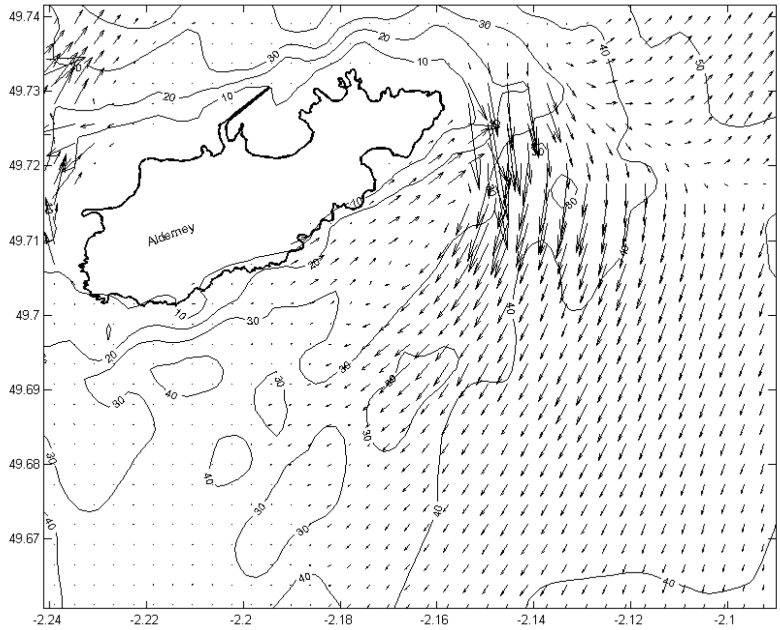

Fig. 4. Residual sediment transport around Alderney for baseline case (no artificial energy extraction). Contours are water depths (in metres) relative to mean sea level. For clarity, every second modelled vector has been plotted in both the x- and y-directions.

4. Energy Extraction

A momentum sink was incorporated in the 3D POLCOMS model code, with turbine characteristics parameterised from an OpenHydro turbine (with a 15 m d iameter), the preferred technology supplier for Alderney Renewable Energy (ARE) (http://www.are.gb.com/technology-developers.php). Details of the OpenHydro power curve were taken from Bedard et al. [13], with a cut-in speed of 0.7 m/s, a rated power of 1.5 MW (at 2.57 m /s), and an assumed efficiency (at the point of extraction) of a constant 35%. Applying a minimum lateral spacing of 3 turbine widths and a minimum downstream spacing of 15 turbine widths to eliminate lateral and wake effects, respectively (e.g. [10]), a simple rectangular array of 200 OpenHydro devices (i.e. a 300 M W array) can easily be accommodated by each of the 1.85 × 1.85 km development blocks marked in Fig. 2. In this study, simulations were performed only for blocks T47 and T60.

4.1. Energy Extraction Results

The results are presented in this section as difference plots, i.e. the difference between each of the artificial energy extraction simulations *minus* the baseline simulation. In the region of energy extraction, the magnitude of mean velocity was reduced by around 0.05 m/s for each of the energy extraction scenarios (T47 and T60) (Fig. 5). The reduction in velocity was not localised to the turbine array, but extended a distance of up to 10 km from the array. Despite local reductions in the magnitude of velocity, the far-field velocity was increased by a similar magnitude (0.05 m/s), particularly to the northwest of Alderney. Changes to the sediment transport followed a similar pattern to velocity (Fig. 6). The instantaneous predictions of sediment transport were applied to a 2D continuity equation to predict the change in bed level over the 30 year life-cycle of a TEC device (Fig. 7). Again, the morphodynamic impact was non-localised, with bed level changes of about a metre occurring over a 30 year period. However, the most important result in terms of the main aim of this study is that a 300 MW TEC array would have a negligible impact on the morphodynamics of the South Banks, maintained by recirculating tidal flows in the lee of the island. However, the morphodynamics of the region will be significantly altered by such large-scale exploitation of the tidal stream resource, and this effect will be evident up to 10 km from the point of extraction.

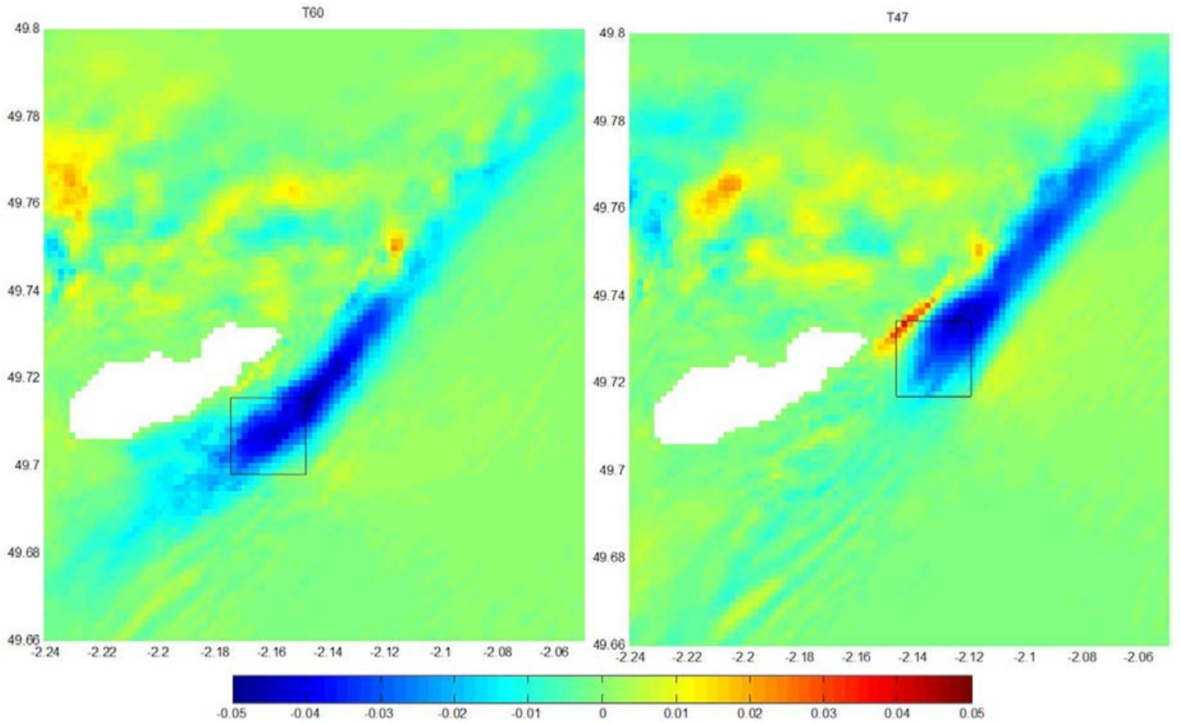

Fig. 5. Change in the magnitude of velocity (in m/s) due to energy extraction, averaged over a spring-neap cycle. Boxes show the limits of the TEC array for each case (T60 and T47).

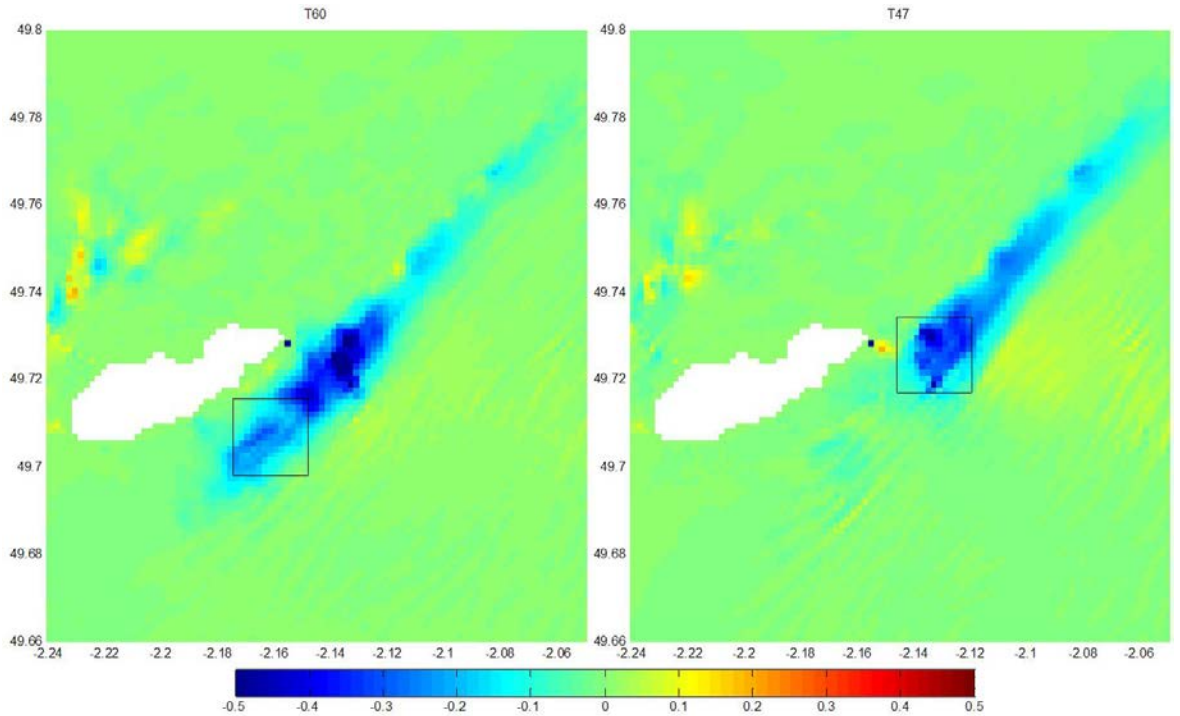

Fig. 6. Change in the magnitude of sediment transport for medium sand due to energy extraction, averaged over a spring-neap cycle. Boxes show the limits of the TEC array for each case (T60 and T47).

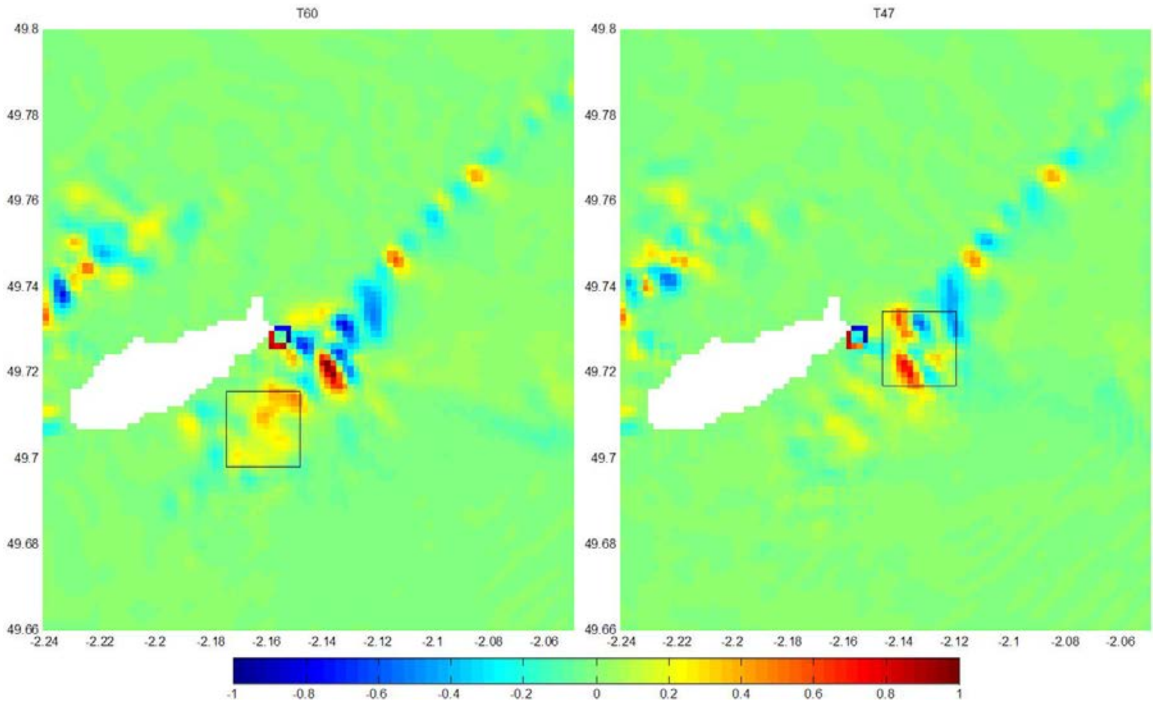

Fig. 7. Change in bed level (in metres) due to energy extraction, extrapolated to the 30-year life-cycle of a TEC device. Boxes show the limits of the TEC array for each case (T60 and T47).

5. Discussion and Conclusions

Strong tidal flow past islands and headlands leads to the generation of island wakes and headland eddies, and the formation of associated sand banks. Such strong tidal flows past islands and headlands are attractive regions in which to exploit the tidal stream resource. This study has demonstrated that despite extracting a relatively large amount of energy from the tidal streams in the vicinity of an island (a rated 300 MW TEC array), little change to the morphodynamics of the sand bank (formed by recirculating tidal currents in the lee of the island) occurs. This result is insensitive to the location of the TEC array in relation to the island. However, over the 30 year life-cycle of a TEC device, the morphodynamics of the surrounding region will change by up to a metre with such large-scale exploitation of the tidal stream resource.

References

[1] S.J. Couch and I.G. Bryden, Tidal current energy extraction: hydrodynamic resource characteristics, Proceedings of the Institution of Mechanical Engineers, Part M: Journal of Engineering for the Maritime Environment 220, 2006, pp. 185-194.

[2] S.J. Couch and I.G. Bryden, Large-scale physical response of the tidal system to energy extraction and its significance for informing environmental and ecological impact assessment, In: Proceedings Oceans 2007-Europe International Conference; 2007. pp. 912–916.

[3] The Robert Gordon University, A scoping study for an environmental impact field programme in tidal current energy, DTI Publication URN 02/882, 2002.

[4] S.P. Neill, E.J. Litt, S.J. Couch and A.G. Davies, The impact of tidal stream turbines on large-scale sediment dynamics, Renewable Energy 34, 2009, pp. 2803-2812.

[5] S.J. Couch and I.G. Bryden, ME1 - marine energy extraction: tidal resource analysis, Renewable Energy 31, 2006, pp. 133-139.

[6] R. Soulsby, Dynamics of marine sands, Thomas Telford, 1997, pp. 176.

[7] I.S. Robinson, Tidal vorticity and residual circulation, Deep-Sea Research 28, 1981, pp. 195-212.

[8] R.D. Pingree, The formation of the Shambles and other banks by tidal stirring of the seas, Journal of the Marine Biological Association of the United Kingdom 58, 1978, pp. 211-226.

[9] W.M.J. Batten, A.S. Bahaj, A.F. Molland, J.R. Chaplin and Sustainable Energy Research Group, Experimentally validated numerical method for the hydrodynamic design of horizontal axis tidal turbines, Ocean Engineering 34, 2007, pp. 1013-1020.

[10] L. Myers and A.S. Bahaj, Simulated electrical power potential harnessed by marine current turbine arrays in the Alderney Race, Renewable Energy 30, 2005, pp. 1713-1731.

[11] H.M. Pantin, The sea-bed sediments around the United Kingdom: their bathymetric and physical environment, grain size, mineral composition and associated bedforms, British Geological Survey Report SB/90/1, 1991, 47 pp.

[12] J.T. Holt and I.D. James, An s coordinate density evolving model of the northwest European continental shelf: 1 m odel description and density structure, Journal of Geophysical Research 106, 2001, pp. 14,015-14,034.

[13] R. Bedard, M. Previsic, O. Siddiqui, G. Hagerman and M. Robinson, Survey and Characterization of TISEC Devices, report number TP-004-NA, EPRI, pp. 56-64.

Experimental and numerical results of rotor power and thrust of a tidal turbine operating at yaw and in waves

Pascal W. Galloway[1,*], Luke E. Myers[1], AbuBakr S. Bahaj[1]

[1] *Sustainable Energy Research Group, School of Civil Engineering and the Environment, University of Southampton, Southampton, SO17 1BJ, UK.*
**Corresponding Author Tel +44(0)23 80595458, E-mail: P.W.Galloway@soton.ac.uk*

Abstract: Little has been done to investigate the behaviour of Marine Current Energy Converters (MCECs) in unsteady flow caused by wave motion and yaw. The additional loading applied to the rotor through the action of waves and whilst operating at yaw could dictate the structural design of blades as well as the proximity to the water surface. The strongly bi-directional nature of the flow encountered at many tidal energy sites may lead to devices employing zero rotor yaw control. Subsequent reductions in device capital cost may outweigh reduced power production and increased dynamic loading for a rotor operating at yaw. The experiments presented in this paper were conducted using a 1/20th scale 3-bladed horizontal axis MCEC at a large towing tank facility. The turbine had the capability to measure thrust and torque via a custom waterproof dynamometer. A BEM (Blade Element Momentum) code developed within the university was modified to include wave and yaw, with a view to further understanding the primary loading upon the rotor and individual blades.

Keywords: *marine current energy converter, wave-current interaction, strain gauge, loading*

1. Introduction

One of the enduring topics of interest in the field of coastal and offshore engineering is that of wave-current interactions and their effect on static and dynamic structures. The co-existence of waves and currents is a common feature in the marine environment [1]. Waves are strained and refracted by currents, causing exchanges of mass, momentum and energy to occur between the waves and mean flow [2]. The main energy in the coastal region can be attributed to tides, surges and wind waves. Interactions occur between these different 'waves' because the tides and surges change the mean water depth and current field experienced by the waves [3]. The usual approach to the interaction problem has been to ignore the interaction between waves and currents and simply add the two together (using their particle velocity vectors) so as to calculate the forces on a body [4].

Marine Current Energy Converter (MCEC) technology is currently at the prototype stage where unique devices are being deployed at specific sites or marine energy testing centers. There is little detailed knowledge of the flow field properties at highly energetic tidal energy sites [5]. Generally peak flow speeds are measured but the effect of wave and bed generated turbulence is neglected. The effect this will have on MCECs is unclear, which may lead to prototype devices being installed at sheltered locations where these effects are minimised [5]. If this becomes a trend with developers it may result in reduced energy capture as blade diameters are constrained and potentially higher energy flows are not utilised. MCECs of a given rated power typically experience four times the thrust of a wind turbine of the same rated power, even though the MCEC will be significantly smaller in diameter. Thus it is expected that rotor loading and general structural integrity could be significant for MCEC devices. Therefore the need to quantitatively assess the blade/rotor loading caused by wave-current interaction is clear. At present, few experimental wave-current studies have been conducted in the presence of MCECs. One particular study combined Blade Element Momentum (BEM) theory for wind turbines and linear wave theory to predict rotor torque and thrust and to assess the influence of waves on the dynamic properties of bending moments at the root of rotor blades [6]. The outcomes were limited, particularly those for the blade loading. In the field, research carried out at the European Marine Energy Centre showed that in a water depth of 45m, wave effects penetrated as far down as 15m whilst turbulence from the bottom boundary layer penetrated up as much as 17m. This resulted in approximately a third of the water column remaining relatively tranquil [7]. If blade loading in the more turbulent regions could be quantified then this may allow for greater energy capture from larger diameter rotors.

2. Methodology

2.1. Towing Tank Experiment

The experiments presented in this paper were conducted in a wave/towing tank (60m long x 3.7m wide x 1.8m deep). A 1/20th - scale tidal turbine model (see Fig.1) was equipped with the capability to measure rotor thrust and torque (utilising a waterproof dynamometer) and rate of rotation (via optical sensors). The parameters varied included: TSR (tip-speed-ratio), turbine yaw and turbine submergence depth. The blades utilised a NACA 48XX profile with varying thickness and twist along the chord length. The waves used had a height of 0.1m and a 1.34s intrinsic period; current speed was 0.9ms^{-1}.

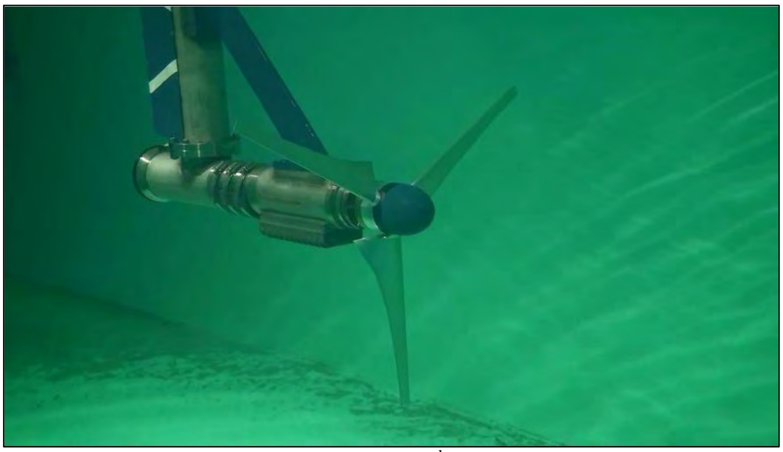

Fig. 1. Underwater photo of 1/20th scale tidal turbine model

The design of the thrust-torque dynamometer utilised for this work is discussed previously [8] and was based on the extensive work carried out by Molland and Turnock [9] for their research on ship propellers. A wireless telemetry system located inside the turbine nacelle collected filtered and amplified signals from the strain gauges before data was conveyed above the waterline via a s ealed umbilical cable. The model turbine is a F roude scaled representation of a 16m diameter MCEC. The maximum scaled current speed would be 4m/s, which is significant for a suitable MCEC location; however it is significantly lower than the maximum current speed of 8.55m/s used in the experiments conducted by Barltrop [6]. High velocities tend to be used in turbine experiments because a low Reynolds number can degrade the dynamical properties of the airfoil and can be a source of irregularity between the experimental data and simulation data [6]. Laboratory experiments are useful for approximating these wave-current phenomena since little detailed knowledge exists for tidal energy sites since there has never before been the need for such data [5]. The problem is that the use of a towing tank results in no actual Doppler shift in the waves because there is no real current present (see section 2.2). More complex facilities such as a circulating water channel with wave-making facilities would be more representative; however depths would need to be at least 2m with the ability to generate waves from a range of directions relative to the current.

2.2. Numerical Model

Numerical modelling has shown that the influence of waves complicates the flow with its influence being more than just adding turbulence. The dynamic part of the waves causes significant oscillations in the power and thrust, which in-turn influence the 'quality' of the electrical power production. High frequency oscillations (known as flicker) occur. It is thought that this flicker is caused by variations of the angle of attack under the influence of wave motion [10]. The nature of wave-current interaction is complex: If a current encounters a wave in the same flow direction, the wave height decreases with an increase in wavelength, whilst the current speed increases. The opposite is true if the current encounters a wave in the opposite flow direction [3].

A Doppler shift is observed when surface waves and current velocities interact. The primary effect of a current is to change the frequency of the waves due to a Doppler shift. The observed angular frequency, ω, of the ωaves in a frame of reference moving ωith the current, σ, the intrinsic angular frequency and the wave number, k, is given by:

$$\omega = \sigma + kU \quad (1)$$

This relationship describes how the observed wave frequency reduces or increases based on current velocity. A Doppler shift is valid in the case of a constant current, but a more complex effect is noted in the case of sheared currents. Use of linear wave theory superimposed on a uniform current does not give a strictly accurate representation of wave-current interaction effects. It is however a straightforward approach and may yield adequate results for a MCEC. Linear wave theory has been found to be a fairly accurate representation of wave-current interaction in depths of water greater than 12.5m and with significant wave heights lower than 5m for the purposes of dispersion [3].

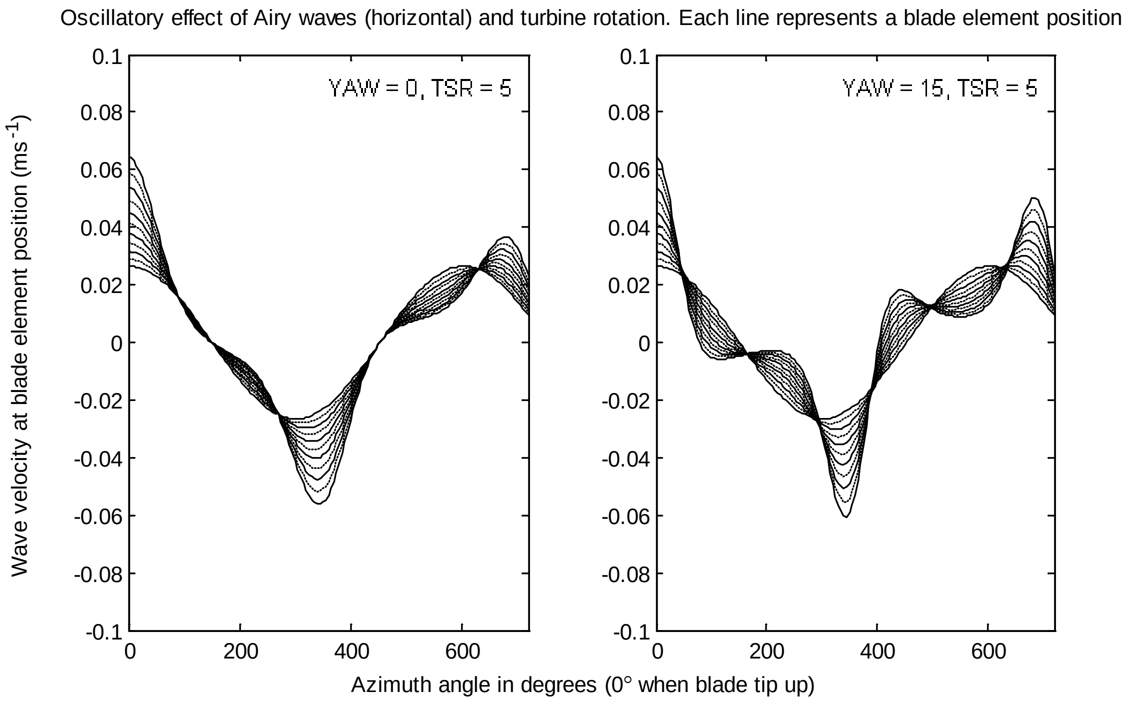

Fig. 2. 1st order wave-current interaction velocities as seen at individual blade elements over two revolutions. The left figure is for zero yaw, the right figure is for 15° yaw. The largest oscillations can be observed at the outer element i.e. at X=1, the tip of the blade (X = elemental radius/blade radius)

It is well known that BEM theory is commonly used by wind turbine designers for predicting loads and power outputs for wind turbines. Although this theory is readily applicable to MCECs there are some differences. Wind for example does not have a characteristic property that resembles wave-current interaction; therefore this must be taken into account when designing prototype MCECs. A BEM code has been modified to include the effect of monochromatic waves on a uniform current with the inclusion of yawed flow if desired. The model assumes that there is no distortion to the incoming flow field or lateral velocity variation and that rotor speed is constant. An example of the wave velocities observed at a single blade can be seen in Fig.2. These velocities are calculated using linear wave theory with a D oppler shift. Based on BEM geometry, these velocities are then calculated instantaneously at each blade element for a given TSR and yaw angle. This output then feeds directly into the BEM code (see Fig.3 for an outline of the numerical model).

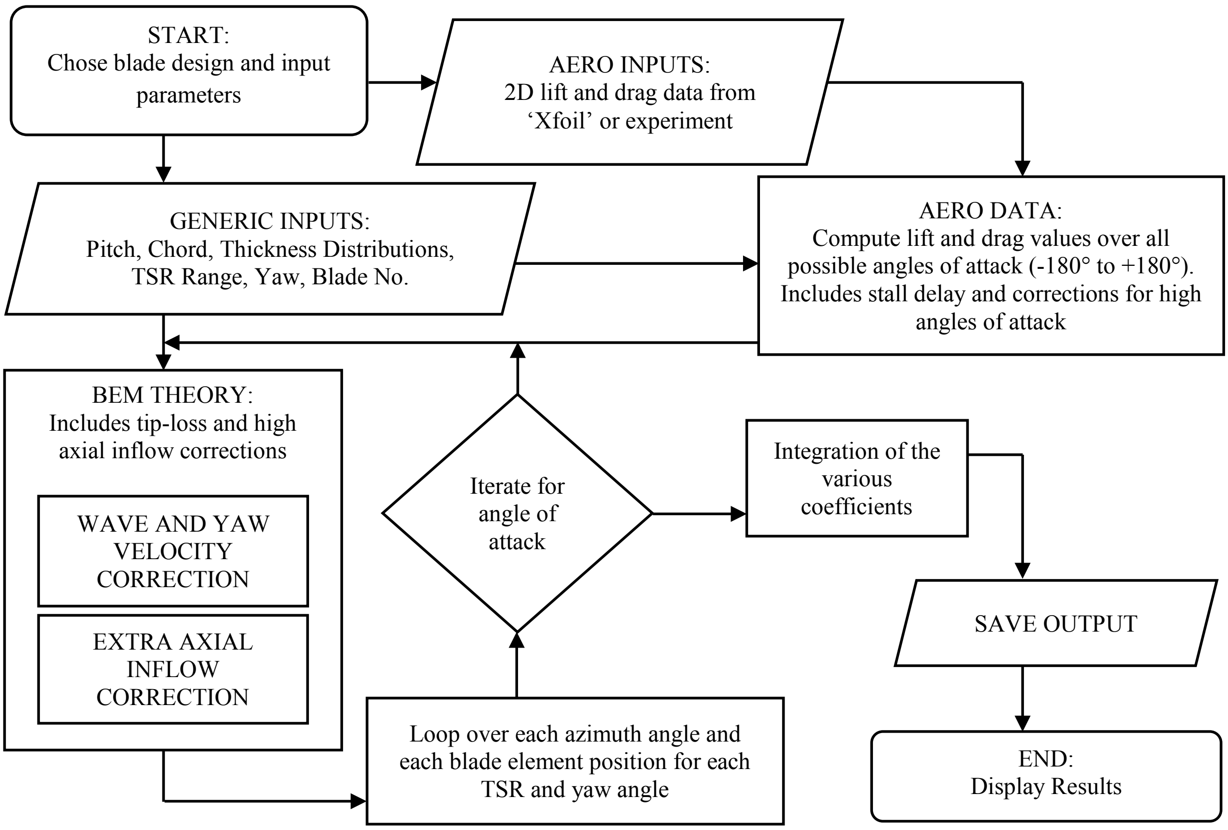

Fig. 3. Flow diagram for BEM numerical model showing the processes involved

3. Results and Discussion

The model MCEC (Fig.1) was used to acquire measurements of thrust, torque and rotor speed for both yawed and wave environments. Fig.4 shows the comparison between experimental data and numerical model for a yawed and un-yawed case. Blockage corrections by Barnsley and Wellicome [11] have been applied to the data. This is a requirement since measurements tend to be over predicted in relatively narrow channels (blockage is ~7%). Figures 5-8 are for a NACA 63-8XX blade, used for comparison with Bahaj et al. [12]. Results show good agreement, which when viewed alongside Fig.4, gives some confidence that the numerical model is valid. No figure is included to show the effect of waves on mean C_P and C_T because the resulting mean wave velocity at the rotor is approximately zero.

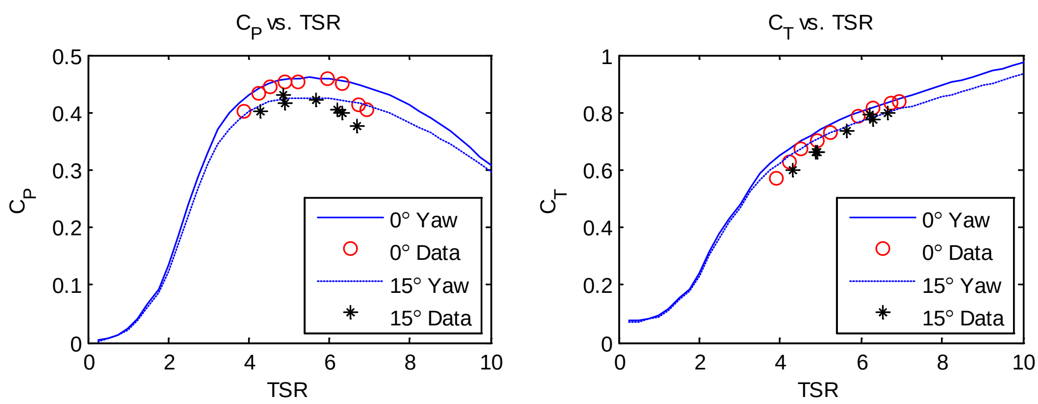

Fig. 4. Left: Power coefficient (CP) vs. TSR for 0° yaw and 15° yaw with experimental data included for comparison. Right: Thrust coefficient (CT) vs. TSR for respective yaw angles

The effect of waves is pronounced when investigating the azimuthal variation of C_P and C_T however, and has serious implications for the fatigue loading of blades as shown in Figures 5 and 6. A few of the parameters used in BEM are shown in these figures and the range over which they vary is represented by the plot line thickness. In Fig.5, the gradient of C_P is calculated using several of the other variables shown in the figure, amongst others. At zero gradient, C_{P_MAX} occurs at 85% blade radius, which is also the region of maximum power variation. This model assumes constant rotor speed which is unlikely to occur in reality. The variations seen in the angle of attack are likely to cause acceleration and deceleration of the rotor which may lead to a greater range of C_P.

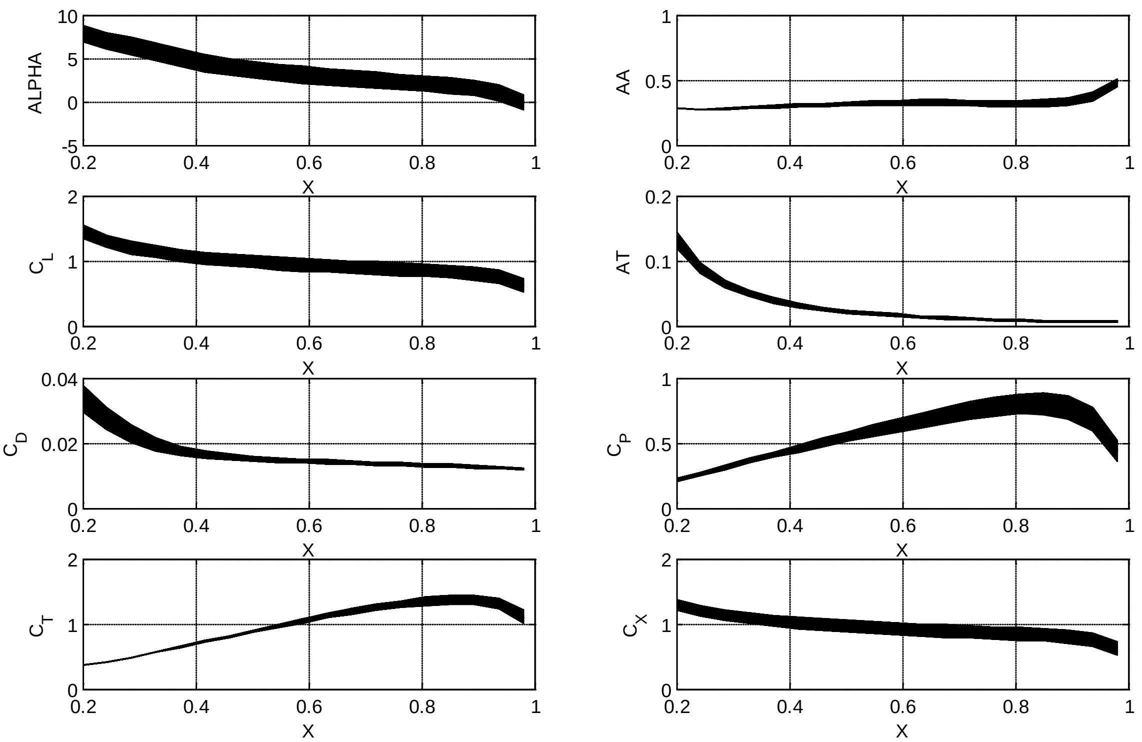

Fig. 4. Plots showing change in Alpha (angle of attack), C_L (lift coeff'), C_D (drag coeff'), AA (axial inflow factor), AT (tangential inflow factor), C_P (power coeff'), C_T (thrust coeff'), C_X (axial force coeff') across the blade span. Line thickness in each plot shows the effect of azimuthal variation. Only small waves are shown here. TSR = 6, Yaw = 0°

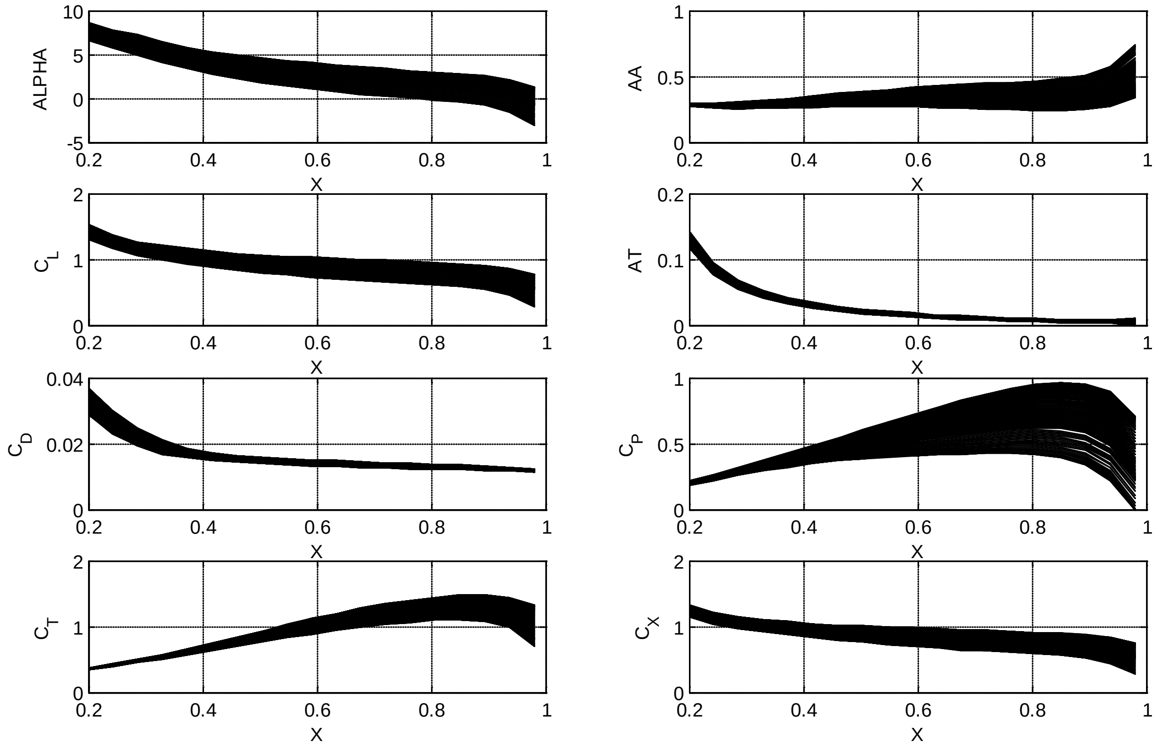

Fig. 5. See Fig.5 for description. Small waves and 15° yaw are shown here. TSR = 6, Yaw = 15°

This vindicates the concerns of flicker due to varying angle of attack (see section 2.2); since high frequency oscillations in voltage, caused by rapid changes in rotor speed, can lead to flicker in the power.

When a turbine is yawed to the flow, both power and thrust are reduced (see Fig.4). This is only apparent above 7.5° yaw with an approximate 20% power reduction at 22.5° yaw [8]. This is a noticeable difference and is likely to be higher than the 20% suggested because the rotor experiences a reduced effective velocity in yawed flow, hence reduced TSR.

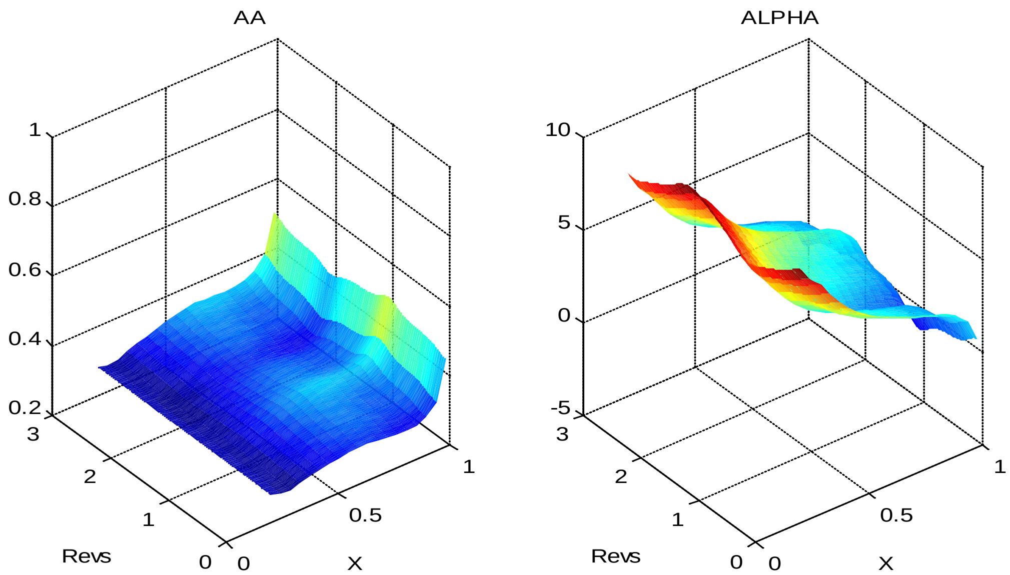

Fig. 6. Surface plots showing axial inflow factor and angle of attack from Fig.5 varying with blade radius and azimuth (3 revolutions)

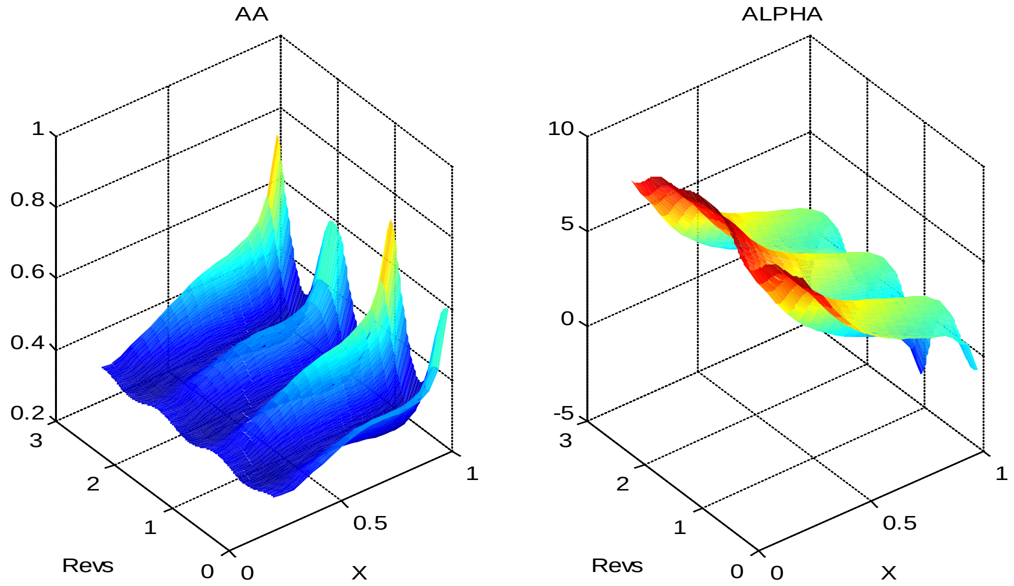

Fig. 7. Surface plots showing axial inflow factor and angle of attack from Fig.6 varying with blade radius and azimuth (3 revolutions)

The inclusion of yaw dramatically increases the range over which some of the parameters vary (see Fig.6). CP in particular varies ~3 times more at 85% blade radius for 15° of yaw. Surface plots in Figures 7 and 8 have been included to show how the axial inflow factor and the angle of attack vary over 3 blade revolutions, with and without yaw (15°). It should be noted that in Fig.8, the waves have less influence than yaw in the power producing region of the blade. This is an important point because the yaw effect can easily be avoided with the use of a yaw drive.

4. Further Work

This research is ongoing and further work will include more detailed experiments including additional testing at yaw into waves and measurement of individual blade loading. When the effects of linear theory have been properly evaluated, the next phase of testing will be to verify findings using waves on a non-uniform current. Barltrop [6] showed that the bending moments at roots of MCEC blades were found to fluctuate significantly; 50% of the mean value for out-of-plane bending moments and 100% of the mean value for in-plane bending moments. This justifies the need for individual blade loading experiments. In addition, steeper waves were found to impose lower bending moments in both directions about the roots of the rotor blade. It should also be noted that the in-plane bending moment is affected by the gravity bending moment component, so a neutrally buoyant blade would be desirable, if not impractical for a small model.

The BEM code will be expanded to describe the loading effects on a turbine blade in more detail. Further work will include modelling of blade acceleration, gravity effects and added mass, with a view to providing a model for fatigue analysis. This model could then be used for the design of optimised MCEC blades for tidal environments.

5. Conclusions

It has been demonstrated that waves are likely to have a detrimental impact on MCECs. This is not a significant problem in terms of power output, other than to further complicate the power electronics required for smoothing the power/flicker. The main issue with wave-current interaction around a MCEC is the cyclic loading, which will likely result in accelerated fatigue to the rotor and blades. This is particularly evident in the axial flow direction. Another important consideration is whether a rotor yaw drive is required at any specific tidal site. Large amounts of directional swing will occur around headlands and can cause a significant reduction in power and increase in dynamic loading if a yaw drive is omitted. The continuing work presented in this paper will eventually assist in the structural design of MCEC rotor blades, quantify the loading effects caused by waves and maximise rotor diameter to achieve a robust, high energy yield device.

References

[1] C. Swan, R. L. James, A simple analytical model for surface water waves on a depth-varying current, Applied Ocean Research, Vol. 22, 2001, pp. 331-347.

[2] J. A. Smith, Wave-Current Interaction in Finite Depth. Journal of Physical Oceanography, Vol.36, 2006, pp. 1403-1419.

[3] J. Wolf, D. Prandle, Some observations of wave-current interaction, Coastal Engineering, Vol. 37, (1999), pp. 471-485.

[4] M. A. Srokosz, Models of Wave-Current Interaction, Advances in Underwater Technology, Ocean Engineering, Vol.12, 1987, pp. 313-325.

[5] L. E. Myers, A. S. Bahaj, Scale reproduction of the flow field for tidal energy converters, Proc. 10th World Renewable Energy Congress, Glasgow, UK, 2008.

[6] N. Barltrop, et al. Wave-current interactions in marine current turbines, Proc. 6th European Wave and Tidal Conference, Glasgow, UK, 2005, pp. 33-38.

[7] J. V. Norris, E. Droniou, Update on E MEC activities, resource description, and characterisation of wave-induced velocities in a tidal flow, Proc. 7th European Wave and Tidal Energy Conference, Porto, Portugal, 2007.

[8] P. W. Galloway, L. E., Myers, A. S. Bahaj, Studies of a scale tidal turbine in close proximity to waves, Proc. 3rd International Conference on Ocean Energy, Bilbao, Spain, 2010.

[9] A. F. Molland, The design, construction and calibration of a five-component strain gauge wind tunnel dynamometer, University of Southampton, Ship Science Report, 1/77, ISSN 0140-3818, 1976.

[10] C. Abonnel, et al. Some aspects of EDF modelling and testing activities, within its marine current energy research and development project, Proc. 6th European Wave and Tidal Conference, Glasgow, UK, 2005, pp. 1-10.

[11] Barnsley and Wellicome, Final report on the 2nd phase of development and testing of a horizontal axis wind turbine test rig for the investigation of stall regulation aerodynamics, carried out under ETSU agreement E.5A/CON5103/1746, 1990.

[12] A. S. Bahaj, et al. Experimental Investigation into the Hydrodynamic Performance of Marine Current Turbines, Sustainable Energy Series, Report 3, 2005.

Hydro-environmental Impact Assessment of the Significance of the Shape of Arrays of Tidal Stream Turbines

Reza Ahmadian[1,*], Roger Falconer[1] and BettinaBockelmann-Evans[1]

[1] Hydro-environmental Research Centre, Cardiff School of Engineering, Cardiff University, UK
** Corresponding author. Tel: +44 29208 75713, Fax: +44 29208 74939, E-mail: AhmadianR@cardiff.ac.uk*

Abstract: This study focuses on far-field hydro-environmental impacts of turbine arrays, with different shapes located in the Severn Estuary and Bristol Channel, UK, using a dynamically linked 1-D/2-D hydro-environmental model. The estuary, including the Bristol Channel, is approximately 200 km long and has the third highest rise and fall of tide in the world, with typical spring tidal range of over 14 m, whilst the spring tidal currents in the estuary are well in excess of 2 m/s. There are a number of tidal renewable energy options being considered around the Severn Estuary, including but not limited to: tidal stream turbines, offshore tidal impoundments and a barrage - at various locations. The model was used to predict the hydrodynamic, sediment transport and water quality processes as well as power output predictions. In order to simulate the impact of the tidal stream turbines, the model was refined and the turbines were included as momentum sinks in the momentum equation.

This study shows that the impact of the arrays on the water levels was negligible. However, the impact on velocities was more significant and the flow was retarded both upstream and downstream of the arrays, whilst it was faster on the side of the arrays. It was found that changes in the suspended sediment concentrations did not follow a simple pattern and that more detailed model studies are required to achieve a better understanding of this process. Finally, it was found that the power generated was dependent on the array layouts with the power output of different arrays used in this study varied by up to 20%.

Keywords: *Marine renewable energy, Hydro-environmental modelling, Tidal stream turbines, Severn Estuary and Bristol Channel.*

1. Introduction

The European Union have introduced targets among member states to increase the share of renewable energy in the overall energy consumption to 20% of total energy budget by 2020, this is almost three times the levels of 2008. Amongst the different types of renewable energy, marine renewable energy is an emerging energy sector with a bright future. Tidal devices and, in particular, tidal stream turbines have attracted considerable interest in recent years, due to the vast resources available in parts of the EU, modularity, minimal visual impact and their predictable energy generation.

As for many other emerging renewable schemes, the environmental impacts of tidal stream turbines are not clear and therefore need to be investigated before considering any site for deployment of such turbines. Although every single tidal stream device has a small footprint, the overall impact of an array of turbines can only be investigated by considering the scale of the array.

This study focuses on hydro-environmental modelling of different arrays of turbines and investigating the impact of the shape and density of the arrays on the flow, water levels, sediment transport and faecal bacteria concentrations as well as the energy output. The site selected for this study is the Severn Estuary and Bristol Channel, UK (shown in Fig. 1), which has the third largest tidal range in the world with typical spring and neap tidal ranges peaking at over 14 m and 7 m respectively, and the spring tidal currents are well in the excess of 2m/s. The site is one of the most attractive sites for marine renewable energy schemes and a number of schemes, including several barrages sites, lagoons and stream turbines have been proposed for the area.

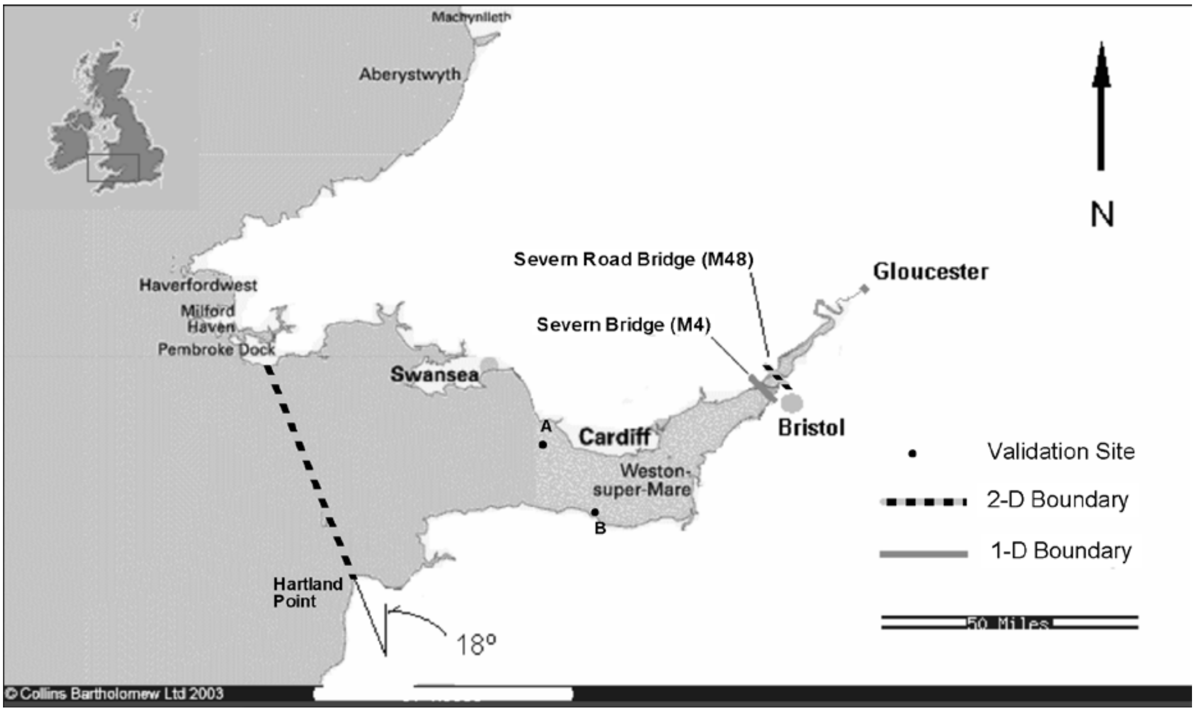

Fig 1. The model domain extent and validation sites. Site A: Southerndown Site, B: Minehead Site (Source: Yang et al. [1])

2. Hydro-Environmental Modelling Methodology

The dynamically linked DIVAST (Depth Integrated Velocities And Solute Transport) and FASTER (Flow And Solute Transport in Estuaries and Rivers) models were implemented to model the hydro-environmental impacts of the stream turbines. The modelling domain was extended from the outer Bristol Channel, close to Lundy Island (where an imaginary line between Milford Haven and Hartland Head can be drawn) at the western end of the domain to Gloucester at the eastern extremity (Fig. 1). Both, DIVAST and FASTER models are based on a finite difference alternating direction implicit solution of the Reynolds Averaged Navier-Stokes equations and the solute transport equation in 2D and 1D, for the hydrodynamic, sediment transport and water quality process predictions respectively[2]. The solute/sediment concentrations were calculated considering the effects of dispersion, diffusion, decay, adsorption and desorption as well as deposition and erosion.

The 2D downstream boundary was a water level boundary and the water level values for the simulation period at this location were obtained from the Proudman Oceanographic Laboratory (POL) Irish Sea model. Since this boundary was so far seawards of the region of interest, the concentrations of faecal indicator organisms were set to zero along the downstream boundary. The 2D upstream boundary was a flow boundary, flow and all the water quality indicators were dynamically transferred through the 1D-2D link. A flow rate varying between $60 m^3/s$ and $106 m^3/s$ was used as a 1-D upstream model boundary condition, at Gloucester. The downstream boundary of the 1D model, located close to the Severn Bridge, was specified as a water level boundary and the values of the water levels were acquired from the 2D model. A structured $200 \times 200 m^2$ grid was used for the 2D model while the 1D model was consisted of four reaches and two junctions with an average distance between the two consecutive cross-sections being approximately 240 m.

2.1. Governing Equation

Only the 2D model governing equations are briefly explained in this section, for more information on the 2D and 1D models refer to: Falconer[3] and Kashfipour[4]. The 2D hydrodynamic equations used in this model are based on the depth-integrated three-dimensional Reynolds equations for incompressible and unsteady turbulent flows. Also, the effects of the bottom friction, wind shear and the earth's rotation are included to give for the x-direction[5]:

$$\frac{\partial \xi}{\partial t}+\frac{\partial q_x}{\partial x}+\frac{\partial q_y}{\partial x}=0 \qquad (1)$$

$$\frac{\partial q_x}{\partial t}+\beta\left[\frac{\partial u q_x}{\partial x}+\frac{\partial v q_x}{\partial y}\right]=f q_y-gH\frac{\partial \xi}{\partial x}+\frac{\tau_{xw}}{\rho}-\frac{\tau_{xb}}{\rho}+\varepsilon\left[2\frac{\partial^2 q_x}{\partial x^2}+\frac{\partial^2 q_x}{\partial y^2}+\frac{\partial^2 q_y}{\partial x \partial y}\right] \qquad (2)$$

where q_x, q_y = discharges per unit width in the x, y directions ($m^2\ s^{-1}$), ζ = water surface elevation above datum (m), H = total water depth (m), β = momentum correction factor for non-uniform vertical velocity profile, f = Coriolis parameter (rad s^{-1}), g = gravitational acceleration (ms^{-2}), τ_{xw}, τ_{xb} = surface and bed shear stress components respectively in the x-direction (N m^{-2}), and ε = depth averaged eddy viscosity. The equation for the y-direction can be written similarly to that given for the x-direction (i.e. equation (2)).

The 2D advective-diffusion equation for predicting solute transport is acquired by integrating the 3D solute mass balance equation over the depth, giving:

$$\frac{\partial \phi H}{\partial t}+\frac{\partial \phi q_x}{\partial x}+\frac{\partial \phi q_x}{\partial y}-\frac{\partial}{\partial x}\left[HD_{xx}\frac{\partial \phi}{\partial x}+HD_{xy}\frac{\partial \phi}{\partial y}\right]-\frac{\partial}{\partial y}\left[HD_{yx}\frac{\partial \phi}{\partial x}+HD_{yy}\frac{\partial \phi}{\partial y}\right]=H\sum\Phi \qquad (3)$$

where ϕ = depth averaged concentration (unit/volume) or temperature (°C), H = total water depth (m) and $\Sigma\Phi$ = total depth average concentration of the source or sink solute. The bacteria decay can be modelled using a first order decay formulation according to Chick's Law[6] and given as:

$$\frac{dC}{dt}=-KC \qquad (4)$$

where K = decay coefficient, generally expressed in units of day^{-1}; t = time (s^{-1}) and C = bacterial concentration, expressed herein as Colony-Forming Units (CFU) per 100ml.

Some researches have shown that the concentration of Faecal Indicator Bacteria (FIB) on bed sediments can be 100-2000 times higher than the concentrations within the water column[7, 8, 9]. This suggests that the sediment re-suspension or deposition can increase or decrease the bacteria levels, respectively. This emphasises the importance of including the interaction of sediment and bacteria while predicting the bacteria concentration. Hence, to model the bacteria processes more realistically, the interaction of the sediment and bacteria has been included in the model as outlined in: Stapleton et al.[10, 11], Yang et al.[1] and Ahmadian et al.[12].

2.2. Model Calibration and Validation

The model predictions were initially calibrated using Admiralty Chart data and finally the field data collected by Stapleton et al. [10, 11] at two locations at two sites (shown in Fig. 1) were used to validate the model predictions. The model predictions showed good agreement with the validation data, more information regarding the model validation can be found in Ahmadian et al.[12]. Typical comparisons between the measured and predicted water elevations, current speeds, sediment fluxes and faecal bacteria concentrations are shown in Fig. 2 and Fig. 3 respectively.

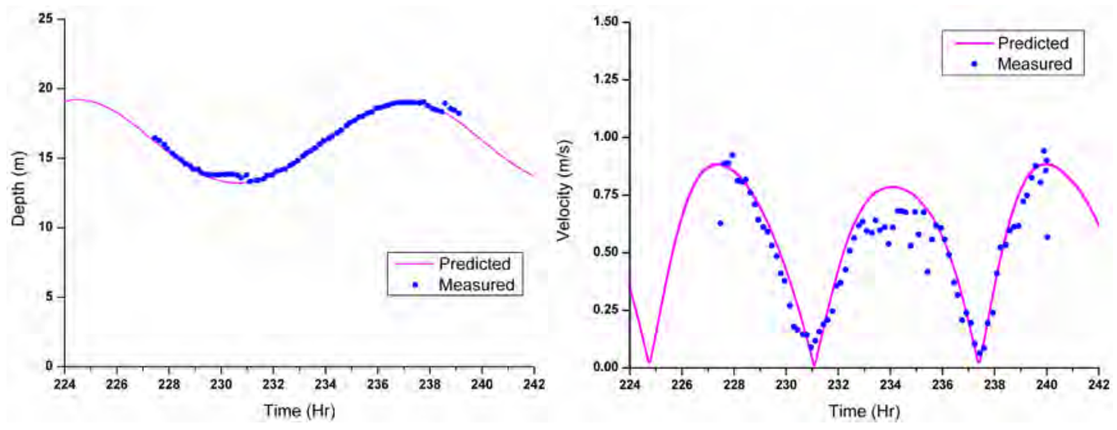

Fig 2. Comparison of predicted and measured water elevations (left) and current speeds (right) at Minehead (site B)

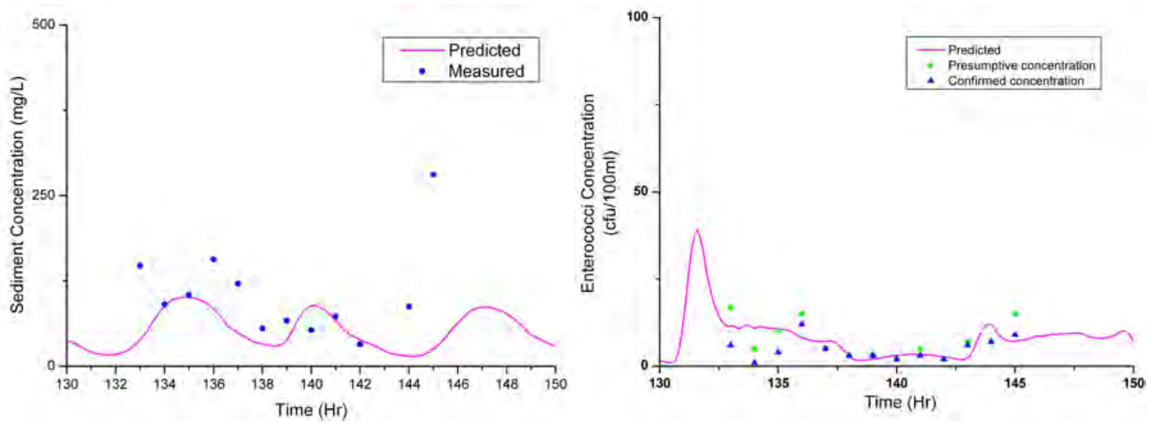

Fig 3. Comparison of predicted and measured suspended sediment concentrations (left) and enterococci concentrations (right) at Southerndown (Site A)

2.3. Turbines Modelling

Using the same analogy as used for wind turbines, the energy flux available for a turbine is [13]:

$$P = \frac{1}{2} C_p \rho A U^3 \tag{5}$$

where P = energy flux (W m^{-2}), ρ = water density (kg m^{-3}), A = area of the control volume (m^2), U = component of the water flow velocity perpendicular to the cross-section of the channel (ms^{-1}) and C_p = power coefficient. Energy extraction by turbines, consequently, causes a thrust force (T) induced on the turbine in the direction of flow and can be calculated as [13]:

$$T = \frac{1}{2} C_T \rho A U^2 \tag{6}$$

where C_T = thrust coefficient. It is shown that both the power and thrust coefficients are related to the hub pitch and varies with the Tip Speed Ratio (TSR)[13]. In this study, the momentum equation (Eq. 2) was modified to include the impact of the turbines.

3. Modelling Results

The model was then applied to three imaginary arrays of turbines in the Severn Estuary and Bristol Channel (illustrated in Fig. 4), and the impacts of the arrays on water levels, current speed, sediment transport and faecal bacteria levels were investigated. These arrays are arbitrary and were chosen purely for the model demonstration purposes and none of the protocols required for a site selected for deployment of turbines[14] have been taken into account in selecting these sites. It was assumed that the same number of turbineswere deployed in each formation. Formations a and b occupied the same area and consequently, have the same number of turbines per unit area, which will be referred to as the array density in this paper, while the density of the formation c is more than 10 times less than the formations a and b.

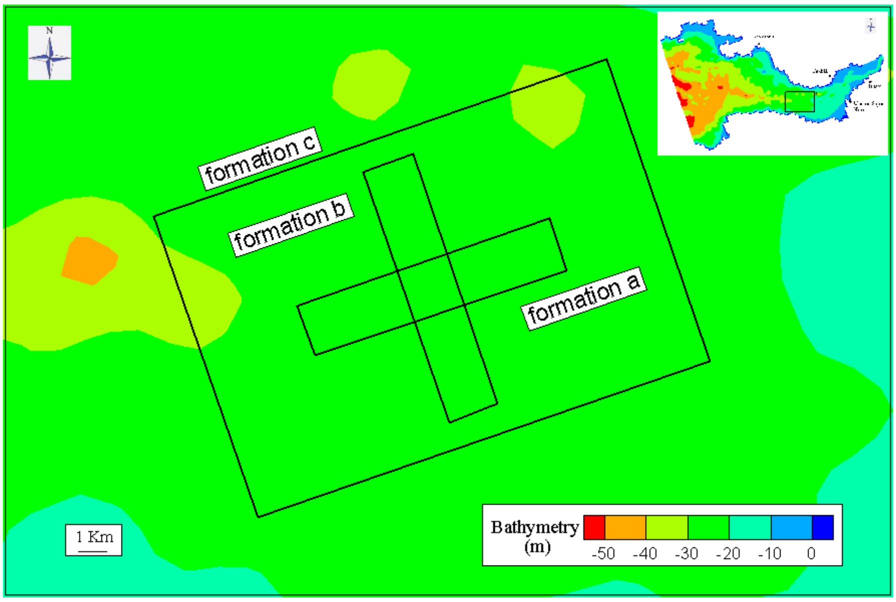

Figure 4: Array Formations

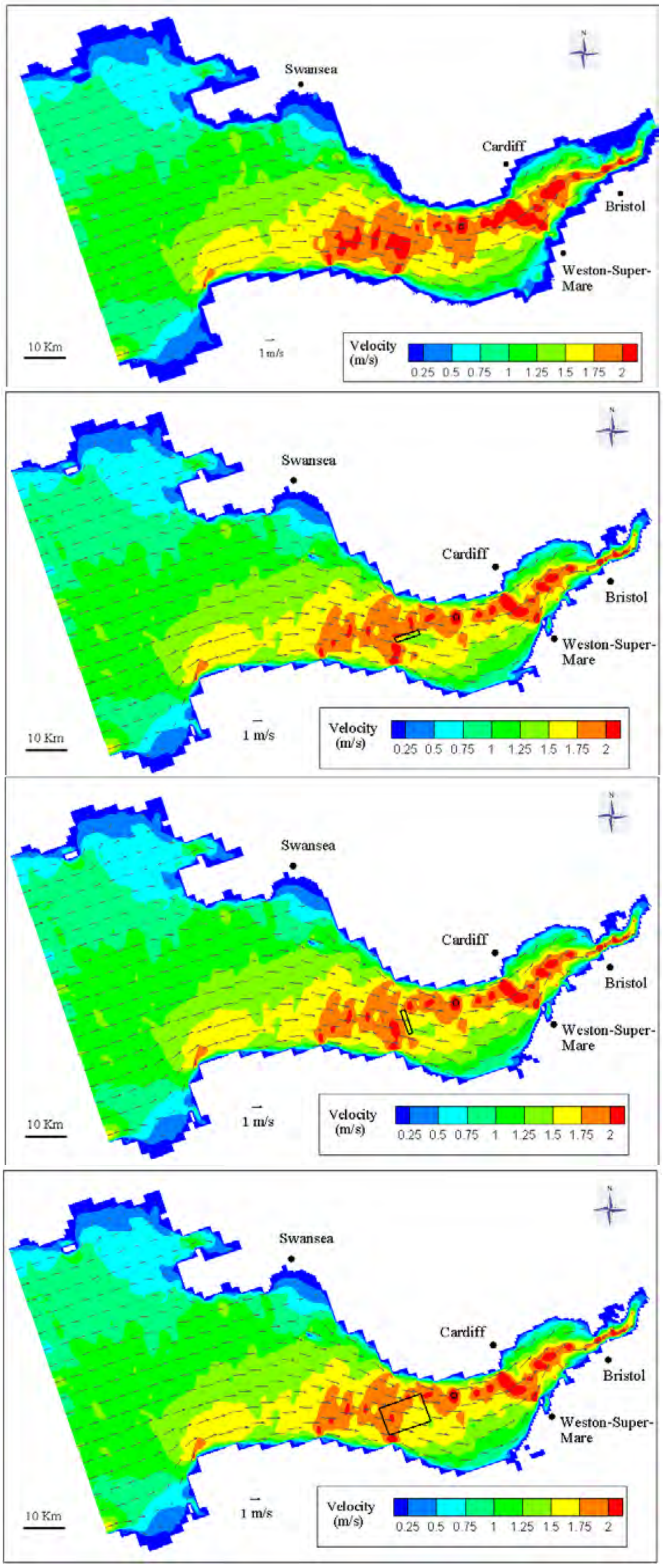

(i) *(ii)* *(iii)* *(iv)*

Figure5: Comparison of the velocities across the estuary without (i) and w ith different array formations; "formation a"(ii), "formation b"(iii) and "formation c"(iv) at mean flood at Barry (red dot)

The current speeds in the estuary at mean flood at Barry (red dot) before including the arrays and with the different arrays are shown in Fig. 5. Although, in this study it was assumed that the turbines can rotate to face the flow and subsequently the flow speed is equal to the effective velocity on the turbine, it can be seen that arrays with the same density but different orientations can impact the flow differently. It can also be seen that the arrays with a smaller density would change the currents to a much lesser extent while the average electricity generated by each turbine in this array can be up to 50% more than the average electricity generated by the turbines in the denser arrays. It was also found that the arrays would not change the water levels noticeably, however, as a result of changes in the currents sediment transport the faecal bacteria levels would be altered. These results are not shown here in the interest of space, however, publication of results will follow.

4. Conclusions

The dynamically linked 1-D/2-D hydro-environmental model of the Severn Estuary and Bristol Channel has been refined to assess the hydro-environmental impacts of an arbitrary array of tidal stream turbines by including the turbines as momentum sinks in the momentum equation. The model without the turbines was first calibrated and then was validated against field data.

The model was used to study the hydro-environmental far-field impacts of different shapes of an array of tidal turbines and the electricity generated. It was found that the impact of any formation of the arrays on the water levels were negligible. However, the impacts on velocities were more significant and the flow was retarded both upstream and downstream of the arrays, while it was faster on the side of the arrays. Although, this pattern was consistent for all the arrays, the extent of changes in the velocity was different regarding to the array formation. These changes were less significant for a less dense array (formation c), however, the average electricity generated by each turbine in this array was up to 50% more than the average electricity generated by the turbines in the denser arrays. Finally it was also found that the changes in the sediment and faecal bacteria levels were higher in the denser arrays.

5. Acknowledgements

The study is carried out as a part of MAREN project which is part funded by the European Regional Development Fund (ERDF) through the Atlantic Area Transnational Programme (INTERREG IV).

References

[1] Yang, L., Lin, B. and Falconer, R. A., 2008. Modelling enteric bacteria levels in coastal and estuarine waters. Proceedings of Institution of Civil Engineers, Engineering and Computational Mechanics, 161(4), 179-186.

[2] Kashefipour, S. M., Lin, B., Harris, E. L. and Falconer, R. A., 2002. Hydro-environmental modelling for bathing water compliance of an estuarine basin. Water Research, 36(7), 1854-1868.

[3] Falconer, R. A., (1992). Flow and water quality modelling in coastal and inland waters. Journal of Hydraulic Research, IAHR, 30(4), 437-452.

[4] Kashefipour, S.M., Falconer, R.A., Lin, B., Harris, E.L. (2000). FASTER Model Reference Manual. Hydro-environmental Research Centre Report, Cardiff University.

[5] Falconer, R.A. (1993). An introduction to nearly horizontal flows. In: Abbott, M.B. and Price, W.A., Coastal, Estuarial and Harbour Engineers' Reference Book. London: E & FN Spon Ltd., pp. 27-36.

[6] Chick, H. (1910). The Process Of Disinfection By Chemical Agencies And Hot Water. Journal of Hygiene. 10 (2), pp. 237-286.

[7] Marshall, K.C. (1978). The effects of surfaces on microbial activity. Water Pollution Microbiology. vol. 2, pp. 51–70.

[8] Burton, G.A., Gunnison, D. and Lanza, G.R. (1987). Survival of Pathogenic Bacteria in Various Freshwater Sediments. Applied and Environmental Microbiology, 53(4), pp. 633-638.

[9] Obiri-Danso, K. and Johns, K. (2000). Intertidal sediments as reservoirs for hippurate negative campylobacters, salmonellae and faecal indicators in three EU recognised bathing waters in North West England. Water Research. 34(2), pp. 519-527.

[10] Stapleton, C.M., Wyer, M.D., Kay, D., Bradford, M., Humphrey, N., Wilkinson, J., Lin, B., Yang, Y., Falconer, R.A., Watkins, J., Francis, C.A., Crowther, J., Paul, N.D., Jones, K. and McDonald, A.T., 2007a. Fate and Transport of Particles in Estuaries, Volume II: Estimation of Enterococci Inputs to the Severn Estuary from Point and Diffuse Sources. Environment Agency Science Report SC000002/SR2, Bristol: Environment Agency.

[11] Stapleton, C.M., Wyer, M.D., Kay, D., Bradford, M., Humphrey, N., Wilkinson, J., Lin, B., Yang, Y., Falconer, R.A., Watkins, J., Francis, C.A., Crowther, J., Paul, N.D., Jones, K. and McDonald, A.T., 2007b. Fate and Transport of Particles in Estuaries, Volume IV: Numerical Modelling for Bathing Water Enterococci Estimation in the Severn Estuary. Environment Agency Science Report SC000002/SR4, Bristol: Environment Agency.

[12] Ahmadian, R., Falconer, R.A. and Lin, B.L. (2010). Hydro-environmental modelling of proposed Severn barrage, UK. Proceedings of the Institution of Civil Engineers, Energy, 163(EN3), pp 107–117.

[13] Bahaja, A.S., Mollandb, A.F., Chaplina, J.R. and Batten, W.M.J., 2007. Power and thrust coefficients of marine current turbines operating under various hydrodynamic conditions of flow in cavitation tunnels and towing tanks. Renewable Energy, 32, pp. 407–426.

[14] Willis, M., Masters, I., Thomas, S., Gallie, R., Loman, J., Cook, A., Ahmadian , A., Falconer, R., Lin, D., Gao, G., Cross, M., Croft, N., Williams, A., Muhasilovic, M., Horsfall, I., Fidler, R., Wooldridge, C., Fryett, I., Evans, P., O'Doherty, T., O'Doherty, D., and Mason-Jones, A., 2010. Tidal Turbine Deployment in the Bristol Channel – A Case Study, Proceeding of Institution of Civil Engineers- Journal of Energy, 163(3), pp. 107–117.

Experimental investigation of the effects of the presence and operation of tidal turbine arrays in a split tidal channel

Tim Daly[1*], Luke. E. Myers[1], AbuBakr S. Bahaj[1]

[1] *Sustainable Energy Research Group, University of Southampton, Southampton, United Kingdom*
** Corresponding author. Tel: +44 2380592134, E-mail: td2e09@soton.ac.uk*

Abstract: The installation of arrays and farms is the next major step in the development of tidal energy converters. Many tidal farms are currently in the process of development. A number of studies have also identified potentially lucrative sites for future farm and array development elsewhere. In some of these sites, the flow velocities can at least in part be attributed to the presence of constraining landmasses and the resultant splitting of channels into two or more sub channels. Given the cubic relationship between flow velocity and kinetic energy flux, even modest acceleration in these areas can cause a considerable increase the potential power available.
The analysis in this paper investigates flow acceleration effects in a split tidal channel due to the presence of tidal turbine arrays. As well as their presence, the effect of changing lateral and longitudinal position of the array and number of turbines in the array was also examined. Results show that flow acceleration of up to 14% can occur in an empty channel due to the presence of tidal arrays. This could potentially have major implications for tidal farm design in areas where channels branch into multiple sub channels.

Keywords: *Split tidal channel, Obstruction, Actuator fences, Flow acceleration, Acoustic Doppler velocimeter.*

1. Introduction

Studies have shown that the presence of tidal turbine arrays in any channel has the potential to have a significant effect of the surrounding flow environment [1]. They will also impact human activities such as shipping and sensitive environmental processes such as sediment transport, shore erosion and fish migration. Many areas worldwide in which split tidal channels are present have been identified as having high potential tidal energy resources. Examples include the Sound of Islay, Scotland, UK [2], Bay of Fundy, Canada [3] and Puget Sound, Washington, USA [4]. In areas such as these, aforementioned effects are likely to be greater, as placing turbines in one sub channel may alter the flow in some or all other sub channels. While many of these effects will obviously depend on the bathymetry of the site in question, there will undoubtedly be many generic effects which will be common to all sites of this kind.

This paper outlines the methods and results of experimentation carried out to examine some of the effects of tidal turbine arrays located in split tidal channels. Experimentation was carried out in the University of Southampton Chilworth hydraulics laboratory using a circulating water channel, actuator fences and acoustic Doppler velocimeters (ADV). The hypothetical site investigated was a simple channel which splits into two equally sized sub channels due to the presence of an impenetrable landmass between them. One of the sub channels had a tidal array installed, while the other was left empty. The resultant flow velocity in the empty sub channel was compared to the natural flow velocity to determine the percentage increase which resulted due to energy extraction.

2. Review of previous studies

Despite the high velocity magnitudes present in areas of split tidal channels, there is considerable variability in the bathymetry and hydrodynamic environment from site to site. This makes these areas much more complex to analyse from a resource assessment and environmental impact point of view. Also unlike single channel areas, it can be very difficult to determine theoretical expressions which will be applicable to all sites. One study which aimed to develop such theoretical expressions is outlined in [5]. The paper presents the case of a simple channel connected to two infinite oceans, and divided into two equal sub channels by an island in the centre. One sub channel has energy extracted by tidal energy converters, while the other is left empty. The authors derive expressions for power extracted by turbines and total fluid power as functions of head drop across the turbines and head drop across the entire channel between the two oceans respectively. The authors conclude that a maximum of 38.49% of total fluid power can be extracted, a figure which agrees with estimates for efficiency developed from single channel extraction theory developed by Garrett and Cummins in [6].

A site specific analysis of an area known as Johnstone Strait was carried out in [7]. The Johnstone Strait region consists of a number of sub channels, and the authors used both analytical methods developed by Garrett and Cummins [6] and a numerical model to examine the maximum power extracted by turbines in a total of four different sub channels. The authors found that their numerical model agreed reasonably well with the analytical theory developed in [8] for two particular cases. However for the other two investigated instances, theory was not valid, as the theory developed is only valid for instances where the flow of water cannot be diverted away from the sub channels where tidal turbines are installed [7]. Further analysis also examined some effects to the hydrodynamic environment by comparing natural tidal heights and amplitudes with those observed following energy extraction.

These studies use different methods of accounting for the presence of turbines, with [5] using head loss coefficients to calculate head drops and resultant power values, and [7] increasing natural bottom friction coefficient to include the effects of turbines presence. However undoubtedly the biggest difference is that [7] acknowledges the effects of energy extraction in different areas on the surrounding area, and attempts to quantify it briefly by examining changes to tidal amplitude and height. While [5] estimates high possible extractable power for an area of Johnstone Strait, there is no way for a potential developer to determine whether the changes to the surrounding hydrodynamic environment will render extraction of this energy unacceptable from an environmental point of view.

In contrast to both of these studies, the far field effects of tidal energy extraction was the sole subject of investigation in an analysis of four different tidal site configurations carried out in [8]. The four types of channel networks investigated were:
(a): A single constriction, which is a simple narrowing of a tidal channel.
(b): A multiply connected network, where flow is diverted from one channel into two sub channels, each of which contains a single constriction, and which meet again later in the flow.
(c): A branching network, where flow is diverted from one channel into two sub channels each of which contains a constriction. However these sub channels do not meet later in the flow.
(d): Serial constrictions, where a single channel contains a number of areas where constrictions are present.

Analytical methods were used to examine far field effects included shallow water equations, the conservation of mass and the conservation of energy. Results found that the largest tidal amplitude changes occur in the Branching network, biggest changes in kinetic power density occurring in the multiply connected network and changes to transport amplitude and frictional power dissipation approximately equal in all cases.

These three investigations all contain elements of resource assessment which are crucial to the process of designing and installing a tidal turbine farm. However all rely solely on analytical and numerical models and no experimental results are present in these analyses. Section 3 outlines the methodology and reasoning for experimentation carried out to examine the changes to the hydrodynamic environment of a network of channels due to the presence of tidal energy converters. It is hoped that this analysis will further aid in the exploitation of the maximum potential energy in these sites with minimal and justifiable environmental effects.

3. Experimental method

3.1. Flume setup

The experimentation for this investigation was carried out in the indoor flume of the University of Southampton Chilworth hydraulics laboratory. The flume is a conventional gravity fed flume, with water pumped from sumps and through a flow channel, and mass flow rate, depth and flow velocity magnitude controlled via valves and a tail gate. The working section is 21m in length, 1.37m wide with a maximum flow depth of 0.5m. A 100mm wide dividing wall was placed along the streamwise centerline of the flume over a length of 4m (Fig. 1). The wall was placed between 8.5m and 12.5m from the inlet of the 21m channel. This split the flow into two hypothetical sub channels in a similar fashion to an impenetrable landmass in a real tidal channel.

3.2. Turbine array simulation

Tidal turbine arrays were represented in the Chilworth flume using porous actuator fences. The porous actuator fence is a convenient alternative to rotating turbines in the analysis of tidal farms and arrays. The main difference between fences and turbines is opposed to extracting kinetic energy from a fluid, actuator fences convert this energy to small scale turbulence in their wake. Other differences include the inability of fences to induce swirl effects in the flow and the differences in the structure of vortices shed from both. These factors mean that actuator fences are unsuitable for examining farm or array power output or the structure of the near wake of tidal arrays.

However analysis in [9] has shown that they are highly accurate in predicting the far wake effects of tidal turbine farms, which are likely to impact on farm layout and surrounding flow environment. Actuator fences also have the advantage of being easier and cheaper to construct than turbines. They are also advantageous for numerical modeling, as CFD simulations with actuator fences can be run in steady state as opposed to unsteady state for rotating turbines, and also require much less complex meshes.
Two actuator fences were used in this analysis. They were created from 300mm wide and 100mm high sheets of PVC with a thickness of 4mm. Holes were drilled in the sheets to achieve the desired open to total area ratio's (porosities).

3.3. Flow velocity magnitude measurements

All flow velocity measurements were taken using an acoustic Doppler velocimeter (ADV). The instrument used for this work was set to sample at 50Hz, just below the noise floor. The sample volume is cylindrical with a fixed diameter of 6mm. the volume height is user-defined and was chosen to be 3mm. Larger sample volumes will intercept more suspended matter in the water leading to stronger acoustic return signals and greater accuracy. However this can be negated as velocity shear between the top and bottom of the sample volume can lead to inaccuracies. Due to the high levels of suspended matter in the Chilworth flume, no doubt arising from being located in a hard water area, the signal strengths were found to be very strong. With the water depth set to 0.3m the sample height represented 1% of the depth thus ensuring that velocity shear was minimal across measurement volume. To eliminate any errors which may have occurred due to random velocity fluctuations, the data were filtered subsequent to experimentation. The method used in this instance was the velocity correlation filter outlined in [10]. Other filtering methods determine the criteria upon whether a measurement is invalid on the basis of the relationship between successive measurements. These methods would be unsuitable for this analysis, as groups of random fluctuations are likely to exist due to the turbulent nature of the flow downstream of the actuator fences. The velocity correlation filter is more suitable to the present study as the criteria for determining the validity of a measurement is calculated based on its relationship to all velocity measurements in the sample.

Fig.1. Front and rear of split mechanism in Chilworth channel.

3.4. Base flow map and actuator fence positioning

3.4.1. Analysis of natural flow environment

Initial flow mapping work was conducted in the absence of actuator fences in order to quantify the baseline flow environment with the split present. The depth was set to 0.3m and the depth-averaged flow velocity was approximately 0.3m/s. Comprehensive flow velocity measurements were taken laterally (cross-flume) and throughout the depth upstream of the wall split, and also in the sub channels on both sides of the wall. This velocity deficit would be able to give a measure of the extent to which the flow slowed down or accelerated due to the presence and various positions of actuator fences and is given by the expression:

$$U_{deficit} = 1 - \frac{U_w}{U_o} \quad (1)$$

Where $U_{deficit}$ is the velocity deficit, U_w is the velocity at a specific point in the wake of the disk and U_o is the natural freestream flow velocity at this specific point.

3.4.2. Wake mapping of actuator fences

An actuator fence with porosity (ratio of open to total area) of 0.38 was placed in the centre of one of the sub channels at a distance of 0.4m downstream of the front of the split, which was also 8.9m from the inlet of the flume. This setup is displayed graphically in Fig. 2. Flow velocity measurements were then taken in both sub channels. The first position to be measured was 3 fence diameters downstream of the fence and up to 21 diameters downstream of it in increments of 3 diameters. For each downstream position, several lateral positions were taken, while for each lateral position, 8 flow depths in increments of 30mm depth were taken. A similar analysis was carried out for the case of two actuator fences being present in a single sub channel. In this case two fences of porosity 0.38 and 0.4 were placed alongside each other. This case represented a very high blockage ratio, as the total width of the sub channel was approximately 635mm and the width of the two fences combined was 600mm. Once again the wake was examined by taking flow velocity measurements at several positions downstream of the fences, in both channels, using the ADV.

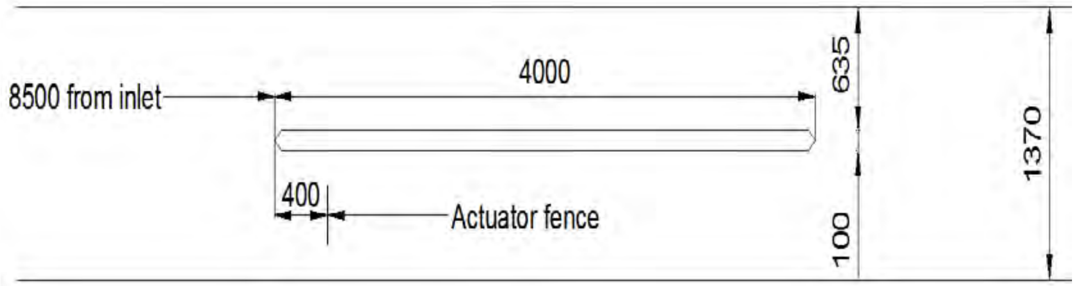

Fig.2. Plan view of Chilworth channel with porous actuator fence and split present (all dimensions in mm)

3.4.3. Flow acceleration analysis

As well as wake mapping in both channels, flow acceleration effects in the empty sub channel were examined. ADV's were positioned at two lateral points in the empty channel at a distance of 0.4m from the front of the wall split, or 8.9m from the inlet to the channel (Fig. 3). In the case of a sub channel with a single fence, a fence of porosity 0.4 was used. The fence was placed in 3 lateral positions, with the centre of the fence being positioned 180mm, 320mm and 460mm from the sidewall of the flume. For each of these lateral positions, the fence was also placed in the same downstream position as the front of the split, and was then moved gradually back in 100mm increments to 500mm downstream of the front of the split, then in 200mm increments up to 2000mm downstream. For each of these fence positions, the ADV recorded the flow velocity magnitude at the aforementioned points in the empty sub channel. Similar analysis was carried out for the case of a sub channel with two actuator fences present. Due to the fences occupying the vast majority of the width of the channel, changes to lateral position were not examined. Instead only the changes to the downstream positions were examined exactly as described for the case of a single fence. The high blockage ratio also meant that flow acceleration effects were anticipated.

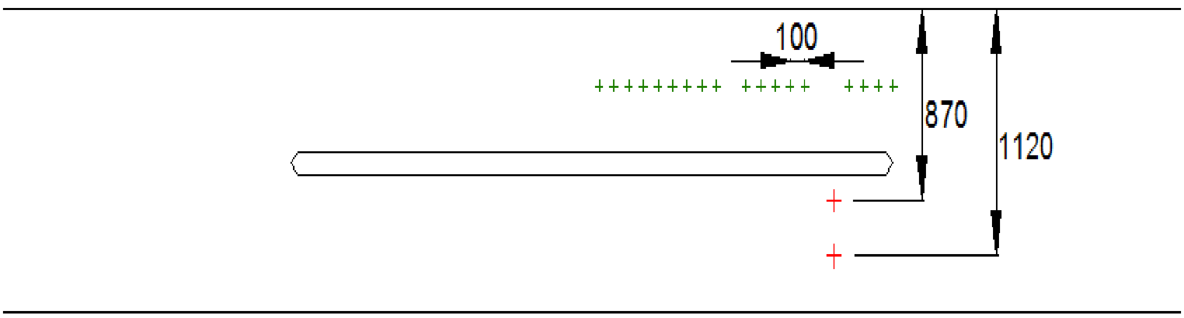

Fig.3: Diagram of Chilworth flume setup indicating location of split, measurement points in empty channel (indicated in red) and points where fence centre is located (indicated in green).

4. Results and discussion

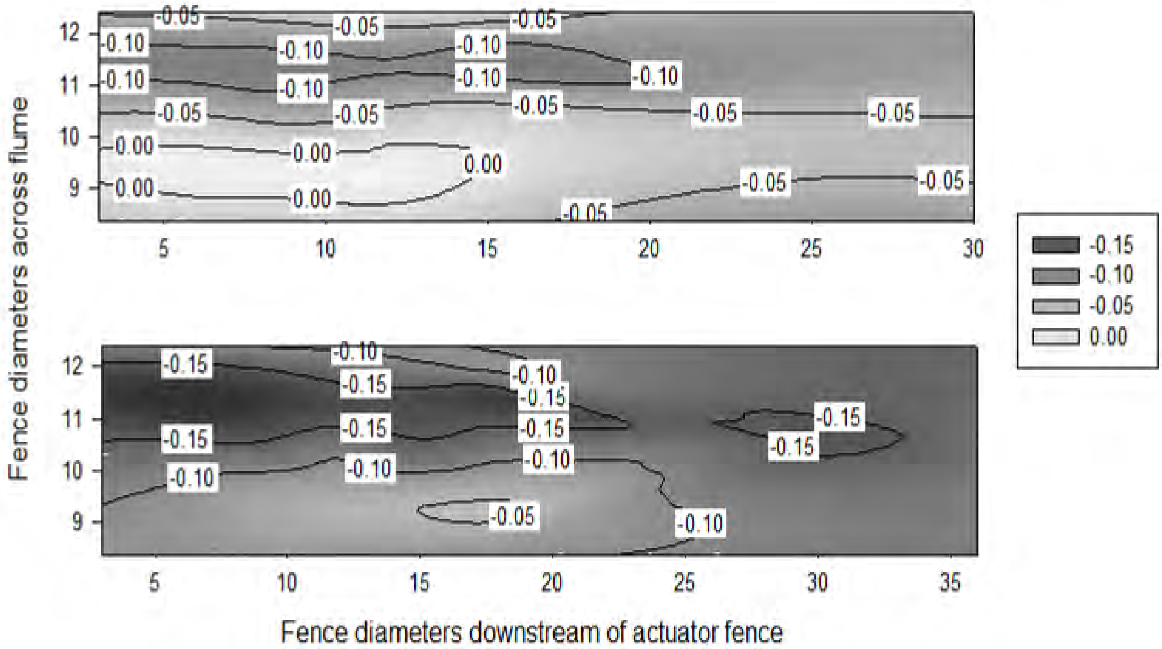

Fig.4. Contour plots showing velocity deficit variations in empty sub channel downstream of single 0.38 porosity fence (top) and downstream of 0.38 and 0.4 porosity fence (bottom).

Figure 4 shows the results of the wake mapping analysis of the areas downstream of both the single fence (top figure) and two fences (bottom figure), as discussed in section 3.4.2. These plots show that some flow acceleration is present in both cases, but also that it is much greater when two fences are present in the opposite channel. Velocity deficit values are zero or very close to zero in the top figure, while they approach values of -0.15 in the bottom figure.

Figures 5 and 6 show the results of the flow acceleration analysis outlined in section 3.4.3. These also demonstrate the presence of flow acceleration due to the presence of fences in the opposite channel. In the case of a single fence in figure 5, there is no immediately apparent definite pattern or relationship between fence position, both laterally and in the downstream direction, and the percentage increase in freestream velocity magnitude. There is only a small difference between the readings given by the ADV positioned at 870mm from the sidewall (left) and that positioned 1100mm from the sidewall (right). Despite this lack of any definite relationship, it should be noted that the flow acceleration is quite small in itself, being 7% or less. Also the Chilworth flume has a variation in flow velocity at any point of approximately between 1% and 2% for any flow rate. For such small changes to flow, a lack of any definite relationship between the investigated parameters is not an unexpected result.

Much higher flow acceleration is observed from the results for the case of two actuator fences as displayed in figure 6. The scatter plot shows flow acceleration of between 8% and 14%. 14% flow acceleration is a potentially significant result from a tidal farm perspective. If the installation of more tidal converters in this empty channel could be justified both economically and environmentally, there is potential for up to 48% more power to be

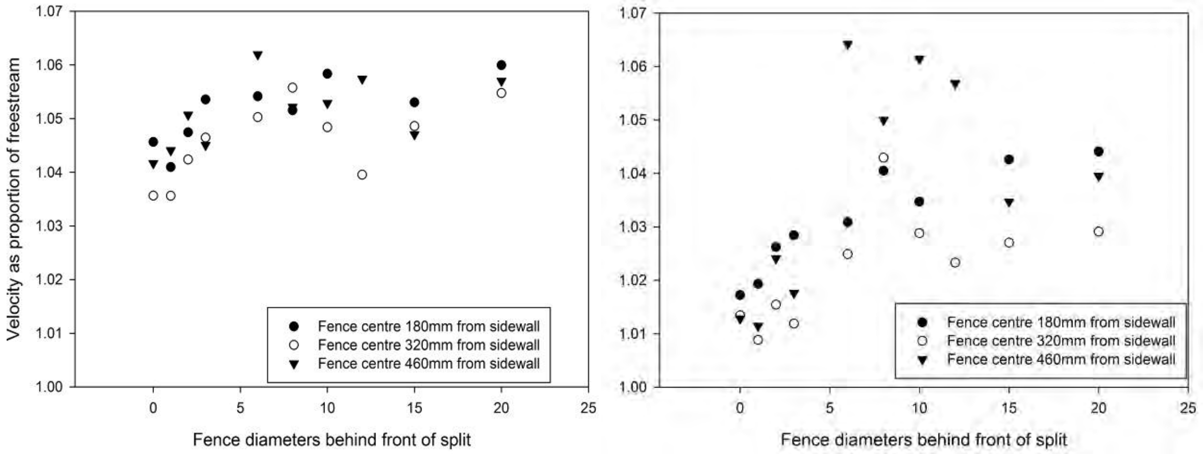

Fig.5. Flow acceleration in empty sub channel at lateral positions of 870mm (left) and 1120mm (right) due to movement of single actuator fence in opposite channel.

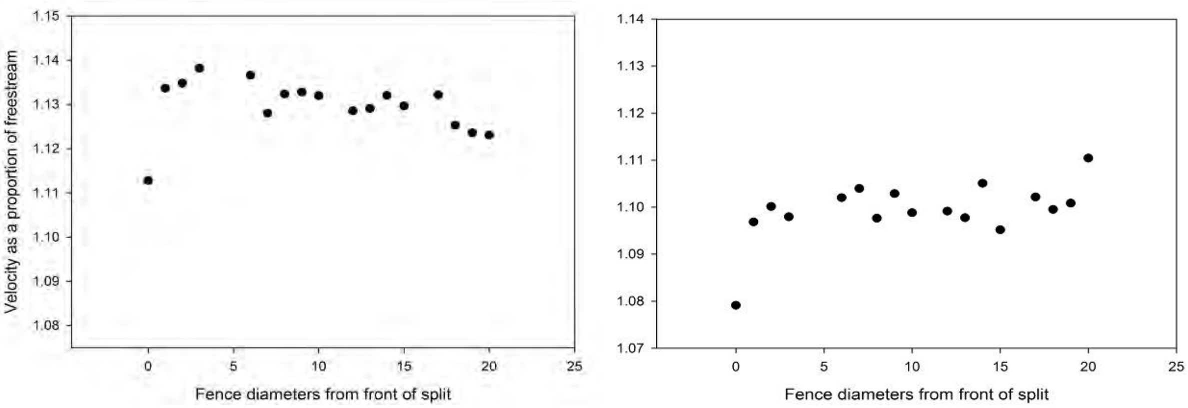

Fig.6. Flow acceleration in empty sub channel at lateral positions of 870mm (left) and 1120mm (right) due to movement of two side by side actuator fences in opposite channel.

extracted than without arrays in the other sub channel. However this would obviously be dependent on other factors such as internal turbine efficiency. It is also interesting to note from the scatter plots that the percentage acceleration is higher closer to the split than further laterally along the channel. This only occurs for the case of two fences. This might suggest that the presence of a greater number of turbines in an array may cause the flow to diverge further upstream than smaller arrays. Nearer to the split, there is also some reduction in flow acceleration as the array is moved further back from the split. This is another result which does not appear to happen further laterally across the channel. This may suggest that the flow is steadier and developed further away from the split, and that changes to longitudinal positioning of the array may only affect flow velocities in certain regions of the empty sub channel.

5. Conclusions and future work

The single actuator fence in this analysis occupied approximately $1/6^{th}$ of the total area of one sub channel ($1/3^{rd}$ of the depth and ½ of the width), and resulted in relatively low flow acceleration. There was also no obvious relationship between acceleration and either longitudinal or lateral position. In contrast, two actuator fences occupying $1/3^{rd}$ of the total area resulted in much higher acceleration, in some cases up to 14%, with some dependence on longitudinal position apparent. These results suggest that total area blocked by turbines in a sub channel has implications for flow acceleration effects. Future work will examine this relationship between acceleration and blockage by using different sized actuator fences in one sub channel.

Higher flow acceleration in the region closer to the split also suggests that the initiation of flow divergence between the two sub channels may be dependent on the area blocked in one sub channel. Future work will examine the area upstream of the front of the tidal split in an attempt to determine at what point flow divergence begins and how dependent is the point of flow divergence on the area occupied by turbines. Results also show that high flow acceleration still occurs even when the actuator fences are a relatively large distance downstream of the front of the split. Future experimentation will attempt to determine at what array position downstream of the split flow acceleration will no longer exist.

References

[1] T. Daly, L.E. Myers, A.S. Bahaj, Experimental analysis of the local flow effects around single row tidal turbine arrays, Proceedings of the 3rd International Conference on Ocean Energy, 2010.

[2] A. Mortimer, Tidal power with Hammerfest Strom technology: Towards commercialisation, Proceedings of 3rd International Conference on Ocean Energy, 2010.

[3] R.H. Karsten, J.M. McMillan, M.J. Lickley, R.D. Haynes, Assessment of the tidal current energy in the Minas Passage, Bay of Fundy, Proceedings of the Institution of Mechanical Engineers, Part A: Journal of Power and Energy 222, 5, pp. 493- 507

[4] B.L. Polagye, M. Kawase, P. Malte, In-stream tidal energy potential of Puget sound, Washington, Proceedings of the Institution of Mechanical Engineers, Part A: Journal of Power and Energy 223, 5, pp. 571- 587

[5] J.F. Atwater, G.A. Lawrence, Power potential of a split tidal channel, Renewable energy 35, 2, pp. 329-332.

[6] C. Garrett, P. Cummins, The power potential of tidal currents in channels, Proceedings of the Royal Society A: Mathematical, Physical and Engineering Sciences, 461, 2060, pp. 2563-2572.

[7] G. Sutherland, M. Foreman, C. Garrett, Tidal current energy assessment for Johnstone Strait, Vancouver Island, Proceedings of the Institution of Mechanical Engineers, Part A: Journal of Power and Energy 221, 2, pp. 147- 157

[8] B.L. Polagye, P.C. Malte, Far field dynamics of tidal energy extraction in channel networks, Renewable energy, 36, 1, 222-234.

[9] L.E. Myers, A.S. Bahaj, Experimental analysis of the flow field around horizontal axis tidal turbines by use of scale mesh disk rotor simulators, Ocean engineering, 37, 2-3, 218-227.

[10] L. Cea, J. Puertas, L. Pena, Velocity measurements on highly turbulent free surface flow using ADV, Experiments in fluids 42, 3, pp. 333-348.

The downstream wake response of marine current energy converters operating in shallow tidal flows

Jack Giles[1,2*], Luke Myers[1], AbuBakr Bahaj[1], Bob Shelmerdine[2]

[1]University of Southampton, Southampton, UK
[2] IT Power Ltd., Bristol, UK
* Corresponding author. Tel: +44 7855037885, E-mail: jack.giles@soton.ac.uk

Abstract: This paper presents findings from an experimental study investigating the downstream wake response from marine current energy convertors operating in various degrees of vertical flow constraint. The paper investigates deep vertically unconstrained sites, mid-depth sites and there is a particular emphasis on shallow tidal stream sites. Shallow tidal resources could be utilised for the deployment of first generation farms. The nature of the downstream wake flow will be a critical factor when determining the farm layout and the wake length is heavily influenced by the flow depth or ratio of rotor diameter to flow depth. A porous actuator disk is used to model the marine current energy convertor and an Acoustic Doppler Velocimeter is used to map the downstream wake. Linear scaling of length ratios suggests mid depth sites of 30-50m will produce the shortest wake lengths and for deeper and shallower sites the wake length increases. It is hoped that these relationships between vertical flow constraint and wake length will help with the layout design of tidal stream farms.

Keywords: *wake, vertical flow constraint, shallow tidal flows, farms.*

Nomenclature

C_t	*thrust coefficient*	
U_{def}	*velocity deficit*	$m{\cdot}s^{-1}$
U_w	*wake velocity*	$m{\cdot}s^{-1}$
U_o	*free-stream velocity at hub height*	$m{\cdot}s^{-1}$
I	*turbulence intensity*	%
$\overline{U}$	*Mean velocity of sample*	$m{\cdot}s^{-1}$
D	*actuator disk diameter*	m
u	*downstream velocity component*	$m{\cdot}s^{-1}$
v	*lateral velocity component*	$m{\cdot}s^{-1}$
w	*vertical velocity component*	$m{\cdot}s^{-1}$

1. Introduction

Shallow tidal flows hold a number of advantages for first generation tidal stream farms. Shallow flows, of depths less than 20m, often have a reduced cross-sectional area suitable for energy extraction compared with deeper channels, but they also have other benefits including close proximity to the shore with many sites situated away from shipping channels. This could make construction and grid connection both easier and more economically feasible. Fig. 1 presents results showing potential sites for device deployments in shallow tidal flows in the UK. The data for bathymetry and mean spring peak velocities was obtained from the BWEA "Marine Energy Resource Atlas" [1] and the layers were manipulated using geographic information system (GIS) software. The highlighted areas show sites with depths between 10-20m and spring peak velocities of greater than 1.5m/s.

When deploying a farm of Marine Current Energy Converters (MCECs), the nature of the downstream wake flow will be a critical factor when determining the farm layout and packing density. It is known that the wake length is heavily influenced by the flow depth or the degree of vertical flow constraint. This paper presents experimental findings of the flow fields around scale MCEC simulators operating in a circulating flume at varying depths to represent the range of depths present at the many sites suitable for MCEC deployment. Examples of shallow tidal sites include; the Bristol Channel, the Humber Estuary and areas around the Channel Islands (see Fig. 1). Deeper flows exist in the Pentland Firth and in various locations around the West of Scotland.

Previous work presented by Myers et al. [2] concluded that MCECs operating in shallow fast-moving flow regimes will see a difference in the downstream flow field compared with devices installed in deeper water. It was stated that the effects of sea bed proximity have shown that wake recovery is not as favourable when the flow field is very deep beneath the rotor disk. This is due to reduced shear forces and lack of accelerated flow generated by the close proximity of the sea bed and surface that serve to drive wake dissipation. This paper presents work developed from the previous study [2] to further investigate the effects of vertical flow confinement on the downstream wake development of MCECs. A thorough understanding of wake development is critical for the optimisation of the downstream device spacing in tidal stream farms. Minimising the downstream spacing will enable a higher farm device density and hence higher yields from a specific site.

For a multiple-row MCEC array, longitudinal spacing of devices is expected to be great enough to ensure that downstream devices have an incoming flow regime (and hence power production) that is comparable to devices located upstream. However, at spatially constrained sites this approach to spacing may be tightened in order to increase energy capture per surface area of the site and to reduce electrical connection costs. It is postulated that there may be an optimum device height to flow depth ratio that will lead to the minimisation of downstream wake length. For sites that are deeper or shallower than this optimum depth range, the downstream wake length is expected to increase. Whilst an explanation has been provided for deeper flows [2] it is expected that in a very shallow flow vertical blockage is high and flow acceleration above and below the MCEC will be restricted. Both of these factors are expected to result in reduced mixing between the wake and ambient flow thus increasing wake length.

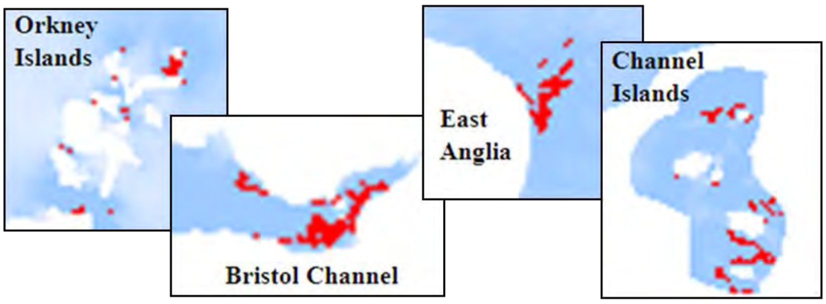

Fig. 1 Potential UK first generation shallow tidal flow sites, not to scale.

2. Methodology

In order to conduct the testing at a reasonable scale a porous mesh disk was used to model a horizontal axis turbine (often referred to as actuator disks). Actuators are now an accepted method for modelling MCECs and have been extensively used for horizontal axis turbines, but the method could equally be used to model vertical axis and oscillating hydrofoil devices. Actuator and momentum theory is discussed extensively by Burton et al. [3]. Work concerning the use of small scale actuator disks for the representation of far wake conditions has been addressed by a number of authors for both wind and tidal energy applications [4,5] . The principle difference between flow fields around actuators and full scale MCECs is the representation of the near wake and these differences are generally known to dissipate in less than four rotor diameters downstream [6,7].

For this work the principle parameters that require replication from large to small scale are [2]:

a) Device thrust force controlled through the level of actuator disk porosity (ratio of open to closed area).
b) Linear scaling of length ratios such as disk diameter to water depth and channel width.
c) Replication of ambient flow field conditions such as Froude number, vertical velocity profile and turbulence intensities. Full-scale and model Reynolds numbers cannot achieve parity at small scale but should lie within the turbulent classification.

Testing was conducted at a scale of 1:100 using actuator disks of 0.1m diameter. The porous actuator's impedance was specified using an empirical relationship between thrust coefficient (C_t) and plate porosity. This relationship was developed from a combination of experimental findings from the University of Southampton and from equations presented by Whelan et al. [8]. The actuator disk used is of the same porosity as that used in Myers et al. [2].

The actuator disk was mounted on a thin stainless steel support arm which made up part of a pivot arrangement to magnify the small thrust forces on the actuator disk. The rig can be seen in Fig. 2, a 10N button load cell was used to measure the total thrust force.

Shallow-depth experiments were conducted in the tilting flume at the Chilworth hydraulics laboratory, University of Southampton, UK. The working section of this flume is 21m in length, 1.37m wide and a maximum depth of 0.4m for steady operation.

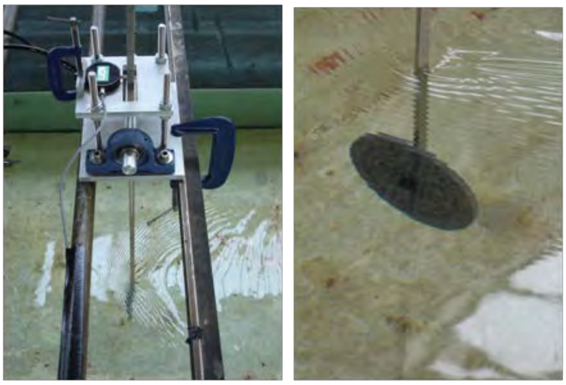

Fig. 2 Actuator lever arm rig (left) actuator disk mounted on lever arm (right)

The vertically unconstrained results which were used to compare with the constrained tests were presented by Myers et al. [2] and were conducted in the IFERMER circulating channel, Boulogne sur Mer, France. The channel has a working section of 18m in length, 4m wide and 2m deep. The downstream wake was mapped using a high frequency Acoustic Doppler Velocimeter (ADV). Operational issues and the accuracy of ADVs have been addressed at length in many publications [9-11]. The ADV was set to sample at 50Hz. For each data point 7500 readings were taken over a 150 second period.

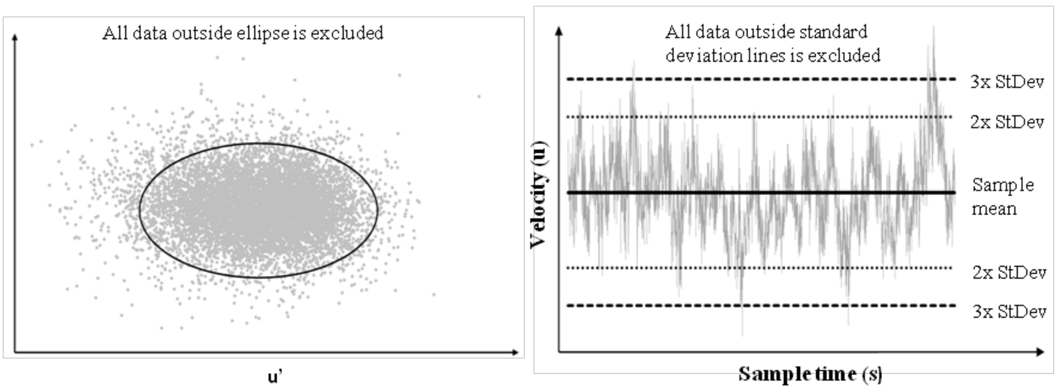

Fig. 3 Velocity correlation filtering method (left) and minimum/maximum filter (right).

Data was filtered to remove noise and spurious points (Fig. 3, shows data spikes) although the large quantity of suspended particles in the Chilworth channel minimised sample errors. Filtering is required to improve measurements of higher order flow effects such as turbulence intensity and shear stresses as spikes in the data give the impression of increasing energy within the flow. However filtering has a very small effect for mean flow velocities as spikes are generally equally positive and negative. All samples were filtered using a velocity cross-correlation filter ultimately chosen due to ease of use and effectiveness after a single pass [12]. This method plots the varying components of velocity against each other and constructs an ellipsoid in 3-dimensional space to exclude any data points that deviate significantly from the sample mean (Fig. 3, left). Similar filters can be set up to remove statistically or physically improbable values. Table 1 compares the velocity cross-correlation filter to a minimum-maximum filter (Fig. 3, right) that removes time-series values ±3 standard deviations from the sample mean. The effectiveness of the cross-correlation filter for the turbulence data is apparent.

Table 1 Minimum/maximum and velocity correlation filter comparison.

Sample	u-plane velocity ($m.s^{-1}$)				u-plane turbulence intensity (%)			
	Raw	Min/ max	Vel. Cor.	% Change from raw	Raw	Min/ max	Vel. Cor.	% Change from raw
1	0.245	0.245	0.246	+0.54	9.80	9.56	7.43	-24.18
2	0.295	0.295	0.291	-1.29	18.86	18.86	15.17	-19.54
3	0.286	0.286	0.286	-0.11	11.30	10.59	8.91	-21.14
4	0.287	0.286	0.284	-0.93	13.47	11.55	10.05	-25.41
5	0.246	0.246	0.247	+0.56	9.31	9.26	7.31	-21.45

The recovery of the wake is defined in terms of velocity deficit; this is a non-dimensional number relative to the free-stream flow speed at hub height and the wake velocity, defined by Eq. (1).

$$U_{def} = 1 - U_w / U_o \tag{1}$$

The ambient turbulence intensities in the circulating channel used during this study were approximately 6-8% and were calculated in all three planes (u,v,w). Turbulence intensity is commonly defined as the root-mean-squared of the turbulent velocity fluctuations divided by the mean velocity of the sample. Table 2 details the parameters of the constrained flow tests conducted as part of this work and the previously conducted unconstrained flow tests conducted at the IFERMER facility. Dimensions are detailed in disk diameters (D).

Table 2 experimental test parameters.

Test	Water depth	Channel width	Actuator centre from surface	Depth-averaged Froude No.	Depth-averaged Reynolds No.	Disk height/depth ratio
1	4.0	13	2.00	0.15	$1.2x10^5$	0.25
2	3.0	13	1.50	0.15	$7.8x10^4$	0.33
3	2.5	13	1.25	0.15	$5.7x10^4$	0.40
4	2.0	13	1.00	0.15	$4.2x10^4$	0.50
5	1.5	13	0.75	0.15	$2.7x10^4$	0.66
6*	20	40	2.00	0.113	$9.9x10^5$	0.05

*unconstrained test conducted at IFERMER, France.

Myers et al. [2] showed experimentally for a constant depth the wake velocity deficit is independent of velocity (for a representative range of Froude numbers).

3. Results and Discussion

Three cases from Table 2 will be addressed herein; A deep-unconstrained tidal site (test #6), a mid-depth tidal site (test #1) and a shallow-depth tidal site (test #4).

3.1. Free-stream results

Fig. 4 (left) shows the normalised vertical velocity profiles for the three cases, these are the free-stream results from the Chilworth and IFREMER facilities. Depth is expressed in terms of disk (or rotor, full scale) diameters (D). The velocity profile at Chilworth is well developed but the close proximity of the bed induces a more pronounced gradient that leads to disparate mass flow rates above and below the disk, this is most noticeable in the shallow-depth scenario. Flow speed in the deep site case is similar above and below the disk.

Fig. 4 (right) shows the ambient turbulence intensities in all three planes (u,v,w) for the deep-unconstrained and mid-depth scenarios (IFERMER and Chilworth channels, respectively). At the Chilworth facility the presence of the flume bed 2-diameters below the disk causes an increase in turbulence intensity immediately above the bed. u and v components are of a similar magnitude at 6-7% whilst turbulence intensity in the vertical plane is slightly greater. The IFERMER channel turbulence intensity is more constant with depth close to the disk. The turbulence intensity in the vertical plane is much lower than at Chilworth. The difference occurs due to the nature with which water is delivered to the upstream end of the working section.

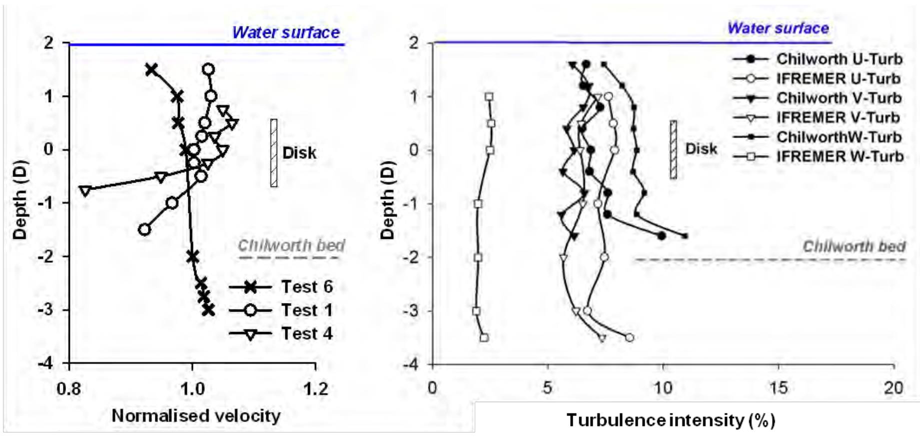

Fig. 4 Normalised vertical velocity profiles at the Chilworth and IFERMER water channels (left) and Turbulence intensities (right).

3.2. Wake length

Fig. 5 shows the longitudinal centre plane velocity deficits for the three depth cases. It is clear that in the mid-depth case the wake is broken down in a significantly shorter downstream distance than in the deeper and shallower cases (approximately 6D). This results from flow acceleration above and below the actuator disk that acts to break the wake down through greater lateral turbulent mixing. This effect was postulated by Myers et al. [2] and is reinforced following analysis of these results.

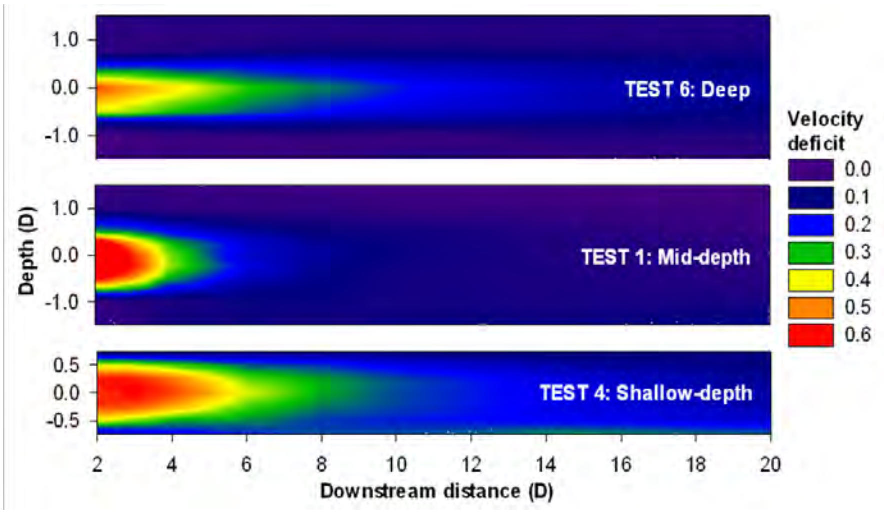

Fig. 5 Centre plane velocity deficit profiles; deep-site, mid-depth site & shallow-depth site.

The wake persists much further downstream in the deep-unconstrained and shallow depth cases (10-12D downstream), this results from restrictions in flow acceleration around the MCEC. In the deep-unconstrained case vertical blockage is low and hence flow acceleration is reduced, thus allowing the wake to persist further downstream. In the shallow flow scenario vertical blockage is high and hence local flow acceleration above and below the MCEC is restricted, again allowing wake to persist further downstream.

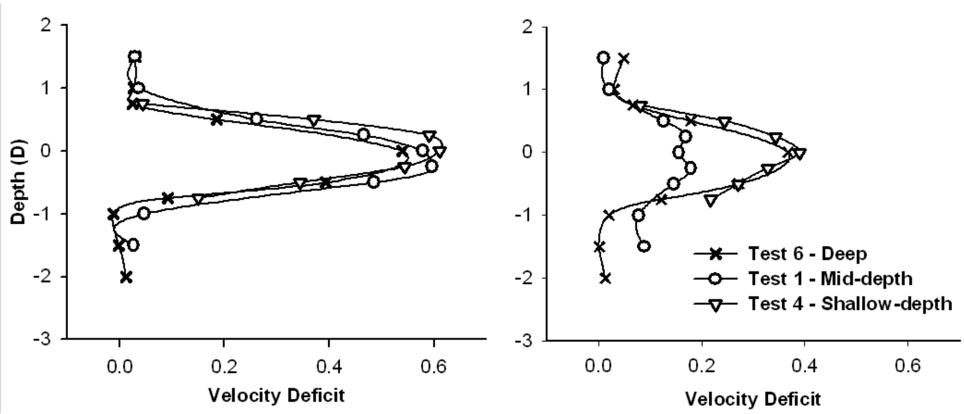

Fig. 6 Vertical velocity deficits at 3 diameters downstream (left) and 6 diameters (right)

Fig. 6 shows vertical line plots of velocity deficit at two downstream locations for all three depth cases. Looking at the 3D downstream graph it is clear that the initial velocity deficits directly behind a MCEC are similar irrespective of the vertical flow constraint; this is because wake is re-energised by turbulent mixing from the surrounding flow and in the near wake this effect is less pronounced. Further downstream e.g. 6D, the effects of varying degrees of vertical blockage can be seen. The deep and shallow cases give similar profiles, whereas the velocity deficits for the mid-depth case are reduced considerably because of increased turbulent mixing between the wake and accelerated surrounding flow. The effects of flow acceleration in the mid-depth case can be observed.

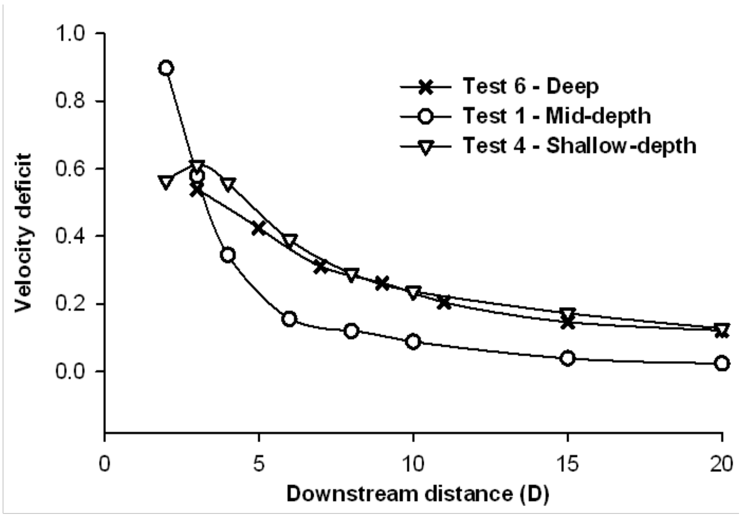

Fig. 7 Disk centreline velocity deficit comparison.

Fig. 7 shows the downstream centreline deficits. As suggested by Fig. 5 the wake recovers much more quickly in the mid-depth case. Again the principal mechanism for this is flow acceleration around the disk which serves to break up the wake more rapidly. In Fig. 7 the similarities in terms of downstream velocity deficits between the shallow and deep cases are clearly illustrated.

3.3. Farm row optimisation

This section highlights the significance and importance of this work to tidal stream farm design and optimisation. Fig. 8 shows there is an optimum rotor diameter/flow depth ratio in terms of wake recovery and minimising downstream wake length. Three different downstream location cases are compared for all the tests detailed in Table 2. It appears that 0.25 is the optimum rotor diameter/flow depth ratio for minimising downstream spacing. At full scale this might equate to a site with a depth range of 30-50m depending on the rotor diameter.

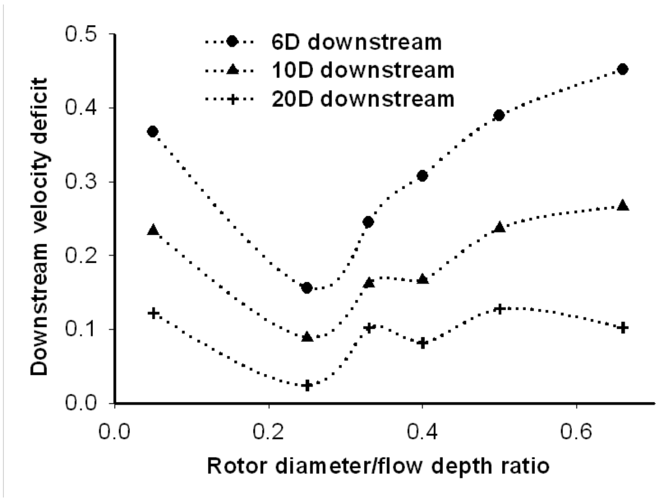

Fig. 8 Optimum rotor diameter/flow depth ratio in terms of wake recovery

4. Conclusions

From the results presented in this paper, it is critical that tidal stream farms or arrays are optimised in terms of downstream spacing and packing density, it will thus be important to tune the downstream device spacing to the local flow depth. Although at spatially constrained sites the spacing may be tightened in order to increase energy capture per surface area of the site and to reduce electricity connection costs. It is anticipated that many first generation sites will be located in shallow tidal flows and hence the longer wake lengths compared with mid-depth sites must be factored into the design process. In terms of the full scale significance and to reduce wake length, the optimum rotor diameter/flow depth ratio is 0.25. This would equate to a flow depth range of 30-50m depending on the rotor diameter.

The wake length is controlled by the degree of lateral flow mixing between the retarded wake flow and the surrounded accelerated free-stream flow. Increased wake length in very deep and very shallow flows result from vertical blockage, in a deep flow vertical blockage is minimal and hence local flow acceleration around the wake is reduced. In a very shallow flow vertical blockage is high and flow acceleration above and below the MCEC is restricted. Both these factors result in less lateral flow mixing and thus increased wake length. It is hoped that the relationship between vertical flow constraint and wake length will help with the layout design of future tidal stream farms.

Acknowledgements

This work has been conducted as part of an Engineering Doctorate study and has been jointly funded by the European and Physical Sciences Research Council (EPSRC) and IT Power Ltd. Work at IFERMER was funded by the Marine Environment Tests and Research Infrastructure (METRI II) programme and the UK Technology Strategy Board. “Performance characteristics and optimisation of marine current energy converter arrays”, project number T/06/00241/00/00.

References

[1] ABP, ‘Atlas of UK Marine Renewable Energy Resources: Technical Report’, ABP Marine Environmental Research Ltd, Department for Business, Enterprise & Regulatory Reform, 2008.

[2] L. Myers, A.S. Bahaj, G. Germain, J. Giles, ‘Flow boundary interaction effects for marine current energy conversion devices’, World Renewable Energy Congress X, Glasgow, 2008.

[3] T. Burton, D. Sharpe, N. Jenkins, E. Bossanyi, ‘Wind Energy Handbook’, Wiley, 2001

[4] A.S. Bahaj, L. Myers, M.D. Thomson, N. Jorge, ‘Characterising the wake of horizontal axis marine current turbines’, 7th European Wave and Tidal Energy Conference, Porto, Portugal, 2007.

[5] L. Myers, A.S. Bahaj, R.I. Rawlinson-Smith, M.D. Thomson, ‘The effect of boundary proximity upon the wake structure of horizontal axis marine current turbines’, 27th International Conference on Offshore Mechanics and Arctic Engineering, Estoril, Portugal, 2008.

[6] P. J. Connel, R.L. George, ‘The wake of the MOD-0A1 wind turbine at two rotor diameters downwind on 3 December 1981’, Pacific Northwest Laboratory, Battelle, U.S., 1982.

[7] P.E.J. Vermuelen, ‘Mixing of simulated wind turbine wakes in turbulent shear flow’, TNO Rep. 79-09974, Apeldoorn, Holland, 1979.

[8] J. Whelan, M. Thomson, J.M.R. Graham, J. Peiro, ‘Modelling of free surface proximity and wave induced velocities around a horizontal axis tidal stream turbine’, 7th European Wave and Tidal Energy Conference, Porto, Portugal, 2007.

[9] A. Lohrmann, R. Cabrera, N. Kraus, M. ASCE, ‘Acoustic-Doppler Velocimeter (ADV) for Laboratory Use’, Fundamentals and Advancements in Hydraulic Measurements and Experimentation, New York, USA, 1994.

[10] G. Voulgaris, J.H. Trowbridge, ‘Evaluation of the Acoustic Doppler Velocimeter (ADV) for Turbulence Measurements’, Journal of Atmospheric and Oceanic Technology, 1998, 15, pp. 272 – 289.

[11] P.J. Rusello, A. Lohrmann, E. Siegel, T. Maddux, ‘Improvements in Acoustic Doppler Velocimetery’, The 7th Int. Conf. on Hydroscience and Engineering, Philadelphia, USA, 2006.

[12] L. Cea, J. Puertas, L. Pena, ‘Velocity measurements on highly turbulent free surface flow using ADV’, Experiments in Fluids, 2007, 42, pp. 333 – 348.

Development of a Low Cost Point Absorber Wave Energy Converter for Electric Mobility

Jacob W. Foster[1], Reza Ghorbani[1], Pierre Garambois[2], Emma Jonson[3], Sten Karlsson[3]

[1]*University of Hawai`i at Manoa, Honolulu,USA;*
[2]*INSA, Lyon,France;*
[3]*Chalmers Univ. of Technology, Gothenburg, Sweden*
**Corresponding author: Tel 713-419-666; E-mail: fosterja@hawaii.edu*

Abstract: This paper presents a developing concept of a low cost "point absorber" Wave Energy Converter (WEC). The WEC is unique in that instead of operating with one buoy, two are used to optimize the hydrodynamic response and energy output. This makes the design a three-part system: the surface buoy provides the vertical translation and hosts the primary interface for energy absorption, the power take-off (PTO) device which is a direct drive permanent magnet AC generator, and lastly the tension buoy that feeds through the PTO to the surface buoy. The total cost of the 2 KW WEC is less than $2000 USD including the PMAC generator, power converter and cable to charge the batteries for electric vehicles. The integrated dynamics of the WEC and the PTO are presented using a simplified model of a heaving buoy. The wave energy resource of a test location is analyzed and presented based on data from a global Wave Watch III model surrounding Oahu. The characteristics and distributions of the movement patterns of individual vehicles are measured. It was shown that regenerative braking power has the major role in reducing the total energy consumption and decreasing the size of the required battery to be charged externally by the WEC. In addition the power used by vehicle follows the Rayleigh distribution. Thus, the batteries for individual driver are customizable. This significantly reduces the amount of energy required by distributed WEC generators.

Keywords: *Wave energy conversion, point absorber, electric vehicle*

1. Introduction

Throughout the development of Wave Energy Conversion devices theoretical solutions have been produced for various methods of energy extraction for both point absorbing buoys and oscillating water column devices. Analytical solutions are formulated from the hydrodynamic interaction between the device interfaces with incoming waves (see Evans 1981, Newman 1979; McCormick 1980, Cruz 2008, Garnaud and Mei 2010).

As WEC technologies have evolved some commercial entities have taken the stage in pursuing industrial development of these devices for large scale energy production (Clément et al. 2002). Care is taken into selecting design criteria based on hydrodynamic and power-take-off (PTO) parameters. It is of use to identify these criteria so as to perform a wave climate-wise optimization. This paper presents the design of a wave-energy conversion device and a brief overview of the wave-climate at the location where the device is to be tested. The characteristics and distributions of the movement patterns of individual vehicles are measured. It was shown that regenerative braking power has the major role in reducing the total energy consumption and decreasing the size of the required battery to be charged externally by the WEC. In addition the power used by vehicle follows the Rayleigh distribution. Thus, the batteries for individual driver are customizable. This significantly reduces the amount of energy required by distributed WEC generators.

2. Methodology

To develop a general equation for the power capture capability of this device the analytical solution of a small point absorber, as presented by Garnaud and Mei (2010), is discussed and extended for the WEC device in this section. A wave climate analysis is provided to present base climate criteria of which control variables must be optimized for WEC. The site selected is located off the North East coast of the Island of Oahu where trade-wind seas are predominant.

2.1. Power extraction concept:

The premise for the WEC device is the uniqueness of the power-take-off system. The PTO unit is sealed and anchored to the sea-floor. Housed within are the motor/generator and inertial wheel which are driven via an external capstan (see Fig.1). The design is based on a dry PTO unit. In this setup the PTO is not sealed watertight to be submerged and anchored to the sea-floor (see Fig. 2.). Rather, it is suspended safely above the sea-surface via a column fastened to the concrete anchor-base.

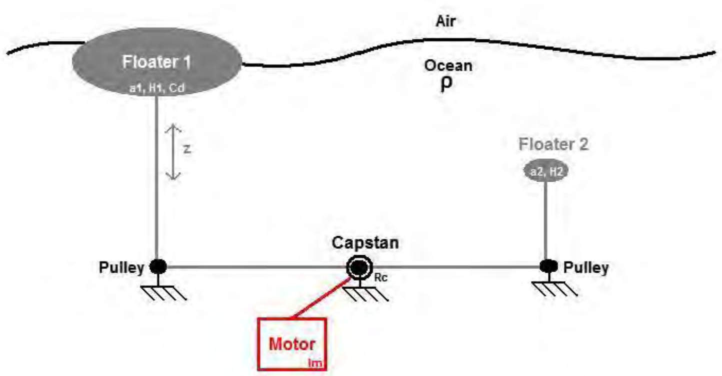

Fig. 1. Schematic of the three-part WEC device

The PTO capstan is the primary interface between the two buoys. Through it, the vertical buoy motion due to forcing from incoming waves is transferred to rotational motion to be resisted by the motor/generator and inertial wheel. While the larger-floating buoy acts as a *point absorber* with incoming waves the smaller submerged buoy provides the required tension to resist slipping between the tension line and the capstan. The tension relationship is defined as:

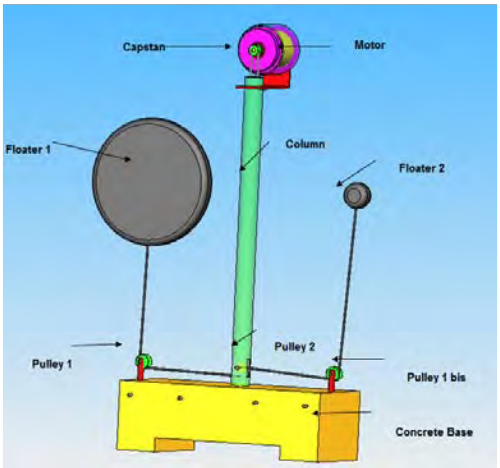

Fig. 2. Dry PTO WEC design

$$T_2 = T_1 e^{\mu * \theta round}, \tag{1}$$

where, $\mu = 0.4$ (the friction coefficient between rope and steel) and T_1; T_2 are the tension on the line approaching the point-absorber and the tension buoy respectively.

Through investigation we find that the required size of tension buoy is significantly smaller than that of the point-absorber. With this in mind we begin to develop the general equation for the average power extraction of the three-part WEC device.

The following formulation for such a solution is an extension of the analytical solution presented by Garnaud and Mei (2010) for a single-small point absorber. To demonstrate the performance of a single degree of freedom system, a buoy responding due to the vertical heave forcing of a wave (with angular frequency ω and amplitude A) is considered. Incoming wave potential is defined as

$$\Phi_I = \varphi_I e^{-i\omega t} \tag{2}$$

with

$$\varphi_I = \frac{Ag}{i\omega}\frac{\cosh(k(z+h))}{\cosh(kh)}e^{ikx} \tag{3}$$

where ω and k are related by the dispersion relation

$$\omega^2 = gk\tanh(kh). \tag{4}$$

At this point Garnaud and Mei (2010) make a simplification based on the small size of the surface buoy relative to incoming wave length, in that the scattered and radiated waves are negligible. This is from the Froude-Krylov approximation where the hydrodynamic pressure on the buoy is dominated by the undisturbed incoming wave (Newman 1979). The vertical excitation force on a buoy of radius, a, and draft, H, becomes

$$i\rho\omega\int\int(0,0,0),dS = \rho gA\pi a^2. \tag{5}$$

We now include the power-take-off influence of the 3-part device to the general WEC equation by assuming the PTO exerts a load of $\omega^2\lambda_g\zeta$ where λ_g is the extraction rate, and ζ is the buoy displacement. The force due to the inertial wheel can be included as $\frac{I*\ddot{\varsigma}}{R_c}$, where I is the inertia the drive system, and R_c is the radius of the capstan. The added buoyancy force on the floating buoy, due to heave is $\pi a_1^2\rho g\varsigma$ then by Newton's law

$$(M_1\varsigma + M_2\varsigma + \frac{I\varsigma}{R^2{}_c})\omega^2 + \lambda_g\varsigma i\omega + \pi\rho g a_1{}^2\varsigma = \pi\rho g a_1{}^2 A, \tag{6}$$

where M_1 and M_2 can be defined from Archimedes principle as:

$$M_1 = \rho\pi a_1{}^2 H_1 \tag{7}$$

and

$$M_2 = \rho\pi a_2{}^2 H_2 / 2. \tag{8}$$

From this we can define a transfer function for amplitude of response as

$$\frac{\varsigma}{A} = \frac{1}{\{\frac{H_1}{g} + \frac{H_2}{2g}(\frac{a_1}{a_2})^2 + \frac{I}{R_c^2\rho\pi a_1^2}\}\omega^2 + \frac{\lambda_g}{\rho\pi a_1^2 g}i\omega + 1} \tag{9}$$

This lets us define the time average rate of energy extraction at a single frequency as

$$P_{buoy} = \overline{\lambda_g [\ \ e(\varsigma e^{i\omega t})]^2} = \frac{1}{2}\omega^2 \lambda_g |\varsigma|^2 \tag{10}$$

or, for an irregular time series of multiple frequencies

$$P_{buoy} = \frac{1}{2}\lambda_g |\dot{\varsigma}|^2 . \tag{11}$$

2.2. Wave climate and optimization schemes

The data for the climate-wise optimization was provided by (Arinaga and Cheung 2011 and Stopa and Cheung 2011). Ten years of wave hindcast parametric spectral data based on significant wave height, H_s, and peak period, T_P, were generated using a global Wave Watch III simulation with a nested output for the Hawaiian Islands. (An explanation of wave power spectrum can be found in Cruz, 2008). Fig. 2 depicts this data in a multivariate histogram displaying the frequency of occurrence in color of a sea-state with parameters $H_{s,}$, T_P along the vertical and horizontal axis.

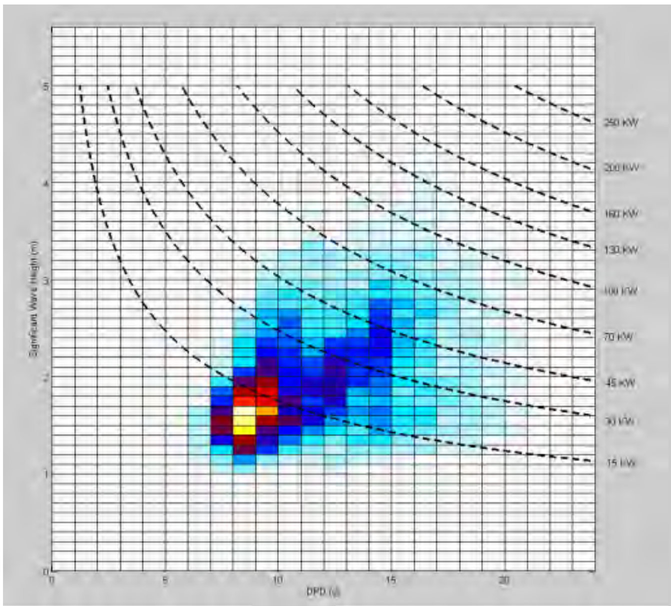

Fig 2. Multivariate histogram of sea-state occurrence with incident wave power contour lines. The horizontal and vertical axis relate to the peak period and significant wave height of a six-hour sea-state respectively. The frequency of occurrence is shown in color, and contour lines depict wave power per sea-state at the associated Tp and Hs per the Bretschneider spectrum approximation.

The contour lines represent the *average power per energy period* within a sea-state at the associated $H_{s,}$, T_P value and are given by:

$$P_o = \rho g^2 \frac{H_s^2 T_e}{64\pi} . \tag{12}$$

This formulation is derived from the statistical moments of a wave power spectrum. For a Bretschneider spectrum

$$S(\omega) = \frac{5}{16} H_s^{\,2} \frac{\omega_p^{\,4}}{\omega^5} e^{-5/4(\frac{\omega_p}{\omega})^4} \tag{13}$$

the following relationship can be defined:

$$T_e = 2\pi \frac{m_{-1}}{m_o} = 0.857 * T_P \, . \tag{14}$$

Where m_{-1}, m_o are spectral moments of the curve, $S(\omega)$. The wave amplitude for any given angular frequency can be found from

$$A = \sqrt{2 * S(\omega) * \omega} \, . \tag{15}$$

The *Capture Width* of a device is used evaluate a WEC's performance at any given frequency. This is the ratio of the *total mean power* absorbed by the WEC to the *mean power per unit wave crest width* of the incident wave train;

$$l(\omega) = \frac{P_{buoy}}{P_o} \, . \tag{16}$$

Since the incident wave power is per unit wave crest width, the absorption width is length dimensional (and ideally greater than the width of the device itself). The total incident wave power in a single sea-state, $S(\omega)$, is given as

$$P_T = \rho g \int_0^\infty S(\omega) c_g(\omega) d\omega \tag{17}$$

where

$$c_g(\omega) = g / 2\omega \tag{18}$$

for deep water, as derived from the dispersion relationship. The power absorption capability in a sea-state can be computed by multiplying the capture width of a WEC at each frequency in the above integral to obtain the total absorbed power. This is defined as

$$P_T = \rho g \int_0^\infty S(\omega) c_g(\omega) l(\omega) \, d\omega \tag{19}$$

Since P_T = f (H_s,, T_P) for each sea-state, a long-term analysis for a single site requires the use of the multivariate histogram to compute the probability of occurrence of sea-states, $S(\omega)$, which may occur during the operational lifetime of the WEC. With this knowledge in hand one can begin to identify variable design parameters to be optimized for device operation. We allow λ_g to be the free variable for power extraction optimization since the extraction rate can be controlled by power delivery mechanisms. If the desire is to optimize the WEC system in a "robust" manner (i.e. that it is suited for a range of sea-states which may occur over the lifetime of the device) this variable is optimized for maximum average power extraction according to Eq. (19) where the capture width $l(\omega)$, by definition, carries λ_g from Eq. (10) and Eq (16).

However, in the interest of fine-tuning the device response for individual incoming sea-states, which may be predicted by meteorological and wave forecast methods, the optimization will be performed on Eq. (11) alone, such that an optimum value of λ_g can be found at each frequency (ω) of a wave power spectrum Eq. (13). To illustrate the latter optimization scheme the generator extraction rate, $\lambda_{g,}$ was set to values of 1000, 5000 and 10000 kg/s respectively.

3. Results

3.1. Wave Buoy Response Simulation

The buoy response was computed in the time domain utilizing the time series simulation platform Simulink from MATLAB. The response transfer function, Eq. (9), was directly applied to a simulated 200 second time series wave-record which was generated by discretizing a Bretschneider Spectrum Eq. (13). The numerical spectrum was formed with a significant wave height was 1.5 meters and peak period of 9 seconds to agree with the typical sea-states at the selected site. Following Eq. (11) the average power extraction of the device is computed, and then by simple integration the energy is calculated and presented. As expected the buoys response experiences a lag of the incoming wave motion and varies significantly based on the selected extraction rate as shown in Fig. 4.

3.2. Electric Vehicle Power Study

A Swedish car movement data project started in June 2010 in the Västra Götaland county, going on until June 2011. The aim is to gather a larger amount of data on the characteristic and distribution of the movement patterns of individual, privately driven cars in Sweden by measurement with gps equipment.

We use data from six cars in the Swedish car movement data project, each driving one day, to investigate the probability distribution of the momentary power consumption. The propulsion is equal to the sum of the aerodynamic drag, frictional forces and the acceleration force.
The potential energy from regenerative braking, i.e. the integral of negative power, is, based on this statistics data, greater than 50% of the propulsion energy (53 MJ compared to 100 MJ). Regenerative braking therefore has good potential for reducing energy use per km driven. The power could be approximated by a Rayleigh probability density function as shown in Fig. 5. The performance of electric vehicles can be improved by modifying the type of the batteries to be a combination of high-power and high-energy batteries. The high-power batteries improve the gas mileage through regenerative braking and the high-energy batteries can be charged by WEC during opportunity charging. This reduces the required number of charging stations and perhaps the total infrastructural cost associated with electric mobility using distributed energy sources.

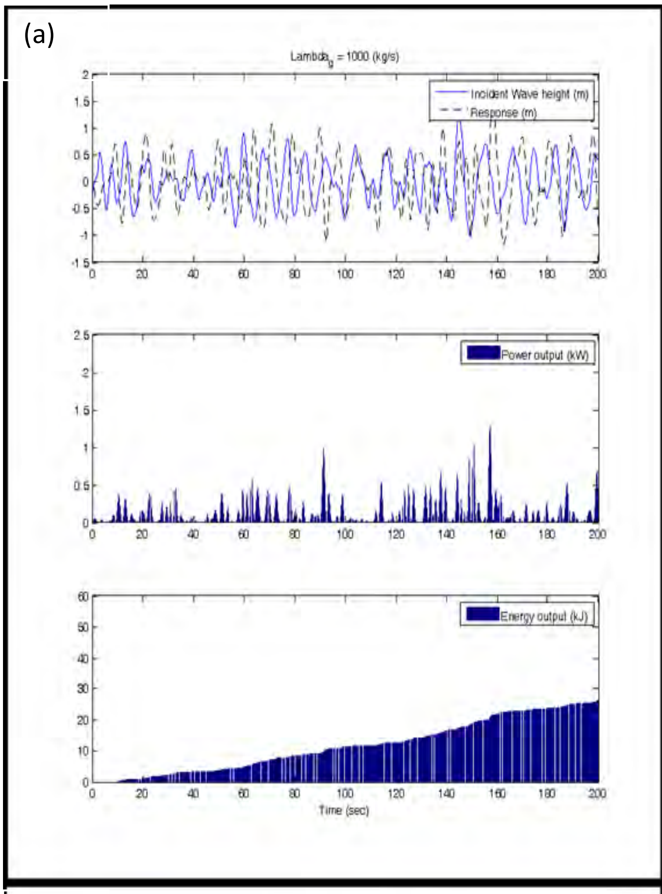

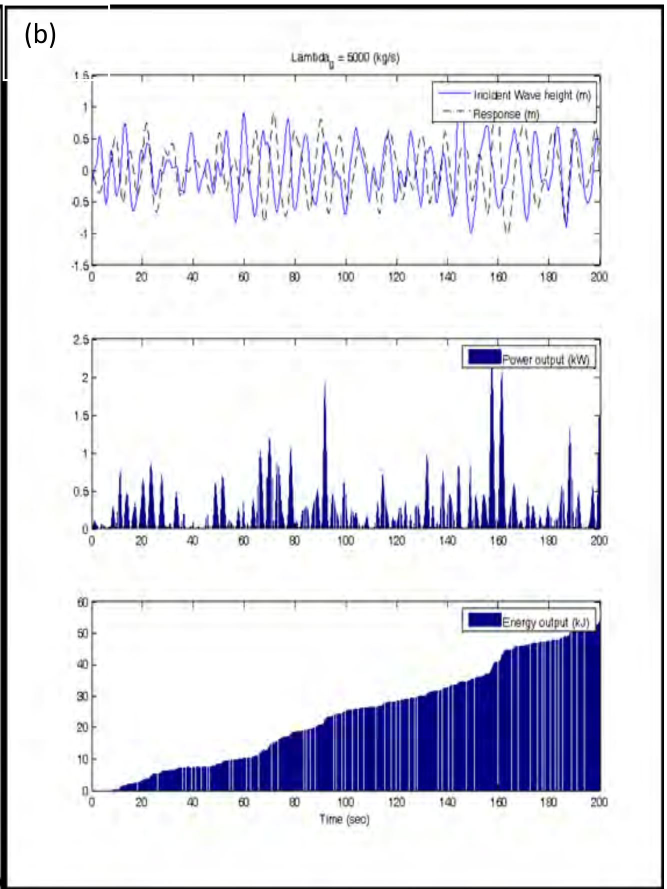

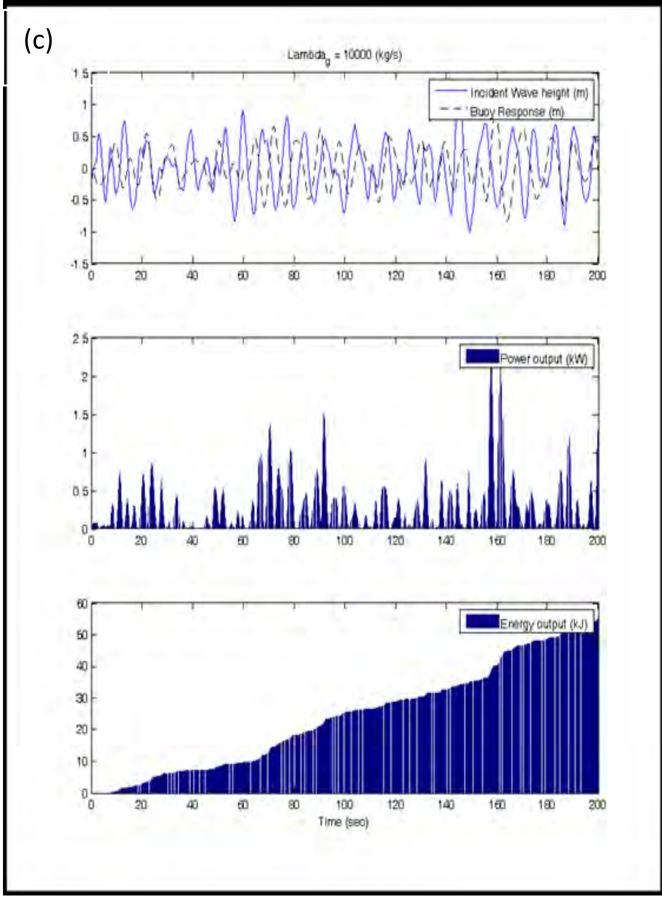

Fig. 4. Buoy Response with λ_g= (a) 1000 kg/s, (b) 5000 kg/s , (c) 10000 kg/s. The buoy response is presented along with the incident wave motion. The power extraction capability is displayed based on the velocity of the buoys response squared and the generator extraction rate. The energy is computed as the integral of the absorbed power.

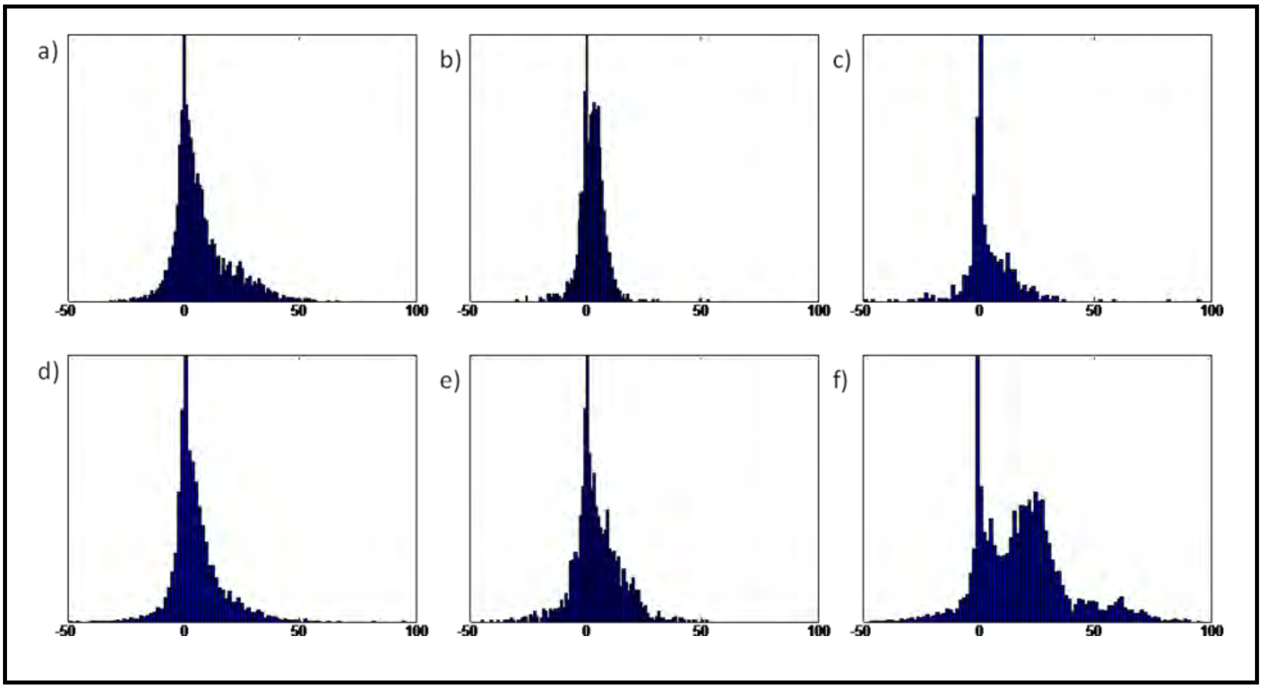

Fig. 5. Probability Histograms

References

[1] Evans, D. V. "Wave-power Absorption by Systems of Oscillating Surface Pressure Distributions." Journal of Fluid Mechanics 114.-1 (1982): 481-99. Print.

[2] Newman, J. "Absorption of Wave Energy by Elongated Bodies." Applied Ocean Research 1.4 (1979): 189-96. Print.

[3] MacCormick, Michael E. Ocean Wave Energy Conversion. 1981. Print.

[4] Cruz, João. Ocean Wave Energy. Berlin: Springer, 2008. Print.

[5] Garnaud, Xavier, and Chiang C. Mei. "Bragg Scattering and Wave-power Extraction by an Array of Small Buoys." Proceedings of the Royal Society 466.2113 (2010): 79-106. Print.

[6] Cle´ment,, Alain, Pat McCullen,, Antonio Falca˜o, Antonio Fiorentino, Fred Gardner, Karin Hammarlund, George Lemonis, Tony Lewis, Kim Nielsen, Simona Petroncini, Teresa Pontes, Phillippe Schild, Bengt-Olov Sjo¨stro¨m, Hans Christian Sørensen, and Tom Thorpe. "Wave Energy in Europe: Current Status and Perspectives." Renewable and Sustainable Energy Reviews 6 (2002): 405-31. Print.

[7] Arinaga, R.A. and Cheung, K.F. Atlas of global wave energy from 10 years of reanalysis and hindcast data. Renewable Energy, in review

[8] Stopa, J.E., Cheung, K.F., and Chen, Y.-L. (2011). Assessment of wave energy resources in Hawaii. Renewable Energy, 36(2), 554-567.